Light-addressable potentiometric sensors based on self-assembled organic monolayer modified silicon on sapphire substrates

Wang, Jian

For additional information about this publication click this link.
http://qmro.qmul.ac.uk/xmlui/handle/123456789/12955

Light-addressable potentiometric sensors based on self-assembled organic monolayer modified silicon on sapphire substrates

by Jian Wang

August 2015

A thesis submitted for the degree of Doctor of Philosophy (Ph.D.) to the

School of Engineering and Materials Science

Queen Mary University of London

Declaration

I certify that the present work is prepared solely by me during the course of my studies at Queen Mary, University of London. It has not been submitted for a degree at this or any other university. Any words and/or figures from the work of other people are fully acknowledged according to standard referencing.

This thesis fully complies with the regulations set by the University of London and the Queen Mary, University of London.

Jian Wang

August 2015

Abstract

Light-addressable potentiometric sensors (LAPS) have become attractive in many chemical and biological sensor applications. This thesis introduces the use of self-assembled organic monolayers (SAMs) as the insulator in LAPS and scanning photo-induced impedance microscopy (SPIM) for the first time. Two types of monolayer assemblies with alkenes (1-octadecene or undecylenic acid) and alkynes (1, 8-nonadiyne) were immobilised on hydrogenated silicon on sapphire (SOS) or silicon through thermal hydrosilylation. Further derivations were performed on the 1, 8-nonadiyne monolayers via "click" reactions. The monolayers were characterised by water contact angle, ellipsometry and X-ray photoelectron spectroscopy (XPS). LAPS/SPIM measurements with SAM-modified SOS showed the same good spatial resolution that was previously obtained with a conventional SiO_2 insulator on SOS, but also a significant improvement in the accuracy of LAPS and the sensitivity of SPIM.

Surface potential imaging using LAPS insulated by SAMs was validated by studying micropatterns of poly(allylamine hydrochloride) (PAH), poly(styrene sulfonate) (PSS) and DNA on a PAH template. Two potential strategies for chemically patterning SAMs on oxide-free SOS or Si substrates were investigated and compared. Microcontact printing (µCP) followed by "click" chemistry is a mild and efficient means of modifying the surface, whereas the combination of photolithography and "click" chemistry is not. LAPS was also shown to be extremely sensitive to surface contamination.

LAPS/SPIM insulated by SAMs can also generate impedance images with high resolution and high sensitivity. Microcapsules labelled with gold nanoparticles (AuNPs) integrated with a femtosecond laser were used for the validation. In contrast, capsules without AuNPs showed no SPIM response at all, indicating that the impregnation with AuNPs can significantly increase the impedance of microcapsules.

Finally, new instrumentation to integrate two-photon fluorescence microscopy with LAPS/SPIM was proposed. Preliminary results have shown that the new technique is promising to produce two-dimensional electrochemical images and two-photon fluorescent images of the cell-attachment area with subcellular resolution.

Publications

1. Jian Wang, Yinglin Zhou, Michael Watkinson, Julien Gautrot, Steffi Krause*. High-sensitivity light-addressable potentiometric sensors using silicon on sapphire functionalized with self-assembled organic monolayers. Sensors and Actuators B: Chemical, 209 (2015) 230-236.

2. Jian Wang, Fan Wu, Michael Watkinson, Jingyuan Zhu, Steffi Krause*. "Click" patterning of self-assembled monolayers on hydrogen-terminated silicon surfaces and their characterization using light-addressable potentiometric sensors. Langmuir, 31 (2015) 9646-54.

Acknowledgments

Table of contents

List of abbreviation

ACP	1-Amino-3-cyclopentene
ADE	10-Aminodec-1-ene
AEG	Anodic electrografting
AFM	Atomic force microscopy
AMC	7-Amino-4-methylcoumarin
4-AP	4-Aminopyridine
API	4-Azidophenyl isothiocyanate
AuNPs	Gold nanoparticles
BSA	Bovine serum albumin
CEG	Cathodic electrografting
CHO-K1	Chinese hamster ovary wild type cells
CHO-M1	Chinese hamster ovary muscarinic type cells
μCP	Microcontact printing
CuAAC	Copper(I)-catalyzed azide alkyne cycloaddition
C-V	Capacitance-voltage
dsDNA	Double-strand DNA
3-D	Three-dimensional
DCM	Dichloromethane
DPN	Dip-pen nanolithography
DQ	Diazonaphthaquinone
DS	Dextran sulfate
ECM	Extracellular matrix
ECIS	Electric cell-substrate impedance sensing
EDC	N-ethyl-N'-(3-dimethylaminopropyl) carbodiimide
EDTA	Ethylene diamine tetraacetic acid
EEC	Equivalent electrical circuit

EIS	Electrolyte-insulator-silicon
EOMOS	Electrolyte-oxide-metal-oxide-silicon
FETs	Field-effect transistors
FLIC	Fluorescence interference contrast
FRA	Frequency response analysis
FTIR	Fourier transform infrared spectroscopy
GL	Gaussian-Lorentzian
GPES	General purpose electrochemical system
Hb	Hemoglobin
HbA1c	Hemoglobin-A1c
HEK 293	Human embryonic kidney cells
HEPES	4-(2-Hydroxyethyl)piperazine-1-ethanesulfonic acid
HRP	Horseradish peroxidase
ICA	Indene carboxyl acid
IgG	Immunoglobulin G
IR	Infrared
ISFETs	Ion-selective field-effect transistors
I-V	Photocurrent-voltage
JFET	Junction field-effect transistor
J-V	Current density-voltage
LBL	Layer-by-layer
LAPS	Light-addressable potentiometric sensor
m-dPEG	m-d-Poly(ethylene glycol)
MESFET	Metal-semiconductor field-effect transistor
MF	Melamine formaldehyde
MIS	Metal-insulator-semiconductor
MISJFET	Metal-insulator-semiconductor junction field-effect transistor
MOS	Metal-oxide-semiconductor

MOSFET	Metal-oxide-semiconductor field-effect transistor
MSE	Mean squared error
MTA	Multi-transistor-array
NHS	*N*-Hydroxysuccinimide
NPs	Nanoparticles
OEG	Oligo(ethylene glycol)
PAH	Poly(allylamine hydrochloride)
PDAC	Poly(diallyldimethylammonium chloride)
PDADMAC	Poly(diallyldimethylammonium chloride)
PDMS	Polydimethylsiloxane
PE	Polyelectrolytes
PEM	Polyelectrolyte multilayer
PL	Poly-lysine
PLOL	Poly-L-ornithine and laminin
PMA	Poly(methacrylic acid)
PLMCs	Polymeric multilayer capsules
PMMA	Poly(methyl methacrylate)
PPy-AuNPs	Polypyrrole-gold nanoparticle
PS	Polystyrene
PSS	Poly(styrene sulfonate)
PVPON	Poly(*N*-vinylpyrrolidone)
RBITC	Rhodamine B isothiocyanate
RGD	Arginine-glycine-aspartic acid
PR	Protamine
ssDNA	Single-strand DNA
SAMs	Self-assembled monolayers
SD	Standard derivation
SOI	Silicon-on-insulator

SOS	Silicon-on-sapphire
SPIM	Scanning photo-induced impedance microscopy
SPL	Scanning probe-based lithography
SPS	Sulfonated poly(styrene)
SSMCC	Sulfo-succinimidyl 4-(*N*-maleimidomethyl)-cyclohexane-1-carboxylate
STM	Scanning tunneling microscopy
t-BOC	*t*-Butyloxycarbonyl
TEA	Tetraethylammonium chloride
TEMPO	Tetramethylpiperidinooxy
TMG	Trimethylgermanyl
TMEDA	*N*, *N*, *N*′, *N*′-Tetramethylethylenediamine
TTF	Transistor-transfer function
UV	Ultraviolet
XPS	X-ray photoelectron spectroscopy
XRR	X-ray reflectivity

List of symbol

a	light absorption coefficient
a_{memb}	chemical activity of ion in membrane
a_{sol}	chemical activity of ion in solution
c	speed of light in vacuum (3.0×10^8 m/s)
C_{ox}	area specific capacitance of oxide
c_s	speed of light in the semiconductor
C	capacitance of MOS
C_{tot}	total capacitance
C_c	capacitance of collapsed microcapsule
C_d	deplection layer capacitance
C_{FB}	flat band capacitance of MOS
C_{ii}	insulator capacitance within illuminated area
$C_{interface}$	interface capacitance (e.g. double layer capacitance)
$C_{insulator}$	insulator capacitance
C_m	capacitance of organic monolayer
C_{m-c}	total capacitance of C_m in series with C_c
C_{m-SU8}	total capacitance of C_m in series with C_{SU8}
C_{min}	minimum total capacitance of MOS
C_M	effective cell membrane capacitance
C_{ox}	oxide capacitance
C_{ox-SU8}	total capacitance of C_{ox} in series with C_{SU8}
C_s	semiconductor capacitance
C_{sc}	space charge layer capacitance
C_{ss}	surface state induced capacitance
C_{SU8}	SU-8 capactitance
d_J	cell-ECM junction width

d_{max}	maximum width of the inversion layer of MOS
d_{ox}	thickness of the insulator (oxide)
e	Euler's constant (e ≈ 2.718)
e_0	electron charge
E	voltage
E_0	standard membrane potential in ISFET
E_B	binding energy of electron
E_c	conduction band energy
E_d	donor energy level
E_F	Fermi energy
E_g	bandgap energy
E_i	intrinsic Fermi energy
E_k	kinetic energy of the emitted photoelectron
E_m	electrical potential difference at the solid/liquid interface
E_{photon}	photon energy
E_v	valence band energy
f	frequency
F	Faraday constant
$F(x_0)$	light intensity at surface point x_0
g	number of quantum states of dopant atoms (2 for a donor and 4 for an acceptor)
g_a	additional light-induced charge carriers generation rate
g_{JM}	area specific leak conductance of the attached cell membrane
h	Planck constant ($6.62606957 \times 10^{-34}$ m^2 kg s^{-1})
I	photocurrent
I_{max}	maximum photocurrent
I_{min}	minimum photocurrent

I_{SD}	source-drain current
J	current density
k	Boltzmann constant (J K^{-1} mol^{-1})
L	diffusion length of minority charge carriers
L_{wr}	distance between working and reference electrodes
n_0	thermal equilibrium concentration of electrons
n_i	intrinsic carrier concentration
n_r	index of refraction
$n(\lambda)$	index of refraction at light wavelength λ
N_a	concentration of acceptors
N_c	effective density of states in the conduction band
N_d	doping concentration
N_v	effective density of states in the valence band
p_0	thermal equilibrium concentration of holes
q	elementary charge
r	radius of the electrode
r_m	photocurrent ratio on SU8-uncoated and coated areas based on organic monolayers
r_J	sheet resistance of the cell-ECM junction
r_p	reflectivity of p-polarized light
r_s	reflectivity of s-polarized light
r_{the}	theory spatial resolution of LAPS
R	gas constant
R_{el}	electrolyte resistance
R_J	cell-ECM junction resistance
t	time
$\tan(\psi)$	magnitude of the reflectivity ratio in ellipsometry

T	temperature
V	bias voltage
V_{ds}	voltage between drain and source
V_E	electrolyte voltage
V_{FB}	flat band voltage
V_g	gate voltage
V_J	voltage of cell-ECM junction with respect to the ground
V_M	voltages of cell with respect to the ground
$V_m(t)$	modulated intracellular voltage at time t
$V_p(t)$	applied AC voltage at time t
V_S	surface potential of the semiconductor
V_T	threshold voltage
w	parameter of beam width for LAPS measurement
x, y, z	directions or positions
z_c	charge of ion
Z	impedance
Δ	light phase difference
ε_0	electric permittivity of vacuum
ε_{ox}	electric permittivity of oxide
$\varepsilon_{PAH/PSS}$	dielectric constant of PAH/PSS layer
ε_s	electric permittivity of semiconductor
θ	water contact angle
κ	conductivity of the electrolyte
λ	light wavelength
λ_L	penetration depth of light in semiconductor
μ_e	electron mobility
μ_h	hole mobility

v	light frequency
ρ	ellipsometry measured complex reflectance ratio
ρ_J	specific resistance of cell-ECM junction
σ	conductivity of semiconductor
$\Delta\sigma$	photoconductivity of semiconductor
τ_p	lifetime of the minority carriers
χ	absorption index of semiconductor
Φ	work function
ω	angular velocity

List of tables

List of figures

1. Introduction

1.1 Background and motivation

It is well known that computers and brains both work electrically but they use different charge carriers (electrons in computer chips and ions in brains). Due to the two different information processors, neuroelectronic devices that can transfer information between the human nervous system and semiconductor-based electronics remain in their infancy. Nevertheless, the scaled down project of understanding the neuron-semiconductor interface has made great progress over the last three decades. To record the electrical information of neural cells or slices of brain tissue on a solid substrate, methods such as optical recording with membrane-bound voltage-sensitive dyes [1, 2], extracellular recording with microelectrodes and field-effect transistors (FETs) [3] have been developed. However, voltage-sensitive dyes suffer from phototoxicity, which prohibits their long-term use [4]. Microelectrodes and FETs are non-invasive techniques and have successfully been used to monitor extracellular action potentials [5] and the impedance of cells [6-8]. However, due to the geometrical restrictions, microelectrodes or FETs are limited to effective sites for measurements [9]. These active sites have diameters of a few μm and are typically separated by 50 μm to 250 μm, making it impossible to investigate subcellular features. In addition, it is hard to control the cell coverage on these active areas and many cells may grow altogether outside the active sites. To improve this situation, a multi-transistor-array (MTA) system using a 1 mm^2 array of 128 × 128 sensor transistors was introduced. It was shown that MTA recording enables the imaging of neuronal activities at a resolution of 7.8 μm [5, 10]. However, the manufacturing of MTA is complicated and expensive, and the resolution of measurements is still limited.

Light-addressable potentiometric sensor (LAPS)/scanning photo-induced impedance microscopy (SPIM) overcomes these problems. Based on an electrolyte-insulator-silicon (EIS) field-effect structure, multi-sites on LAPS/SPIM chips can be addressed by scanning a focused light beam across the sensor substrates, providing information of surface potentials and impedance with lateral resolution. The flat and featureless spatial sensor substrates are of benefit for growing of cells, and the fabrication of LAPS/SPIM is much simpler and cheaper than that of FETs. So far, LAPS has been used successfully for the measurement of extracellular action potentials [11, 12] and

extracellular pH changes [13]. All of the above LAPS measurements suffered from poor, ill-defined resolution of about 10-100 μm. Using silicon-on-sapphire (SOS) substrates and a two-photon effect, submicrometer resolution was achieved [14]. This progress in resolution could contribute to the development of a platform for imaging the ion channel activity and metabolic behaviour of a single cell. Meanwhile, the sensitivity of SPIM has also been improved by using a thin anodic oxide (~7 nm) as the insulator [14]. However, the preparation of the thin anodic oxide is a multi-step process with low throughput.

In this work, we sought to advance the technique of LAPS/SPIM further through the replacement of the insulator with an ultrathin organic monolayer. Self-assembled monolayers (SAMs), which are directly grafted onto silicon without an intervening layer of silicon dioxide, are stable and can be prepared with mild and highly efficient methods [15]. Their excellent insulating effects have been demonstrated in electrochemical impedance measurements [16]. The selective control of surface chemistry and the small thickness are expected to extend the applications of field-effect devices in the fields of chemical and biological sensors [17-20].

The main goal of this project is to develop methods for surface modification and patterning on SOS or Si that allow the use of organic monolayers as the insulator in LAPS and SPIM measurements. To validate the feasibility of SAMs and the surface potential imaging, polyelectrolyte patterns and chemical molecular patterns were used. To demonstrate the high resolution of impedance imaging, polyelectrolyte microcapsules labelled with gold nanoparticles (AuNPs) were addressed and mapped using SPIM measurements. We also sought to develop a novel technique to integrate LAPS/SPIM and two photon fluorescence microscopy in a way that allows simultaneous recording of electrochemical and optical images of single neuronal cells, for example, to measure extracellular potentials and impedance changes in neurons following stimulation and to investigate cell responses to semiconductor substrates in the cell surface attachment area with micrometre resolution.

1.2 Semiconductor fundamentals

1.2.1 Fundamental properties

A semiconductor conducts electricity better than an insulator, such as rubber, but worse than a conductor such as a metal. The unique electric conductive behaviour of a

semiconductor is determined by its unique electronic band structure. Since the energy gap between these bands is 0.1-3 eV, very little energy is required for the electrons to transfer from the almost fully occupied valence band to the almost empty conduction band. In the semiconductor, there are always two types of bandgap: a direct bandgap and an indirect bandgap (see Figure 1.1). In a direct gap, the maximal energy state of the valence band and the minimal energy state of the conduction band are at the same value of the crystal momentum (k-vector), thus making the smallest energy transition occur without changing the crystal momentum. In an indirect gap, however, the maximum energy of the valence band is at a different value of k-vector to the minimum energy of the conduction band, and then a change in momentum is required for the smallest energy transition. Typical examples for direct bandgap semiconductors are GaAs, InP and InSb and for indirect bandgap semiconductors are Si and Ge.
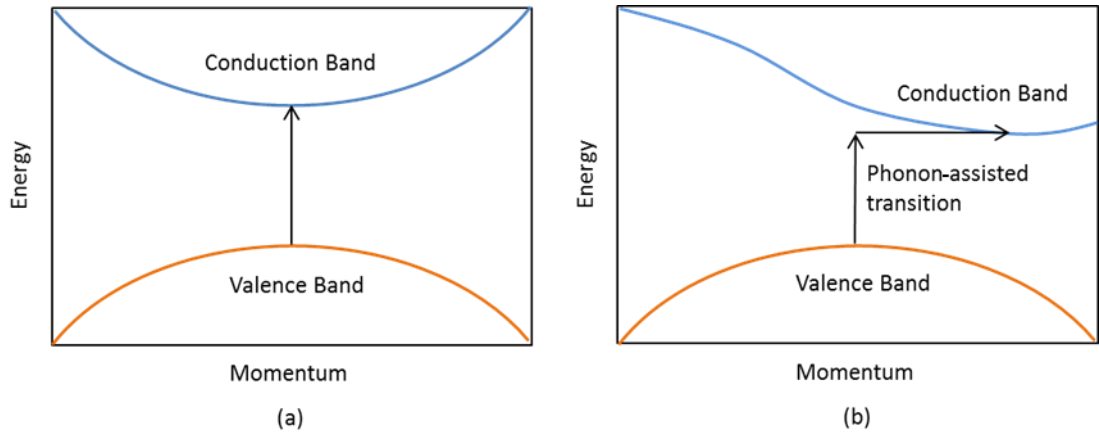
Figure 1.1 Energy bandgap diagram for (a) direct and (b) indirect bandgap.

In a semiconductor, the thermal equilibrium concentrations of free electrons (n_0) and holes (p_0) follow the Law of Mass Action:

$$n_i^2 = n_0 p_0 = N_c N_v \, exp\left[\frac{-E_g}{kT}\right] \quad \text{(Equation 1.1)}$$

Where n_i is the intrinsic carrier concentration; N_c and N_v are the effective density of states in the conduction band and valence band; E_g is the bandgap energy; k is the Boltzmann constant; T is the temperature.

In an intrinsic semiconductor, no impurities are added and the number of electrons and holes are equal to n_i. The Fermi energy level lies in the centre of the energy band gap.

Figure 1.2 shows the intrinsic concentration of carriers for silicon, germanium and gallium arsenide as a function of temperature [21].
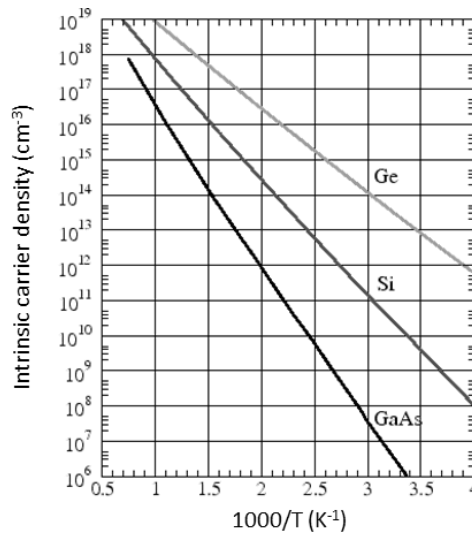
Figure 1.2 Intrinsic carrier concentration as a function of temperature (reproduced from Ref [21]).

For an extrinsic semiconductor, we still have the relationship shown in Equation 1.1. However, the concentrations of electrons and holes and the position of the Fermi level may be changed with the doping of impurities. Figure 1.3 shows the carrier concentration as a function of temperature in silicon doped with 10^{16} cm^{-3} donors and 10^{15} cm^{-3} acceptors.
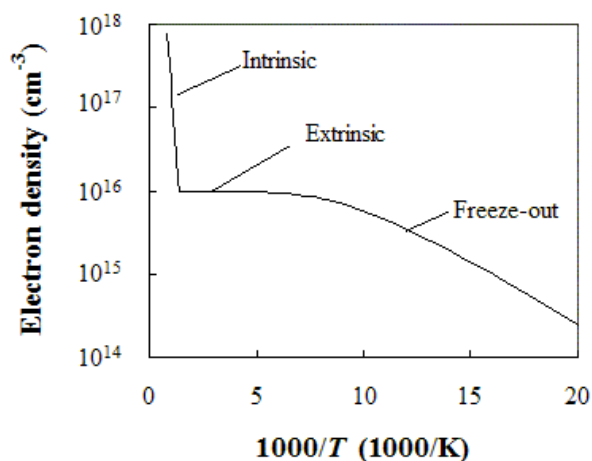
Figure 1.3 Electron concentration versus temperature for silicon doped with 10^{16} cm^{-3} donors and 10^{15} cm^{-3} acceptors (reproduced from Ref [22]).

The movement of free electrons and holes allows the conduction of current in semiconductors. Usually, there are two transport mechanisms related to the motion of charge carriers. One is referred to as carrier drift, which is due to an externally applied electric field. The other one is called carrier diffusion and is caused by carrier density gradients.

1.2.2 Light absorption by semiconductors

In real applications, most semiconductors are in a state of non-equilibrium. This can be caused by illuminating with light or applying a bias voltage. When light irradiates the surface of a semiconductor, some of it will be reflected back, some will be absorbed by the bulk, and some will be transmitted. Due to uniform absorption, the intensity of light depending on its travel distance in the semiconductor is:

$F(x) = F(x_0)e^{-a(x-x_0)}$ (Equation 1.2)

Where $F(x_0)$ is the light intensity at a surface point x_0; a is the light absorption coefficient, which is strongly related to the wavelength of light and the energy bandgap of the semiconductor:

$a = \frac{4\pi \chi n_r}{\lambda}$ (Equation 1.3)

$n_r = c/c_s$ (Equation 1.4)

Where n_r is the index of refraction; c is the speed of light in vacuum (~3×10^8 m/s); c_s is the speed of light in the semiconductor; χ is the absorption index of the semiconductor.

The distance $1/\alpha$ is called the light penetration depth. Figure 1.4 shows the absorption depth related to the light wavelength in different semiconductors.
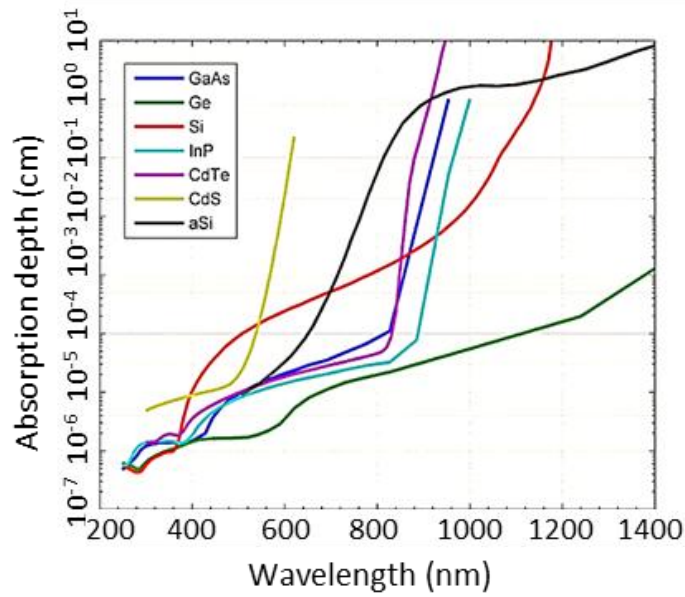
Figure 1.4 Absorption depth depending on light wavelength for different semiconductors [23].

A photon with sufficiently large energy may lead to photoelectron emission in semiconductors. In this process, after absorbing the photon energy, the electron can escape over the surface potential barrier of the material and become a free electron in vacuum (shown in Figure 1.5 (a)). If the photon energy is smaller than the vacuum level energy but greater than the bandgap energy, the excited electrons will transfer from the valence band into the conduction band, generating mobile electron/hole pairs in the semiconductor (shown in Figure 1.5 (b)). In direct bandgap semiconductors, since the k-vector equals zero, an electron/hole pair can be easily generated by absorbing the photon energy. However, in indirect bandgap semiconductors, to generate the electron/hole pair an electron must interact not only with a photon to gain energy, but also with a phonon to either gain or lose momentum. Hence, the carrier generation rate as well as the recombination rate for direct bandgap semiconductors is much higher than that of indirect bandgap semiconductors, which results in a much greater penetration depth of light in indirect semiconductors (such as Si).
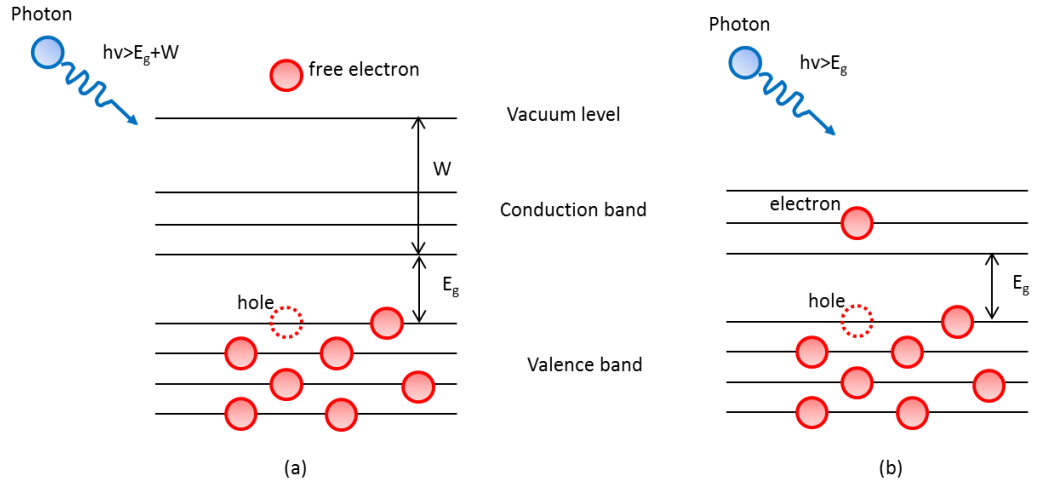
Figure 1.5 (a) Photoelectric emission and (b) electron/hole photogeneration in semiconductors [24].

The generation of electron/hole pairs by light excitation is a non-equilibrium process. For an n-type semiconductor, where $n_0 \gg p_0$, and if the changes of the concentrations of electrons (Δn) and holes (Δp) are much smaller than n_0 [25], then:

$$\frac{d\Delta n}{dt} = \frac{d\Delta p}{dt} = -An_0\Delta p + g_a \quad \text{(Equation 1.5)}$$

$$An_0 = \frac{1}{\tau_p} \quad \text{(Equation 1.6)}$$

Where A is a constant for a given semiconductor; τ_p is the lifetime of the minority carriers, here the holes; g_a is the additional generation rate.

Due to the formation of additional electron/hole pairs, the conductivity of the semiconductor is given by:

$$\sigma = e_0(n_0 + \Delta n)\mu_e + e_0(n_0 + \Delta p)\mu_h \quad \text{(Equation 1.7)}$$

Thus, the photoconductivity of the semiconductor can be written as:

$$\Delta\sigma = \Delta n\mu_e e_0 + \Delta p\mu_h e_0 \quad \text{(Equation 1.8)}$$

Where μ_e and μ_h are the electron and hole mobilities; e_0 is the electron charge.

Photoconductivity induced by band-to-band transition is called intrinsic conductivity. In a semiconductor doped with impurities, the electron can be excited from the impurity level located in the bandgap into the conduction band by absorbing photon

7

energy which is less than the bandgap energy. We term this extrinsic absorption and photoconductivity [25].

So far, it was assumed that a single photon is absorbed during the electron transition from one state to a higher energy state, which means a photon energy $hv \geq E_g$ is required. Here, h is the Planck constant and v is the light frequency. However, if light ($hv < E_g$) with ultrashort pulses and high intensity is applied, two photons can be absorbed simultaneously, resulting in the electron transition. This is a nonlinear process and the energy absorbed by the electron is equal to the sum of the two photons' energies. Two-photon absorption will also give rise to free charge carriers and contribute to the photoconductivity.

1.2.3 Field-effect structures

Figure 1.6 shows the schematic of a metal-insulator-semiconductor (MIS) field-effect structure, the gate contact of which is isolated from the semiconductor by a thin layer of insulator. A bias voltage is applied across the insulator. As the insulator is usually silicon dioxide, the structure is also referred to as metal-oxide-semiconductor (MOS) structure.
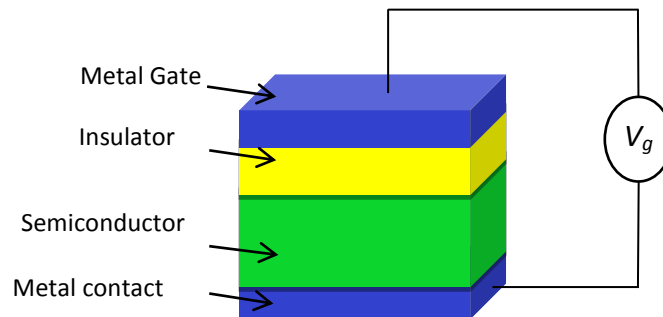
Figure 1.6 Typical field-effect structure.

For a p-type MOS structure, when the gate voltage (V_g) equals the flat band voltage (V_{FB}), the bands are flat (see Figure 1.7 (a)). By applying this voltage, the discrepancy of work functions between metal and semiconductor can be compensated. There is no electrical charge in the semiconductor and thus no voltage drop across it.

When $V_g < V_{FB}$, the majority carriers (holes) are attracted by the negative gate charge and accumulate at the surface of the semiconductor. Consequently, the bands bend upwards. Since the thickness of the accumulation layer is very small, the main potential variation is within the oxide (see Figure 1.7 (b)).
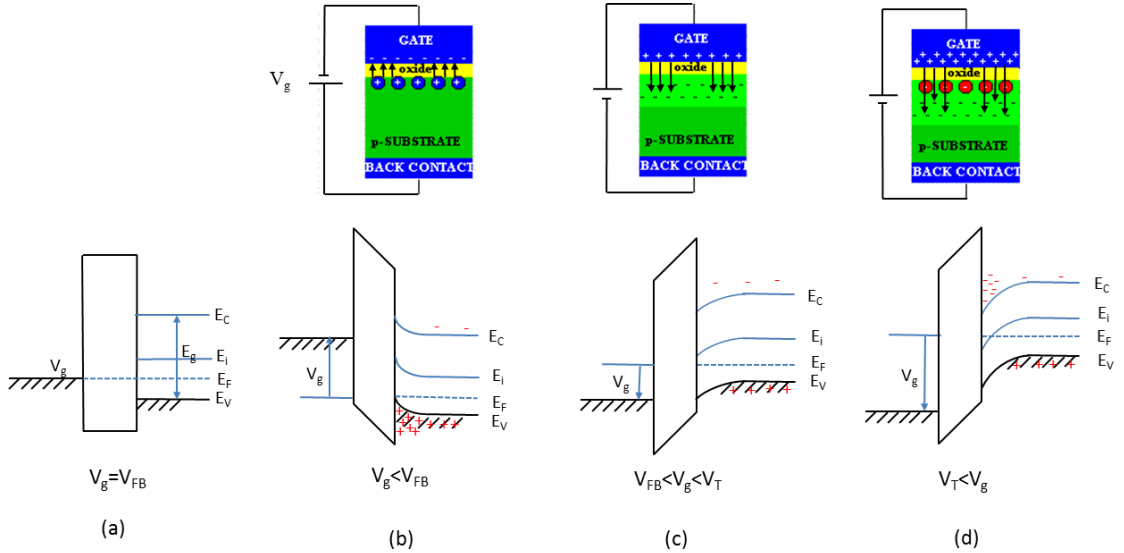
Figure 1.7 Charge distribution and energy band diagrams in an MOS structure (p-type substrate) for (a) flat band, (b) accumulation, (c) depletion, and (d) inversion conditions [26, 27]. V_g is the gate voltage; V_{FB} is the flat band voltage; and V_T is the threshold voltage, which is related to temperature, the doping level and thickness of semiconductors.

When $V_{FB} < V_g < V_T$, the positive charge on the gate repels the holes into the semiconductor substrate, leaving the immobile ionized acceptors on the surface. The Fermi level moves and the bands bend slightly downwards (see Figure 1.7 (c)). The region without mobile charge carrier is termed space charge layer and the width of the depletion layer is given by:

$$d = \sqrt{\frac{2\varepsilon_s\varepsilon_0 V_s}{qN_d}} \quad \text{(Equation 1.9)}$$

Where ε_s is the dielectric constant of the semiconductor; ε_0 is the electric permittivity of vacuum (~8.854 $\times 10^{-12}$ F m^{-1}); V_s is the surface potential of the semiconductor; q is the elementary charge; N_d is the doping concentration.

When the bias voltage exceeds the threshold voltage ($V_T < V_g$), the minority carriers (electrons) are attracted to the interface, forming an inversion layer. The Fermi level in this region crosses the intrinsic Fermi level (E_i) and the bands bend more than in depletion. In the inversion layer, the semiconductor remains in thermal equilibrium and we have:

$$V_s = \frac{kT}{q} ln(\frac{N_a}{n_i}) \quad \text{(Equation 1.10)}$$

Where n_i is the intrinsic hole concentration; N_a is concentration of acceptors.

The width of the inversion layer is usually much smaller than the depletion layer. Once it reaches a maximum value (in strong inversion), it will not change even with a further increase of the bias voltage.

Considering an ideal MOS capacitor with a perfect insulator without charges and surface states, the total capacitance C of the device is:

$$\frac{1}{C} = \frac{dV_g}{dQ} = \frac{1}{C_{ox}} + \frac{1}{C_s} \quad \text{(Equation 1.11)}$$

Where C_{ox} is the oxide capacitance; C_s is the capacitance of semiconductor.

Figure 1.8 (a) shows the capacitance-voltage (C-V) curves of a p-type substrate while neglecting the contact potential between metal and semiconductor. In accumulation, C_s is relatively large, i.e. the total capacitance is approximately equal to the insulator capacitance (C_{ox}). In depletion, the space charge layer acts as a serial dielectric resulting in a decrease of the total capacitance.
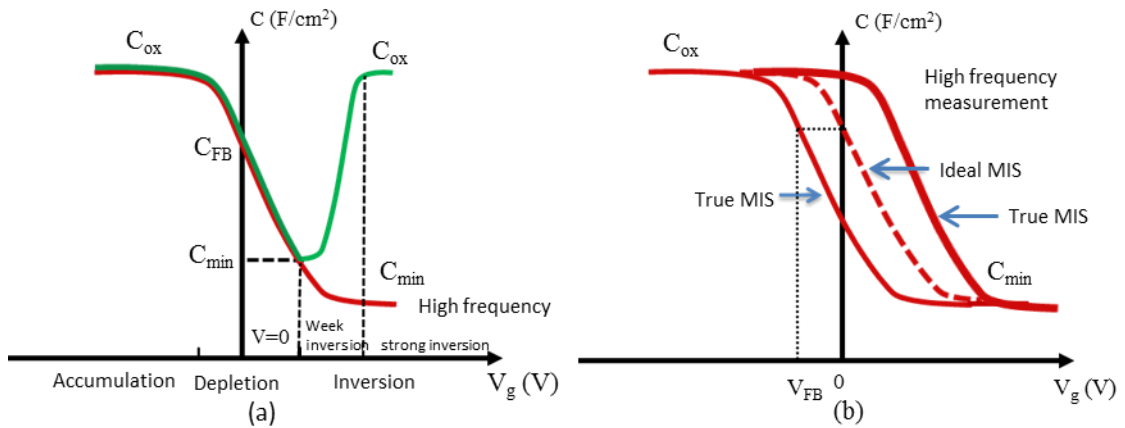
Figure 1.8 (a) Typical C-V curves measured at high and low frequency and (b) effect of the contact potential between semiconductor and metal on the C-V curves of a MIS structure.

When $V_g = 0$, a flat band occurs and the corresponding capacitance is:

$$C_{FB} = C_{ox}/(1 + \frac{\varepsilon_{ox}}{d_{ox}} \sqrt{\frac{kT}{q^2 N_{do} \varepsilon_s}}) \quad \text{(Equation 1.12)}$$

In inversion, if measured at a low frequency (< 100 Hz), the capacitance rises again after falling to a minimum. This is because the electrons in the inversion layer can follow the variation of the AC signal at low frequency. Hence, the capacitance is comparable to the accumulation capacitance and equals to C_{ox} in strong inversion. However, if measured at a high frequency ($> 10^4$ Hz), the capacitance shows no increase and the minimum capacitance (C_{min}) can be written as:

$$\frac{1}{C_{min}} = \frac{1}{C_{ox}} + \frac{1}{C_s(d_{max})} \quad \text{(Equation 1.13)}$$

$$d_{max} = \sqrt{\frac{2\varepsilon_s}{q} \frac{2V_s}{N_a}} \quad \text{(Equation 1.14)}$$

Combining Equations 1.10, 1.13 and 1.14, the following expression can be obtained:

$$\frac{C_{min}}{C_{ox}} = \frac{1}{1 + \frac{\varepsilon_{ox}}{\varepsilon_s} \frac{\sqrt{\frac{4\varepsilon_s kT}{q^2 N_a} ln(\frac{N_a}{n_i})}}{d_{ox}}} \quad \text{(Equation 1.15)}$$

Where d_{max} is the maximum width of the inversion layer; d_{ox} is the thickness of the insulator (oxide). Figure 1.8 (b) illustrates real *C-V* curves considering the difference of work function of metal and semiconductor. It shows either a negative or a positive shift along the voltage axis but no changes in shape.

The field-effect transistor (FET) is a transistor based on field-effect structures. It uses an electric field applied through the gate terminal to control the carriers flow from the source terminal towards the drain terminal. The working principle and applications will be discussed in the following section. Typical FETs include the junction field-effect transistor (JFET), metal-semiconductor field-effect transistor (MESFET) and metal-insulator-semiconductor field-effect transistor (MISFET) [27].

1.3 Chemical sensors based on field-effect structures

1.3.1 Gas-sensitive field-effect transistors

The initial development of gas-sensitive field-effect transistors was the hydrogen-sensitive palladium-gate field-effect transistor, which was introduced by Lundström *et*

al. [28]. In brief, hydrogen molecules absorbed on the palladium gate are dissociated to hydrogen atoms. Hydrogen atoms diffuse to the metal-silicon dioxide interface and give rise to a dipole layer. The dipole layer changes the work function difference between metal and semiconductor and thereby the threshold voltage of the MOS transistor [29].

The sensitivity and selectivity of transistor are determined by the thickness and the composition of gate material and the operational temperature. For example, a thick continuous palladium layer as gate contact is in principle only sensitive to hydrogen or hydrogen-containing gases [30]. However, thin discontinuous platinum or iridium gates show a strong sensitivity to ammonia gas in MOS structures [31]. Besides pure metals, metal phthalocyanine films can be also used as the gate material in the fabrication of NO_2 and Cl_2 gas-sensing transistors [32]. Recently, it was reported that two-dimensional transition metal dichalcogenides with chemical formula MX_2 (M = Mo, W or Ga, and X = S, Se or Te) can be used in FET-based gas sensors [33]. For example, MoS_2 films with a single or a few-layers can be used to detect NO, NO_2, NH_3 and triethylamine gas [34], while multilayer WS_2 nanoflakes show a very high sensitivity for ethanol and NH_3 [33].

1.3.2 Ion-selective field-effect transistors (ISFETs)

An ISFET is a potentiometric device that has been widely used to detect the activity or concentration of ions in solution. In an ISFET, a series combination of a reference electrode, the analyte solution and an ion-sensitive insulator or membrane replaces the metal gate in the MOSFET [35]. Figure 1.9 (a) shows a schematic representation of an ISFET [36]. Similar to the MOSFET, a gate voltage (V_g) is used to produce a conductive channel and control the type and the amount of the charge carriers in the channel, while another voltage (V_{ds}) is applied between the drain and source to create the current flow (drain current) through the channel. The effective gate voltage is affected by the electrical potential difference (E_m) at the solid/liquid interface. As a consequence, the drain current is dependent on E_m as well. E_m is determined by an exchange equilibrium of ions between the sensitive membrane and the analyte solution. Ideally, it can be given by the Nernst equation [37]:

$$E_m = E^{\ominus} + \frac{2.303\,RT}{z_c F} log \frac{a_{sol}}{a_{memb}} \quad \text{(Equation 1.16)}$$

Where $E^{\ominus}$ is the standard potential; R is the gas constant; T is the absolute temperature; z_c is the charge of the ion; F is the Faraday constant; a_{sol} and a_{memb} are the chemical activities of the given ion in the solution and in the membrane, respectively.

Figure 1.9 (b) shows the drain current as a function of the effective gate voltage [36]. By measuring this voltage shift (ΔV), the analyte concentration or composition can be determined.
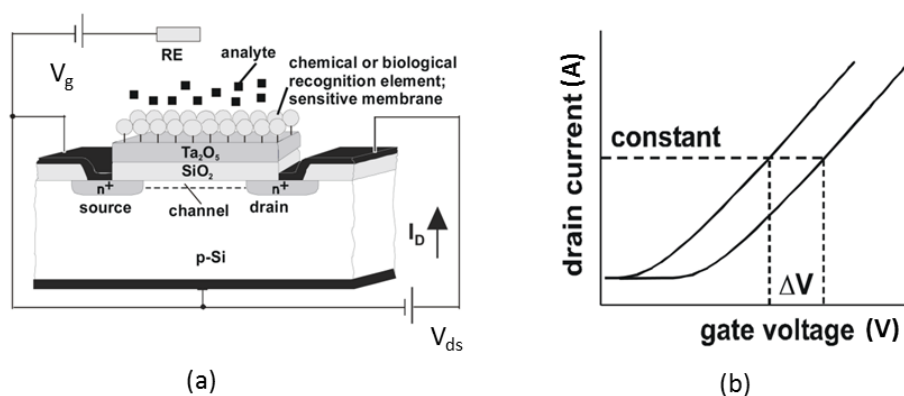
Figure 1.9 (a) Schematic of ISEFT principle; (b) typical gate voltage-drain current curves reproduced from [36].

Generally, an ISFET with a bare gate insulator (for example: SiO_2, Si_3N_4 and Al_2O_3) has pH sensitivity, thus can work as a pH sensor [38-40]. Vlasov and Bratov designed a pH ISFET by thermally growing ZrO_2 or Ta_2O_5 on the SiO_2 layer [40]. It showed a good sensitivity (~56 mV/pH) in the pH range 1-12 and the capability to work in blood or in the stomach. On the other hand, by coupling with ion-selective membranes or molecular receptors, ISFETs can be used to detect different ions (Cl^- [41], K^+ [42], Cu^{2+} [43], Ca^{2+} [44, 45], Fe^{3+} [46] and Cd^{2+}/Pb^{2+} [47]) and molecules (CO_2 [48, 49], lactic acid [49], H_2O_2 [50], creatinine [51] and urea [52, 53]), or for biological sensing (such as DNA [54, 55] and proteins [56, 57]). Qu *et al.* reported a micro-potentiometric immunosensor based on an ISFET [57]. By assembling the antibodies to an electrochemically synthesized polypyrrole-gold nanoparticle (PPy-AuNPs) film, a simple and rapid sensing system for the detection of hemoglobin (Hb) and hemoglobin-A1c (HbA1c) was obtained. The sensor showed a measurement range of 5-20% of HbA1c/Hb ratio that meets the clinical demand. A DNA methylation detector using a novel ISFET-based readout circuit was studied by Kalofonou *et al.*

[54]. It was shown that by determining the differences between unmethylated genes found in cancer development and normal methylated genes, one can identify early signs of cancers through blood circulation.

1.3.3 Electrolyte-insulator-semiconductor (EIS) sensors

An electrolyte-insulator-semiconductor (EIS) sensor is the simplest chemical senor based on field-effect structures. It is derived from an MIS structure, by replacing the metal gate with an electrolyte and a reference electrode, similar to ISFETs described in the last section. However, the drain and source are absent in the EIS sensor, which makes the fabrication much easier and inexpensive. The working principle is analogous to an MOS capacitor (see Section 1.2.3). A bias voltage is applied via the reference electrode and a small AC voltage (~10-50 mV) is applied to measure the capacitance through an impedance analyser. Two different modes are usually adopted during measurements: The capacitance-voltage (*C-V*) and constant-capacitance (ConCap) mode [58]. A typical *C-V* curve has three distinguishable regions, which are accumulation, depletion and inversion that have been described in Section 1.2.3. The curve shifts along the voltage axis due to the potential changes at the insulator/electrolyte interface. Thus, by measuring the voltage shift, the analyte concentration or composition of interest can be determined.

Due to the similar working principle, the results and achievements obtained with ISFETs and EIS sensors are fully transferable. For example, an EIS sensor can be also used for monitoring chemical changes such as pH fluctuation [59], ion-concentration changes, enzymatic reactions [60], affinity binding of molecules (e.g. antigen-antibody reaction, DNA hybridisation) as well as potential changes induced by living biological systems [36].

1.3.4 Scanned light-pulse technique (SLPT)

Scanned light-pulse technique (SLPT) is an imaging technique for chemical sensors based on an MIS structure. In principle, a modulated and well-focused light beam is used to generate photocurrents. When the light is switched on, electron/hole pairs generated by the photon excitation may either recombine at the interface or in the semiconductor bulk, or accumulate at each side of the insulator resulting in a current in the outer circuit. Since the total bias voltage is constant, the increase of the potential difference due to the continuous accumulation of the charge carriers has to be

compensated for by a decrease of the surface potential and thereby the potential inside the space charge layer. Hence, the generation of charge carriers decreases as well as the external current. The current will go to zero when the generation of charge carriers is balanced by the recombination. As the light is switched off, a negative current is produced and it will decrease until the thermal equilibrium is established again.

Figures 1.10 (a) and (b) show the schematic of the modulated light and current transients as a function of time [61, 62]. In an ideal MIS structure, the surface potential is related to the bias voltage, the amount of charge carriers in the space charge layer and the work function of the metal. Figure 1.10 (c) shows the relationship between the output current transient (*I*) and the bias voltage (*V*). The *I-V* curve shifts with the presence of the target gas. This is due to the change of the effective work function of the metal. By scanning a small light beam across the sample, the surface potential at different sites can be obtained and mapped. Figure 1.10 (d) shows the set-up of SLPT.
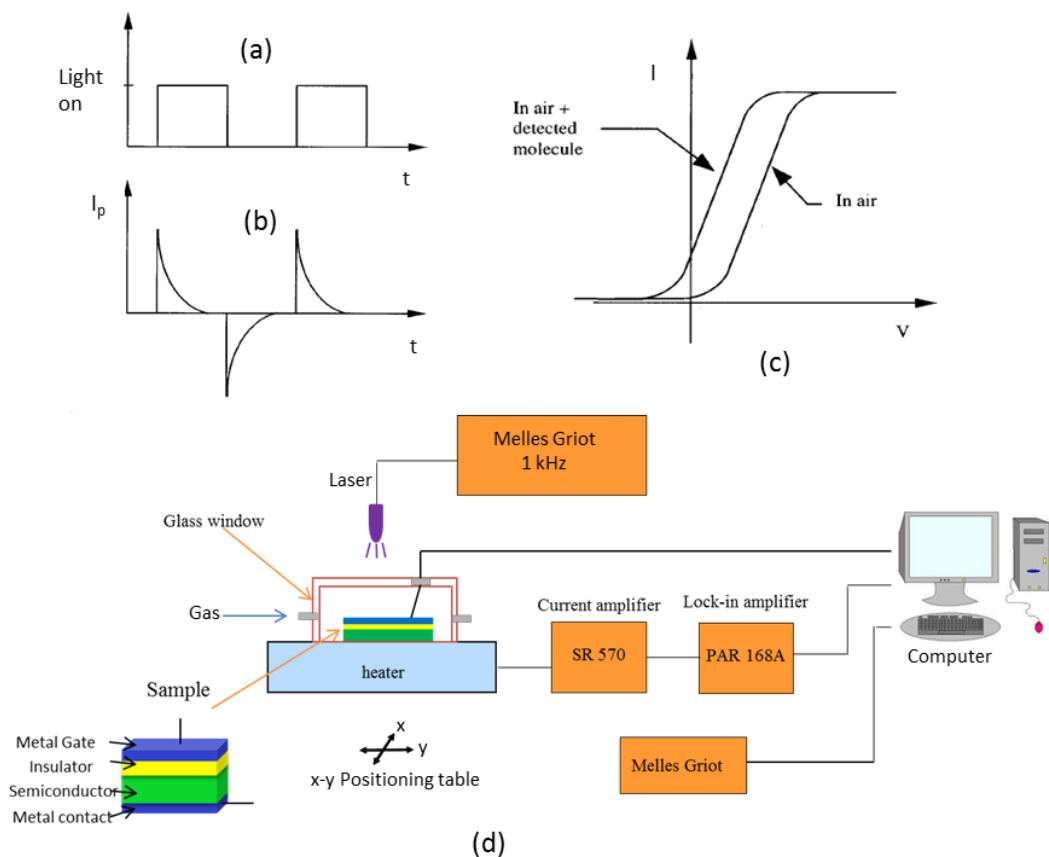
Figure 1.10 Schematic of (a) the modulated light intensity vs. time; (b) photogenerated current signal (I_p) vs. time; (c) output current vs. bias voltage in air and in target gas (reproduced from Ref [62]); (d) the SLPT set-up [63].

SLPT was initially used to study insulator/semiconductor interfaces. Through this new technique, images of the spatial variation in interface state concentration and surface potential have been obtained [61]. It has also been widely used as a gas sensor which can do both the fundamental chemical sensing and the chemical imaging sensing with lateral resolution [62-68]. For example, the sensor responses for H_2 [62, 66], NH_3 [68], C_2H_5OH, C_2H_4, CH_3CHO [65], H_2S [69] and their mixtures [67], by using SLPT have been reported.

Thanks to the feasibility of combinatorial chemistry methods in SLPT, an artificial "electronic nose" was developed by replacing the traditional monotonous gate metal surface with an array of three different metals (Pd, Pt and Ir) [68]. Through this technique, an artificial "olfactory" map depending on the gas composition and temperature can be obtained. Löfdahl *et al.* fabricated a metal gate with a thickness gradient [65], and then investigated the effects of gate metal materials, morphology and thickness on the responses of different gases with minimal numbers of samples. The interaction mechanisms between different analyte gases and metal surfaces have been analysed.

1.3.5 Light-addressable potentiometric sensor (LAPS)/scanning photo-induced impedance microscopy (SPIM)

1.3.5.1 Principle of LAPS/SPIM

The light-addressable potentiometric sensor (LAPS) is a technique derived from EIS and SLPT. Based on an electrolyte-insulator-semiconductor (EIS) structure, a bias voltage is applied between the gate electrode and the semiconductor substrate to create a depletion layer at the semiconductor/insulator interface [70]. A modulated light scans across the substrate to generate electron/hole pairs and causes a detectable photocurrent as in SLPT. The schematic of a LAPS set-up is shown in Figure 1.11 (a) . Since electron/hole pairs are only generated in the illuminated area, LAPS can record local changes of the surface potential, thus determining a particular analyte under test with spatial resolution [70-73]. Krause's group has shown that the same measurement technology can be also used to measure the local impedance and termed this technique scanning photo-induced impedance microscopy (SPIM) [74, 75]. LAPS measures the potential changes as a shift of the depletion region of the photocurrent voltage (*I-V*) curve along the voltage axis, while SPIM measures local impedance changes by

recording the changes of the maximum photocurrent in the inversion region (see Figure 1.11 (b)).
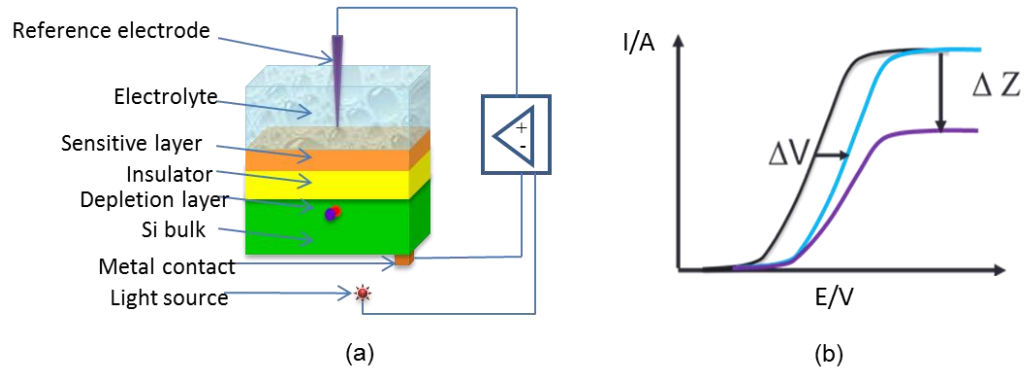
Figure 1.11 (a) Principle of a light-addressable potentiometric sensor (LAPS) [76]; (b) typical photocurrent-voltage (I-V) curves representing the potential shift (from the black curve to the blue one) and impedance changes (from the black curve to the purple one).

1.3.5.2 Resolution of LAPS/SPIM

The spatial resolution in LAPS is limited by the diffusion of minority charge carriers out of the illuminated region. The density of light-induced charge carriers is much smaller than that of the majority charge carriers in doped silicon. Due to the density gradient, only minority carriers diffuse in the silicon bulk and exist for a very short time (less than 1 μs). The diffusion length within the short lifetime of minority carriers is defined as the spatial resolution of LAPS [77]. Two methods have been used to estimate the resolution. One is by using a test pattern, that is, the smallest pattern that can be recognised by LAPS is referred to as the resolution [78-80]. Alternatively, it has also been estimated by the average effective diffusion length of charge carriers [14, 81-83]. Three experimental models have been introduced to measure the effective diffusion length. One is by scanning a focused laser beam across the edge of the gate metal [74] (see Figure 1.12 (a)). When the laser is focused onto the metal, only a small photocurrent is generated because most of the light is absorbed by the metal. While the laser crosses the edge of the metal, the photocurrent increases suddenly and then it decays as the light moves further away. The diffusion length can be estimated from the length of the current decay. The disadvantage of this model is that the measurement is outside the gate area. The second model is based on a backside illumination. A silicon-on-insulator (SOI) substrate with a thin epitaxial film of p-type silicon and a 40 nm

17

thick thermally grown oxide layer was used [84]. The substrate was coated with a photoresist pattern and was then coated with another layer of metal [84]. As shown in Figure 1.12 (b), the photocurrent decreases suddenly when the laser beam moves from the metal surface to the photoresist surface due to the high impedance of the photoresist. The disadvantage of this method is that photocurrent changes due to impedance changes and due to the changes in the reflectivity cannot be separated. The third model is similar to the second one, but with a silicon-on-sapphire (SOS) substrate and the measurement was carried out under genuine LAPS conditions with electrolyte thereby reducing reflection effects caused by the metal layer in previous models (see Figure 1.12 (c)) [14]. To gain the resolution of a genuine LAPS system, the last model will be adopted in this work.
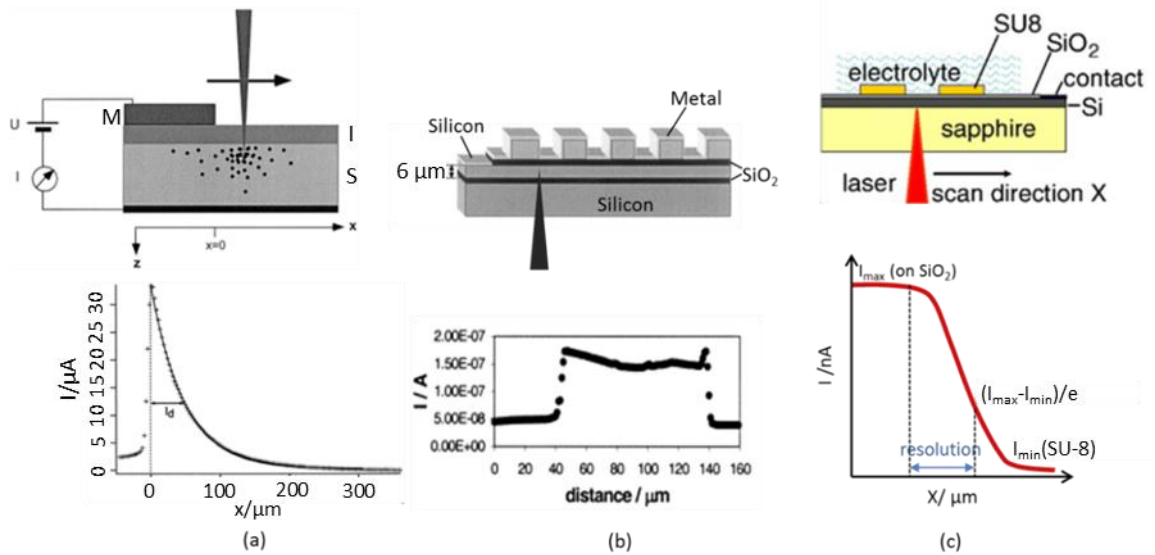
Figure 1.12 Three models for the measurement of the lateral diffusion of light-generated charge carriers (top) and the corresponding photocurrent line scan showing resolution value (bottom). (a) is reproduced from Ref [74]; (b) is reproduced from Ref [84] and (c) is reproduced from Ref [14].

Factors that can influence the spatial resolution of LAPS have been theoretically and experimentally investigated [83, 85]. In the case of front illumination, the theoretical spatial resolution r_{the} can be written as [85]:

$$r_{the}^2 = \frac{2L^2\lambda_L}{L+\lambda_L} + w^2 \quad \text{(Equation 1.17)}$$

Where L is the diffusion length of minority charge carriers; λ_L is the penetration depth of light and w is the parameter of beam width. Equation 1.17 indicates that the lateral resolution can be improved by decreasing λ_L and w (i.e. using light with a shorter wavelength and a better focus) and by decreasing the diffusion length L (i.e. decreasing the recombination lifetime of the minority charge carriers or increasing the doping level of semiconductors).

For example, "when a laser with a wavelength of 488 nm illuminates the sample from the front, 63% of the light would be absorbed within the depletion layer and not be subjected to much lateral spread" [85]. That means a short wavelength laser results in an improvement in the resolution. However, if the laser illuminates the back of the semiconductor, the effect of light wavelength on the resolution is related to the thickness of the semiconductor. For an ultra-thin semiconductor, the resolution dependence on the laser wavelength is similar to the front illumination case [14]. However, for a thick silicon substrate, because of the effect of light absorption during the light travelling through the bulk of silicon, the longer the laser wavelength, the better is the spatial resolution [78].

The focus of the laser is mainly due to the laser mode, diffraction and spherical aberration [86]. The laser mode is determined by the laser and beam delivery system. The diffraction and spherical aberration are affected by the lens shape and the lens focal length. Krause *et al.* have estimated a spot diameter (1.3 μm) of the laser with a wavelength of 430 nm used in SPIM measurements and the effective diffusion length of minority charge carriers (0.57 μm) in the semiconductor when using a 1 μm thick Si layer on a SOS substrate [74]. They suggested that submicrometer resolution is possible by optimizing the optical set-up, such as using an objective lens with higher numerical aperture [74]. Later, they introduced a two-photon effect strategy to improve the spatial resolution. That is, using a femtosecond laser with low energy photons ($E_{photon} < E_g$) rather than a traditionally used laser with high energy photons ($E_{photon} > E_g$) to generate photocurrents (see Section 1.2.3). If a laser beam is focused into the space charge layer from the back, light has to travel through the bulk of the semiconductor. In the case of a single-photon effect, charge carriers are generated throughout the whole bulk of the semiconductor, causing additional lateral diffusion and thus poor resolution. However, for the case of the two-photon effect, electron/hole pairs can be generated only in the focus close to the space charge layer, hence, the

spatial resolution can be significantly improved (see Figures 1.13 (a) and (b)) [14, 74]. Recently, a novel combined light source has been proposed by Guo *et al.* to improve the spatial resolution of LAPS [87]. In this illumination system (see Figure 1.13 (c)), a single modulated light is used to generate photocurrents as it usually does, and it is surrounded by a ring of constant light sources to generate a sheath with high concentration of charge carriers to suppress the lateral diffusion of carriers generated by the modulated light.
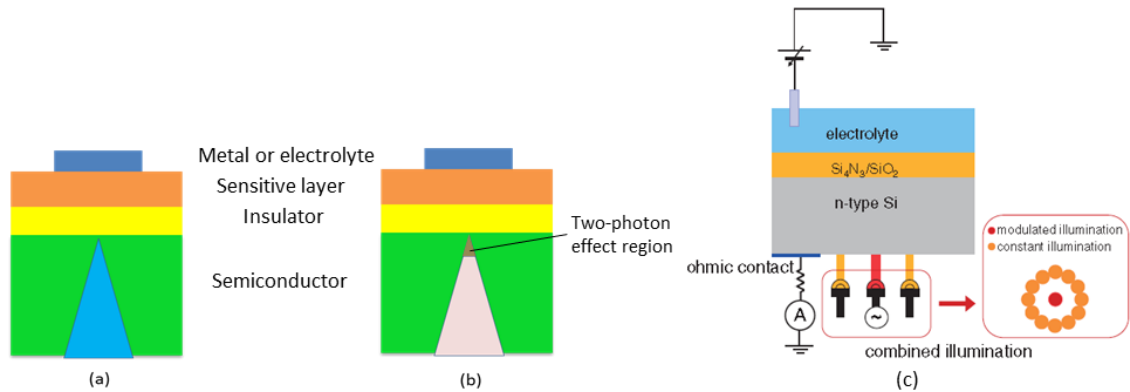
Figure 1.13 (a) In the case of a single photon effect, charge carriers are generated throughout the bulk of the semiconductor and (b) in the case of the two-photon effect charge carrier generation is confined to a small volume close to the focus [14]. (c) LAPS set-up with a combined illumination system (reproduced from Ref [87]).

As a direct bandgap semiconductor, GaAs has a smaller diffusion length of minority charge carriers than normal silicon. The effective diffusion length was shown to be about 3 μm in a 500 μm thick GaAs substrate [81]. However, it is difficult to obtain a high quality gate insulator on GaAs with low leakage current. Amorphous silicon, with a diffusion length of minority charge carriers as short as 120 nm, is another promising material to improve the spatial resolution [82]. However, it is also difficult to obtain an insulator with good quality on the surface. As the amorphous silicon was deposited onto a glass substrate, the multi-reflection in the glass layer limits its application.

Increasing the doping density in a semiconductor can also improve the spatial resolution. Since doping ions may act as scattering centres for free carriers, they can reduce the diffusion length of charge carriers [83]. However, attempts to improve the resolution by increasing the doping level always lead to a significant loss in

photocurrent intensity. A highly doped semiconductor, which behaves like a metal, has no space charge layer and thus no photocurrent generation.

Another important way to improve the spatial resolution is reducing the thickness of the semiconductor. When the thickness is very small, the spatial resolution is no longer determined by the diffusion length of minority charge carriers but by the thickness of the semiconductor. This strategy can be used for both cases of front illumination and back illumination. For example, with back illumination, Nakao *et al.* have improved the spatial resolution from 500 μm to 100 μm and finally to 10 μm by reducing the thickness of silicon from 600 μm to 100 μm and to 20 μm [78, 80, 88]. However, in this case, "the resolution was determined by the size of differently doped islands in the silicon resembling a microelectrode array rather than a homogenous LAPS substrate" [14, 74]. The use of SOI with 7 μm silicon, 1 μm buried oxide and 400 μm silicon handle has achieved a good resolution of 13 μm with back illumination [74]. The disadvantage is that after the etching of the back silicon handle layer, the ultra-thin silicon membrane distorts easily resulting in a difference of the focus distance over the whole sample. An SOS substrate was also used to improve the spatial resolution. For instance, a resolution of 5 μm was obtained by using a 0.5 μm silicon-on-sapphire substrate with back illumination [79], while a submicron resolution of 0.57 μm was achieved by using a 1 μm silicon-on-sapphire substrate with front illumination [74].

So far, the best resolution measured by using the genuine LAPS set-up with back illumination is about 0.8 μm [14]. This is achieved by using an SOS substrate (0.5 μm silicon, 475 μm sapphire) and a femtosecond laser (λ = 1250 nm) to generate photocurrents with a two-photon effect [14]. When a single-photon effect (λ = 405 nm) was used, a resolution of 1.5 μm was obtained. Both of the two measurements were performed with a microscope objective with a correction ring to correct for spherical aberration. Since the principle of SPIM is similar to LAPS, the method for improving resolution exploited in LAPS can be readily used in SPIM [14, 75].

1.3.5.3 Accuracy of LAPS

The structure for LAPS/SPIM can be represented by the electrical equivalent circuit shown in Figure 1.14 [76]. When LAPS/SPIM is operated with a fixed light source and at a constant bias voltage and the sensitive layer is absent, assuming the capacitance of

$C_{interface}$ is negligible, the detectable photocurrent *I* can be written with the simplified equation [76]:

$$I = I_p \frac{C_{insulator}}{C_{insulator} + C_{sc} + C_{ss}} \quad \text{(Equation 1.18)}$$

Where I_p is the photon-induced current; $C_{insulator}$ is the insulator capacitance; C_{sc} is the space charge layer capacitance, which depends on the applied bias voltage thus making the photocurrent a function of the bias voltage; C_{ss} is the surface state induced capacitance. From Equation 1.18, it is obvious that the steepness of the photocurrent-voltage (*I-V*) curve is mainly related to the capacitance of the insulator and the density of the interface states. The greater the insulator capacitance and/or the lower the interface state density, the steeper are the *I-V* curves, resulting in a higher accuracy of LAPS [89-91]. Even though LAPS has been studied for about 30 years and many efforts have been made to improve its spatial resolution, very little effort has been made to improve its accuracy.
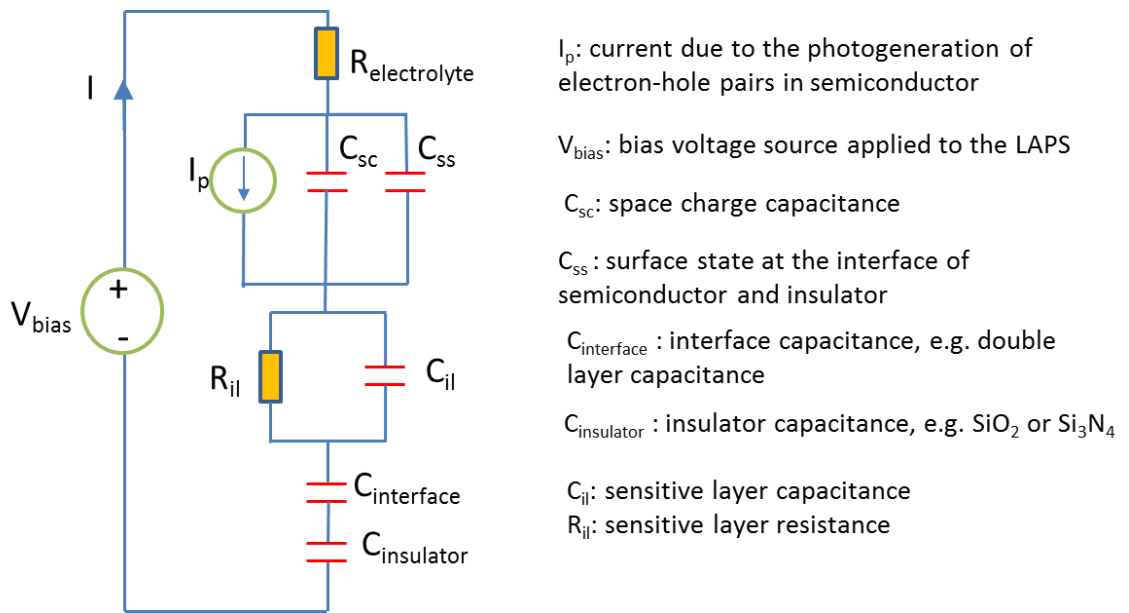
Figure 1.14 Electrical equivalent circuit of a LAPS structure [76].

Due to the good stability and easy fabrication process, insulators typically used in the semiconductor industry, such as thermally grown silicon oxide and silicon nitride, have been widely employed in LAPS/SPIM [92]. To obtain a high accuracy of LAPS and a high sensitivity of SPIM measurements, a thin oxide layer with few defects is required. As it is impossible to grow good quality thermal oxide on SOS substrates due to the

different expansion coefficients of silicon and sapphire, a thin anodic oxide (~6.7 nm) followed by annealing was used to achieve a high accuracy of LAPS [14].

1.3.5.4 Applications of LAPS/SPIM

Thanks to the fact that LAPS belongs to the family of field-effect sensors, all the results initially achieved with ISFETs and EIS sensors can readily be adapted to LAPS. Similar to ISFETs, LAPS has been widely used to detect various ions, such as H^+ [71], K^+, Mg^{2+}, Ca^{2+} [93], Pb^{2+}, Cb^{2+}, Zn^{2+} [94] cations, as well as NO_3^-, SO_4^{2-} [72] and F^- [95] anions, by preparing corresponding ion-selective films on LAPS chips and measuring the potential shifts resulting from ion binding. For instance, a coating that had been developed for ISFETs was successfully used in LAPS measurements. The electrode was a combination of Al_2O_3/SiO_2 and a PVC-based membrane, which can detect K^+, Ca^{2+} and Mg^{2+} based on a LAPS system [93].

It is well known that LAPS was initially designed for biochemical and biological sensing. Most of these applications, including the detection of urea, penicillin, glucose [60, 96], tryptophan [97], *Escherichia coli* colonies activities [98, 99] and cellular metabolism [100-104], are actually based on the pH sensitivity of LAPS. In 1999, Seki *et al.* reported novel potentiometric biosensors based on LAPS [93]. By immobilizing glucose oxidase, penicillinase and urease on the Al_2O_3/SiO_2 films, one can detect glucose, penicillin and urea, respectively, with a linear relationship between the analyte concentration and the potential. Later, they developed another potentiometric microbial assay for tryptophan sensing [97]. Essentially, *Escherichia coliWP2*, which require tryptophan for growth, were cultured on a LAPS substrate, and the acidification rate related to the concentration of tryptophan was monitored. A linear relation was observed in the range of 0-15 μM tryptophan. Recently, Wu *et al*. developed a label-free DNA biosensor based on a multi-spot LAPS system [105]. A polyelectrolyte layer of PAH absorbed on the SiO_2 layer was used as the template for DNA immobilisation and hybridization. The photocurrent curves showed that a high sensor response (83 mV) was obtained due to the immobilisation of probe single-stranded DNA (ssDNA). After hybridization, the voltage shifts increased from 5 mV to 32 mV with the increase of the concentration of complementary DNA from 0.1 nM to 5 μM [105].

There are also many studies focused on the metabolic activity of living cells. In general, these measurements are operated by measuring the local medium pH changes induced by metabolic products such as H^+, CO_2 or lactic acid. Taking advantage of having spatial resolution, Stein *et al.* cultured two different types of cells on different segments of one sensor, which is shown in Figure 1.15. One type of cell was wild type Chinese hamster ovary cells (CHO-K1) without any response to carbachol; while the other one was transfected muscarinic type cells (CHO-M1), which are sensitive to carbachol. As expected, the response upon the addition of carbachol to the medium was observed only in the location cultured with CHO-M1 [100]. Hu *et al.* introduced a novel microphysiometer with a constant voltage detection mode to study the metabolic activity of human breast cancer cells [102]. The results showed a sensitive and rapid detection in real time by using a microphysiometer.
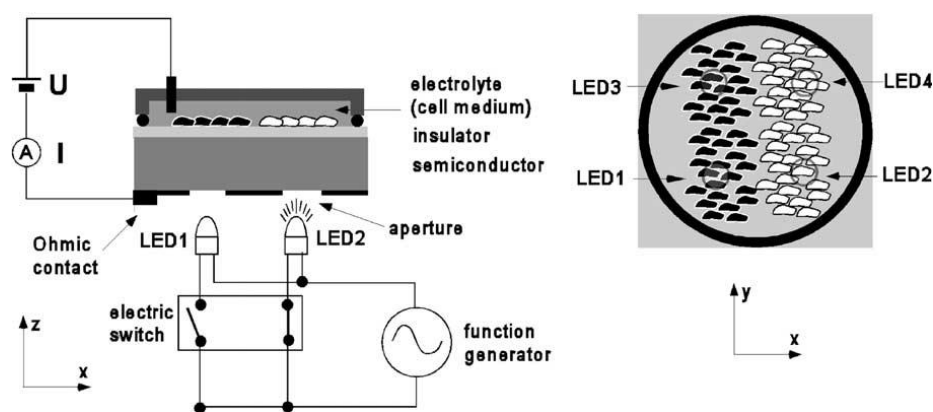
Figure 1.15 Schematic of the LAPS set-up for spatially resolved monitoring of cellular metabolic activity (reproduced from Ref [100]).

On the other hand, as a potentiometric sensor, LAPS can also detect the cell action potentials in response to stimulus [106-109]. When excitable cells are cultured on LAPS, cell activities such as ionic currents or mechanical beating can be reflected by the photocurrent fluctuation in the depletion region. Ismail *et al.* investigated the stimulated action potential of ganglion neuron cells of *L.stagnalis* by using LAPS in which the insulator surface was coated with a 4 nm thick layer of poly-L-ornithine and laminin (PLOL) [106]. The results showed that the potential sensitivity of LAPS and cell adhesion were significantly improved by the coating of PLOL, allowing LAPS to work as a cell-semiconductor hybrid. Later on, Wang's group carried out other work on this application of LAPS [107-109]. For example, they studied the cardiotoxicity effects from different drugs (amiodarone, levofloxacin, sparfloxacin and noradrenaline)

on the extension of ventricular action potentials of cardiomyocytes [108]. The rapid and punctual properties of the sensor indicate that LAPS can be used for high-throughput pharmacological toxicity investigation. Furthermore, they developed an olfactory-based biosensor to detect the odorant molecules [109]. Essentially, the olfactory sensory neurons from 3-day-old Sprague-Dawley rats were cultured on a LAPS substrate and a sensor response between the extracellular potential firings and the concentration of diacetyl in the range of 0.1 μM to 100 μM was observed.

In fact, few of the applications of LAPS discussed above have actually benefitted from the advantage of spatial resolution. As a chemical imaging sensor, LAPS is expected to visualize the two-dimensional distribution of a specific chemical species within the solution or provide two-dimensional maps of living cells or cell signalling. To implement this application, a new "chemical image scanner" system based on a linear LED array and frequency division multiplex was proposed to visualize the spatial distribution of chemical species. A scan time of 6.4 s for an ion concentration image at a resolution of 16 pixels $\times$ 128 lines was achieved with the new system [110]. Later, an organic-LED displace was introduced as the light source in LAPS by the same group [111]. It enabled a higher measurement resolution and a distinct miniaturisation of the system. In addition, the measurement time of chemical images was dramatically reduced by a factor of 40 compared to the traditional display used in LAPS. Figure 1.16 (a) shows an example of a chemical image with the word "LAPS", which was written with a polymer resist. The same system was used to visualize an enzymatic reaction in a microfluidic channel [112]. The spatiotemporal changes of pH distribution induced by the enzymatic reaction are shown in Figure 1.16 (b). On the other hand, Krause's group has obtained impedance images of polymers (poly(methyl methacrylate) (PMMA) [74] and cellulose acetate [75]) and photoresist [14] with micron to sub-micron resolution by using a femtosecond laser (see Figure 1.16 (c)).

(a)

(b)

(c)
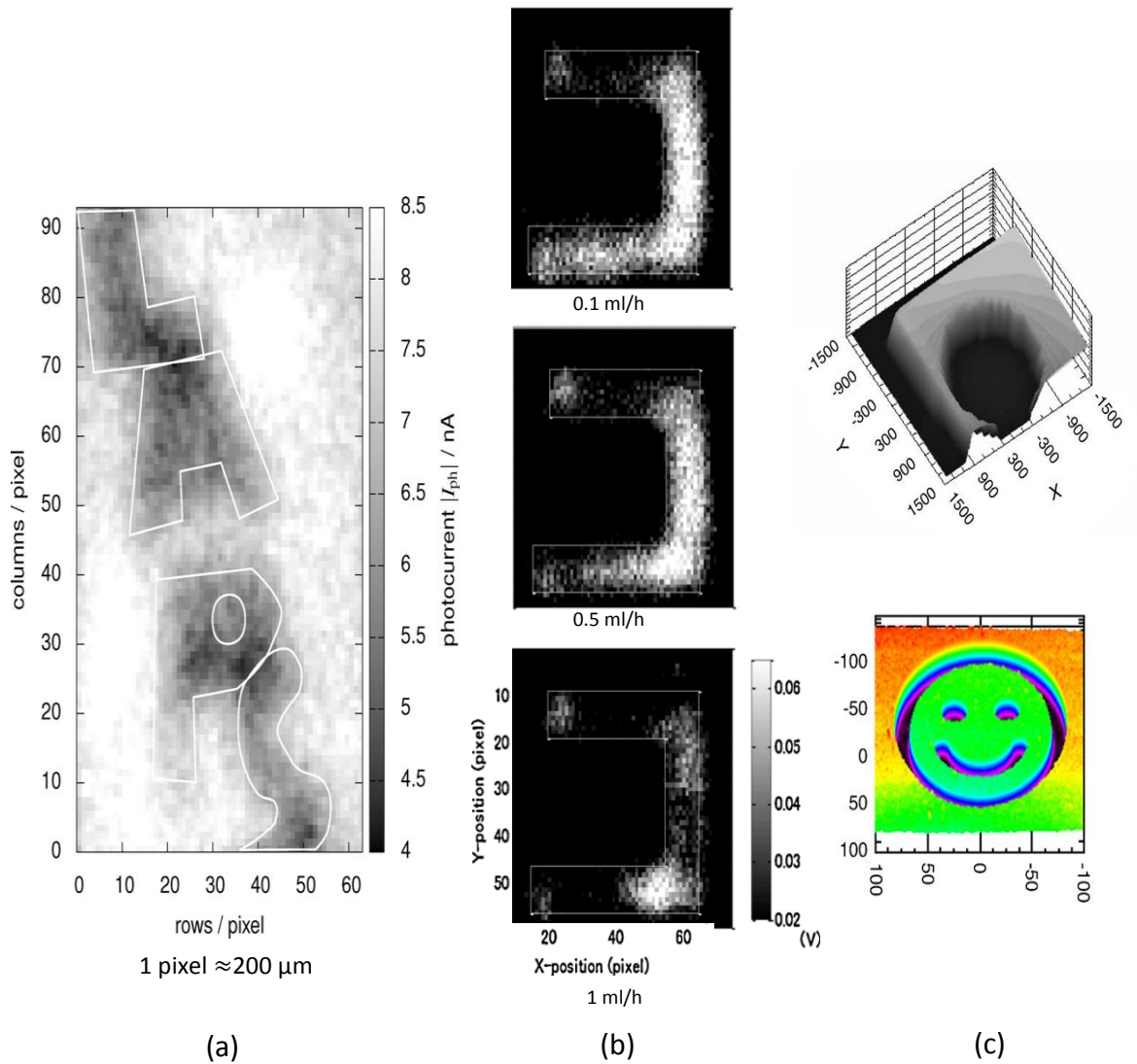
Figure 1.16 Photocurrent images of (a) polymer resist with a measurement spot size of
2 × 1 pixels (1 pixel ≈ 200 μm) and a modulation frequency of 1.74 kHz (reproduced
from Ref [111]); (b) enzymatic reaction in the microfluidic channel recorded at
different flow rates (0.1 ml/h, 0.5 ml/h and 1.0 ml/h) of urea solution (1 pixel ≈
200 μm) (reproduced from Ref [112]) and (c) PMMA dot on the gate area of a
SOI/SiO$_2$ structure with a 7 μm thick silicon membrane (top, scale in μm) (reproduced
from Ref [74]) and SU-8 pattern on an SOS substrate with an anodic oxide using two-
photon effect laser with 1250 nm wavelength and 1 kHz frequency (bottom, scale in μm)
(reproduced from Ref [14]).

1.4 Cell-semiconductor hybrids based on field-effect structures

1.4.1 Cell junctions

Cell junctions are the interactions of cells with other cells or the extracellular matrix (ECM). They exist within the tissue of some organisms and can be classified into three categories, which are occluding junctions (tight junctions), communicating junctions (gap junctions) and anchoring junctions (include adherens junction, desmosomes and hemidesmosomes) [113]. Occluding junctions chemically seal extracellular pathways and prevent the movement of small molecules between cells. Generally, they are present in different types of epithelial cells. Communicating junctions, however, allow chemical or electrical signals to be transmitted between adjacent cells. Anchoring junctions offer mechanical contacts of cells to other cells or surrounding extracellular matrix. Figure 1.17 (a) shows the epithelial cell junctions schematically [114].

(a)   (b)
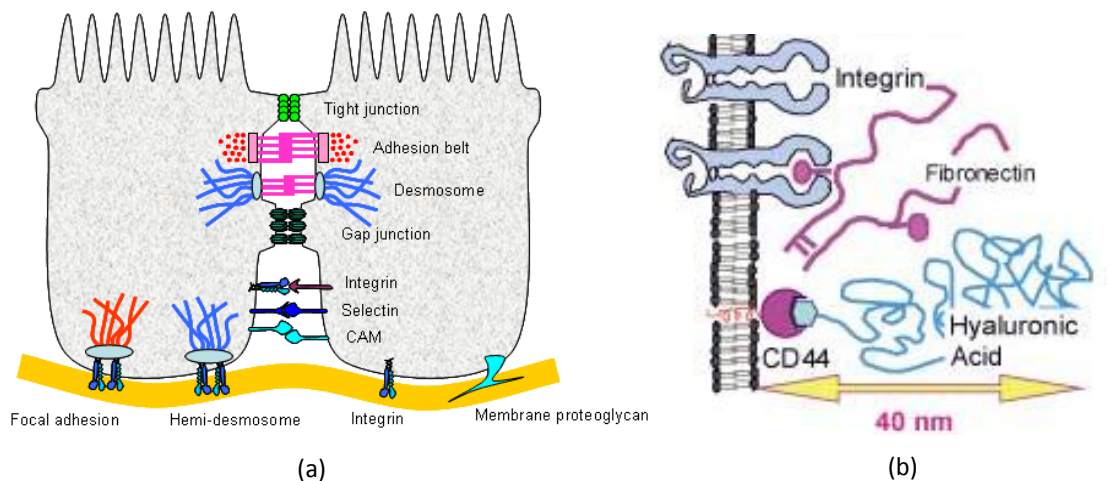
Figure 1.17 (a) Cell-cell and cell-matrix junctions in epithelial cells (reproduced from Ref [114]) (b) cell adhesion model on extracellular matrix (reproduced from Ref [115]).

To study the cell-semiconductor hybrids system, it is critical to understand the interactions of cells with semiconductor surfaces. It is well known that cells attach to the extracellular matrix through the link of the transmembrane adhesion proteins (receptor) and the proteins/glycosaminoglycan (ligand) deposited on the substrate. Common transmembrane receptors include integrins and the CD44 antigen. As the most versatile type of receptor, after activation, integrins bind various ligand proteins such as fibronectin, laminin and collagen. CD44 antigen is a cell surface glycoprotein

that mainly binds to hyaluronic acid and also interacts with other ligands such as collagens and osteopontin. A model of the cell adhesion to extracellular matrix is shown in Figure 1.17 (b). These interactions between acceptors and ligands may act as repulsive spacers and cause a cleft with a certain distance between the cell and extracellular matrix [115].

1.4.2 Neuron transistors based on field-effect transistors (FETs)

1.4.2.1 Models

As an inert substrate for cell culture, silicon has been widely applied to produce neuron-semiconductor chips. To study the neuroelectronic interface with electrochemical measurements, a metal-free field-effect transistor was used. Figure 1.18 shows the typical set-up of a neuron transistor [7]. An AC voltage ($V_p(t)$) with respect to the electrolyte (ground) was applied to the neuron using a patch pipette fused to the neuron cell. Bias voltages with respect to the electrolyte were applied to the bulk silicon (*B*), source (*S*), and drain (*D*). The modulated intracellular voltage $V_m(t)$ couples through the cell membrane into the junction and eventually affects the silicon transistor, resulting in a coupling of ionic signals in the neural cell and electronic signals in the silicon substrate.
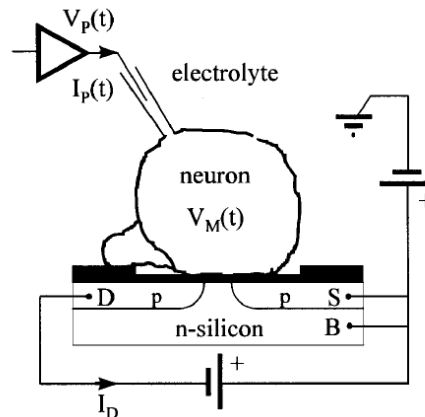
Figure 1.18 Set-up of a neuron transistor [7].

Since a cleft with a certain distance determined by the adhesion proteins always exists between the cell and substrate, to model the cell-silicon junction circuit, the effect of the cleft should be taken into account. Two different equivalent electrical circuit models were introduced by Fromherz' group to describe the current-voltage relationship of the neuron transistor [2, 8]. One is a two-dimensional area-contact, and

the other one is a zero-dimensional point-contact, which are shown in Figures 1.19 (a) and (b), respectively.
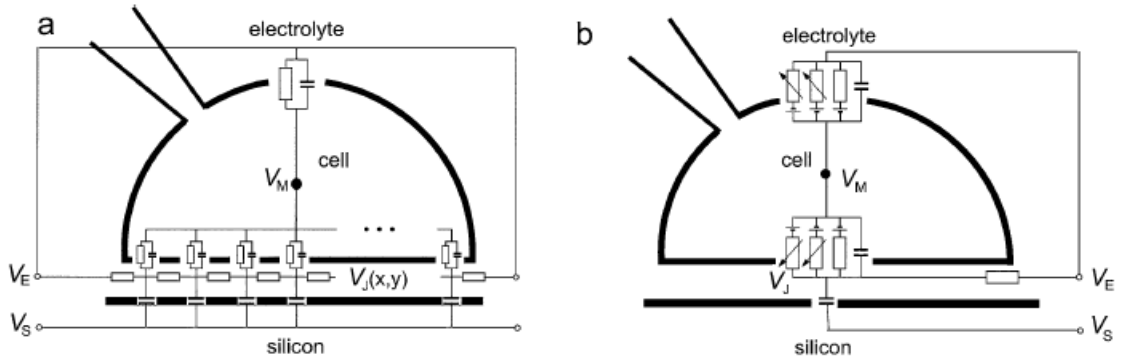
Figure 1.19 (a) AC circuit of area-contact model and (b) DC circuit of point-contact model with voltage dependent ion conductance [8]. V_M, V_J and V_S are the voltages of cell, junction and silicon with respect to the electrolyte voltage V_E.

1.4.2.2 Cleft of neuron-silicon junction

In the models presented in Figure 1.19, the capacitances of the cell membrane and silicon chip are usually known and the ion conductance information of the membrane can be found from the literature. Hence, it is essential to study the unknown properties of junctions (such as the resistance and width of the junction) between cell and transistor. The junction is filled with bulk electrolyte. A small width and a large specific resistance and contact area are beneficial for achieving a highly sensitive recording of neuron activity.

The resistance of the junction can be measured through the transistor recording [116-118]. For example, Weis *et al.* investigated the junction resistance of a single Retzius neuron cell cultured on the 16 transistors coated with poly-lysine [118]. When the cell was stimulated with a modulation voltage V_M by patch pipette, modulation source-drain currents I_{SD} from every transistor were produced and identified with the voltage of junction V_J. A sheet resistance of the junction (46 MΩ) was evaluated from the transfer function V_J/V_M with the area contact model recorded by one of the transistors. In addition, they also investigated the condition of one Retzius cell cultured on one transistor (see Figure 1.20 (a)), and two types of the transfer function spectra were obtained (see Figures 1.20 (b) and (c)) [116]. When fitting the spectra with the point-contact model, type A showed a free cell membrane conductance (0.36 mS cm^{-2}) and a

small sheet resistance (7.7 MΩ). However, for type B the membrane conductance and the sheet resistance increased to 38.5 mS cm^{-2} and 41 MΩ, respectively, indicating the opening of ion channels of the neuron.
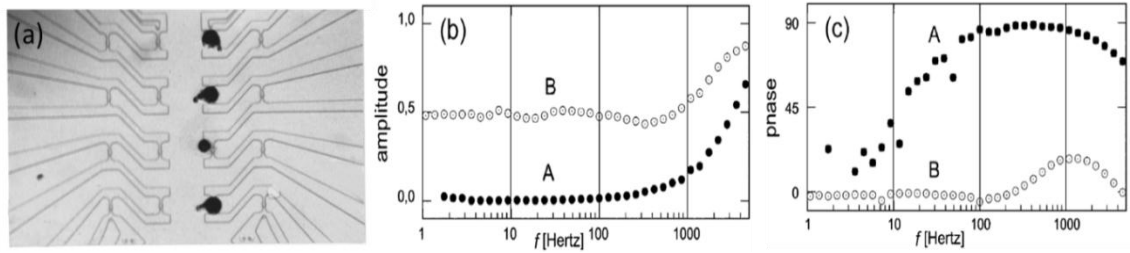
Figure 1.20 (a) Micro-graph of the Retzius neuron cells cultured on 16 channels transistor; two typical types (A and B) of (b) amplitude and (c) phase spectra of the voltage transfer function V_J/V_M recorded by the transistors [116].

The width of the junction can be evaluated from the resulting extracellular voltage profile using the area-contact model. Once the sheet resistance r_J (46 MΩ) was known, the junction width was estimated to be 22 nm using the relationship of $r_J = \rho_J/d_J$ ($\rho_J \approx 100 \ \Omega$ cm) [118]. Another more direct way to evaluate the junction width is using fluorescence interference contrast (FLIC) microscopy which was also developed by Fromherz' group [1, 2, 119]. For example, a distance of 50 nm between the neural cells from rat brain and poly-L-lysine modified silicon chip was obtained by FLIC [2]. A similar result (~54 nm) was concluded for nerve cells from rat hippocampus cultured on the same surface. However, in the case of human embryonic kidney (HEK 293) cells, which were cultured on a fibronectin modified silicon surface, the cleft width was around 75 nm [1]. It was demonstrated that by changing the resistivity of the bulk electrolyte solution, the junction width stays constant, however, the sheet resistance of the junction changes proportionally [1].

1.4.2.3 Applications

At the early stage, the neuron transistor was used to record the neuronal activity of individual neural cells or the activity induced by the capacitive stimulation from a transistor. For example, a bistable switching of the attached membrane conductance induced by the mechanical deformation of cells was recorded using the neuron-transistor [120]. The change of the conductance may be due to the activation of ion channels and/or the self-gating effect within the adhesive cell membrane. The neuron-

transistor was also used to record action potentials of neurons (i.e. rat hippocampal neurons [121] or left upper quadrant neurons from the abdominal ganglia of *Aplysia californica* [122]) and the activity of ion channels such as recombinant maxi-K (Ca) channels [123] and voltage-gated EAG K$^+$ channels in HEK 293 cells [124]. Moreover, by capacitive stimulation from the silicon chip, the activation of recombinant NaV1.4 sodium channels [125] and the opening of Kv1.3 potassium channels [126] in HEK293 were recorded. To achieve a high capacitance and thus a sufficient strength of electrical coupling, thin films of HfO$_2$ (10 nm) and TiO$_2$ (17 nm) were used as the insulator, respectively.

Neuronal networks have been successfully interfaced with silicon transistors in order to monitor the output of synaptically connected neurons [127]. Fromherz' group has shown that a semiconductor chip can be directly joined with an excitatory chemical synapse between two different neurons from pond snails [128]. The snail's presynaptic cell was stimulated with a chip capacitor and the action potential of the postsynaptic cell was recorded with a transistor. This study will benefit the long-term investigations of memory in neuronal nets and the development of biochips for chemicals interfering with synaptical activity.

The introduction of the multi-transistor-array (MTA) with an electrolyte-oxide-metal-oxide-silicon (EOMOS) structure implements the two-dimensional recording of the activity of neuronal networks or even brain slices [4, 10, 129, 130]. Figure 1.21 (a) shows the schematic cross-section of a sensor transistor with EOMOS configuration [129]. Unlike the traditional FET, the chip has a chemically homogeneous and inert surface of TiO$_2$ which benefits cells growth [129]. The sensor transistor with its intrinsic gate oxide is buried in the chip and it is connected to the chip surface via a metallic pathway. Figure 1.21 (b) shows the real image of the surface of MTA which consists of 128×128 sensor transistors on 1 mm^2 with a pitch of 7.8 μm [129]. To study neuronal networks with a spatial resolution, snail neurons were cultured on the sensor surface, and a network of neurons (marked with "I", "II", "III") joined by electrical synapses was formed (see Figure 1.21 (c)). When neuron "I" was stimulated with an impaled micropipette, a burst of action potentials was induced, and then, postsynaptic neurons "II" and "III" were excited subsequently by coupling via electrical synapses. Figure 1.21 (d) shows the recording of neuronal excitation of neuron "I", "II" and "III" according to time; while Figure 1.21 (e) shows the

extracellular voltage maps of the neuronal network corresponding to the area marked in Figure 1.21 (c) and the time marked by arrows in Figure 1.21 (d) [4]. More recently, MTA was applied to electrically stimulate retinal neurons in epiretinal and subretinal configuration, offering the possibility of partial restoration of visual function [130].
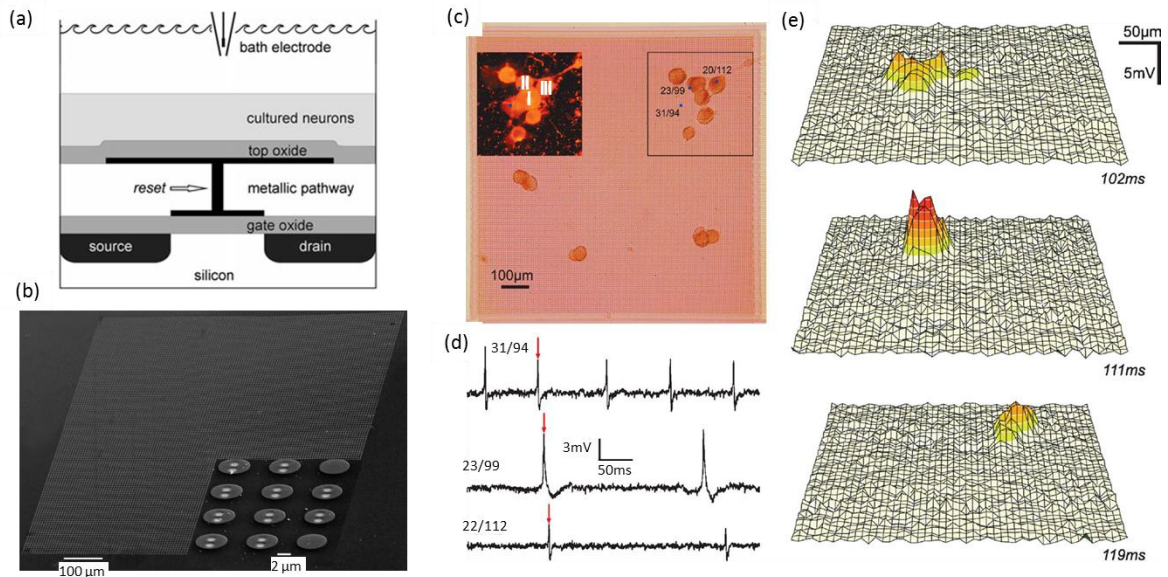
Figure 1.21 (a) Schematic cross-section of a sensor transistor with EOMOS configuration (reproduced from Ref [129]). (b) Scanning electron micrograph of the surface of multi-transistor array (MTA) which consists of 128×128 sensor transistors on 1 mm^2 with a pitch of 7.8 μm (inset: blow up) (reproduced from Ref [129]) (c) Array of sensor transistors with twelve snail neurons cultured for 24 hours (inset: the fluorescence micrograph of the marked square area which shows a network of neurons "I", "II", "III" joined by electrical synapses). (d) Recordings of three selected sensor transistors beneath the three neurons (the arrows mark the time chosen for plotting the maps). (e) Extracellular voltage maps of the neuronal network on an area of 375 μm × 375 μm corresponding to the area marked in (c) (reproduced from Ref [4]).

The ultimate application of neuron transistors is to develop neuroelectronic devices, which are hybrid systems that can integrate electronic circuits with typical features of neuronal dynamics and memory. These brain-like devices might be used in medical treatment such as neuroprosthetics, pharmacological remedies and radiotherapy, which will potentially affect the whole of society.

1.4.3 Cell impedance spectroscopy based on FETs

When normal cells attach and spread on an electrode, they can be simply considered as insulating particles to hinder current flow. The traditional method to measure the cell insulating effect is electric cell-substrate impedance sensing (ECIS), which was developed by Giaever's group. As a commercially available system, it can detect the cell impedance as a function of frequency and provide cell morphological information [131]. However, as it is confined by the size of the gold electrode, ECIS can only work with a layer of cells or a few cells, making the real single cell measurements difficult [132].

To overcome the restriction, Fromherz and Ingebrandt introduced a transistor-transfer function (TTF) method based on field-effect transistor (FETs) to observe the cell-matrix binding event [117, 133]. The experimental set-up is similar to the neuron transistor described in section 1.4.2. The only difference is that the cell is stimulated by an electrode in the bulk electrolyte instead of an invasive patch pipette fused to the cell. Generally, a transistor with 16-channel open-gate FET array was used and each gate size is smaller than the typical adhesion area of a single cell, which means the signals from a single cell and/or no cell can be detected simultaneously.
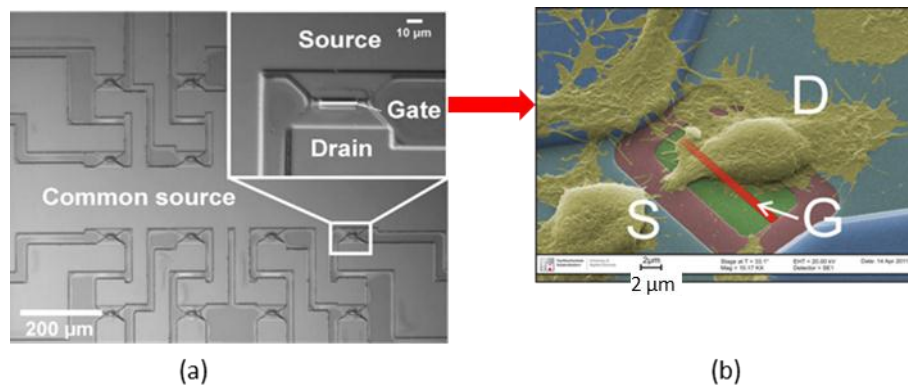
Figure 1.22 (a) The structure of the transistor with 16-channel open-gate FET array (reproduced from Ref [133]); (b) scanning electron microscopic image of a HEK293 cell attached to the transistor. "S" and "D" represent source and drain. "G" marks the electrically sensitive part of the transistor (reproduced from Ref [132]).

A typical structure of the transistor and a sample image for a single cell attaching to the gate of a transistor are shown in Figure 1.22. The TTF method specifically involves the recording of the transfer function, which is defined by the ratio of the input and

output voltage signals collected by lock-in amplifier. To simplify the equivalent electrical circuit (EEC), the point-contact model is always used and the active elements such as ion-channel activity are neglected.

By using this method, Kiessling *et al*. concluded the specific resistance of the junction between a red blood cell and the silicon chip (280 ± 60 Ω cm) was 4 times larger than the specific resistance of the bulk electrolyte (74 Ω cm) [117].

In Ingebrandt's method, the v_{out} was directly transformed from the source-drain currents [133]. Figure 1.23 (a) shows the EEC for a single cell attached to the transistor, while (b) shows typical transfer function results of the gates with cell and without cell based on the circuit model of (a) [133].
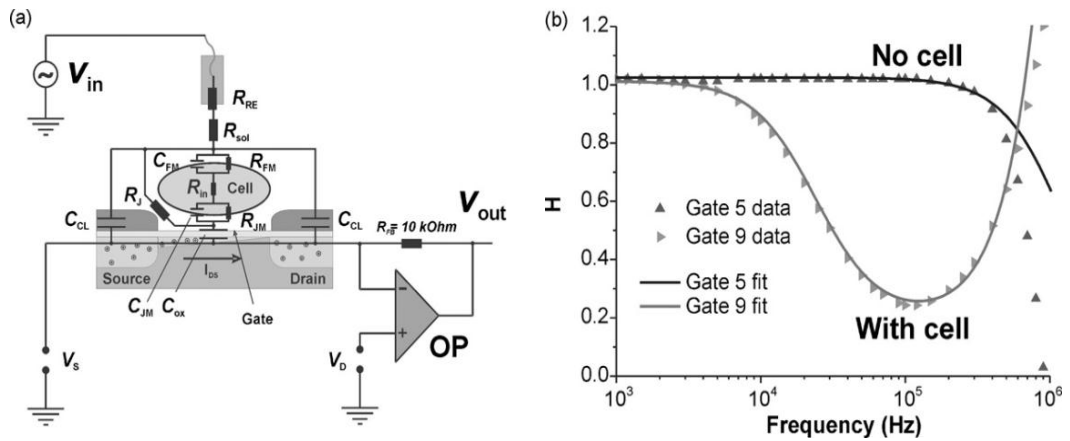
Figure 1.23 (a) Equivalent electrical circuit model for a single cell attached to one gate of the transistor (b) typical transfer function results for the gates with cell and without cell using the model of (a) (reproduced from Ref [133]).

By fitting the TTF spectra with the EEC described in [133], cell adhesion related parameters such as junction resistance R_J and the effective membrane capacitance C_M (series combination of the free membrane capacitance and attached membrane capacitance) can be estimated [132-135]. Here, a high R_J indicates strong cell adhesion strength, and a large C_M reflects a flat morphology of cells. Based on this theory, single HEK293 cell adhesion events caused by chemical treatments [133], H441 cell death induced by nanoparticles [135], anti-cancer drug action of HEK293 and H441 cells [132], and the human T cell adhesion and migration on different pre-treated surfaces [134] have been investigated. For example, when a HEK293 cell was treated with trypsin which can gradually detach the cell from the transistor, the transfer function

values increased, approaching the values without cell attachment. However, if the cell is treated with AmpB, one can decompose the cell membrane and enhance the cell fragment attachment with a bigger area, the transfer function decreased. The results demonstrated the high sensitivity and selectivity of the system to cell-binding status. Furthermore, they have measured the interactions between single human CD8$^+$ T cells and FET substrates modified with fibronectin, anti-CD3 antibody or anti-LFA-1 antibody [134]. Table 1.1 shows the transfer function fitting results described in [134]. Specifically, when cell migration activity occurred, the transfer function signals fluctuated which can be recorded by the same system.

Table 1.1 A summary of CD8$^+$ cell adhesion related parameters of R_J and C_M fitting from the transfer function with the electric circuit model mentioned above [134].

	R_J (MΩ)	C_M (pF)
Fibronectin	1.23	1.52
CD3	4.71	0.50
LFA-1	2.95	2.16

1.5 Self-assembled organic monolayers (SAMs) on hydrogen-terminated silicon substrates

Self-assembled monolayers (SAMs), which are directly bonded to silicon without an intervening layer of silicon dioxide, have been attracting intense attention over the last two decades [17, 136, 137]. The absence of a SiO$_2$ layer allows the direct coupling between organic molecules and silicon substrates, offering the opportunity to study the kinetics and mechanisms of the involved grafting reactions systematically, thus contributing to the design of new reactions in organic or organometallic synthesis [138]. It is well known that siloxane monolayers (Si-O-Si-R) are unstable and prone to hydrolytic cleavage in electrolyte solutions [139]. However, a Si-C bond, which is well-defined and chemically stable, makes their long-term use in ambient conditions and aqueous solution possible. In addition, the selective control of surface chemistry in hydrosilylation enables the easy and diverse modification and functionalisation of the silicon surface. This will allow us to take full advantage of intrinsic electronic

properties of silicon, thus broadening the range of applications in biosensors and molecular electronics [17-20].

1.5.1 Hydrosilylation methods

1.5.1.1 Hydrosilylation by reaction with unsaturated molecules

Linford *et al.* reported the first modification of the silicon surface with a covalent linkage of densely packed alkyl chains in the presence of diacyl peroxides [140]. They suggested that heat causes the decomposition of diacyl peroxides ($[CH_3(CH_2)_nC(O)O]_2$, $n = 16$ or 10) to alkyl radicals ($CH_3(CH_2)_nC(O)O\cdot$), and that this is followed by the grafting onto the silicon dangling bond. They proved that 1-alkenes and alkynes could also form high-quality monolayers on silicon upon reaction with the free-radical of diacyl peroxides [141]. The prepared monolayers showed a similar or better stability to hot solvents, acids and HF solution compared with alkylsiloxane monolayers. The control experiments indicated that heat (≥ 150 °C) without initiator can also trigger the monolayer formation on H-Si. Later, they developed a photochemical method to produce hydrocarbon monolayers by illuminating with ultraviolet light (350 nm) [142]. A surface propagated radical chain mechanism for the monolayer formation on H-Si has been proposed, which is depicted in Figure 1.24 [17, 142]. In short, when H-Si is irradiated with UV-light or initiated with radical precursors, a dangling bond is created. This silyl radical site can add to unsaturated hydrocarbon molecules and extract hydrogen from the neighbouring H-Si, thus reaction propagation occurs [141, 142].
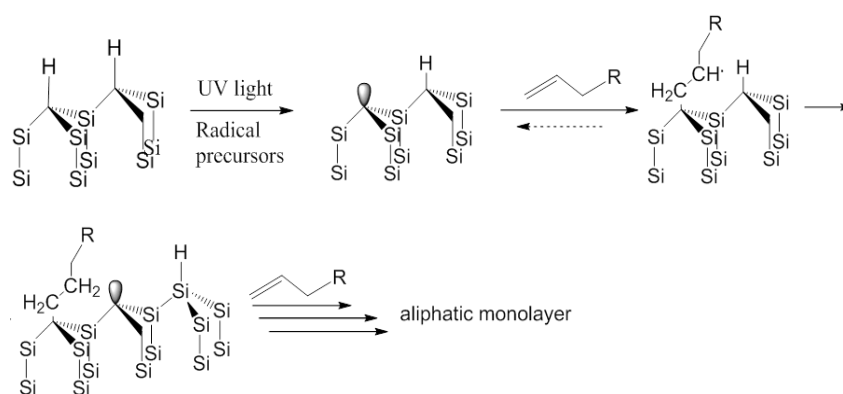
Figure 1.24 Chain propagation mechanism for the reaction of H-Si (111) with unsaturated hydrocarbon [17, 142].

As mentioned above, hydrosilylation with unsaturated hydrocarbons can be initiated by various methods, however, the most widely used are thermal-[143-150] and photon-

induced methods [151-156]. Regarding the thermal method, the hydrosilylation reaction time and temperature are different for different types of hydrocarbons. Even for the same type, the reaction conditions vary from lab-to-lab. For example, a variety of functionalised and non-functionalised 1-alkenes were successfully modified on the H-Si (100) surface by heating up to 200 ℃ for 2 h. The monolayers produced showed high thermal stability, which provided a new pathway to further functionalise the silicon surface [143]. Undecylenic acid layers were deposited on hydrogen-terminated porous silicon at 95 ℃. The reaction occurred only at the C=C double bond, leaving the terminal acid functional group intact [149]. The same monolayer was obtained by keeping the H-Si (111) in degassed undecylenic acid solution at 180 ℃ overnight [18]. 1-Alkenes and 1-alkynes with chain lengths from C_{12} to C_{18} were grafted onto H-Si (111) surfaces at 100 ℃ for 6 h [150]. The influence of the different linkage groups on the monolayer was investigated. Results showed the alkenyl monolayers presented a better quality and surface coverage than the alkyl monolayers. Recently, Gooding and Ciampi have made significant contributions to the alkenyl monolayer modification and further functionalisation of silicon [146, 147, 157, 158]. A symmetrical reactant (1, 8-nonadiyne) was chosen as the starting material and it was covalently bonded onto the silicon by heating to 170 ℃ for 3 h. The alkyne-terminated monolayer provides considerable opportunities for further functionalisation by straightforward and high yielding copper(I)-catalyzed azide alkyne cycloaddition (CuAAC) "click" reactions [147].

The photochemical reaction on H-terminated Si surfaces has also been intensively investigated. A direct photochemical reaction (UV, 6 mW cm^{-2}, 312 nm) of undecylenic acid on H-Si (111) surfaces was reported by Faucheux [151, 152]. With the evidence of IR spectroscopy and AFM, fairly dense monolayers with a surface coverage of 35% (maximum theoretical value ~50%) were obtained. After washing in hot acetic acid, the modified surface was atomically smooth and was terminated with intact carboxyl end groups. Besides undecylenic acid, a series of ω-functionalised alkyl monolayers (such as $-(CH_2)_{11}CH_3$, $-(CH_2)_{10}COOC_2H_5$ and $-(CH_2)_{11}OH$) have been prepared on oxide-free silicon surfaces through UV-induced hydrosilylation [159]. Interestingly, the reactions of unsaturated molecules (1-alkenes and 1-alkynes) on H-Si surfaces also occurred under visible light (447-658 cm^{-1}) irradiation [154-156]. To achieve a highly dense monolayer, the reaction time was increased to 10 h, compared

with 3 h for UV illumination. This mild technique allows grafting of organic molecules with photo-labile groups.

Besides these thermal- and photon- induced methods, Perring's group has reported the chemical reaction of olefins with H-Si (111) surfaces using a mild method [160, 161]. That is, with the presence of 0.1 mol% of 4-(decanoate)-2, 2, 6, 6-tetramethylpiperidinooxy (TEMPO-C_{10}), monolayers such as 1-octadecene or undecylenic acid were assembled onto the silicon in one step at room temperature without UV-light. The effect of TEMPO in the hydrosilylation reaction is not fully determined, however, the necessity to use it to obtain well-ordered SAMs has been claimed [160, 161].

1.5.1.2 Hydrosilylation by alkyl Grignard reactions

Bansal *et al.* published an alternative method referring to a two-step halogenation/Grignard route to modify H-Si surfaces with organic monolayers [162, 163]. In the first step, Si-Cl bonds were formed by exposing H-Si to PCl_5 for 10-60 min at 80-100 °C. Subsequently, the chlorine-terminated silicon was transferred to different alkyl-Grignard (RMgX) reagents for 30 min to 8 days at 80 °C. The XPS and Fourier transform infrared spectroscopy (FTIR) results demonstrated that oxide free and diversely functionalised silicon surfaces were achieved by using this simple and general approach. Electrochemical measurements showed excellent current density-potential properties, indicating the resistance of monolayers to oxidation. Figure 1.25 shows the schematic of the two-step halogenation/alkylation reaction with Grignard reagents [162].
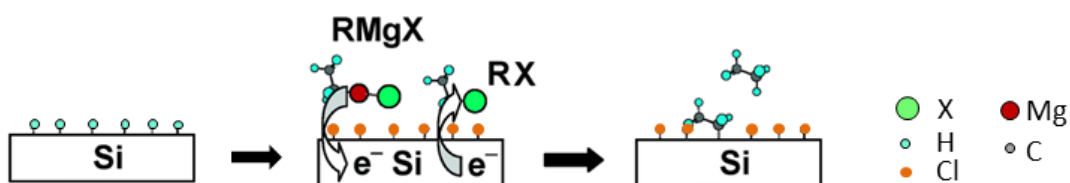
Figure 1.25 Schedule of two-step reaction sequence with Grignard reagents (reproduced from Ref [162]).

Due to the non-polar character of the methyl group, the reaction with H-Si is hindered by a high kinetic barrier. However, Dubois *et al.* explored an electrochemical activation approach to overcome this barrier with Grignard reagents [164]. When the

reaction was carried out in an ether/CH$_3$MgI solution, over 80% of hydrogen on porous silicon was substituted by methyl groups in a few minutes. The reaction routes were also used for the flat silicon surface modification [165]. Based on the experimental results, a reaction scheme involving a three-step mechanism for the electrochemical grafting from Grignard reagents was proposed (shown below) [166, 167].

$$RMgX \rightarrow R^{\cdot} + MgX^{+} + e^{-} \quad \text{(Equation 1.19 (a))}$$

$$RX + e\text{-} \rightarrow R^{\cdot} + X^{-} \quad \text{(Equation 1.19 (b))}$$

$$\equiv Si - H + R^{\cdot} \rightarrow \equiv Si^{\cdot} + RH \quad \text{(Equation 1.20)}$$

$$\equiv Si^{\cdot} + R^{\cdot} \rightarrow \equiv Si - R \quad \text{(Equation 1.21 (a))}$$

$$\equiv Si^{\cdot} + RMgX \rightarrow \equiv Si - R + MgX^{+}e^{-} \quad \text{(Equation 1.21 (b))}$$

$$\equiv Si^{\cdot} + RX \rightarrow \equiv Si - X + R^{\cdot} \quad \text{(Equation 1.21 (c))}$$

$$\equiv Si - X + RMgX \rightarrow \equiv Si - R + MgX_2 \quad \text{(Equation 1.22)}$$
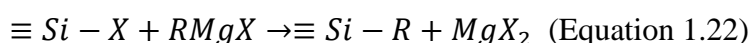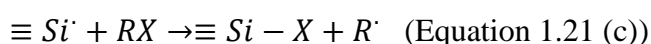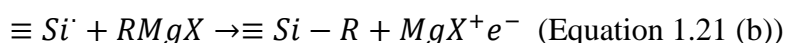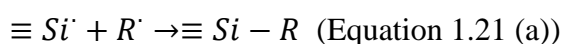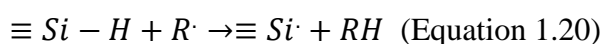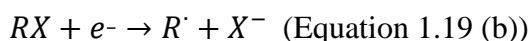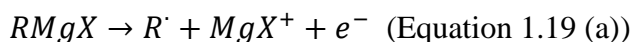
To further study the Grignard-induced hydrosilylation, Boukherroub *et al.* surprisingly found that a one-step reaction of an alkyl Grignard reagent (alkylmagnesium bromide) with a silicon surface was possible [168]. These directly modified surfaces had similar characteristics to those modified by the photochemical method or the two-step halogenation/Grignard method. After several weeks, no measurable deterioration was observed, indicating a good stability of the prepared monolayer [168]. However, since the surface contamination by metal ions is inevitable, it is difficult to produce really clean, dense monolayers using Grignard chemistry [169].

1.5.1.3 Electrochemical approaches for hydrosilylation

As an alternative way to generate radicals, an electrochemical method was introduced for organic monolayer formation on silicon. In this method, the H-Si surface is firstly electro-initiated, which is followed by the covalent binding of organic molecules to the silicon substrate. A typical three-electrode electrochemical set-up for monolayer grafting is shown in Figure 1.26 (a), where the working electrode is the silicon substrate on which the monolayers are formed [170].

In 1998, the electrochemical method for hydrosilylation was developed by Allongue's group for the first time. They prepared the H-Si (111) surfaces with a direct Si-phenyl bond by electrochemical reduction of commercially available aryl diazonium salts [171-173]. By using this method, a variety of functional groups, such as Br, NO_2, CN, NH_2, COOH and C_nH_{2n+1} ($n = 1, 4, 12$) have been introduced to the monolayers and the following reaction mechanism was suggested [172]:

$$N \equiv N^{\oplus} - Ar - X + e^- \rightarrow Ar^{\cdot} - X + N_2 \text{ (Equation 1.23)}$$

$$\equiv Si - H + Ar^{\cdot} - X \rightarrow \equiv Si^{\cdot} + H - Ar - X \text{ (Equation 1.24)}$$

$$\equiv Si^{\cdot} + Ar^{\cdot} - X \rightarrow \equiv Si - Ar - X \text{ (Equation 1.25)}$$

$$\equiv Si - H + H_2O + e^- \rightarrow \equiv Si^{\cdot} + H_2 + OH^- \text{ (Equation 1.26 (a))}$$

$$\equiv Si^{\cdot} + H_2O + e^- \rightarrow \equiv Si - H + OH^- \text{ (Equation 1.25 (b))}$$
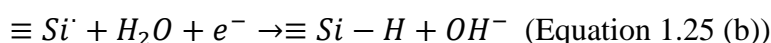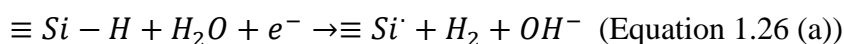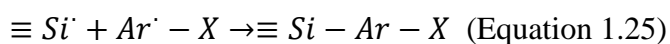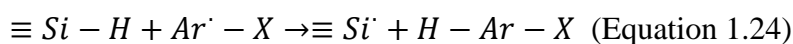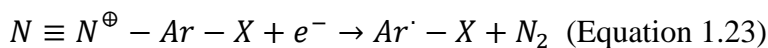
It was reported that the prepared substrates were capable of resisting HF solution. A low density of electronic states at the interface of silicon and the organic monolayer was determined by capacitance-voltage measurements, indicating the possibility for microelectronics processing and applications of SAM-modified silicon [173].

Robins *et al.* investigated the electrochemical grafting of alkynes on porous silicon using different polarity of the bias voltage [174]. The results showed that cathodic electrografting (CEG) causes alkyne attachment to the H-Si surface, while anodic electrografting (AEG) produces an alkyl surface (see Figure 1.26 (b)).

(a)   (b)
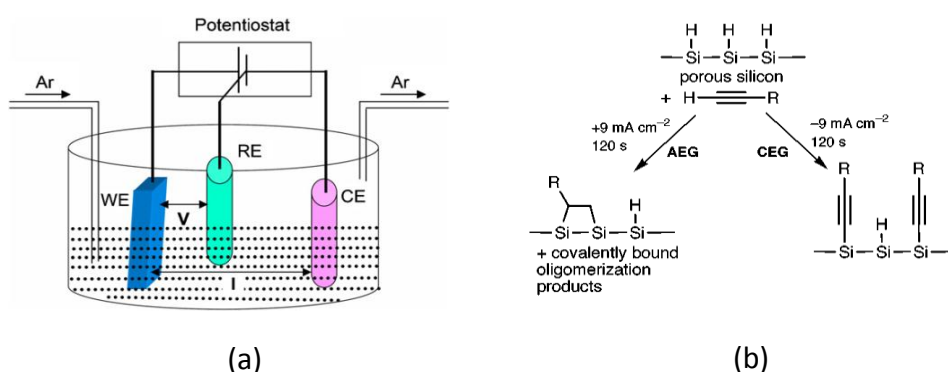
Figure 1.26 (a) Three-electrode electrochemical set-up for electrografting of organic molecules (reproduced from Ref [170]) (b) schematic for CEG and AEG electrochemical reactions (reproduced from Ref [174]).

Cattaruzza *et al.* compared the covalent bond density of carboxyl-terminated monolayers on p-Si prepared by thermal and photo-induced and CEG methods [175, 176]. They applied a stepwise procedure with a fluorescent probe to determine the quality of monolayers. It involved the formation of an amide-terminated monolayer by the amidation reaction of carboxyl and 7-amino-4-methylcoumarin (AMC), followed by intensive washing of the surface to remove any physisorbed molecules. The AMC was then detached from the surface and was quantified by a fluorescence analysis. A highest carboxyl density was observed for the sample prepared by the CEG method, which may due to the negative potential protecting the silicon from oxidation.

1.5.2 Further derivation of ω-functionalised 1-alkene monolayers

The formation of SAMs on a silicon surface is not only used for the passivation or chemical stabilisation of the silicon, but also for the modification of surface properties in a controlled way. For example, the SAM-modified silicon can be further modified with oligonucleotide chains through covalent binding, thus providing DNA arrays for biosensing.

Hamers and Smith proposed different cases for the modification of well-defined DNA on silicon surfaces [177-179]. In one case, ω-unsaturated alkyl esters were prepared on a Si (111) surface using UV-irradiation, and were then saponified to leave a carboxylate group to electrostatically bind with poly-lysine (PL). Finally, thiol-modified DNA was attached to the modified surface using the hetero-bifunctional cross-linker of sulfo-succinimidyl 4-(*N*-maleimidomethyl)-cyclohexane-1-carboxylate (SSMCC) (Figure 1.27 (a)) [177]. To simplify the reaction scheme, in the other two cases, *t*-butyloxycarbonyl (*t*-BOC)-protected amines (10-aminodec-1-ene (ADE) or 1-amino-3-cyclopentene (ACP)) were directly attached onto the silicon surface via a UV-method, shown in Figures 1.27 (b) and (c) [178, 179]. The hybridization experiments of the immobilised DNA exhibited excellent specificity, good sensitivity and chemical stability, indicating that the coupling of nucleic acid as biomolecular recognition elements to silicon surface was successful [177].
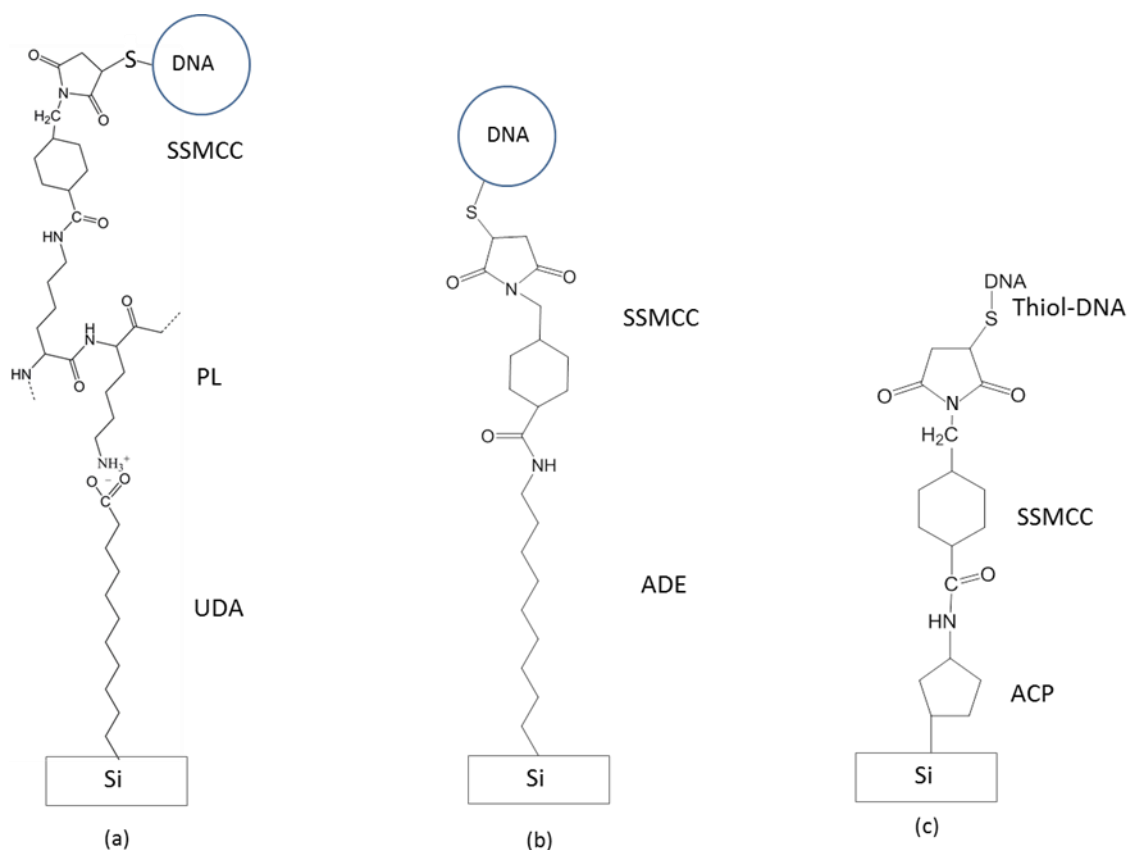
Figure 1.27 Methods for the immobilisation of DNA on amine-modified silicon surfaces. Route (a) is reproduced from Ref [177], (b) is reproduced from Ref [178] and (c) is from Ref [179].

On the other hand, since a carboxyl-terminated surface can be directly obtained without any protection step [20, 160, 180], the classical *N*-ethyl-*N'*-(3-dimethylaminopropyl) carbodiimide/*N*-hydroxysuccinimide (EDC/NHS) activation route was used to yield the "activated" ester ($Si(CH_2)_{10}$–COO–N[CO–CH$_2$–CH$_2$–CO]) for further derivatization (see Figure 1.28 (a)) [181, 182]. As expected, an amino-modified biomolecule, such as DNA, can be reacted with the "activated" ester through the classical amidation (shown in Figure 1.28 (b)) [18, 20]. Touahir *et al.* have studied the various possible reaction paths of EDC/NHS chemistry by infrared spectroscopy and proposed an optimal reaction condition to maximize the yield of succinimidyl ester on the silicon surface. ssDNA oligomers (6-aminohexyl-polyA, 25 mers) or biotin were successfully anchored onto the activated surface [18]. Voicu *et al.* described an approach for patterning the silicon surface with site-directed immobilisation of DNA. Good specificity and excellent stability were obtained under hybridization and dehybridization conditions of DNA [20].
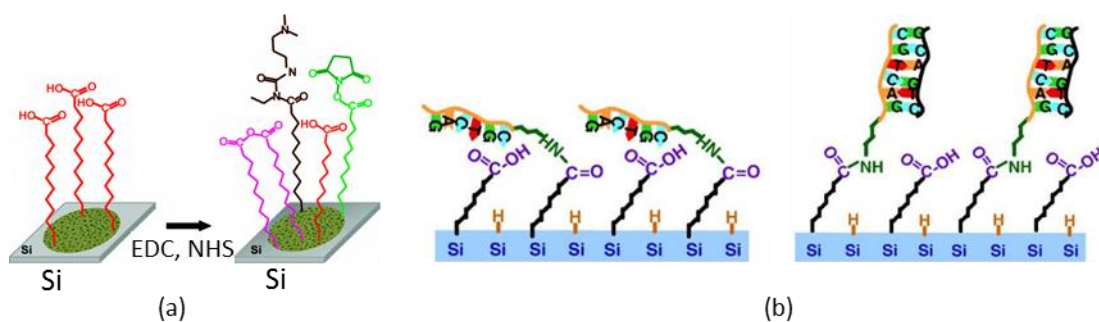
Figure 1.28 (a) Schematic illustration of products from EDC/NHS activation reactions on carboxyl-terminated surface [181] (b) schematic illustration of the coupling of ssDNA on a NHS-activated Si surface (left) and the hybridization with the complementary DNA (right) [18].

1.5.3 Further derivation of SAMs via "click" chemistry

Besides the routes mentioned above, a new surface chemistry which is termed "click" chemistry can be also used for further surface modifications [147, 148, 183-188]. The concept of "click" chemistry was first described by Sharpless' group in 2001 [189] and covered a wide range of chemical reactions. An ideal "click" reaction occurs under very mild conditions with high yield and with minimal by-products. Without doubt, the most well-documented reaction within the suite of "click" reactions is the copper(I)-catalyzed azide alkyne cycloaddition (CuAAC) reaction. Figure 1.29 shows the mechanism for CuAAC reaction suggested by Worrell *et al.*, which involves two copper atoms in the catalytic cycle [190]. One copper atom is σ-bonded to the acetylide while the second one is π-bonded, forming catalytically active complex **1**. This complex reversibly coordinates an organic azide, forming copper-azide-acetylide complex **2**. Following this step, nucleophilic attack at N-3 of the azide by the β-carbon of the acetylide forms intermediate **3**. The ligand exchange in this intermediate is faster than the formation of the second C-N bond, which results in ring closure and the formation of triazolide **4**. Finally, triazole product **5** is formed by protonolysis reactions and the catalyst ligand complex is regenerated for further reaction cycles [190].
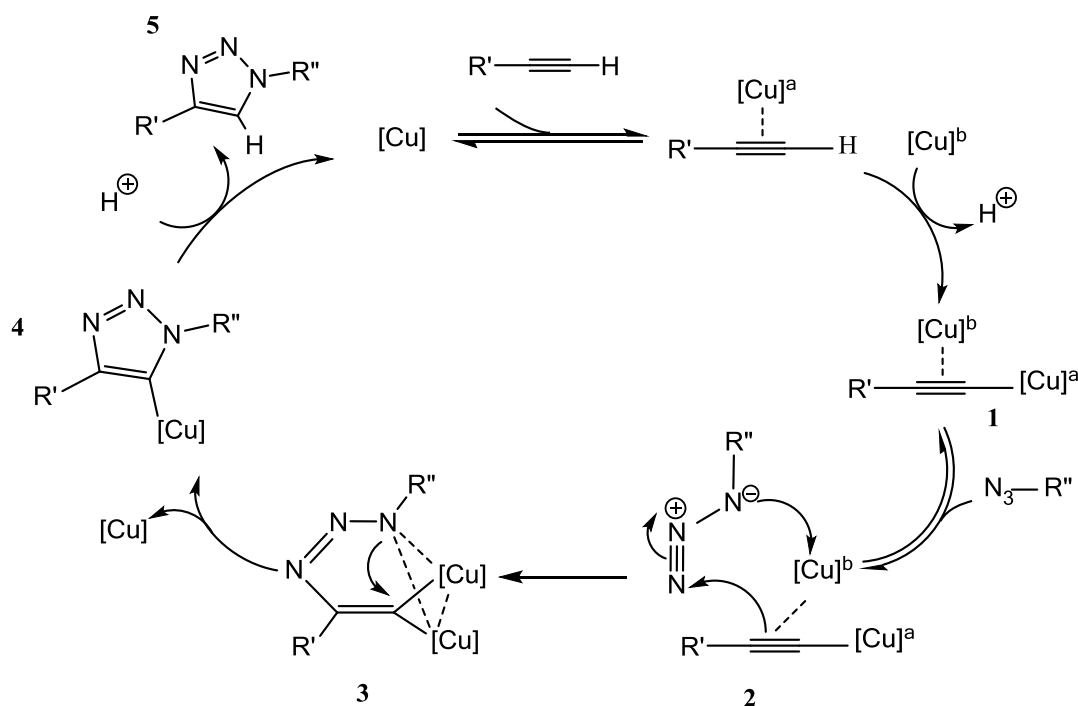
Figure 1.29 CuAAC "click" reaction mechanism [190].

Recently, the CuAAC reaction has been frequently applied to the surface modification of silicon and allows engineering the architecture and function of materials in an efficient and modular way [147, 157, 191]. Usually, it involves the formation of the Si-C bound with a "clickable" platform such as an alkyne on the silicon surface, followed by a further derivation by CuAAC reaction. Figure 1.30 shows three strategies for "click" chemistry on silicon substrates using CuAAC reactions [146, 147, 187, 192].

Heath's group developed the functionalisation approach on the silicon surface with three steps: chlorination, alkylation and "click" chemistry [192]. The detailed procedure is shown in Figure 1.30 (a). Specifically, the electroactive *p*-benzoquinone molecule was clicked onto the silicon surface and was reduced electrochemically to yield an amine-terminated group. Molecules such as ferrocene or biotin with carboxyl groups were then selectively immobilised onto the amine, which provided a way to covalently bind inorganic or biomolecules onto silicon surfaces.
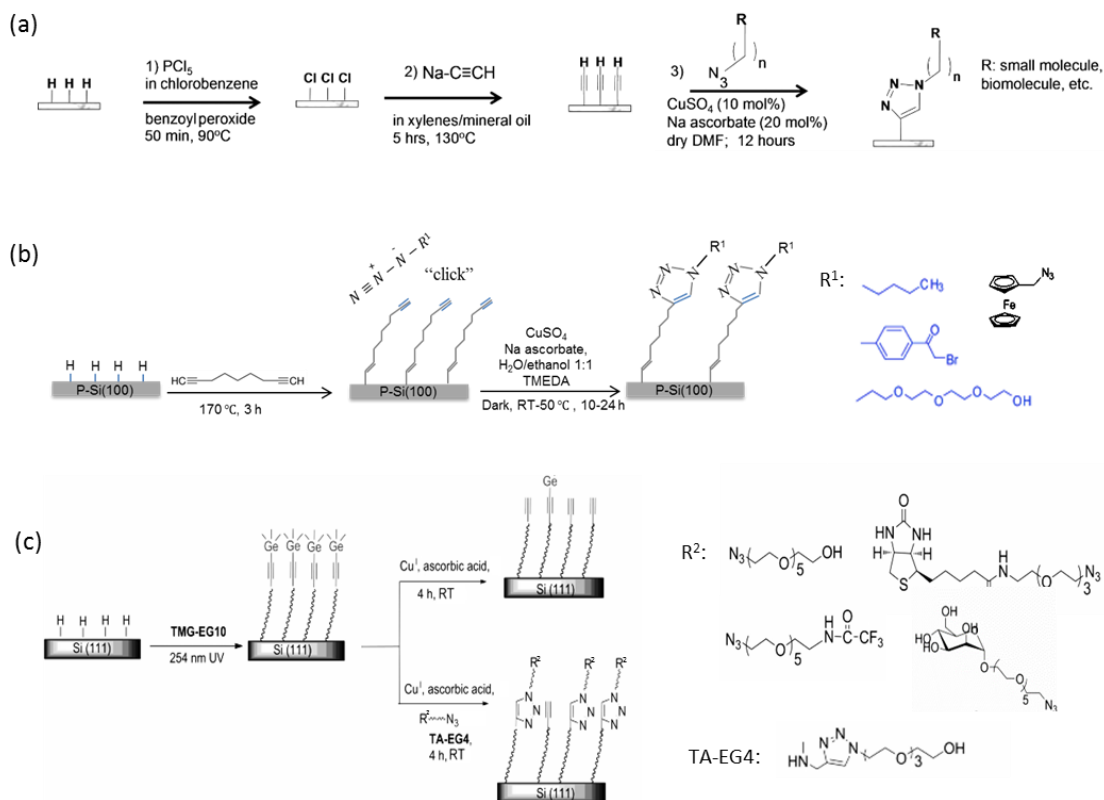
Figure 1.30 Different strategies for CuAAC "click" functionalisation of acetylene-terminated silicon (reproduced from Ref [146, 147, 157, 188]).

Gooding's group has reported a different "clickable" platform. The commercially available 1, 8-nonadiyne was grafted onto the H-Si surface, and then different azides were attached via CuAAC "click" coupling reaction (see Figure 1.30 (b)) [146, 147, 157, 188]. For example, to exploit the electrochemical application of SAM-modified silicon [146], an azide-substituted analogue of the redox-active species of ferrocene was immobilised onto the surface to transfer electrons through the organic monolayers. The results showed that nearly ideal surface electrochemistry of the prepared samples was achieved. Through prolonged electrochemical cycling measurements, the monolayer was still shown to be highly resistant to silicon oxidation. In the same group, ssDNA was immobilised onto 1, 8-nonadiyne and undecylenic acid-modified silicon surfaces via "click" chemistry and EDC/NHS chemistry, respectively [193]. Since DNA is highly negatively charged, when impedance measurements were performed with a charged redox probe ($[Fe(CN)_6]^{3-/4-}$), the charge transfer resistance was significantly changed due to the hybridization/dehybridization of DNA. The results indicated that both types of samples were readily used as electrochemical DNA sensors, but that the 1, 8-nonadiyne passivated silicon was more stable and able to

45

resist surface oxidation during the measurements. Figure 1.31 (a) shows the "click" chemistry strategy of DNA immobilisation and the Nyquist plots for single-stranded, complementary and non-complementary target DNA on silicon electrodes with bovine serum albumin (BSA) as an anti-fouling agent.

Based on the same "clickable" platform, Shamsi *et al.* prepared an 11 residue peptide with an RGD (Arginine-glycine-aspartic acid) sequence on silicon in two steps. First, the peptide was modified with 4-azidophenyl isothiocyanate (API) through the reaction of the amino group and the isothiocyanate group, and then the azide-modified peptide was clicked onto the diyne-modified silicon surface [148]. Since RGD peptides are important in cellular attachment, this approach opens the door to the application of silicon in cell-based biosensors and tissue engineering.

Furthermore, Qin *et al.* developed another new versatile "clickable" platform with trimethylgermanyl (TMG)-protected alkynyl groups on the silicon surface [187] (see Figure 1.30 (c)). The TMG groups could be easily removed in Cu(I) solutions thus allowing a single-step CuAAC reaction with good yields. This efficient grafting scheme was demonstrated by the attachment of oligo(ethylene glycol) (OEG)-azide onto the TMG-alkyne surface, which resulted in surfaces highly resistant to nonspecific adsorption of proteins (fibrinogen). They also demonstrated that biotin-azide and mannose-azide could be clicked to the monolayer platform and could specifically capture targets of concanavalin A and avidin on silicon surfaces (see Figure 1.31 (b)).
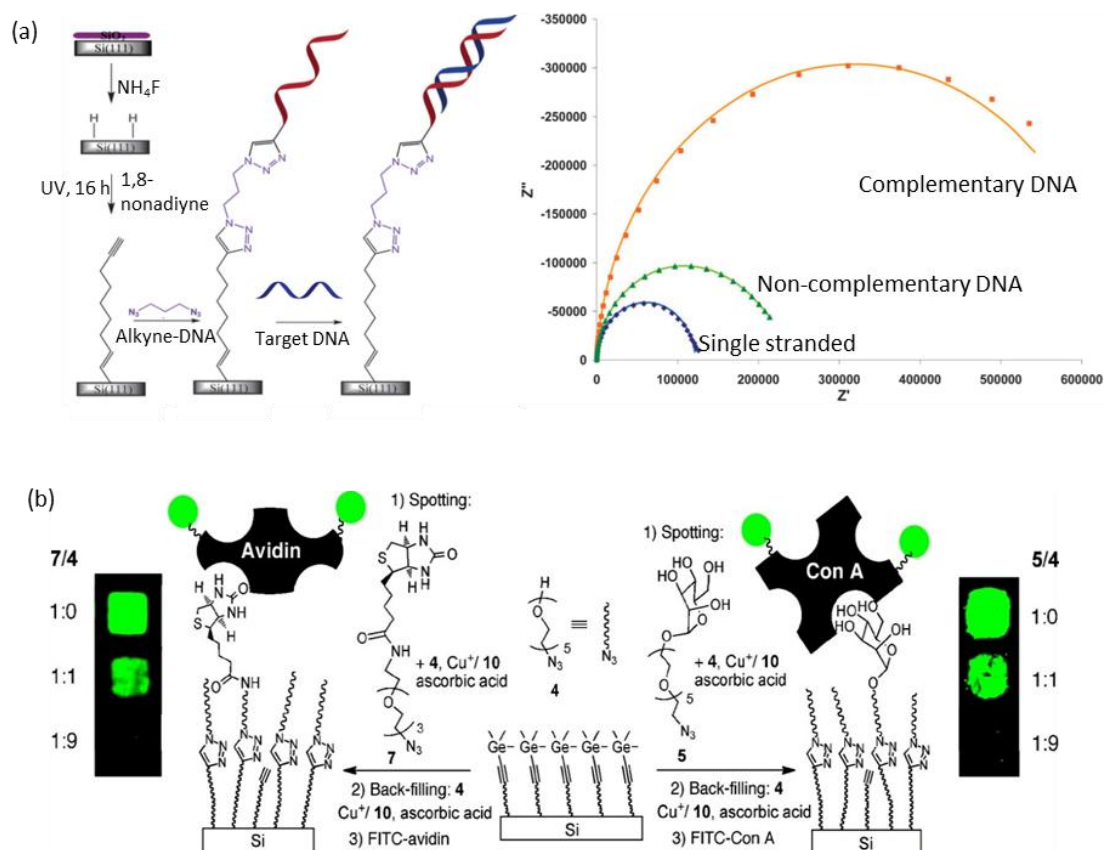
Figure 1.31 (a) Schematic for DNA immobilisation on silicon surface via "click" chemistry method (left) and the impedance spectra for sensors with single-stranded, complementary and non-complementary DNA measured in a redox solution containing 5 mM ([Fe(CN)$_6$]$^{3-/4-}$ and 0.1 M KCl at 0.2 V (right) (reproduced from Ref [193]). (b) Attachment of the biotin-azide and mannose-azide with the OEG-azide on the TMG-alkynyl-terminated films by CuAAC reaction, followed by back-filling with the OEG-N$_3$ and binding with FITC-labeled avidin and concanavalin A (reproduced from Ref [187]).

1.5.4 Summary

SAMs directly bonded to silicon surfaces via Si-C covalent bonds have attracted strong interest due to their potential applications in chemical and biological sensors. Of particular relevance to this work is the use of the organic monolayer as an insulator to optimize the sensitivity and flexibility of LAPS/SPIM in the application of cell-based biosensors. Different methods to perform the hydrosilylation and further modifications on silicon surfaces have been listed above. In this work, the thermal, noncatalyzed hydrosilylation method is chosen to assemble monolayers on H-Si or H-SOS from commercially available chemicals of undecylenic acid and 1, 8-nonadiyne, as both of

the monolayers thus generated have been investigated intensively and reliable reaction routes to their formations have been established. In addition, the undecylenic acid monolayer can be further modified easily with biological probes such as DNA oligomers or proteins though a classical amidation reaction, while the 1, 8-nonadiyne monolayer can be further functionalised with target molecules via "click" chemistry.

Since it is the first time that a SAM has been used as the insulator in LAPS/SPIM, its feasibility has to be validated. To estimate the spatial resolution of LAPS/SPIM and to validate the surface potential imaging, a surface with contrast either in impedance or in potential should be prepared. In the following section, the typical methods for surface patterning will be presented.

1.6 Surface patterning methods

1.6.1 Photolithography

Photolithography, which is extensively used in the microfabrication of semiconductors, is a process to transfer geometric patterns on a mask to the surface of silicon. The typical procedure of photolithography is shown in Figure 1.32. First, the substrate is covered with photoresist by spin-coating. After pre-baking, the photoresist is exposed through a mask to UV-light to cause a chemical change. The sample is then rinsed with a developer, which can remove some of the photoresist. For a positive photoresist, UV-exposed parts are soluble in the developer, however, for a negative one, unexposed regions are soluble. In some applications an etching step is required. A liquid or plasma chemical agent is used to etch the sample surface which is not protected by photoresist. Finally, if the photoresist is no longer needed, it can be removed by using the resist stripper.
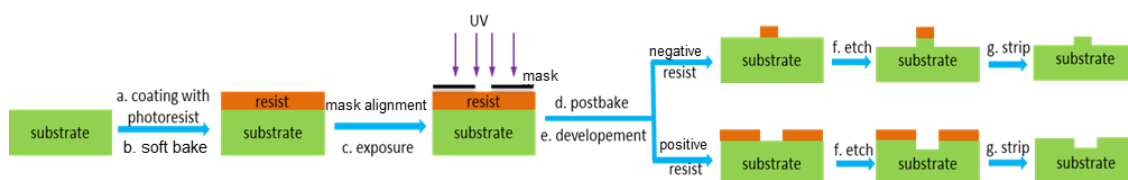
Figure 1.32 Representation of photolithographic processing steps.

Recently, photolithography has been exploited in the fabrication of patterns on silicon surfaces with various molecules [194-196] or biological components (such as

antibodies [197], peptides [198, 199] and DNA [200, 201]) for label-free biosensing or living cells patterning [197, 202, 203]. Zhu *et al.* have reported a strategy for chemically patterning 1, 8-nonadiyne monolayer modified porous silicon with two different species (-OEG-OCH$_3$ and -OEG-OH) using photolithography with a positive photoresist followed by surface modification "click" chemistry [194, 195]. Initially, a metal film was pre-coated onto the 1, 8-nonadiyne monolayer modified-surface in order to exclude the photoresist from the silicon pores, although, the metal film was found to have an adverse effect on the efficiency of the "click" reaction and the metal layer was consequently eliminated [195]. Figure 1.33 shows the improved procedure for chemically patterning [195]. Firstly, a positive photoresist (AZ6612) pattern was prepared on the 1, 8-nonadiyne modified porous silicon by photolithography (step a). Then the first azide species (azido-OEG–OCH$_3$) was attached to the unprotected regions via "click" reaction (step b). The remaining surfaces including the internal pore walls were "clicked" with another azide (azido-OEG–OH) (step d) after the removal of photoresist (step c). Finally, the discretely functionalised substrate was successfully used for selective positioning of BSA and gelatin (step e).
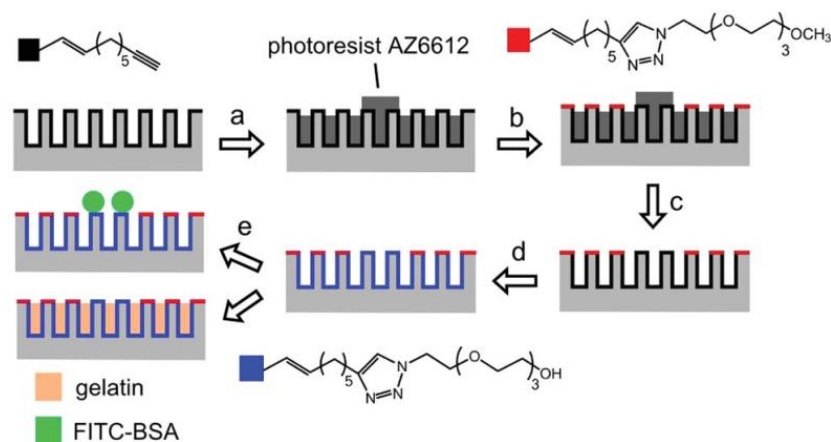
Figure 1.33 Procedure for chemical patterning of porous silicon with different azide species using the combined technique of photolithography and "click" chemistry (reproduced from Ref [195]).

Antibodies, which are large proteins with three-dimensional (3-D) structure, were patterned on silicon substrates with a positive photoresist [197]. To preserve the biological activity, sucrose was used to stabilize the antibody before photoresist processing was undertaken. Then oxygen plasma was applied to selectively etch the immobilised antibody uncovered by the photoresist. Marchesan *et al.* prepared 50 μm-

deep microwells modified with amino acids or small peptides by using a negative photoresist SU-8. The process involved three steps, including the bromine-functionalised thin film formation, microwell fabrication using the standard photolithography procedure for SU-8 and amino acids or small peptides immobilisation through displacing the activated bromine [198]. They also exploited the application of the functionalised microwells in two ways. One is further immobilised with enzyme horseradish peroxidase (HRP) via EDC coupling to produce a biochemical assay (see Figure 1.34 (a)), while the other one is modified with an RGD-peptide which can improve the cell attachment (see Figure 1.34 (b)).
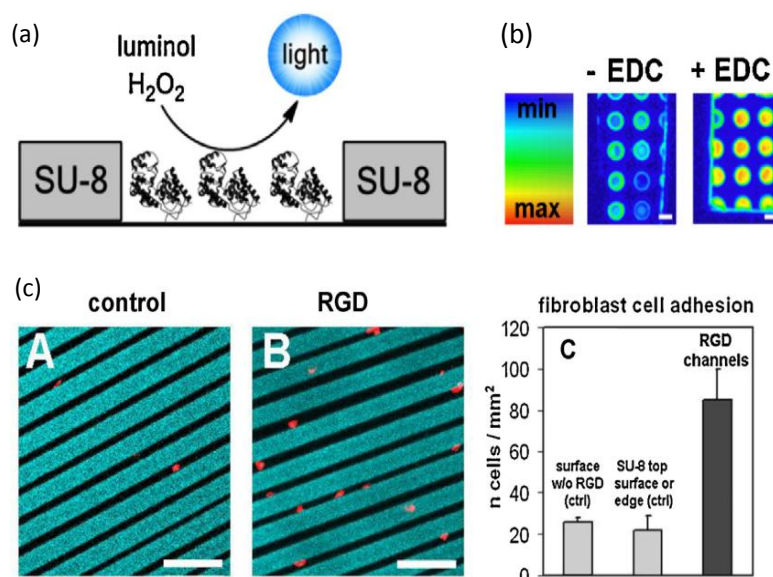
Figure 1.34 (a) HRP reaction in the wells; (b) HRP luminescence assay with (right) or without (left) the EDC coupling agent; (c) fluorescent microscopy images of fibroblast cell adhesion without (left) and with (middle) the RGD-peptide inside of the microchannels, while the right graph displaying the cell counting within 0.6 mm^2 of different areas on the micropatterns (reproduced from Ref [204]).

Instead of the covalent functionalisation schemes which involved very elaborate procedures for patterning, Prashanth *et al.* described a non-covalent method based on electrostatic assembly and lithographic patterning [201]. In brief, polyelectrolyte multilayers were prepared by alternatively spin-coating polycations and polyanions onto a photoresist-patterned substrate. After washing off the photoresist, proteins or DNA were attached onto the polyelectrolyte array via electrostatic absorption. It was believed that this method could be used for patterning and functionalisation at different types of substrates including plastics.

50

1.6.2 Microcontact printing (μCP)

Microcontact printing (μCP), which was introduced by Whitesides's group [205, 206], has been widely applied to print desired patterns from a master polydimethylsiloxane (PDMS) stamp onto the host substrate. Unlike photolithography, typical μCP does not require dust-free conditions or harsh chemical treatments, making it a facile and low-cost technique in the application of surface chemistry and cell biology [207]. Generally, a typical procedure of μCP starts with the fabrication of a PDMS stamp, and is followed by inking the stamp in the target solution and then making physical contact with the substrate. Through μCP, various materials including antibody [208], cell-adhesive protein [209-211] or RGD peptide [212, 213], liposomes [214], DNA [215-217] and SAMs [207, 218, 219] can be patterned onto the substrates surface. Usually, the binding mechanisms between the ink materials and substrates can be concluded to be through ionic interactions and covalent binding.

1.6.2.1 Ionic interaction

Csucs *et al.* printed peptide (RGD)-functionalised poly-L-lysine-g-poly(ethylene glycol) (PLL-g-PEG) onto tissue culture polystyrene (TCPS) or glass substrates through electrostatic absorption [212]. Furthermore, they modified the non-printed areas with non-functionalised PLL-g-PEG to resist protein and cell attachment. Both cell types (human foreskin fibroblasts and fidh epidermal keratocytes) showed highly selective interactions with the chemically patterned surface. Similarly, to study the cell growth and viability depending on the local geometry of the substrate, fibronectin- or vinculin-coated adhesive islands with different size and spaces were prepared using μCP [209]. This investigation provides an attractive way to regulate the tissue microenvironment and architecture.

Lange *et al.* produced DNA arrays using μCP method. Before patterning, the PDMS stamp was treated with oxygen plasma and then modified with (aminopropyl)triethoxysilane to obtain a positively charged surface for DNA absorption [217]. Figure 1.35 (a) shows the printing procedure and the resultant images. Besides, Kidambi *et al.* combined μCP with a layer-by-layer (LBL) assembly technique to create 3-D patterned microstructure films [207]. Figure 1.35 (b) shows the stamping process of m-d-poly-(ethylene glycol) (m-dPEG) acid on a poly(diallyldimethylammonium chloride) (PDAC)/Sulfonated poly(styrene) (SPS)

multilayer polyelectrolyte template. The results indicated that by adjusting the pH of the m-dPEG acid ink solution, one can control the transfer efficiency of the patterns from PDMS stamp to polyelectrolyte films. Using the same approach they also fabricated the bilayer lipid membrane (BLMs) and liposomes arrays on the patterned polyelectrolyte multilayer (PEM)/m-dPEG acid substrate [214].

(b)
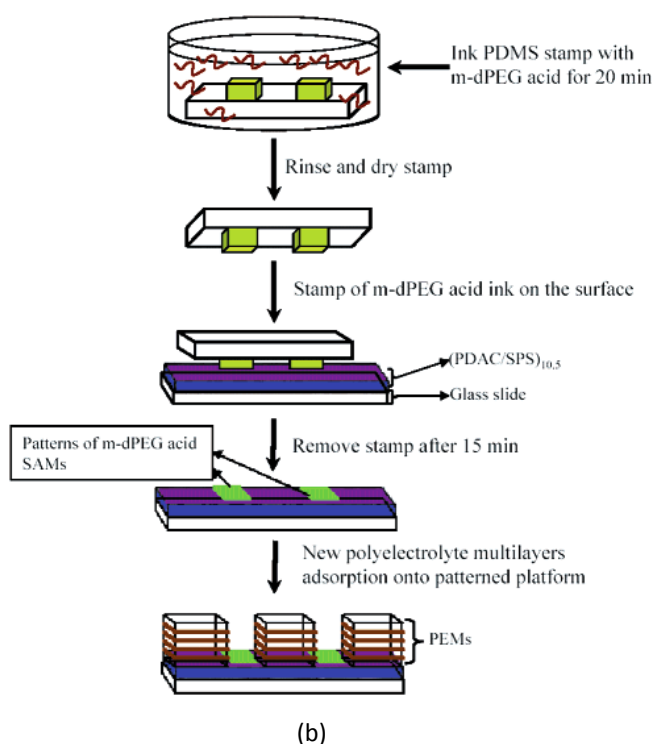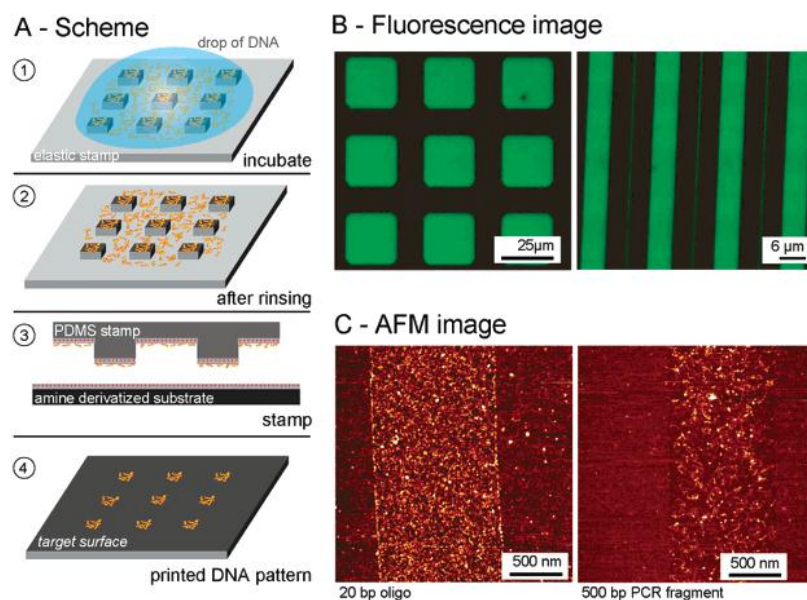
Figure 1.35 (a) Scheme of μCP of DNA (left A) and fluorescence images of the printed FITC-labelled DNA on glass (right top B) and the AFM images (right bottom C) [217] (b) scheme of stamping m-dPEG acid on a PDAC/SPS multilayer template [207].

1.6.2.2 Covalent binding

As mentioned above, the mechanism of μCP also includes covalent binding between the substrate and the ink solution. Huck *et al.* reported the first example of peptide synthesis on a silicon surface by μCP of BOC-protected amino acids onto a reactive amine SAM [213]. Induced by the nanoscale confinement between PDMS stamp and SAM-modified surface, the amide-bond can be formed without the presence of catalysts.
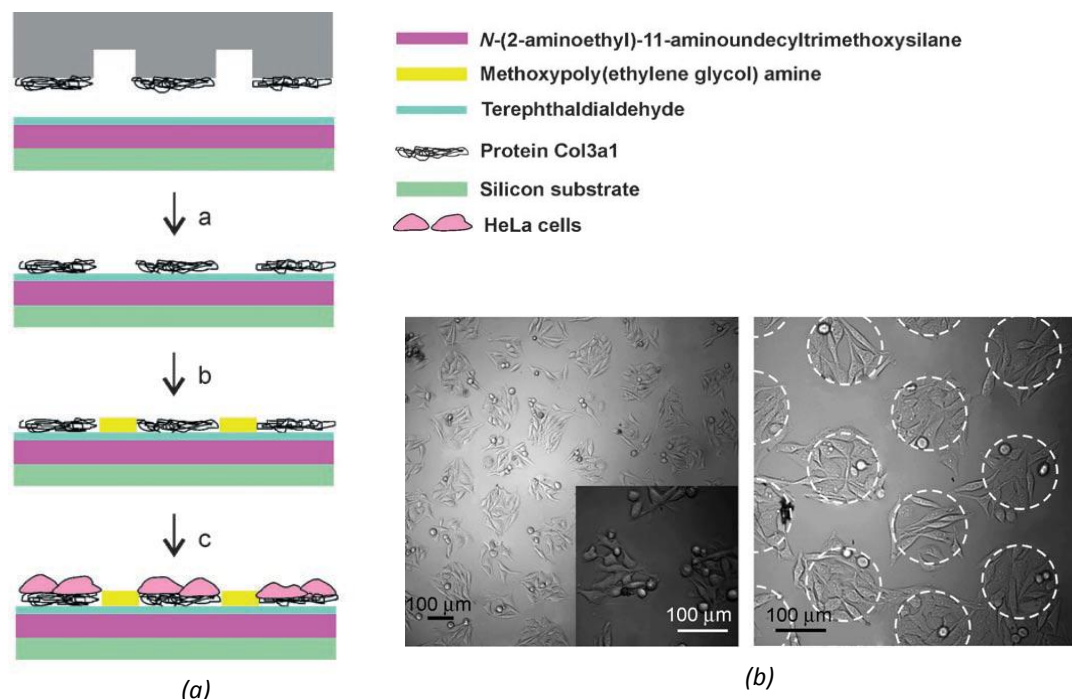
Figure 1.36 (a) Scheme of surface modification and cell patterning through μCP of protein col3a1; (b) the microscopy images of the HeLa cells patterns (reproduced from Ref [211]).

Ravoo and Reihoudt have intensively investigated covalent binding using μCP. For example, they covalently printed cytophilic proteins, which benefit cell adhesion, onto aldehyde-terminated SAMs on gold or silicon oxide substrates [211]. Figure 1.36 (a) shows the schematic representation of surface modification and cell patterning through μCP of protein col3a1, while Figure 1.36 (b) shows the microscope images of the HeLa cells patterns. Interestingly, they also elegantly demonstrated that a "click" reaction can be also performed via μCP in copper(I)-free solution within a short reaction time, thus providing a straightforward way for the fabrication of biomolecular microarrays on silicon [183, 215, 218]. Taking advantage of the copper-free condition,

acetylene-modified DNA was directly immobilised onto the azide-substituted SAM-modified surface using µCP [215]. The effect of the acetylene positions and amounts on the DNA hybridization was studied (see Figure 1.37) and the results indicated that acetylene modification at the 5' terminus produced the maximum hybridization. DNA modified with more than one acetylene linker showed no hybridization with its complementary strand.
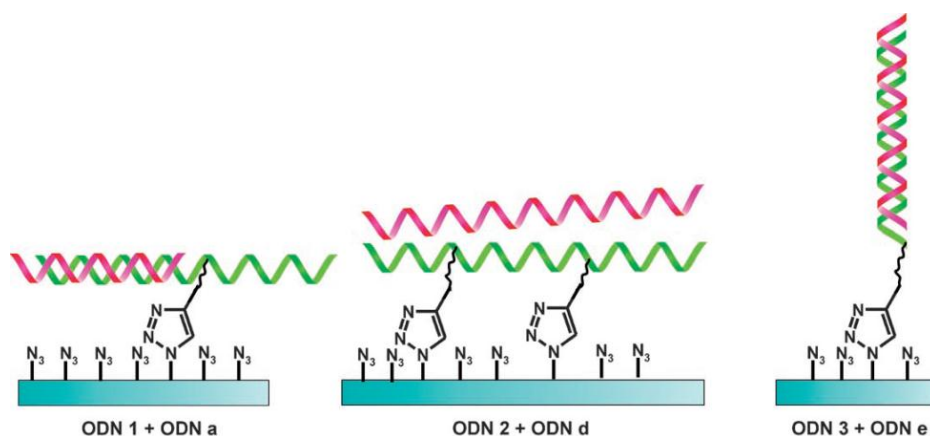
Figure 1.37 Immobilisation of DNA with acetylene units in different positions and hybridization with complementary strands (reproduced from Ref [215]).

1.6.3 Scanning probe-based lithography (SPL)

Scanning probe-based lithography (SPL) is a technology that can not only introduce specific chemical modifications on substrates, but can also create precise patterns on the surface with a molecular-level resolution. Based on scanning probe microscopes, it can be triggered by atomic force microscopy (AFM) such as dip-pen nanolithography (DPN) and scanning tunneling microscope (STM). Generally, AFM is operated in air or liquid media under constant-voltage mode, while STM is performed in vacuum, air or liquid under constant current mode. Schematic for SPL based on AFM and STM are shown in Figure 1.38 (a) and (b) respectively [220].
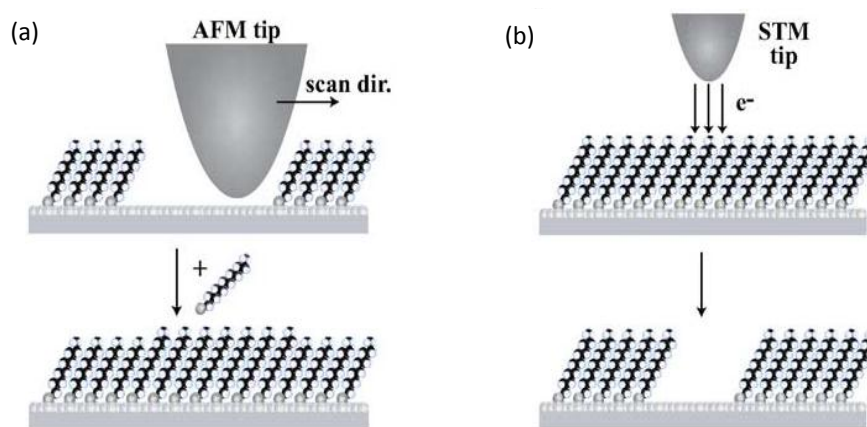
Figure 1.38 Schematic for SPL induced by AFM nanografting (a) and STM desorption (b) (reproduced from Ref [220]).

DPN, which was first published by Piner *et al*., was initially applied to immobilise thiols on a gold surface [221]. Since then, it has been used for fabricating nanopatterns of molecules such as DNA [222], proteins [223, 224], viruses [225], polymers [226] and SAMs [227] on a variety of substrates by using chemically modified AFM tips. For example, Mirkin's group produced a biologically active protein array by covalently binding to templates of DPN-generated 11-mercaptoundecanoyl-*N*-hydroxysuccinimide ester (NHSC$_{11}$SH) SAMs on a gold surface [224]. It was reported that DPN can also be used with "click" chemistry to produce lithographed monolayers with azide derivatives on a silicon surface [227].

Among all the SPL approaches, STM-based lithography possesses the highest spatial resolution providing single organic molecule precision. Perkins *et al.* produced patterns of an (aminoethylaminomethyl) phenethyltrimethoxysilane (PED) monolayer on a silicon surface using STM lithography [228]. These patterns, which were trenches with ~15 nm width and 3 nm of edge roughness, resulted from the combination of a passivation process on the silicon surface and STM lithography. When performed at a very low electron energy (~10 eV), fine lines (~15 nm) modified with alkylthiols and alkylsiloxanes monolayers can be obtained with STM lithography technology [229]. Besides SAMs, STM lithography has been used successfully to produce patterns of metal halide films and e-beam resists [230].

1.6.4 Summary

Considering the biosensor applications and the resolution of LAPS/SPIM, a pattern with extremely high resolution is actually unnecessary. Hence, photolithography and

µCP are adopted in this work. To measure the lateral resolution of LAPS/SPIM based on the SAM-modified SOS substrate, a clearly defined edge on the surface has to be fabricated. For that purpose, films of SU-8 with sharp edges are formed on the surface of SOS substrates by photolithography. To validate the surface potential imaging, the comparatively facile and clean method of µCP is used to fabricate chemical patterns.

Another model system suitable for investigating the impedance and potential-imaging capabilities of LAPS/SPIM is polyelectrolyte microcapsules. The following section will present the preparation of microcapsules and their properties.

1.7 Polymeric multilayer capsules

1.7.1 Preparation process

Polymeric multilayer capsules (PMLCs) are based on the layer-by-layer (LBL) adsorption of oppositely charged macromolecules, such as polyelectrolytes (PE), on colloidal particles [231]. Here, polyelectrolytes are polymers bearing charged groups in the repeating units. Once dissolved in aqueous solution, these groups will dissociate and generate free ions, resulting in an electrically conductive and viscous solution. Generally, three steps are involved to produce PMLCs (see Figure 1.39) [232]. First, colloidal templates with specific size and shapes are deposited with polymer "A" carrying opposite charges. Second, the polymer "A"-coated particles are treated with an oppositely charged polymer "B" and then again with polymer "A". The alternating process is performed until the desired number of polymer layers are formed on the colloidal templates. After each polymer deposition, the excess polyelectrolyte is removed by cycles of centrifugation and washing. Finally, the colloidal cores are dissolved by chemical or thermal treatment and a suspension of hollow PMLCs is obtained.
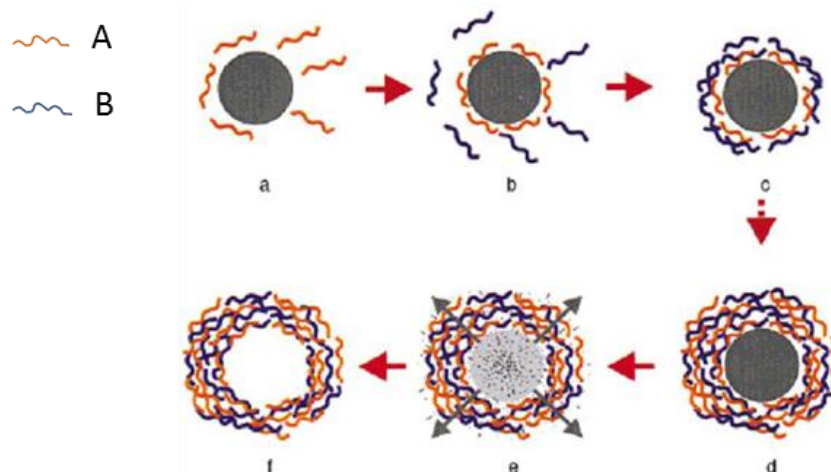
Figure 1.39 Schematic representation of the LbL capsule preparation process (reproduced from Ref [232]).

1.7.2 Templates and shell compositions

Microcapsules can be constructed on organic or inorganic templates. The most commonly used organic templates are melamine formaldehyde (MF) [233], polystyrene (PS) [234] and poly methyl methacrylate (PMMA) [235]. Acidic media or organic solvents are required to dissolve the polymer cores. For example, 0.1 M HCl solution was used to dissolve MF cores [233]. Inorganic templates, which can be decomposed under relatively mild conditions, have been intensively investigated in recent years. Carbonate particles (such as $CaCO_3$ [236, 237], $MnCO_3$ [238] and $CdCO_3$ [239]) and highly monodisperse silicon dioxide (SiO_2) particles [240] have been used as templates for capsule preparation. Among them, $CaCO_3$ can be dissolved in aqueous ethylene diamine tetraacetic acid (EDTA) [237], while SiO_2 can be decomposed in 1 M HF solutions [240]. Besides the organic and inorganic particles, biological materials such as living cells [241], liquid droplets such as oil emulsion [242] and even micro air bubbles have been also used for capsule preparation.

In terms of the shell composition of capsules, the most commonly used materials are polyelectrolyte pairs. One of the typical examples is poly(allylamine hydrochloride) (PAH) and sodium poly(styrene sulfonate) (PSS), which can yield stable capsules constructed on a variety of templates [243-245]. In addition, poly(diallyldimethylammonium chloride)/poly(styrene sulfonate) (PDADMAC/PSS) [246], poly(*N*-vinylpyrrolidone)/poly(methacrylic acid) (PVPON/PMA) [247] and

dextran sulfate/protamine (DS/PR) [248, 249] pairs have also been reported as bilayers in the microcapsule fabrication (see Figure 1.40).
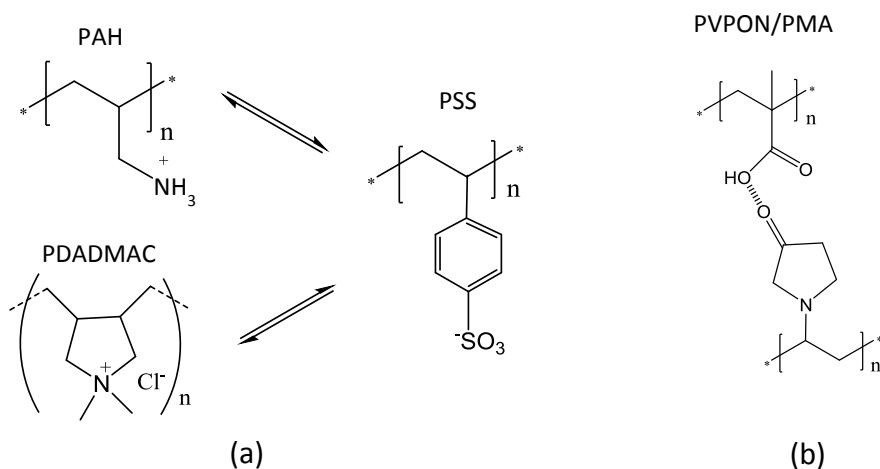
Figure 1.40 (a) Structures of positively charged polymers of PAH and PDADMAC which can form a complex with negatively charged PSS through electrostatic interactions; (b) structure of PVPON/PMA polymer complex formed through hydrogen bonding.

Due to the unique chemical and physical properties of gold nanoparticles (AuNPs) and their numerous applications in electrochemical sensing [250-252], medical diagnostic [253] and drug delivery [254], the idea to combine AuNPs with microcapsules is of particular interest [255, 256]. Since simply mixing the gold nanoparticles with capsules causes the coagulation of capsules, a LBL self-assembly method to insert AuNPs in the polymeric multilayers has been developed by Dong *et al*. [255].

1.7.3 Properties and applications

Due to the properties of encapsulation and release, PMLCs show promising applications in the areas of medicine (drug, vaccines or nucleic acids delivery), food (nutrient preservation) and cosmetics (fragrance protection and continuous release) industries. A variety of physical and chemical approaches have been exploited to release entrapped materials. For the physical method, optical activation (including ultraviolet, visible and infrared light) [257], magnetic field [258], ultrasound [259] and heat [260] are widely adopted. Regarding the chemical approach, changes in the environmental conditions of pH [261], ion concentration [262] and enzyme concentration [263] are effective ways to trigger the release of capsules.

2. Experiments

2.1 Materials

Silicon-on-sapphire (SOS) with a 0.5 μm thick silicon (100) layer (boron doped, 0.05 Ω cm) and a 1 μm thick silicon (100) layer (boron doped, 0.1 Ω cm) on a 475 μm thick sapphire substrate was purchased from Monocrystal, Russia. Double-polished silicon (100) wafer (boron doped, 10-30 Ω cm) was purchased from Si-Mat, Germany. For SOS, unless noted otherwise, that with 1 μm thick silicon was used in the work described in this thesis.

Zero grade argon (BOConline, UK) was dried and purified through an oxygen/moisture trap (Agilent Technologies, USA). All chemicals, unless noted otherwise, were purchased from Sigma-Aldrich and were used as received without further purification. Table 2.1 shows the chemicals and reagents that have been used in this work. 1, 8-Nonadiyne (98%) was redistilled before use. First, 1, 8-nonadiyne was mixed with sodium borohydride and stirred under dry argon at room temperature overnight. Then it was redistilled under reduced pressure (95 ℃, 23-30 Torr) and stored under argon prior to use. Dichloromethane (DCM) was redistilled before use. Pure water (18.2 Ω cm) from a three-stage Millipore Milli-Q 185 water purification system (Millipore, USA) was used to prepare solutions.

Table 2.1 Chemicals and reagents.

Chemical name	Grade
Hydrogen peroxide	Semiconductor grade, $\geq 30\%$
Sulfuric acid	Semiconductor grade, 95-97%
Hydrofluoric acid	Semiconductor grade, 49-51%
Hydrochloric acid	ACS regent, 37%
Acetic acid	ACS reagent, $\geq 99.7\%$
1-Octadecene	GC, $\geq 95.0\%$
Undecylenic acid	Puriss., 98-100.5%
1,8-Nonadiyne	98%
Sodium borohydride	99.99% Trace metals basis
11-Azido-3,6,9-trioxaundecan-1-amine	Technical, $\geq 90\%$ (GC)
4-Azidobenzoic acid solution	~0.2 M in *tert*-butyl methyl ether, $\geq 95.0\%$
Sodium ascorbate	$\geq 98\%$
Copper(II) sulfate pentahydrate	ACS reagent, $\geq 98.0\%$
N, *N*, *N'*, *N'*-Tetramethylethylenediamine (TMEDA)	$\geq 99.5\%$, purified by redistillation
Poly(allylamine hydrochloride) (PAH, 70 kDa)	-
Poly(styrenesulfonate sodium salt) (PSS, 70 kDa)	-
Ethanol (EtOH)	Absolute, Puriss., $\geq 99.8\%$
Dichloromethane	HPLC
Acetone	HPLC
Sodium chloride	ACS regent, $\geq 99\%$
Potassium chloride	ACS reagent, 99.0-100.5%
Calcium chloride	99.99% trace metals basis
Magnesium chloride	BioReagent, $\geq 97.0\%$
Phosphate buffer saline (pH 7.4, tablet)	-
Carbonate-bicarbonate buffer (pH 9.6, capsule)	-
Trizma basis	Puriss., $\geq 99.7\%$

2.2 Methods

2.2.1 Ohmic contact

SOS and silicon wafers were cut into 7 mm $\times$ 7 mm pieces using a diamond tipped cutter. In order to form the ohmic contact, chips were etched in 10% HF solution for 30 s, and then 30 nm chromium and 150 nm gold were thermally evaporated onto the sample corner through a mask using an Edwards Coating System E306A. Finally, samples were heated to 300 ℃ for 5 min to let the deposited chromium and gold diffuse into the silicon bulk.

2.2.2 Monolayer formation

2.2.2.1 Sample cleaning

The SOS or silicon sample was cleaned in acetone in an ultrasonic bath for 5 min and blown dry with nitrogen gas. Then it was immersed in a hot piranha solution (3:1 H_2SO_4 (96%)/H_2O_2 (30%)) at 100 ℃ for 30 min and rinsed copiously with Milli-Q water.

2.2.2.2 Assembly of alkyl monolayers from undecylenic acid and 1-octadecene

The cleaned SOS or Si sample was transferred to 10% HF solution and chemically etched for 5 min to obtain a hydrogen-terminated surface (H-SOS/H-Si). During the sample cleaning and etching, undecylenic acid was deoxygenated under argon in a Schlenk tube at 90 ℃ for 30 min and then cooled to room temperature under continuous bubbling of argon. The freshly prepared H-SOS/H-Si substrate was transferred into the Schlenk tube with continuous argon bubbling for 30 min. Grafting was performed overnight at 160 ℃ adapting a procedure described elsewhere [264]. The modified surface (surface U1) was then rinsed in hot acetic acid at 75 ℃ and copious amounts of water. Figure 2.1 shows the process for the monolayer formation. For the reaction of SOS or Si surface with 1-octadecene, a temperature of 180 ℃ was used. After the reaction, the sample (surface O1) was rinsed successively with tetrahydrofuran and DCM and blown dry with nitrogen.
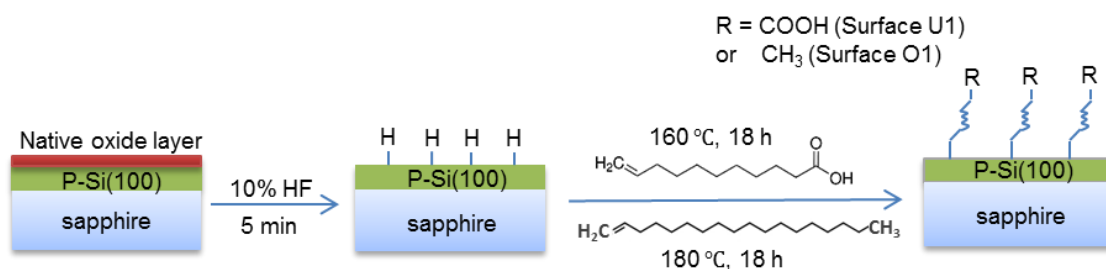
Figure 2.1 Process of the undecylenic acid /1-octadecene monolayer formation.

2.2.2.3 Assembly of alkyne-terminated alkenyl monolayers from 1, 8-nonadiyne

Assembly of the 1, 8-nonadiyne monolayer followed the procedure reported by Gooding's group [146, 147, 157]. The cleaned SOS or Si substrate was transferred to 2.5% HF solution and chemically etched for 90 s to obtain the H-SOS/H-Si substrate. During the cleaning and etching time, the redistilled 1, 8-nonadiyne was transferred into a Schlenk tube and was degassed by freeze-pump-thaw cycles until no gas bubble evolved from the solution. Then, the freshly prepared H-SOS/H-Si sample was transferred into the degassed 1, 8-nonadiyne and left for 3 h at 165 °C under an argon stream. After cooling to room temperature, the functionalised surface (surface N1) was then rinsed in copious amounts of redistilled DCM and blown dry with nitrogen before characterisation or further modification. Figure 2.2 shows the process for the 1, 8-nonadiyne monolayer formation.
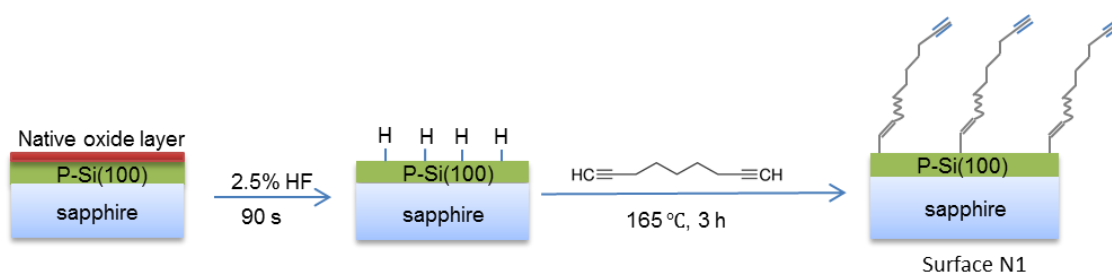
Figure 2.2 Process of the 1, 8-nonadiyne monolayer formation.

2.2.2.4 Functionalisation of alkyne monolayers via CuAAC "click" reaction

The 1, 8-nonadiyne monolayer-modified SOS or Si sample (surface N1, prepared in Section 2.2.2.3) was transferred into a vessel containing the "click" solution of the azide (15 mM, ethanol/water 2:1), copper(II) sulfate pentahydrate (1.1 mol% relative to the azide), sodium ascorbate (10 mol% relative to the azide) and TMEDA (0.45 mM). The reaction was carried out in the dark at room temperature for 24 h. Two

different azides were used: 1-Azido-3, 6, 9-trioxaundecan-1-amine (azido-OEG-NH$_2$) yields a surface terminated with amino groups (surface N2), while 4-azidobenzoic acid gives a carboxyl-terminated surface (surface A1). The unreacted reagents were removed by rinsing the substrate consecutively with copious amounts of EtOH, then water and EtOH. Then, the sample was placed in a 0.5 M hydrochloric acid solution for 2 min to remove the residual copper [265]. Finally, it was washed with copious amounts of water and ethanol. Figure 2.3 shows the process for "click" modification on 1, 8-nonadiyne.
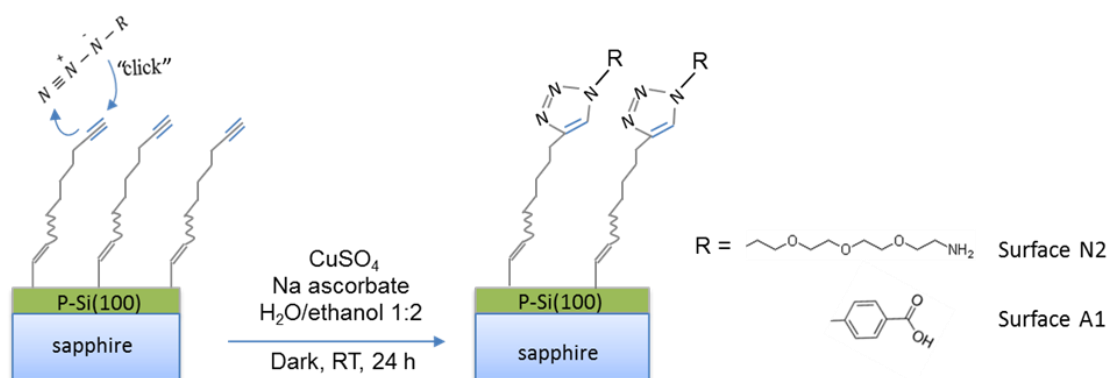
Figure 2.3 Process of CuAAC "click" chemistry on 1, 8-nonadiyne-modified SOS.

2.3 Surface characterisation

2.3.1 Contact angle measurements

Contact angle measurement is a technique to measure the ability of a liquid, such as water or organic solvent, to spread on the solid surface. A contact angle (θ) is the angle between the outline tangent of the droplet and the contact solid surface. It changes with the change of solid surface materials. For example, when a surface is functionalised with a material with a better liquid affinity, it has a smaller contact angle. The principle for this instrument is quite simple. When a drop of liquid is deposited on a solid surface, its image is captured by a camera under illumination and then the contact angle is recorded.

In this work, the water wettability of different monolayers-modified SOS samples was measured by using a Drop Shape Analysis System (Krüss DSA100, Germany). 1 μl of ultrapure water was carefully deposited onto the surface and the advancing contact

angles were measured immediately. Three spots were measured on each sample and averaged.

2.3.2 Ellipsometry

Ellipsometry is commonly used to determine a thin film thickness and optical constants. It offers the advantages of high precision and sensitivity. It is also non-destructive and easy-to-use. Figure 2.4 shows a schematic representation of the ellipsometer and the instrument used in this work. Essentially, it measures the change in the polarization state of the laser beam induced by the reflection from (or transmission through) the sample, which is defined as the ratio of the reflectivity of p-polarized light (r_p) over s-polarized light (r_s):

$$tan(\psi) \cdot e^{i\Delta} = \rho = \frac{r_p}{r_s} \quad \text{(Equation 2.1)}$$

Where ρ is the measured complex reflectance ratio; $tan(\psi)$ is the magnitude of the reflectivity ratio; Δ is the phase difference. Since ellipsometry is an indirect method, a model analysis must be performed to obtain optical constants of the sample.
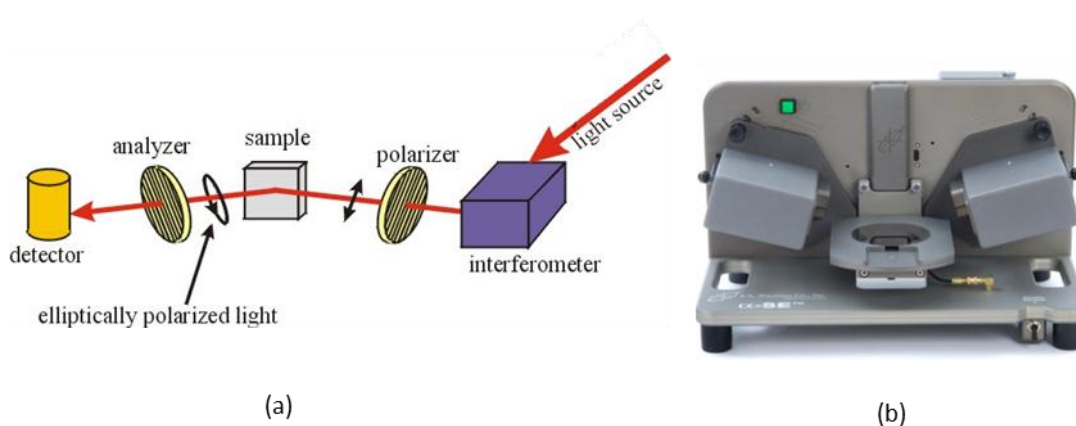
Figure 2.4 (a) Schematic representation of an ellipsometer reproduced from Ref [266];
(b) photographic image of the ellipsometry instrument used in this work.

In this work, an alpha-SE® Spectroscopic Ellipsometer and the CompleteEASE software (J.A. Woollam Co. Inc., USA) for data collection and analysis were used to measure the thickness of the organic monolayers assembled on silicon. Even though this ellipsometer is designed for both opaque and nonopaque substrates, to simplify the data analysis model, all organic monolayers were immobilised onto opaque Si substrates instead of transparent SOS substrates for ellipsometry. The wavelength

range for measurements was 380-900 nm and the angle of incidence was 70°. First, optical constants of refractive index (n) and imaginary refractive index (k) were determined from a freshly etched H-Si (n = 3.877, k = 0.051). Then, the monolayer thickness was modelled as a single layer absorbed on the H-Si substrate using the Cauchy model in the software, which allows a known index of refraction (1.46) to be specified at a specific wavelength (632.8 nm). The Cauchy equation describes the index of refraction using three parameters:

$$n(\lambda) = A + \frac{B}{\lambda^2} + \frac{C}{\lambda^4} \quad \text{(Equation 2.2)}$$

Where A is 1.46, B and C were set between ± 1 nm^2 and ± 0.25 nm^4, respectively. The reported values are the average of at least three measurements taken at different spots on one sample.

2.3.3 X-ray photoelectron spectroscopy

X-ray photoelectron spectroscopy (XPS) is a surface sensitive qualitative and quantitative spectroscopic technique based on the photoelectric effect. As a weakly destructive technique, it can be applied to measure the surface chemical composition and chemical state of solid samples, including metals, ceramics and polymers.

In XPS, the sample is illuminated with a soft X-ray source (AlKα or MgKα) under an ultrahigh vacuum (UHV, $P < 10^{-9}$ mbar). Photoelectrons are ionised from the surface of the solid sample due to the photoelectric effect. The binding energy of electron E_B can be determined by:

$$E_B = h\upsilon - E_k + \Phi \quad \text{(Equation 2.3)}$$

Where $h\upsilon$ is the photon energy, E_k is the kinetic energy of the emitted photoelectron and Φ is the work function. Since the photon energy of the X-ray is known and the work function is a constant in practice, after measuring the kinetic energy of the emitted photoelectron, the electron binding energy, which is associated with elements and chemical bonds (chemical states), can be determined.

In this work, a Kratos Axis Nova spectrometer (nanoLAB of Newcastle University, UK) was used to obtain the XPS results. Survey scans were carried out over the 1100-0 eV range with a 1.0 eV step size, a 100 ms dwell time, and an analyzer pass energy of 100 eV. High-resolution scans were run with a 0.1 eV step size, a dwell time of

100 ms, and the analyser pass energy set to 20 eV. For alkyl- or alkynes-modified substrates, the scan regions were Si 2p (97-107 eV), C 1s (278-294 eV), and O 1s (526-542 eV). For further "click"-functionalised substrates, additional N 1s (392-408 eV) and Cu $2p_{3/2}$ (926-938 eV) regions were investigated.

The CasaXPS software (nanoLAB of Newcastle University, UK) was used to analyse the spectra. The background was subtracted using the Shirley routine, and then the spectra were fitted with a line shape following the mixed Gaussian-Lorentzian (GL) functions.

2.3.4 Fluorescence microscopy

A fluorescence microscope is an optical microscope that uses fluorescence to generate an image. When a fluorescent sample is irradiated with a light at a specific wavelength, it absorbs the light and emits detectable light with a longer wavelength. This phenomenon is known as Stokes' shift [267]. The greater the Stokes' shift, the easier it is to separate excitation light from emission light. Two spectral filters are used in the microscopy: one allows only the light with wavelength matching the fluorescent sample to go through, while the second one separates the weaker emitted light from the much stronger irradiation light. The sample can either be naturally fluorescent or be labelled with fluorescent chemicals.

In this work, all fluorescent images were obtained using the Leica Epifluorescence Microscope DMI 4000B.

2.3.5 Atomic force microscopy

Atomic Force Microscope (AFM) is one of a family of scanning probe microscopes having a very high resolution. Based on the measurement of atomic forces, such as van der Waals, capillary, chemical bonding, electrostatic and magnetic forces, it is commonly used to detect surface morphology, providing the information of surface roughness, thickness and material distribution. In addition, it can be applied to image the structure of polymers, nanostructures and intermolecular interactions, or the structure of biological molecules and cellular components. AFM can also be used to perform nanolithography, that is, modify the surface deliberately by scratching or creating desired structures or patterns onto the specimen surface.

The principle of a general AFM is shown in Figure 2.5. An extremely sharp tip is mounted on the end of a tiny cantilever spring, which is moved by a mechanical scanner over the sample surface. If the interaction/force between the tip and the sample surface changes, the force acting on the tip will also change, causing the varying of the bending of the cantilever according to Hooke's law. A laser beam pointed at the tip detects the bending and reflects it to the position-sensitive detector (quadrant photodiode).

In this work, AFM (Dimension Icon, Bruker, US) in PeakForce TUNA mode was used to image the patterns produced by μCP and photolithography and the collapsed microcapsules. In this mode, the instrument automatically optimizes scan parameters, such as setpoint, gain and scan rate. A Bruker's PeakForce TUNA tip (Au coating, spring constant of 0.4 N/m) was used for scanning. Moreover, for local conductivity measurements of microcapsules, a DC bias voltage at 1 V was applied between the AFM tip and the sample substrate.
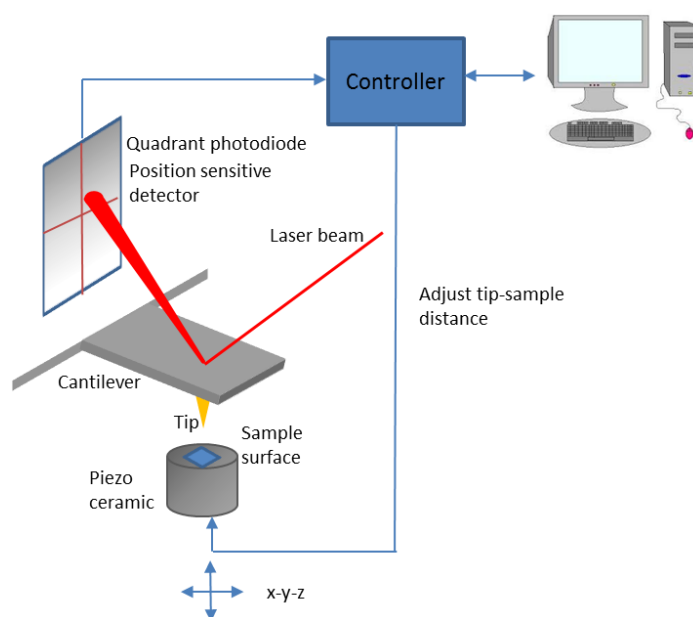
Figure 2.5 Schematic representation of the AFM instrument [268].

2.4 LAPS/SPIM measurements set-up

Figure 2.6 shows the experimental set-up for photocurrent measurements. Lasers used for LAPS/SPIM measurements include a diode laser LD1539 (Laser 2000, $\lambda = 405$ nm, 1 mW), an infrared laser (Laser 2000, $\lambda = 1064$ nm, up to 150 mV), and a Cr-Forsterite femtosecond laser (DEL MAR PHOTONICS, $\lambda = 1250$ nm, 80 fs pulses, 200 mW,

80 MHz). The 405 nm laser was modulated electronically (see light profile "a" in Figure 2.6). The other two lasers were modulated using a chopper (see light profile "b" in Figure 2.6). The modulation frequency was 1 kHz for all photocurrent measurements except for frequency-dependent measurements. The beam profile of the 405 nm laser was improved using a spatial filter and a collimating lens, while the beams of the IR laser and femtosecond laser passed through a beam expander. All lasers were focused onto the silicon layer of the SOS substrate through the same objective (LD Plan-NEOFLUAR 40×) with a correction ring (Zeiss, numerical aperture 0.6), which allowed to correct for spherical aberration caused by focussing through a solid substrate (sapphire). For ~0.5 mm thick sapphire substrates (refractive index: ~1.77), the correction ring was adjusted to 0.48 mm. The sample holder was mounted onto an M-VP-25XL XYZ positioning system with a 10 nm motion sensitivity on all axes (Newport, UK). AC photocurrents were measured using an EG&G 7260 lock-in amplifier. In all measurements, SOS substrates were used as the working electrode. A platinum electrode with a serial capacitor of 4.7 μF and a Ag/AgCl (3 M KCl) electrode in parallel were used as the counter and reference electrodes. The control software was written in LabView 8.2 version by Dr Shihong Jiang [14].

For LAPS/SPIM resolution measurements and the imaging of patterns, the 405 nm laser was used. For the high-resolution electrochemical imaging of microcapsules, the 1250 nm femtosecond laser was adopted. For the imaging of rat B50 neuroblastoma cells, the 405 nm laser combined with 1064 nm IR laser were used. A digital camera (EOS 600D, Canon) was integrated to record the *in-situ* images of the microcapsules and cells attached to the SOS substrate (see light profile "c" in Figure 2.6).
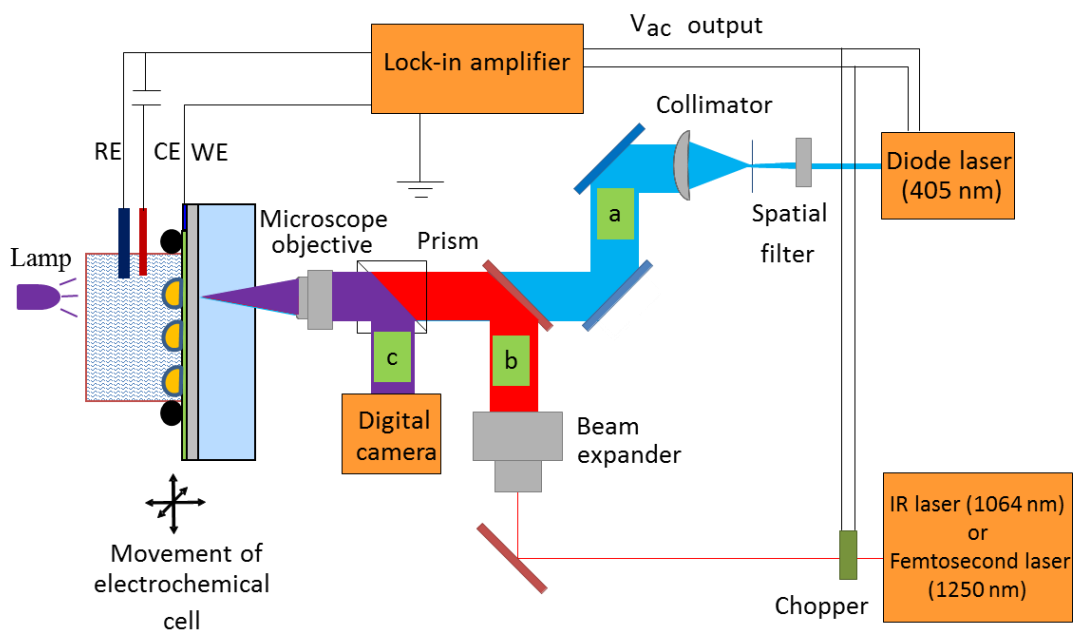
Figure 2.6 Experimental set-up for photocurrent measurements.

3. LAPS/SPIM substrates with self-assembled organic monolayers as the insulator

3.1 Introduction

Due to the advantage of being label-free and having spatial resolution, LAPS has been widely used for different kinds of sensors (as described in Section 1.3.5.4). Many efforts have been made to improve the spatial resolution of LAPS (as described in Section 1.3.5.2). So far, the best resolution measured by using a genuine LAPS set-up with back illumination is about 0.8 μm, which was achieved by using an SOS substrate (0.5 μm silicon, 475 μm sapphire) and a femtosecond laser ($\lambda = 1250$ nm) to generate the photocurrent [14]. As mentioned in Section 1.3.5.3, a thinner insulator layer with a higher capacitance improves the accuracy of LAPS and the sensitivity of SPIM. For example, by using a thin anodic oxide layer instead of a traditional thermally grown silicon oxide layer, a higher sensitivity of SPIM can be obtained [14]. However, the preparation of the thin anodic oxide layer is a multi-step process with low throughput.

Self-assembled monolayers (SAMs), which are ultra-thin films directly grafted onto silicon, are stable and can be prepared with mild and highly efficient methods. The preparation methods, advantages and promising applications of SAMs have been described in detail in Section 1.5. Their excellent insulating properties have been demonstrated in electrochemical impedance measurements [16]. The small thickness of SAMs and the selective control of surface chemistry provide the opportunity to broaden the applications of silicon-based electronic devices in the fields of biochemical and biological sensors [17-20].

The aim of this study was to advance the technique of LAPS/SPIM further through the replacement of the insulator with an ultra-thin SAM. First, SOS or Si substrates were modified with a 1-octadecene monolayer through thermally-induced hydrosilylation. Since a carboxyl-terminated silicon surface can be directly obtained without a protection step, as olefinic carboxylic acids react primarily through the alkene moiety [20, 160, 180], an undecylenic acid monolayer was also prepared on SOS or Si substrates. Both of the monolayers were used as the insulator in electrochemical and photocurrent measurements.

3.2 Experimental section

All chemicals and reagents used in this chapter, unless noted otherwise, were as listed in Chapter 2. The photoresist SU-8 2000.5 and EC solvent were purchased from Chestech Ltd., UK. A KARL SUSS MJB3 UV400 mask aligner was used for UV-exposure.

The processes of 1-octadecene and undecylenic acid monolayer formations on SOS or Si were as described in Chapter 2. Both SOS substrates with 0.5 μm thick silicon and 1 μm thick silicon were used.

The capacitance-voltage (*C-V*) curve for undecylenic acid-modified SOS was measured at 1 kHz with a scanning step potential of 0.1 V using an Autolab PGSTAT 30 with frequency response analysis (FRA), while the DC leakage current was measured in a range of 0-0.9 V with a sweep rate of 0.01 V/s using an Autolab PGSTAT 30 with general purpose electrochemical system (GPES). This voltage range was chosen as it was consistent with the range used in LAPS measurements. The measurements involved a monolayer-modified SOS substrate as the working electrode, a platinum rod as the counter electrode and an Ag/AgCl (3 M KCl) electrode as the reference electrode. All measurements were carried out in 10 mM Tris buffer solution containing 137 mM NaCl and 2.7 mM KCl at room temperature and in the dark.

The set-up for the measurement of pH sensitivity of LAPS was shown in Section 2.4. Buffers with the following compositions: pH 3-7.5, citric acid/sodium phosphate dibasic; pH 8.5, trizma base; pH 9.4, carbonate/bicarbonate were used. All buffers contained 137 mM NaCl and 2.7 mM KCl.

To measure the spatial resolution of LAPS/SPIM, films of SU-8 2000.5 with sharp edges were formed on SOS substrates by photolithography. The photolithography process has been described elsewhere [86]. Briefly, SU-8 2000.5 was spin-coated onto the SAM-modified substrate at 800 rpm for 30 s and then 3000 rpm for 30 s. After spin-coating, the films were baked at 95 ℃ for 2 min on a hot plate. The films were exposed to UV-light (405 nm) through a mask using a mask aligner then baked at 95 ℃ for another 2 min. The substrate was developed in EC solvent for 20 s. The spatial resolution of LAPS/SPIM was measured by scanning a focused laser beam from a monolayer-modified surface to an SU-8-coated part of the sample using back

illumination while biasing the sample towards inversion (see Figure 3.1 (a)). Measuring in inversion means that the photocurrent contrast between coated and uncoated parts of the sample is caused entirely by the difference in impedance of the monolayer and the SU-8-coated monolayer resulting in a SPIM measurement. The sharp edge of the photoresist allows a precise evaluation of the resolution. A photocurrent curve along the x or y direction was obtained and the resolution was estimated from the distance required to achieve a photocurrent drop to 1/e of the total drop (see Figure 3.1 (b)).
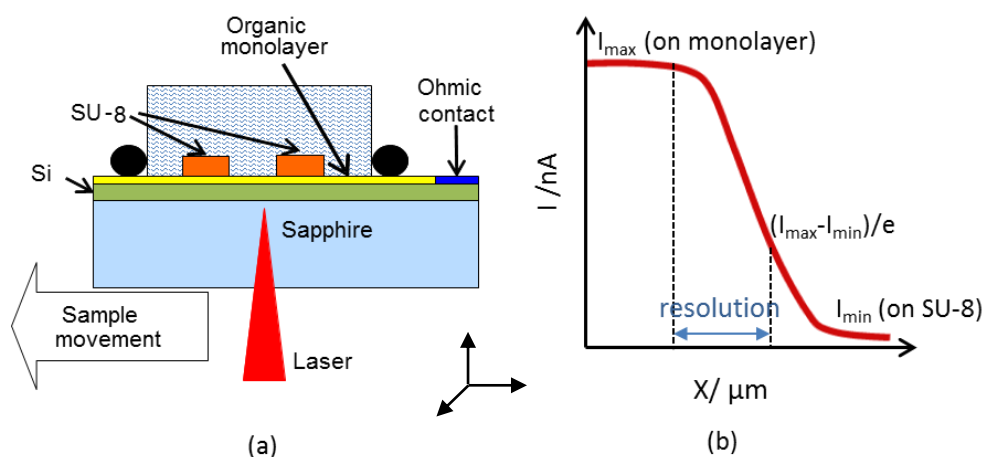
Figure 3.1 (a) Representation of the resolution measurement of LAPS/SPIM (b) typical photocurrent line scan curve and the resolution estimated from the curve.

3.3 Characterisation of alkyl monolayers on SOS or Si

3.3.1 Contact angle measurements

Figures 3.2 (a) and (b) show water drops on 1-octadecence and undecylenic acid-modified SOS substrates, respectively. The corresponding advancing contact angles are listed in Table 3.1 and are comparable with literature values [143, 150, 160] . It is expected that the water contact angle of an alkyl-terminated surface (~103 °) is higher than that of carboxyl-terminated surface (~66 °), due to the greater hydrophobicity of the alkyl groups [160, 269].
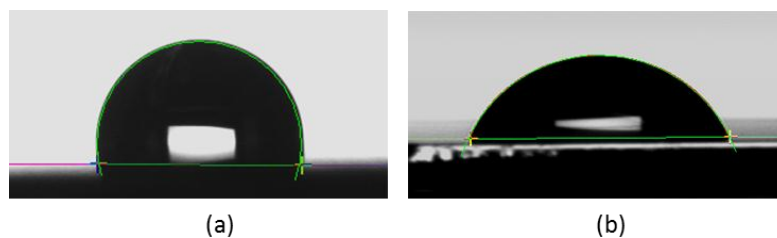
Figure 3.2 Advancing water contact angle measurements on (a) 1-octadecence- and (b) undecylenic acid-modified SOS substrates.

Table 3.1 Advancing water contact angles and ellipsometry results of 1-octadecene (surface O1) and undecylenic acid monolayers (surface U1) on H-SOS/H-Si.

Surface	Water contact angle (°)	Ellipsometry thickness (Å)
O1	103 ± 1	18.5 ± 0.4
U1	66 ± 3	10.2 ± 0.8

3.3.2 Ellipsometry

Figures 3.3 (a) and (b) show the experimental amplitude ratio (*Psi (Ψ)*) and phase different Delta (Δ) data and the best-fitted models of 1-octadecene- and undecylenic acid-modified silicon, respectively. The measured thicknesses of the monolayers are listed in Table 3.1, which are similar to previously reported results [150, 193]. The thicknesses of the 1-octadecene monolayer (18.5 Å) and undecylenic acid monolayer (10.2 Å) are both smaller than the theoretically calculated molecule length for 1-octadecene (23.1 Å) [150] and undecylenic acid (12.2 Å) , indicating tilt angles of ~36 ° and ~33 °, respectively, between the axis of the molecule and the surface normal.
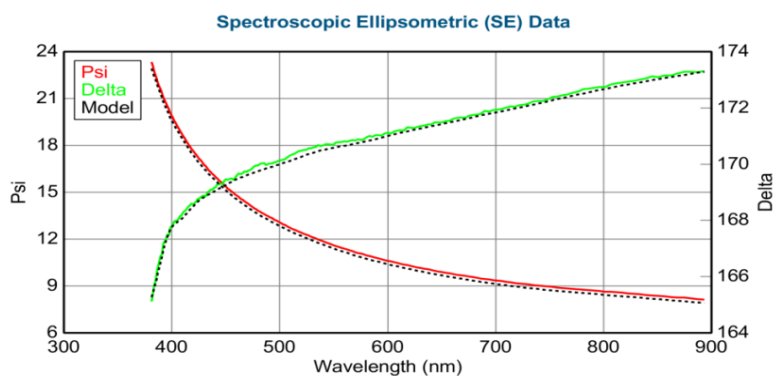
(a)
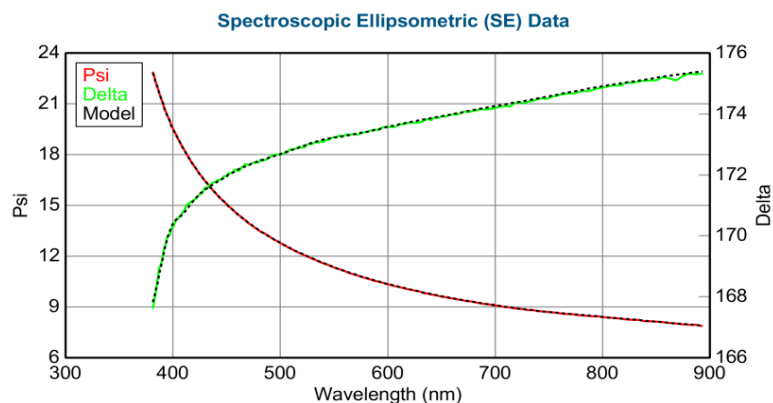
(b)

Figure 3.3 Experimental Psi (Ψ) and Delta (Δ) and the best-fit models for ellipsometry measurememts of silicon modified with (a) 1-octadecene (fitting parameters: mean squared error (MSE) = 4.811; B = -0.02736 ±0.041550; C = 0.00273 ±0.004696) and (b) undecylenic acid (fitting parameters: MSE = 0.494; B = -0.01769 ±0.008212; C = 0.00189 ±0.00092535).

3.3.3 XPS measurements

As both, 1-octadecene and undecylenic acid were expected to react with the H-SOS/H-Si in a similar manner and undecylenic acid was considered more useful for further modification, only the undecylenic acid modified surface was investigated with XPS. The XPS survey spectrum of the modified SOS surface showed the presence of Si, C, and O (see Figure 3.4 (a)), indicating the successful modification of monolayers on the SOS substrate. The high resolution scan evaluates the chemical states of each element through its core electron binding energies. Precise determinations of binding energies are made through the use of curve fitting routines applied to the peaks. For all fittings shown in this thesis, the background was subtracted using the Shirley routine, and then the spectra were fitted with mixed Gaussian-Lorentzian (GL) functions. The narrow

74

scan spectrum of the C 1s region included a main C-C peak (~285.0 eV) and two small peaks of C-C=O (~286.1 eV) and C=O (~289.6 eV) (Figure 3.4 (b)). The binding energies observed are in good agreement with results reported elsewhere [177, 193]. A small oxidized silicon signal centred at 103 eV was observed from the high-resolution Si 2p scan (Figure 3.4 (c)) indicating that the monolayer had some defects with residual oxide remaining on the surface due to the ingress of air to the SOS substrate.
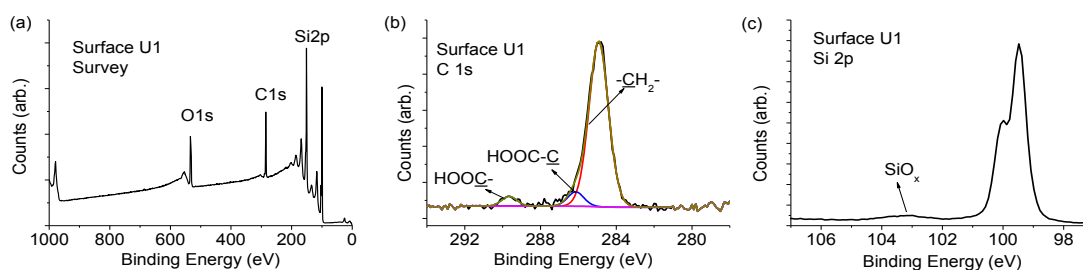
Figure 3.4 (a) XPS survey scan of undecylenic acid monolayer-modified SOS (surface U1). High-resolution scans for (b) carbon and (c) silicon.

3.3.4 Electrochemical measurements of undecylenic acid-modified SOS

An ideal monolayer/silicon interface can be represented by a series of two capacitors (at high frequency) if the Helmholtz double-layer capacitance is ignored [16]:

$C_{tot}^{-1} = C_{sc}^{-1} + C_m^{-1}$ (Equation 3.1)

Where C_{tot} is the total capacitance, C_{sc} is the space charge capacitance of silicon and C_m is the capacitance of the monolayer. In the depletion and inversion regions, the total capacitance is mainly dominated by C_{sc}, which is significantly smaller than C_m. However, in the accumulation region, the total capacitance is determined by the capacitance of the monolayer. Hence, by measuring the capacitance-voltage (*C-V*) curve, the capacitance of the monolayer can be evaluated.

Figure 3.5 (a) shows the *C-V* curve of an undecylenic acid-modified SOS electrode in Tris buffer solution. The shape of the curve indicates a low density of interface states [151]. A clear plateau (~1.7 µF cm^{-2}) is observed in the accumulation region, which is in good agreement with a previous report [16] and can be approximated as the capacitance of the monolayer C_m. As expected, the monolayer has a higher capacitance compared to the ultrathin anodic oxide (~0.3 µF cm^{-2}) measured at the same frequency (1 kHz) [86]. Current density-voltage (*J-V*) measurements were also performed to

confirm the insulating properties of the monolayer (Figure 3.5 (b)). Low leakage current density (< 0.5 μA cm^{-2}) at inversion voltage (0.8 V, *vs*. Ag/AgCl) was obtained, demonstrating the suitability of the organic monolayer as an insulator.
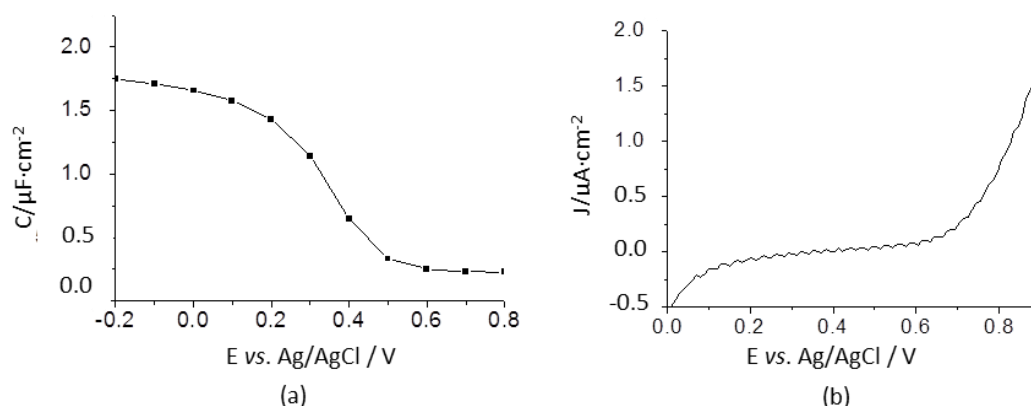
Figure 3.5 (a) C-V curve (1 kHz, scanning step potential: 0.1 V) and (b) J-V curve (scanning step size: 0.01 V/s) measured with an undecylenic acid-modified SOS substrate in 10 mM Tris buffer (pH 7.4) containing 137 mM NaCl and 2.7 mM KCl in the dark.

3.4 Resolution measurements carried out with different monolayers and lasers

As previously shown [14], a good lateral resolution of photocurrent measurements has been achieved using an SOS substrate with an anodic oxide as the insulator. In this work, further investigations on the possibility of achieving similar results using a considerably thinner insulator consisting only of an organic monolayer were carried out. Figure 3.6 (a) shows the photocurrent line scans for an SOS substrate (0.5 μm thickness silicon) modified with 1-octadecene monolayers at different laser wavelengths (contributed by Dr Yinglin Zhou [270]) in inversion (0.9 V, *vs*. Ag/AgCl). The results clearly show that the resolution obtained using a single-photon effect can be improved by reducing the laser wavelength since the focus is wavelength dependent. However, even at a wavelength as short as 405 nm, the resolution was limited to 1.6 μm, presumably due to stray light and multiple reflections in the sapphire substrate, which can also cause a photocurrent. These effects can be reduced using a two-photon effect. The substrate modified with a 1-octadecene monolayer showed sub-micrometer resolution at a wavelength of 1250 nm, which has smaller energy than the band gap of silicon and can induce a two-photon effect as shown previously [14]. The resolution

obtained at different wavelengths is comparable to the resolution measured previously using a SOS substrate with an anodic oxide [14]. The resolution of undecylenic acid monolayer modified SOS substrates with different silicon thicknesses was also investigated (see Figure 3.6 (b), contributed by Dr Yinglin Zhou). Undecylenic acid-modified SOS with a 0.5 μm thick silicon layer showed the same resolution (1.6 μm) as the 1-octadecene-modified samples with the same silicon thickness. However, using SOS with a 1 μm thick silicon layer resulted in a somewhat worse resolution of 2.0 μm.
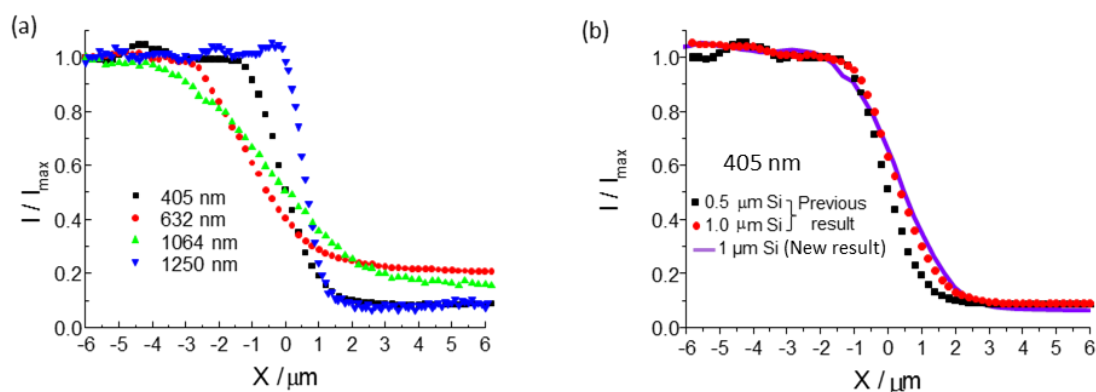
Figure 3.6 Normalised photocurrent line scans across SU-8 edge (a) at different laser wavelengths using SOS substrate (0.5 μm thick silicon) with 1-octadecene grafted onto the silicon as the insulator; estimated resolution: 1.6 μm at 405 nm (I_{max} = 12 nA), 2.2 μm at 632 nm (I_{max} = 27 nA), 3.6 μm at 1064 nm (I_{max} = 60 nA) and 0.8 μm at 1250 nm (I_{max} = 30 nA) (previous results reproduced from Dr Yinglin Zhou [270]); (b) at 405 nm laser using SOS substrate with undecylenic acid grafted onto silicon layers with different thickness; estimated resolution: 1.6 μm for 0.5 μm thick silicon and 2.0 μm for 1 μm thick silicon (previous results reproduced from Dr Yinglin Zhou) and 2.2 μm for 1 μm thick silicon (new results produced in this work). All measurements were performed in 10 mM Tris buffer (pH 7.4) containing 137 mM NaCl and 2.7 mM KCl.

Using undecylenic acid is more attractive as it offers the option of functionalising the surface for different sensor and imaging applications. Meanwhile, using 1 μm thick silicon in conjunction with a laser wavelength of 405 nm has the advantage that most of the light is absorbed by the silicon layer excluding any interference of the light with any biological sample or patterns deposited onto the front side of the sensor. It was therefore decided to carry out further investigations using undecylenic acid-modified SOS substrates with a 1 μm thick silicon layer and a laser wavelength of 405 nm for

LAPS measurements. Before further investigations, the resolution measurement of the undecylenic acid monolayer-modified SOS substrate was repeated and the result was compared with the previous result produced by Dr Yinglin Zhou. A photocurrent line scan across an SU-8 edge at 405 nm wavelength laser with undecylenic acid-modified SOS (1 μm thick silicon) is presented in Figure 3.6 (b) (purple line), which shows a similar resolution (2.2 μm) to the previous data (2.0 μm).

3.5 SPIM sensitivity based on SAM-modified SOS

The sensitivity of SPIM is determined by the capacitance of the insulator. When comparing the photocurrent contrast between SU-8-uncoated and coated areas measured with different wavelengths, a noticeable difference was observed (see Figure 3.6 (a)). The photocurrent ratios measured with 405 nm and 1250 nm were higher than the ratios with 632 nm and 1064 nm. This can be explained with the reflection effect of the deposited SU-8 films. The reflected light can also contribute to the generation of photocurrent thus reducing the photocurrent contrast. However, for the case of the 405 nm laser, most of the light is absorbed within silicon; while for the femtosecond laser (1250 nm), photocurrents can only be generated in the focus.

In order to exclude the reflection effect, photocurrent curves at 405 nm wavelength were used for the evaluation and comparison of the sensitivity of SPIM based on two different insulators (organic monolayer and anodic oxide). A marked difference of the photocurrent contrast was observed between them. The photocurrent ratio for uncoated and coated areas was 12 for the undecylenic acid-modified sample (see Figure 3.6 (b)), but only 3.0 for the anodic oxide-modified sample used previously [14]. This increase in the photocurrent contrast is due to the significantly smaller impedance of the ultrathin organic monolayers compared to the anodic oxide. If considering SU-8 films as a capacitance, from Equation 1.18, the photocurrent ratio for uncoated and coated areas in inversion can be written as:

$$r_m = \frac{C_m}{C_m + C_d} \frac{C_{m-SU8}}{C_{m-SU8} + C_d} \text{ (Equation 3.2)}$$

$$r_{ox} = \frac{C_{ox}}{C_{ox} + C_d} \frac{C_{ox-SU8}}{C_{ox-SU8} + C_d} \text{ (Equation 3.3)}$$

$$C_{m-SU8}^{-1} = C_m^{-1} + C_{SU8}^{-1} \text{ (Equation 3.4)}$$

$$C_{ox-SU8}^{-1} = C_{ox}^{-1} + C_{SU8}^{-1} \quad \text{(Equation 3.5)}$$

Where r_m and r_{ox} are the photocurrent ratios based on an organic monolayer and anodic oxide insulted samples, respectively; C_m, C_{ox}, C_{SU8} and C_d are capacitances of the organic monolayer, anodic oxide, SU-8 film and the depletion layer of silicon. As the impedance of SU-8 film is very large, which means C_{SU8} is very small, r_m/r_{ox} can be simplified as:

$$\frac{r_m}{r_{ox}} = \frac{C_m}{C_{ox}} \frac{C_{ox}+C_d}{C_m+C_d} \quad \text{(Equation 3.6)}$$

Following the discussion in Section 3.3.4, the capacitance contrast between undecylenic acid monolayer (1.7 µF cm^{-2}) and anodic oxide (0.3 µF cm^{-2}) was around 5.7, which was larger than the factor obtained in photocurrent contrast ($\frac{r_m}{r_{ox}} \approx 4$). This discrepancy is actually expected from Equation 3.6 if considering the depletion capacitance of silicon. Another quantity that may cause the discrepancy could be the electrolyte resistance. The serial resistance due to the electrolyte (R_{el}) for an illuminated area of 1.5 µm in diameter can be estimated analogous to microelectrodes of the same size using Equation 3.7 derived for a cell with spherical symmetry [271]:

$$R_{el} = \frac{1}{4\pi\kappa r}\left(1 - \frac{r}{L_{wr}}\right) \quad \text{(Equation 3.7)}$$

Where κ is the conductivity of the electrolyte, r is the radius of the electrode and L_{wr} is the distance between working and reference electrodes.

The impedance for the anodic oxide and organic monolayer can be estimated by:

$$Z = \frac{1}{2\pi f C_{ii}} \quad \text{(Equation 3.8)}$$

Where f is the frequency and C_{ii} is the insulator capacitance within the illuminated area.

The electrolyte resistance was estimated to be 76 kΩ, which is negligible compared to the impedance of the anodic oxide (29 GΩ) or organic monolayer (5.5 GΩ) in the illuminated area. It is therefore thought that the effects of the depletion capacitance on SPIM sensitivity cannot be ignored. Nevertheless, the introduction of organic monolayers indeed shows a significant improvement of the sensitivity.

3.6 pH sensitivity of undecylenic acid modified SOS substrates

Photocurrent measurements using undecylenic acid-modified SOS substrates displayed the expected behaviour for good-quality LAPS substrates. The photocurrent curves (Figure 3.7 (a)) were steep allowing high-accuracy LAPS measurements. The pH sensitivity of the carboxyl-terminated monolayer-modified SOS surface was determined by LAPS. Figure 3.7 shows the normalised photocurrent-voltage (*I-V*) curves measured in a series of pH buffer solutions and the corresponding calibration plot. At low pH (3-4) and at high pH (8.5-9.4), no surface potential shift was detected, while in the pH range of 4-8.5, a linear relationship between voltage and pH was observed with a sensitivity of 30 mV/pH. An effective surface pK_a (~6.3) can be estimated from the pH sensitive range, which is significantly greater than the value of undecylenic acid in solution (~4.9). The increase of the effective pK_a on a surface is in agreement with previously reported results [272]. Since the concentration of carboxyl group on the surface is much higher than that in solution, the electrostatic interactions of terminal groups hinder the acid dissociation on the surface. Furthermore, the pH sensitive range (~4.5) is also significantly greater than typical values for undecylenic acid in solution (~2 pH units), which is consistent with the results reported by Wang et al. who showed that deprotonation of a carboxylic acid monolayer takes place over 4 pH units at a NaCl concentration of 0.15 M [274]. The pH sensitivity of 30 mV/pH is significantly lower to the 59 mV/pH predicted by the Nernst equation. This could be due to activity effects caused by the large surface concentration of carboxylic acid groups.
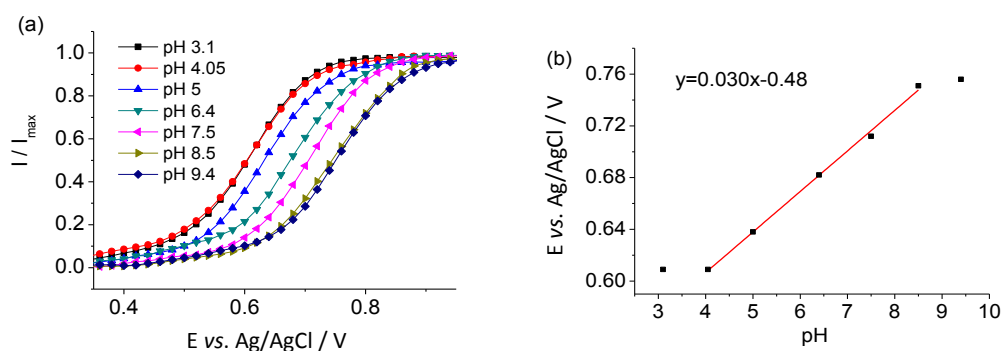
Figure 3.7 (a) Normalised I-V curves of a LAPS structure based on a COOH-terminated monolayer and (b) corresponding calibration plot for a series of different pH values (pH 3.1-7.5: citric acid/sodium phosphate dibasic; pH 8.5: trizma base; pH

9.4: carbonate/bicarbonate; all buffers (10 mM) contained 137 mM NaCl and 2.7 mM KCl).

3.7 Summary

In this chapter, SAMs were successfully modified onto H-SOS/H-Si substrates using a thermal hydrosilylation method. The presence of monolayers on SOS or Si substrates was demonstrated by water contact angle, ellipsometry and XPS measurements. The suitability of the organic monolayers as an insulator was confirmed by *C-V* charactersation and leakage current measurements. A small leakage current density ($\sim$0.7 μA cm^{-2}) measured in inversion and a high capacitance ($\sim$1.7 μF cm^{-2}) of the undecylenic acid monolayer were obtained.

Photocurrent measurements with a 405 nm laser using the undecylenic acid-modified SOS substrates displayed the required behaviour for good-quality LAPS substrates. The pH sensitivity of the carboxyl-terminated surface was 30 mV/pH over a specific pH range determined by LAPS. Good sensitivity and high spatial resolution ($\sim$2.2 μm) of SPIM were obtained. It was clearly demonstrated that the improvement of the sensitivity is mainly due to the employment of an organic monolayer with high capacitance as the insulator. It is the first time that a self-assembled organic monolayer has been used as the insulator in LAPS/SPIM measurements, which will broaden the applicability of LAPS/SPIM by offering a high-accuracy/high-sensitivity of measurements and by introducing a controlled way for surface functionalisation of LAPS/SPIM chips.

4. LAPS imaging on SAM-modified SOS with polyelectrolyte and DNA patterns

4.1 Introduction

As a chemical imaging sensor, LAPS is designed to visualize the two-dimensional distribution of a specific chemical species in solutions. Unfortunately, so far, few of the applications of LAPS have actually taken advantage of this ability to map and image, due to the poor resolution of commonly used LAPS systems. As described in Chapter 3, high resolution of LAPS/SPIM have been achieved using an organic monolayer-modified SOS substrate. In this chapter, the capability of the surface potential imaging of LAPS with a SAM-insulated SOS substrate is investigated.

To validate the LAPS imaging, patterns with potential distributions were required. Polyelectrolytes, which are charged polymers in aqueous solutions, are normally used as templates for patterning various biochemical or biological agents. Microcontact printing (μCP), as a facile and low-cost technique, is the most widely used method to pattern polyelectrolytes through electrostatic attraction [216]. It was reported that poly(allylamine hydrochloride) (PAH) can be successfully printed on poly(ethylene glycol) (PEG) silane-coated glass or polystyrene substrates using an unmodified poly(dimethyl siloxane) (PDMS) stamp [216].

In this work, polyelectrolytes (PAH and PSS) were patterned onto SAM-modified SOS substrates through the electrostatic attraction using μCP. Two different sensor substrates were used: One was modified with undecylenic acid (for PAH patterning), which has been fully studied in Chapter 3; the other one was modified with an amino-terminated monolayer (for PSS patterning), which involved the formation of an alkyne-terminated monolayer and then "click" functionalisation. As an ideal way to modify monolayers with various functional groups, the principle and advantages of "click" chemistry have been described in Section 1.5.3. Since the printed PAH structure is stable and positively charged in aqueous solutions, it can be further used as a template for micropatterning DNA, which is a simple and inexpensive way to generate a DNA microarray [216]. Surface potential images of the substrates patterned with PAH, PAH-DNA and PSS were obtained by using LAPS measurements, indicating that LAPS based on an SAM-modified SOS substrate allows the potential imaging with good resolution and accuracy.

4.2 Experimental section

All chemicals and reagents used in this chapter, unless noted otherwise, were as listed in Chapter 2. A Sylgard 184 poly(dimethyl siloxane) (PDMS) kit was purchased from Dow Corning.

The master for μCP was prepared following a previously reported protocol [275]. PDMS stamps were prepared by using a 10:1 ratio (v/w) of PDMS resin and curing agent. After degassing under vacuum, the PDMS was poured over a prepared silicon master and cured at 50 ℃ overnight. Subsequently, the cured PDMS was peeled off from the master, treated in an oxygen plasma (pressure: 0.8 Torr, generator: 40 kHz/100 W) for 30 s to obtain a hydrophilic surface and then cut into 7 mm ×7 mm pieces. The pattern of the PDMS stamp consisted of circular islands with a diameter of 40 μm and 30 μm gaps.

For photocurrent measurements, the 405 nm wavelength laser modulated electronically and SOS substrates modified with SAMs were used. 10 mM Tris buffer solution containing 137 mM NaCl and 2.7 mM KCl at pH 7.4 was used as the electrolyte.

4.2.1 PAH and PAH-DNA patterns on an undecylenic acid monolayer modified surface

Mixed isomers of rhodamine B isothiocyanate (RBITC) was purchased from Sigma. The oligonucleotide sequences were purchased from Shanghai Sangon Biotechnology Co. Ltd. (Shanghai, China) and have the following sequences: AAG TCC GTG GTA GGG CAG GTT GGG GTG ACT (TBA), AGT CAC CCC AAC CTG CCC TAC CAC GGA CT (rTBA). GeneFinder[TM] was obtained from Zeesan Biotech (China) to label the double-stranded DNA (dsDNA). 10 mM phosphate buffer containing 137 mM NaCl and 2.7 mM KCl at pH 7.4 was used to dissolve the DNA and dye.

The method of undecylenic acid monolayer modification was as described in Section 2.2.2.

PAH labelled with RBITC dye was provided by Dr Qiangying Yi and was prepared following a procedure described elsewhere [276]. Figure 4.1 illustrates the process of printing PAH on an undecylenic acid monolayer-modified SOS substrate. The PDMS stamp was dipped in a 5 mg/ml RBITC-PAH solution for 40 min. The soaked stamp was dried under nitrogen gas and placed onto the substrate for 5 min at room

temperature. After removing the stamp, the patterned substrate was rinsed thoroughly with ultrapure (Milli-Q) water to remove unbound or loosely bound PAH.

After LAPS measurements of the PAH pattern, the sample was coated with dsDNA by incubating with 24 μl of TBA (10 μM) and rTBA (10 μM) in PBS buffer at pH 7.4 for 30 min. The presence of dsDNA was detected by the GeneFinder^{TM} dye, which binds specifically to dsDNA.
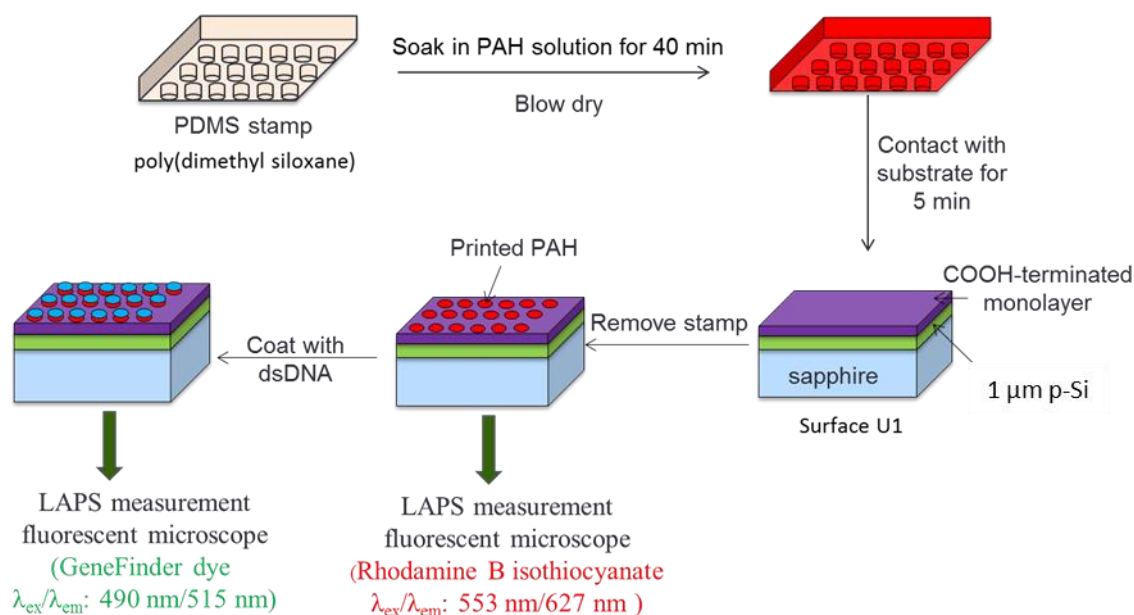
Figure 4.1 Illustration of stamping process of PAH islands and DNA on undecylenic acid monolayer-modified SOS.

4.2.2 PSS patterns on an amino-terminated SOS surface

Methods for 1, 8-nonadiyne monolayer formation and "click" functionalisation with azido-OEG-NH$_2$ on SOS or Si substrates were as described in Section 2.2.2.

Figure 4.2 illustrates the process of printing PSS on a "click"-functionalised amino-terminated SOS surface. The detailed procedure is similar to the one described in the last section.
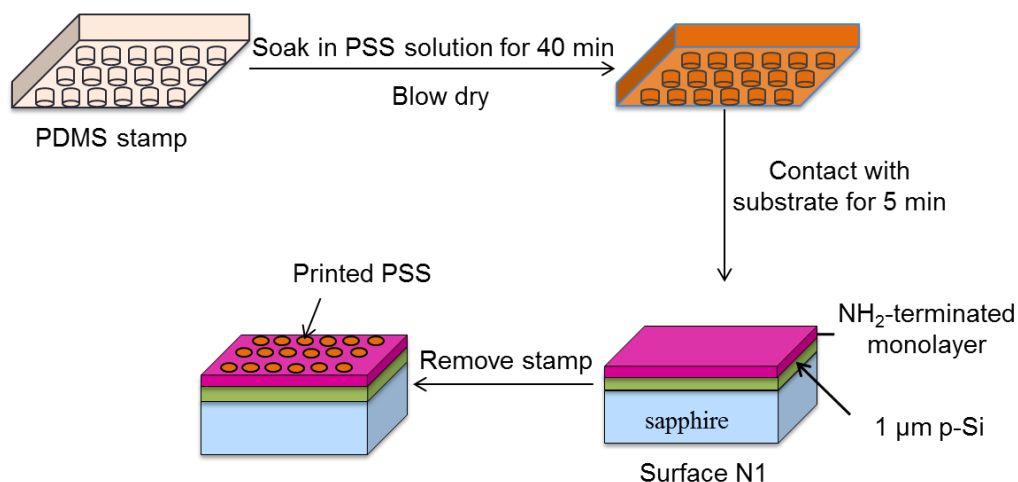
Figure 4.2 Illustration of stamping process of PSS islands on amino-terminated monolayer-modified SOS.

4.3 Characterisation of alkenyl monolayers modified on SOS or Si

The successful formation of undecylenic acid monolayers on SOS or Si substrates has been demonstrated in Chapter 3. Hence, this section only presents the results of surface characterisation on 1, 8-nonadiyne monolayers and further "click"-functionalised SOS or Si substrates.

4.3.1 Contact angle measurements

Figures 4.3 (a) and (b) show water drops on a 1, 8-nonadiyne-modified SOS surface and the surface after "click" chemistry. The advancing contact angle ($88 \pm 1°$) for alkyne-terminated surface (surface N1) is indicative of a hydrophobic monolayer, as expected, and is comparable to literature results [146, 147, 277]. Due to the presence of OEG and amino moieties, the contact angle for the "clicked" surface (surface N2) decreased dramatically by ~51° (see Table 4.1), which is consistent with previously reported values [265, 278].
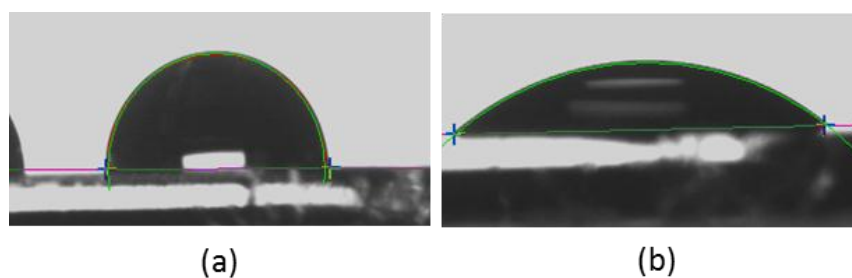
Figure 4.3 Advancing water contact angle measurements on SOS surfaces modified with (a) 1, 8-nonadiyne (surface N1) and (b) OEG-NH$_2$ via "click" chemistry (surface N2).

4.3.2 Ellipsometry

The ellipsometric thickness of 1, 8-nonadiyne monolayer on silicon substrate was 10.6 Å, which is smaller than the refined calculated value (12.2 Å), indicative of a tilt angle of ~30 ° between axis of molecule and surface normal. After the "click" reaction with azido-OEG-NH$_2$, the thickness of the monolayer increased to ~16.0 Å, which is comparable to a thickness of ~17.3 Å determined from X-ray reflectivity (XRR) analysis [265].

Table 4.1 Advancing water contact angles and ellipsometry results of 1, 8-nonadiyne (surface N1) and click-functionalised (OEG-NH$_2$) monolayers (surface N2) on H-SOS/H-Si. Ellipsometry fitting parameters for surface N1: MSE = 0.585; B = -0.03651 ±0.008923; C = 0.00449 ±0.001005; surface N2: MSE = 0.880; B = 0.02089 ± 0.009465; C = 0.00289 ±0.001063.

Surface	Water contact angle (°)	Ellipsometry thickness (Å)
N1	88 ±1	10.6 ±0.4
N2	37 ±1	16.0 ±1.0

4.3.3 XPS measurements

The XPS survey spectrum of the 1, 8-nonadiyne-modified SOS substrate (Figure 4.4 (a)) showed the presence of Si, C, and O, which is in good agreement with published results [146, 147, 277]. C 1s narrow scan included a main C-C peak (~285.0 eV), and two small peaks from Si-<u>C</u>=C (~284.1 eV) and C-O (~286.4 eV), respectively (Figure

4.4 (b)). The C-O peak is attributed to adventitious covalently bound oxygen-bond contaminants, presumably originating from the 1, 8-nonadiyne [277, 279]. The binding energies observed are consistent with the results reported elsewhere [193, 277, 279]. The absence of a Si-O peak in the 101-104 eV region of the high-resolution Si 2p scan (see Figure 4.4 (c)) indicates good quality monolayers that can effectively protect the underlying silicon substrate from oxidation [146-148].
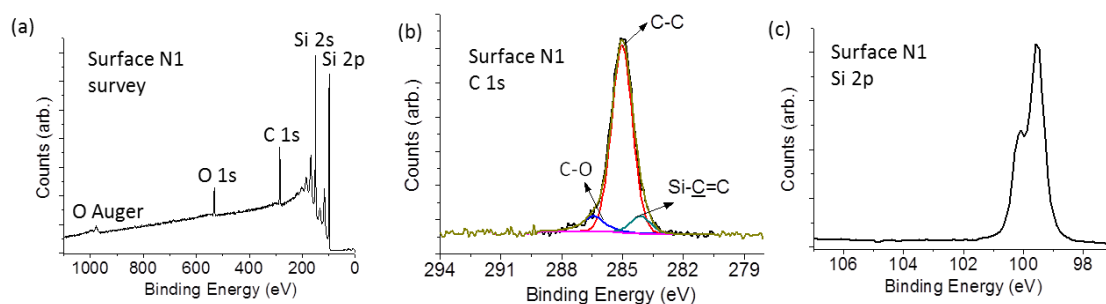
Figure 4.4 (a) XPS survey scan of 1, 8-nonadiyne monolayer-modified SOS (surface N1). High-resolution scans for (b) carbon and (c) silicon.

The successful "click" reaction was demonstrated by XPS results. The XPS survey spectrum of the OEG-NH$_2$-functionalised SOS surface (see Figure 4.5 (a)) shows an N 1s peak at ~401 eV, indicative of a triazole formation. The absence of Cu 2p$_{3/2}$ emission at ~933 eV indicates no residual copper catalyst on the surface. The narrow scan signal of the N 1s region (see Figure 4.5 (b)) was fitted with two peaks at 400.6 eV and 402.2 eV, which are assigned to C-NH$_2$/N-N=N, and N-N=N, respectively [265, 280]. The ratio of the integrated areas (~2.4:1) is smaller than the stoichiometric ratio of 3:1 but is comparable to the literature result (~2.6:1) [265]. The narrow scan from the C 1s region (see Figure 4.5 (c)) was fitted with three peaks assigned to Si-C=C (284.3 eV), C−C (285.3 eV) and C−N/−O (287.1 eV) [158, 265]. Importantly, no SiO$_x$ species was observed in the Si 2p narrow scan, indicating that a high-quality functionalised surface has been prepared (Figure 4.5 (d)).
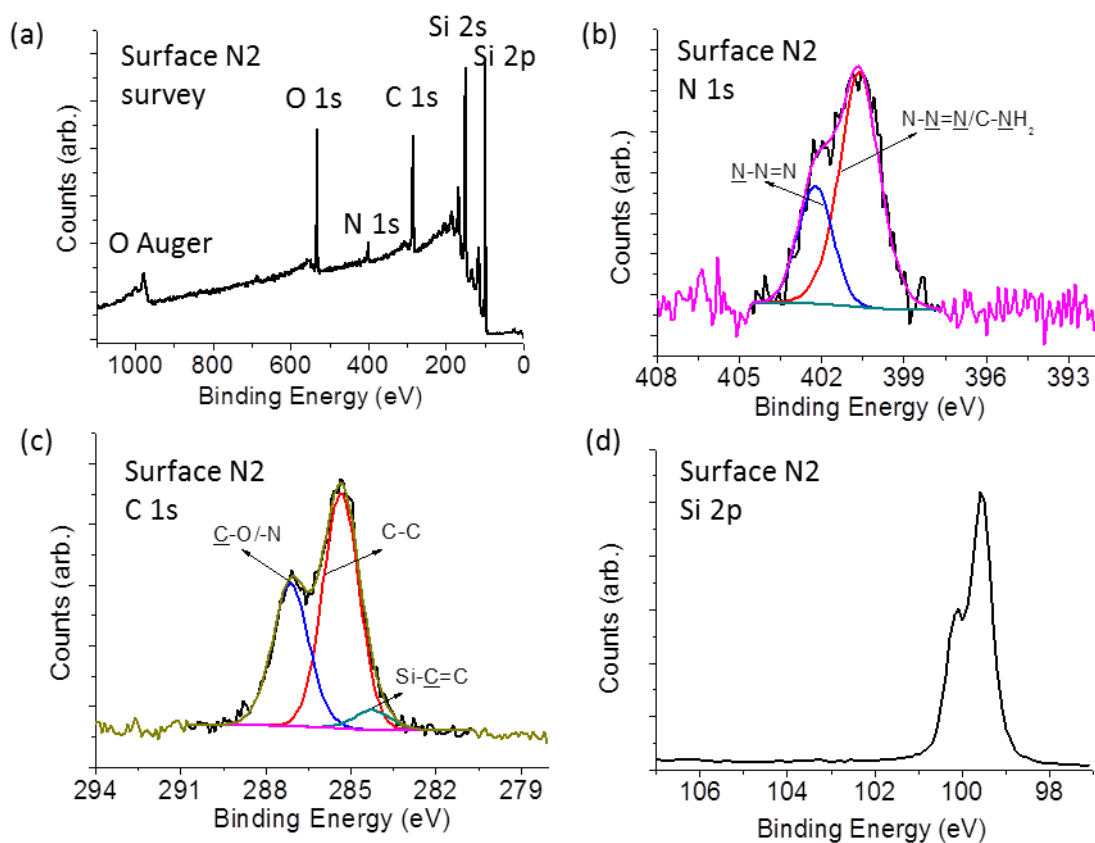
Figure 4.5 (a) XPS survey scan of OEG-NH$_2$-functionalised SOS surface via "click" reaction (surface N2). High-resolution scans for (b) nitrogen, (c) carbon and (d) silicon.

4.4 LAPS imaging with PAH and PAH-DNA-patterned carboxyl-terminated SOS substrates

Figures 4.6 (a) and (b) show the fluorescent microscope image of the RBITC-PAH pattern on undecylenic acid-modified SOS and the corresponding LAPS image measured in depletion region at 0.488 V (*vs*. Ag/AgCl). The fluorescent image demonstrated a good agreement with the LAPS image of the polyelectrolyte pattern. At the chosen voltage, the photocurrent was greater on the PAH pattern (bright islands shown in Figure 4.6 (b)) than on the bare monolayer surface. This corresponds to the positive charge introduced by the polycationic PAH.
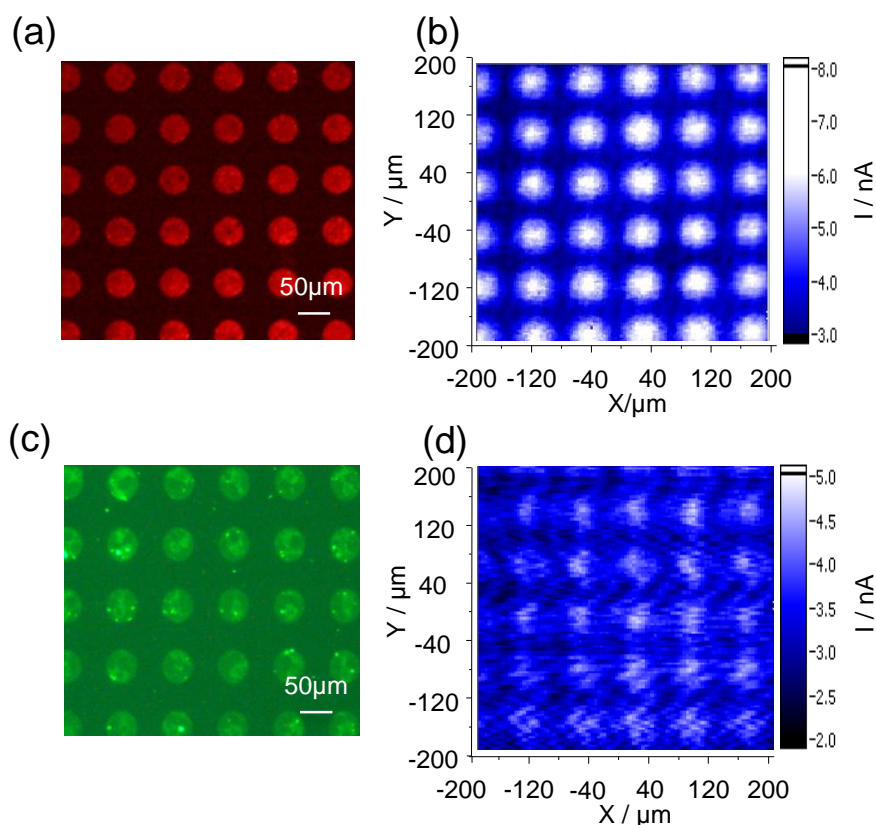
Figure 4.6 RBITC-PAH dots printed on an undecylenic acid modified SOS substrate (a) fluorescent micrograph ;(b) corresponding LAPS image; Gene Finder-labelled dsDNA adsorbed on PAH dots; (c) fluorescence micrograph; (d) corresponding LAPS image; LAPS images (b) and (d) measured at 0.488 V (vs. Ag/AgCl) with a scan range: 400 μm × 400 μm, step size: 2 μm and dwell time: 30 ms. All LAPS images were measured in 10 mM Tris buffer (pH 7.4) containing 137 mM NaCl and 2.7 mM KCl.

Incubating the PAH patterned substrate with DNA solution is a simple and inexpensive way to generate a DNA microarray [216]. PAH-DNA binding is due to electrostatic attraction as DNA carries a negative charge. Figure 4.6 (c) presents the fluorescent microscope image of the Gene Finder[TM]-labelled dsDNA array coated on PAH, which demonstrates a selective deposition of DNA. Figure 4.6 (d) shows the LAPS image of the DNA array measured at 0.488 V. Even though the pattern was still visible, the contrast between coated and uncoated areas decreased compared to the LAPS image before DNA coating. Due to the adsorption of the negatively charged DNA, the surface charge of the coated area became more similar to the surface charge of the undecylenic acid monolayer, which also carries a negative charge.

Photocurrent curves for the areas on the pattern and on the undecylenic acid monolayer before and after DNA adsorption are shown in Figure 4.7. Before dsDNA coating, the lower part of the photocurrent curve on the PAH pattern shifted by -41 mV compared to the bare undecylenic acid-modified surface causing a step to appear in the curve. After dsDNA adsorption, the lower part of the *I-V* curve shifted by +20 mV. This shows that the LAPS devices are capable of measuring surface charge effects with spatial resolution. Adsorbing positively charged PAH to the negatively charged monolayer at pH 7.4 resulted in a shift of the *I-V* curve to negative values. However, after incubating with negatively charged DNA, a negative surface charge was introduced resulting in a positive shift of the *I-V* curve. The directions and orders of magnitude of the potential shifts due to PAH and DNA adsorption are consistent with the result measured by Poghossian *et al.* [273, 281] using capacitance-voltage measurements at p-Si-SiO$_2$-Ta$_2$O$_5$ and p-Si-SiO$_2$ EIS sensors.
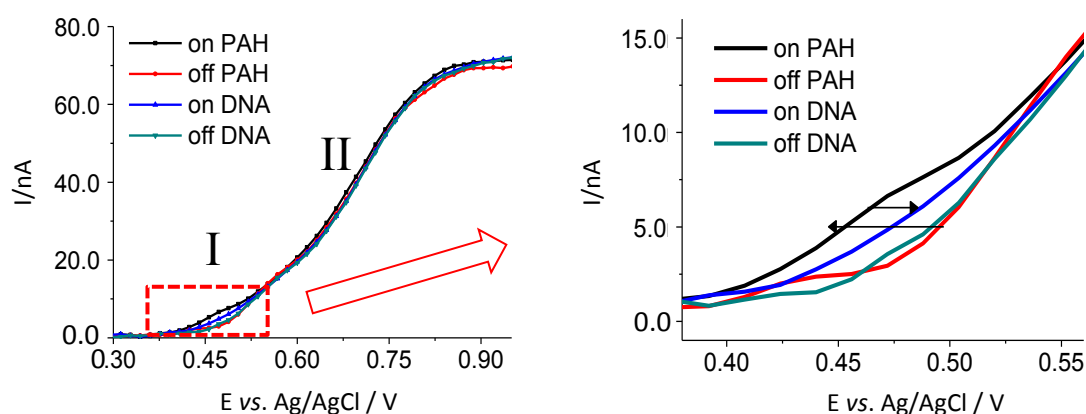
Figure 4.7 I-V curves for PAH and PAH-DNA patterned on a SAM-modified SOS substrate (a) and (b) zoomed graph in part "I". All I-V curves were measured in 10 mM Tris buffer (pH 7.4) containing 137 mM NaCl and 2.7 mM KCl.

When the laser was focused onto the PAH coated part of the sample, a step appeared in the photocurrent curve (Figure 4.7 (a), part "I") as the potential shift due to the change in surface charge appeared only in the lower part "I" of the *I-V* curves. This indicates that within the illuminated part of the sample, areas with different surface charges exist. This behaviour is consistent with incomplete coverage with PAH due to the printing process and is analogous to steps in capacitance voltage curves found in electrolyte/LaF$_3$/silicon structures due to defects in the LaF$_3$ film [282]. Some of the surface was coated with PAH exhibiting a positive surface charge, while other parts of

the surface remained negatively charged due to the undecylenic acid monolayer. Part "I" of the *I-V* curves was clearly affected by the charge of the PAH or PAH-DNA, while part "II" of the *I-V* curves remained unaffected displaying the behaviour of the bare undecylenic acid surface within the pattern. AFM images of a PAH dot confirmed the incomplete adsorption of PAH onto the substrate (Figure 4.8). In some parts of the PAH dot, the undecylenic acid monolayer was exposed. This incomplete coverage may be due to the high roughness (~20 nm) of the SOS surface, resulting in a poor contact with PDMS stamps. The average thickness of the PAH layer estimated from the AFM data was about 4.5-5 nm.
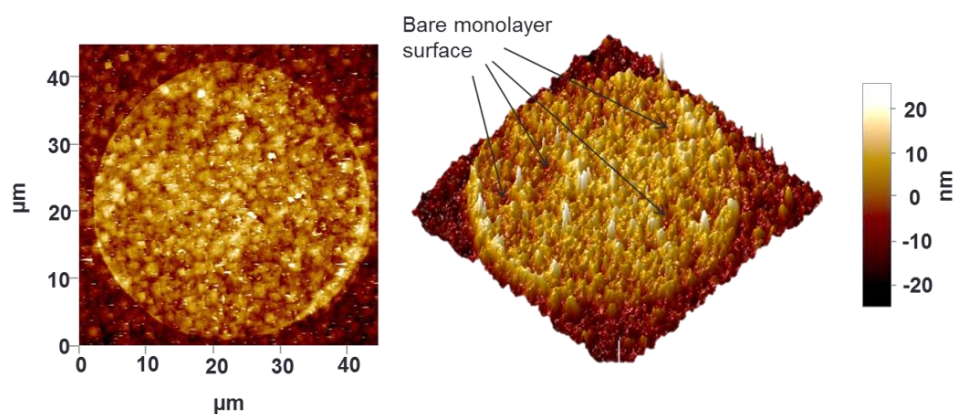
Figure 4.8 AFM analysis of patterned PAH coated on undecylenic acid-modified SOS substrate (PeakForce TUNA mode; 1 nN PeakForce; 256 × 256 pixels).

4.5 LAPS imaging with PSS-patterned amino-terminated SOS substrates

Figures 4.9 (a) and (b) show the LAPS image of the PSS pattern on amino-terminated monolayer-modified SOS measured in depletion at 0.44 V (*vs*. Ag/AgCl) and the corresponding three-dimensional image. The LAPS image of the PSS pattern showed a good agreement with the pattern of the PDMS stamp (circular islands with a diameter of 40 μm and 30 μm gaps). As expected, at the chosen voltage, the photocurrent was lower on PSS (blue islands shown in Figure 4.9 (a)) than on the bare amino-terminated monolayer surface, which is contrary to the PAH pattern.

Photocurrent curves for the areas on the PSS pattern and on the amino-terminated monolayer are shown in Figure 4.9 (c). Similar to the PAH pattern results (see Figure 4.7 (a)), a step also appears in the lower part of the *I-V* curves, which may due to the

same reason that the coverage of PSS on the monolayer surface was incomplete. The lower part of the *I-V* curve on the PSS pattern shifted by +36 mV compared to the background of the amino-terminated monolayer caused by the adsorption of negatively charged PSS to the positively charged monolayer surface at pH 7.4.
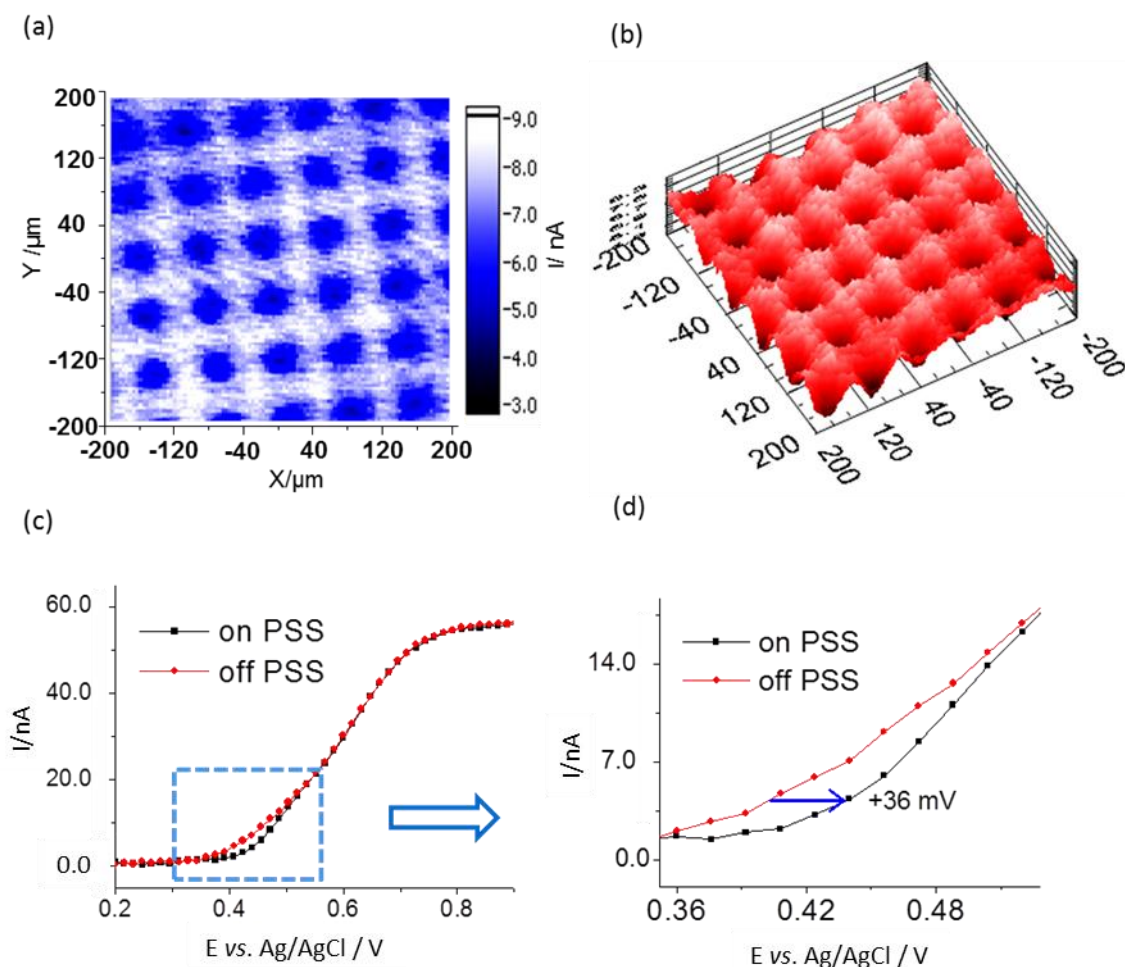
Figure 4.9 PSS dots printed on an amino-terminated SAM-modified SOS substrate (a) LAPS image; (b) corresponding three-dimensional image measured at 0.44 V (vs. Ag/AgCl) (scan range: 400 μm × 400 μm, step size: 2 μm, dwell time: 30 ms); (c) I-V curves on PSS and on amino-terminated SAM and (d) zoomed graph. All measurements were performed in 10 mM Tris buffer (pH 7.4) containing 137 mM NaCl and 2.7 mM KCl.

4.6 Summary

An amino-terminated monolayer was immobilised onto a hydrogenated SOS or Si substrate using CuAAC "click" reactions of azido-OEG-NH$_2$ to an alkyne-terminated monolayer. The successes of the thermally-induced 1, 8-nonadiyne monolayer

formation and the further "click" functionalisation were evidenced by the contact angle, ellipsometry and XPS measurements. No oxidation of the underlying silicon was observed from XPS measurements of both samples before and after "click" chemistry, indicative of a better way to achieve a high quality of organic monolayers on SOS or Si rather than the assembly of alkyl monolayers from undecylenic acid.

LAPS imaging with carboxyl-terminated and amino-terminated monolayer modified SOS substrates was validated by using a PAH/PAH-DNA pattern and a PSS pattern, respectively. The PAH and PSS patterns were prepared using microcontact printing. DNA adsorption on the PAH template pattern was achieved purely by electrostatic interactions. LAPS images for PAH, PAH-DNA and PSS patterns were obtained, which were in good agreement with the corresponding patterns of the PDMS stamp. The adsorption of PAH (positively charged) caused a higher photocurrent and a negative voltage shift in the lower part of the *I-V* curve in depletion, compared to the bare undecylenic acid monolayer. Conversely, the presence of DNA and PSS, which are negatively charged, resulted in a lower photocurrent output and a positive voltage shift of the lower part of *I-V* curves in depletion. The voltage shifts in the lower part of depletion region indicate the capability of LAPS to measure surface charge effects induced by the adsorption of PAH, DNA and PSS. Moreover, incomplete coverage with PAH, DNA and PSS was deduced from the partial shifts in the depletion region of the *I-V* curves and confirmed by AFM images for PAH. This indicates that LAPS may be able to determine the coverage of charged polymers, DNA or other biomolecules.

5. "Click" patterning of SAMs on SOS or Si and their characterisation using LAPS

5.1 Introduction

The patterning of chemical and biochemical molecules on silicon surfaces has become an important aspect of label-free biosensing and cell tissue engineering applications [283, 284]. Self-assembled monolayers (SAMs), as ultrathin resists modified on silicon surfaces, provide an effective platform for such chemical patterning. A variety of techniques have been developed for the formation of patterned SAMs on silicon [206, 220, 285]. The most popular methods are photolithography and μCP, which have both been used to fabricate patterns with various molecules [194-196, 207, 218, 219] or biological components (i.e. DNA [200, 201, 215-217] and peptides [198, 199, 212, 213]).

CuAAC "click" chemistry has been established as a reliable, highly selective and efficient means of directly immobilising various functional molecules onto silicon surfaces. Therefore, through the combination of "click" chemistry and patterning techniques, chemically patterned silicon surfaces could be fabricated. In many cases, organic monolayers on silicon have been patterned by selective removal of parts of the monolayer by exposure to an electron beam [286], UV [287] or visible light [288] using the monolayer as resist or by light-induced deposition on silicon surfaces [289]. In many biosensing or electronic device applications, a perfectly passivating monolayer is required, in which case patterning by photolithography employing a commercial photoresist would be desirable. However, as a result of the high solubility of positive photoresist in most organic solvents, the combined technique of "click" chemistry and photolithography could only be carried out in aqueous solutions, which may limit the application of this method. Zhu *et al.* have reported a strategy for chemically patterning 1, 8-nonadiyne monolayer-modified porous silicon with two different species (-OEG–OCH$_3$ and -OEG–OH) using photolithography with a positive photoresist followed by a surface modification using "click" chemistry [194, 195]. Initially, a metal film was pre-coated on the 1, 8-nonadiyne monolayer modified surface in order to exclude the photoresist from the silicon pores, although, the metal film was found to have an adverse effect on the efficiency of the "click" reaction and the metal layer was consequently eliminated [195]. To the best of our knowledge, there

have been no reports on the effects of photoresist processing on the integrity of SAMs on silicon substrates and the efficacy of their further chemical modification. As an alternative strategy, Ravoo and Reihoudt have elegantly demonstrated that a "click" reaction can be also performed via μCP within a short reaction time, thus providing a straightforward way for the fabrication of biomolecular microarrays on silicon [183, 215, 218]. A siloxane monolayer (Si-O-Si-R) was used as the platform for patterning; however, it was reported that this monolayer was inherently unstable and prone to hydrolytic cleavage in electrolyte solutions [139]. This resulted in an additional silicon dioxide layer, which adversely affects the accuracy of silicon-based bioelectronics devices and biosensors [145] such as LAPS [270]. Thus, if this method is to find utility in the fabrication of chemical patterns on hydrogen-terminated silicon surfaces in these applications, it is essential to eliminate the intervening layer of silicon dioxide [139].

Chapters 3 and 4 have shown that SAMs can be used as the insulator in LAPS/SPIM measurements, which can improve the accuracy of LAPS and the sensitivity of SPIM significantly compared to a traditional silicon dioxide insulator. LAPS imaging with SAM-modified SOS substrates was validated using micropatterns of polyelectrolyte/DNA that were physically adsorbed on the sensor surface. As a result of these advances we wished to exploit the chemical patterning strategy on SAM-modified oxide-free silicon surfaces in order to image cell-surface interactions on patterned surfaces using LAPS. 1, 8-Nonadiyne has been successfully used for the formation of a high-quality monolayer on oxide-free SOS or Si in Chapter 4, and the resultant alkyne-terminated surface provides an ideal platform for CuAAC "click" functionalisation [147, 157, 191, 194, 195, 265, 277], it was therefore used in patterning of a non-oxidized SOS or Si surface. Herein, a comparison of the chemical patterning methods of photolithography and μCP on non-oxidized silicon surfaces integrated with "click" chemistry together with LAPS imaging to validate the molecular patterning were reported.

5.2 Experimental section

All chemicals and reagents used in this chapter, unless noted otherwise, were as listed in Chapter 2. For photocurrent measurements, a laser with 405 nm wavelength modulated electronically and SOS substrates modified with SAMs were used. 10 mM phosphate buffer solution pH 7.4 containing 137 mM NaCl and 2.7 mM KCl was used as the electrolyte.

5.2.1 Photolithography on SAM-modified SOS or Si and "click" modification

The positive photoresist S1818 and the developer Microposit 351 were purchased from Shipley, UK.

The detailed procedures for assemblies of undecylenic acid (surface U1), 1-octadecene (surface O1) and 1, 8-nonadiyne (surface N1) monolayers on SOS or Si, and the "click" functionalisation with azido-OEG-NH$_2$ (surface N2) on surface N1 have been described in Section 2.2.2.

Figure 5.1 (a) illustrates the schedule of photolithographic treatment on surface N1 and the "click" chemistry after the treatment. S1818 patterns were formed on surface N1 with an optimized photolithographic process. First, S1818 was spin-coated onto a 1, 8-nonadiyne-modified substrate at 500 rpm for 5 s and then 5000 rpm for 60 s. After spin-coating, the film was baked at 95 ℃ for 15 min on a hot plate. Then, it was exposed to UV-light (405 nm) for 20 s through a mask (Figure 5.1 (a), route ii) or was exposed over the entire surface (Figure 5.1 (a), route iii) using a mask aligner (KARL SUSS MJB3 UV400). The substrate was then developed in diluted Microposit 351 solution (Microposit 351/water 1:3) for 45 s and washed with pure water and blown dry. To study the effect of photolithography on the underlying SAMs, the substrate was then ultrasonically washed with acetone for 5 min to remove any photoresist and then rinsed with isopropanol and pure water. The UV-exposed parts of surface N3 are therefore identical to surface N4. Surface N4 was transferred into a "click" solution as described in Section 2.2.2.4 to produce surface N5. Moreover, the entire surface N1 was either exposed with UV-light for 20 s (Figure 5.1 (a), route vi) or rinsed in diluted Microposit 351 solution for 40 s (Figure 5.1 (a), route vii) to obtain surfaces N1a and N1b. In order to further investigate the interaction of the photoresist and organic monolayers, the same surface treatments were performed on carboxyl-terminated and alkyl-terminated monolayers to obtain surfaces U2, U3 and O2 (Figure 5.1 (b)).

For ellipsometry and AFM measurements, the photolithographic treatments described above were also adapted for SAM-modified silicon substrates. For AFM measurements, the pattern on surface N3 was structured with stripes of 20 μm width (UV-blocked region) and 10 μm interspace (UV-exposed region), while on surface U2 was patterned with 7 μm wide stripes (UV-blocked region) and 13 μm interspace (UV-exposed region). For LAPS measurements, the pattern is shown in Figure 5.1 (c).
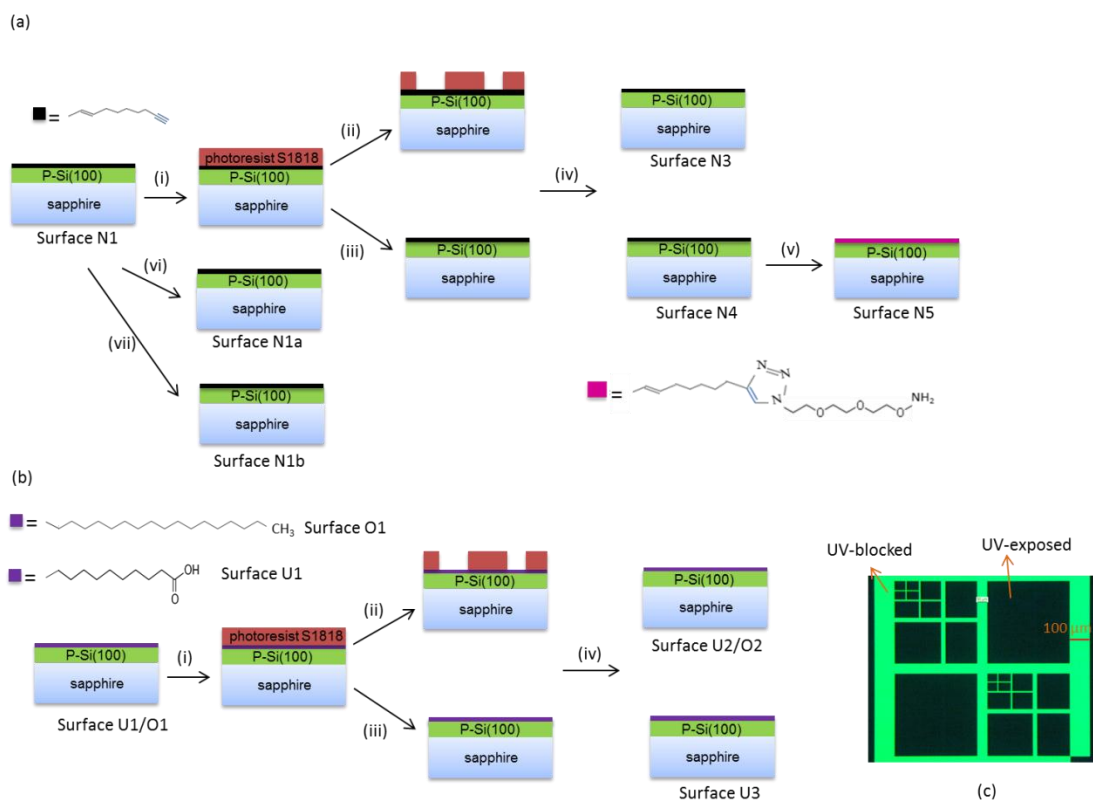
Figure 5.1 (a) Procedure for photolithography on 1, 8-nonadiyne-modified SOS (surface N1) and "click" chemistry on the surface after photolithography: i) S1818 photoresist was spin-coated on surface N1; ii) S1818-coated substrate was exposed to UV-light through a mask with patterns and then developed in diluted Microposit 351 solution; iii) the entire S1818-coated surface was exposed with UV-light and then developed in diluted Microposit 351 solution; iv) samples were ultrasonically washed in acetone and isopropanol to remove the cured photoresist to obtain surfaces N3 and N4; v) azido-OEG-NH$_2$ was attached onto surface N4 via "click" chemistry; vi) the entire surface N1 was exposed with UV-light to obtain surface N1a; vii) surface N1 was rinsed in diluted Microposit 351 solution for 40 s to gain surface N1b (b) the same photolithographic treatment was performed on undecylenic acid/1-octadence-modified SOS to gain surface U2/O2 and U3 (c) the pattern of the mask used for LAPS imaging. For ellipsometry and AFM measurements, the above surface modifications were carried out on silicon substrates.

5.2.2 Microcontact printing (μCP) for "click" modification

The master was prepared following a previously reported protocol [275]. The preparation of PDMS stamps has been described in Section 4.2. The pattern of the PDMS stamp consisted of circular islands with a diameter of 40 μm and 30 μm gaps.

97

Figure 5.2 illustrates the process of "click" chemistry on surface N1 using μCP. The PDMS stamp was dipped in the "click" solution containing azido-OEG-NH$_2$ (see Section 2.2.2.4) for 30 min. The soaked stamp was dried under nitrogen gas and placed onto surface N1 for 3 h at room temperature. The reaction was performed in a closed Petri dish with a moistened tissue for keeping the PDMS stamp wet. After removing the stamp, the unreacted reagents were removed by rinsing the substrate consecutively with copious amounts EtOH, then water and EtOH. Then, the sample was immersed in a 0.5 M HCl solution for 2 min to obtain surface N6 (Figure 5.2 (a)). To characterise the "clicked" surface properly, a chemically homogeneous surface (surface N7) was also prepared using a flat PDMS stamp following the same procedure (Figure 5.2 (b)).
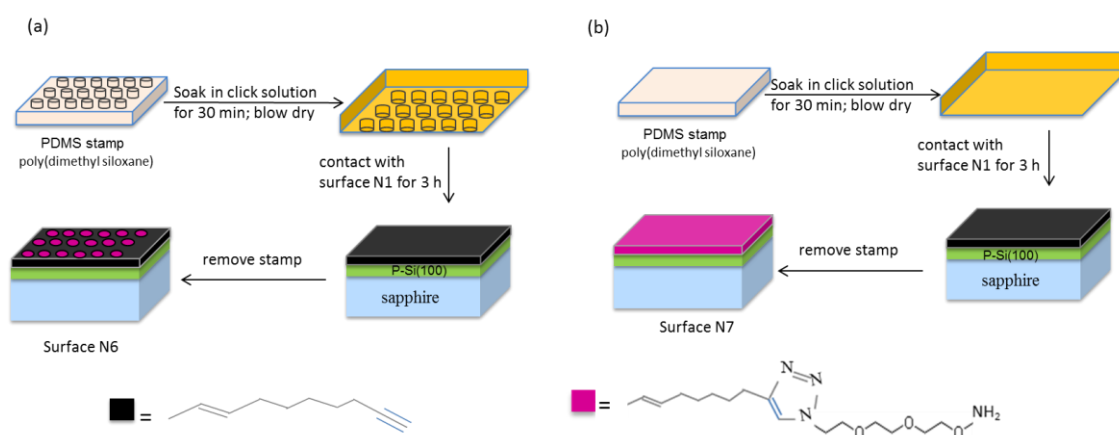
Figure 5.2 Schematic illustration of the μCP chemistry: azido-OEG-NH$_2$ was printed on surface N1 and "click" reactions occurred exclusively in the contact area (surface N6: an array of chemical pattern, surface N7: a homogeneous surface functionalised with azido-OEG-NH$_2$). For ellipsometry and AFM measurements, the above surface modifications were carried out on silicon substrates.

5.3 Photolithography on SAM-modified SOS or Si and "click" chemistry

5.3.1 Photolithography on 1, 8-nonadiyne-modified SOS or Si

Surfaces N1 and N2 were prepared as described in Sections 2.2.2.3 (see Figure 2.2) and 2.2.2.4 (see Figure 2.3), respectively. To study the potential effects of photolithography on alkyne-terminated monolayers and the effect on "click" reactions, surfaces N3-N5 were prepared as described in Figure 5.1 (a). After photolithographic treatment, which involved spin-coating, UV-exposure, development and removal with acetone, the contact angle for surface N4 decreased by ~12 °, indicating a change of the

surface chemistry (see Table 5.1). AFM measurements showed an obvious trace of the pattern on surface N3 (Figure 5.3 (a)), indicative of a chemical reaction with compounds in the photoresist. The average height of the exposed layer, determined from the AFM topography (Figure 5.3 (b)), was ~4.7 Å, which is consistent with the ellipsometry thickness that showed an increase from ~10.6 Å (surface N1) to ~15.5 Å (surface N4) (see Table 5.1).

Table 5.1 Advancing water contact angles and ellipsometry thicknesses of different surfaces. Ellipsometry fitting parameters for surface N1: MSE = 0.585; B = -0.03651 ±0.008923; C = 0.00449 ±0.001005; surface N2: MSE = 0.880; B = 0.02089 ± 0.009465; C = 0.00289 ±0.001063; surface N4: MSE = 1.458; B = -0.05200 ± 0.015621; C = 0.00680 ±0.001759; surface N5: MSE = 1.688; B = -0.02587 ± 0.013578; C = 0.00362 ±0.001525; surface N7: MSE = 1.700; B = -0.02463 ± 0.017874; C = 0.00397 ±0.002002.

Surface	Water contact angle (°)	Ellipsometry thickness (Å)
N1	88 ±1	10.6 ±0.4
N2	37 ±1	16.0 ±1.0
N4	76 ±2	15.5 ±0.3
N5	52 ±4	21.4 ±1.2
N7	46 ±2	15.8 ±0.9

(a) (b)
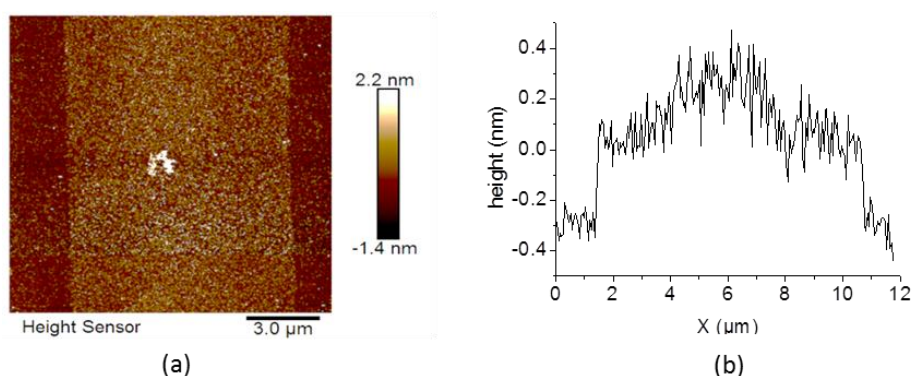
Figure 5.3 (a) AFM images and (b) topography of 1, 8-nonadiyne-modified silicon surface after photolithography treatment involving photoresist coating, UV-exposure, development and finally washing off (surface N3) (PeakForce TUNA mode; 1 nN PeakForce; 256 × 256 pixels).

The chemical modification of the surface was also confirmed by XPS measurements (see Figure 5.4). It was found that the atomic ratios of C/Si and O/Si on surface N4 had increased by factors of ~1.95 and ~3.5, respectively, compared to the results of surface N1 (Figure 5.4 (c)). The Si 2p narrow scan showed minor emissions associated with silicon oxide species (102-104 eV), indicating some oxidized spots were formed in defective regions of the monolayer due to the photolithographic treatment. The area of the oxidized silicon peak was estimated to be ~3% of the total Si intensity, corresponding to ~0.17 monolayers of oxidized silicon [290] (Figure 5.4 (b)). In order to investigate the cause of oxidation, different treatment steps were carried out on surface N1. Figures 5.4 (d) and (e) present the Si 2p narrow scans on surfaces only exposed to UV-light (N1a) and only rinsed with developer (N1b). It can be seen that surface N1a showed no emission of SiO_x, while surface N1b showed a ~0.15 SiO_x fractional monolayer coverage, which reveals that the surface oxidation occurred following washing with the developer rather than after UV-exposure.
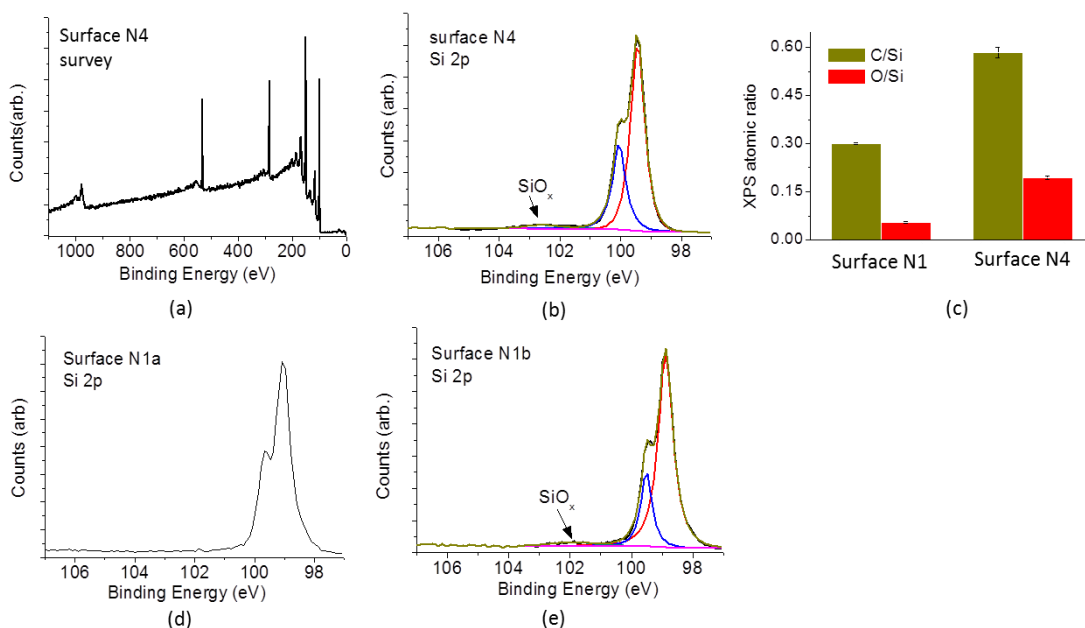
Figure 5.4 (a) XPS survey scan of 1, 8-nonadiyne-modified SOS surface after photolithographic treatment (surface N4) and (b) high-resolution scan for silicon; (c) surface atomic ratio of C/Si and O/Si before photolithographic treatment (surface N1) and after photolithographic treatment (surface N4) evaluated from XPS surveys scans; XPS high-resolution scans for silicon of (d) surface N1a and (e) surface N1b.

It has been established that during exposure to UV-light, the photoactive compound diazonaphthaquinone **1** in a positive photoresist (i.e. S1818 or AZ6612 which has been

used elsewhere [194, 195]) undergoes the loss of N_2 to generate a carbene intermediate **2**. The carbene transforms into a ketene **3,** which then forms carboxylic acid **4**, after reaction with water [291] (Figure 5.5). The carboxylic acid is then dissolved in alkaline developer and removed from the surface. However, due to the multi-step nature of the process and the high reactivity of the intermediates, it has been proposed that particulate contamination may be a constant problem in photolithography [292]. Presumably, in this case either carbene **2** or the photochemically generated ketene intermediate **3** undergoes partial reaction with the alkyne-terminated monolayer, the latter presumably via a [2+2] cycloaddition, resulting in an aromatic-terminated surface.
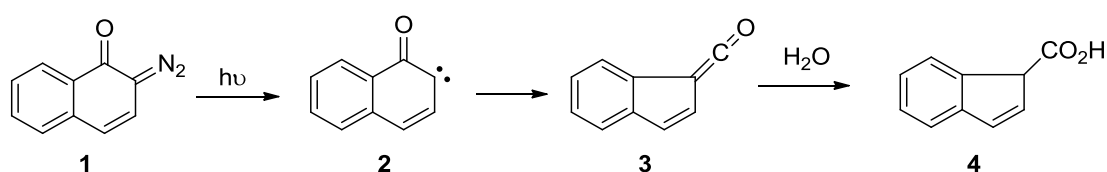
Figure 5.5 Photoreaction of diazonaphthaquinone [291].

LAPS has been validated to be a very accurate technique to detect the properties of surfaces, such as the surface potential, with spatial resolution. Figure 5.6 (a) shows the LAPS image of surface N3 measured at 0.55 V (vs. Ag/AgCl). At the chosen voltage, the photocurrent was slightly smaller on the UV-exposed region (dark strips shown in Figure 5.6 (a)) than on the non-exposed region. Since the changes in maximum photocurrents of the two regions were negligible, the corresponding *I-V* curves were normalised and were presented in Figure 5.6 (b). A positive shift (+21 mV) at the lower part of the photocurrent curve was observed on the UV-exposed region, which corresponds to a more negatively charged surface. Whilst this is an empirical observation, the negative charge may due to two reasons: Firstly, as aromatic compounds readily participate in intramolecular π-π interactions with neighbouring molecules, it is possible, that the indene carboxylic acid (**4**) has been absorbed onto the surface, resulting in a small negative surface charge in aqueous solution. Alternatively, the minor quantity of oxidized silicon shown by XPS to be formed after the photolithographic treatment (see Figure 5.4 (b)) could also contribute to the negative surface charge. The potential shift appearing only in the lower part of *I-V* curves is analogous to results of polyelectrolytes/DNA patterns described in Chapter 4, which can be explained by the incomplete coverage of the negatively charged species.
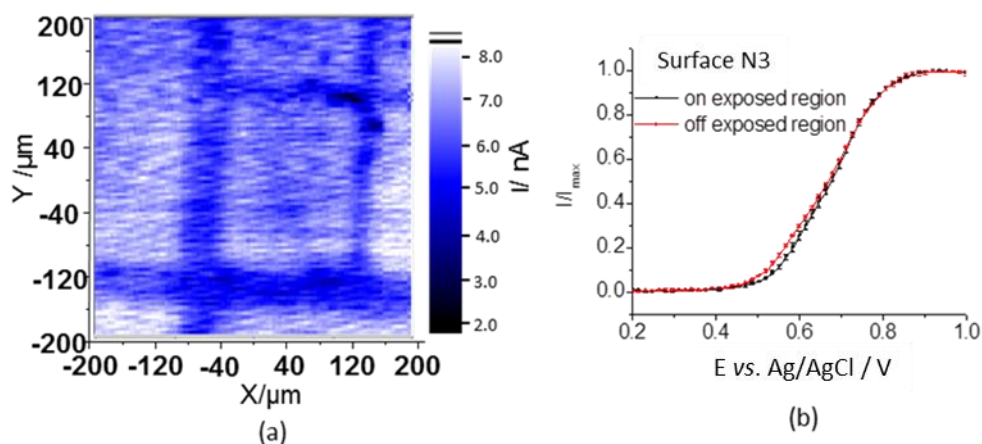
Figure 5.6 (a) LAPS image of 1, 8-nonadiyne-modified SOS substrates following photolithographic treatment; (b) corresponding normalised I-V curves for UV-exposed and non-exposed regions on surface N3. LAPS image was measured at 0.55 V, with a scan range: 400 μm × 400 μm, step size: 2 μm and dwell time: 30 ms. 10 mM phosphate buffer solution pH 7.4 containing 137 mM NaCl and 2.7 mM KCl was used.

5.3.2 Photolithography on alkyl monolayer-modified SOS or Si

In order to further investigate the nature of the chemistry between the photoresist intermediates and organic monolayers, the same surface treatments were performed on carboxyl-terminated and alkyl-terminated monolayers on SOS or Si (see Figure 5.1 (b)). The resultant contact angle for surface U3 increased by ~11 ° (see Table 5.2), indicating a change of the surface chemistry. The AFM image of surface U2 showed an obvious trace of the pattern (Figure 5.7 (a)). The average height of the UV-exposed layer was determined to be ~8 Å (Figure 5.7 (b)), which is consistent with the ellipsometry results that showed an increase of ~10 Å after photolithography (see Table 5.2), again indicating that the carboxyl-terminated monolayer also undergoes unwanted chemical modification.

Table 5.2 Advancing contact angles and ellipsometry thicknesses of undecylenic acid-modified SOS before (surface U1) and after (surface U3) photolithographic treatment. Ellipsometry fitting parameters for surface U1: MSE = 0.494; B = -0.01769 ± 0.008212; C = 0.00189 ±0; surface U2: MSE = 1.183; B = -0.04500 ±0.009360; C = 0.00541 ±0.001056.

Surface	Water contact angle (°)	Ellipsometry thickness (Å)
U1	66 ±3	10.2 ±0.4
U3	75 ±1	20.2 ±0.9

(a)   (b)
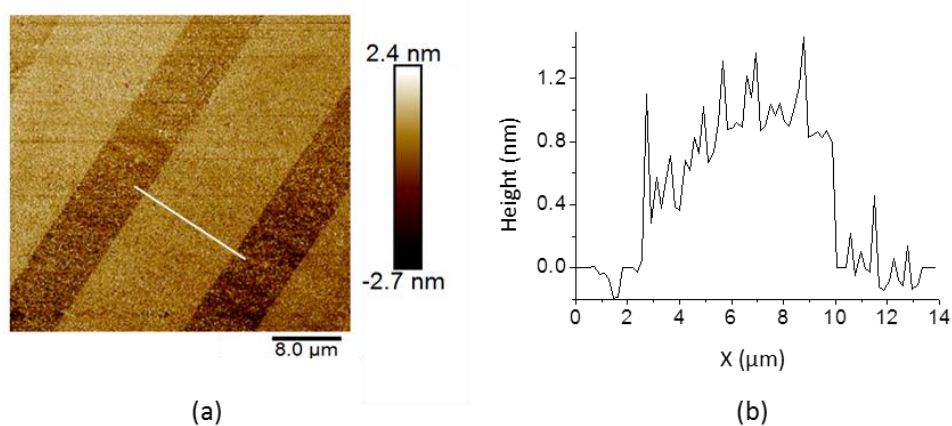
Figure 5.7 (a) AFM image and (b) topography of undecylenic acid monolayer-modified silicon after photolithographic treatment (surface U2) (PeakForce TUNA mode; 1 nN PeakForce; 256 × 256 pixels).

Figure 5.8 (a) shows the LAPS image of surface U2 measured at 0.5 V (*vs.* Ag/AgCl), which revealed the photocurrent to be greater on the UV-exposed region (bright strips shown in Figure 5.8 (a)) than that from the unexposed area, which is the opposite of the result observed for the 1,8-nonadiyne monolayer-modified substrate. The corresponding normalised photocurrent curves showed a shift by -64 mV for the surface exposed with UV-light (see Figure 5.8 (b)) and may be due to the reaction of the carboxylic acid with the ketene, resulting in an aromatic-terminated surface. This surface has less negative charge compared with carboxyl thus causing a negative voltage shift of the *I-V* curve.

In light of this the effect of the photoresist treatment on a saturated hydrocarbon monolayer, which ostensibly contains little chemically reactive functionality was

investigated. In this case, a decreased photocurrent in the LAPS image of the UV-exposed areas following treatment with photoresist was again observed (see Figures 5.8 (c) and (d)) and, as for the 1, 8-nonadiyne modified surface, a lower photocurrent indicated a more negatively charged surface in the exposed areas. As there is unlikely to be any reaction between the monolayer and **3** it would appear to indicate that carbene **2** has undergone C-H bond insertion [293] or the surface was slightly oxidized due to the development process, and that this results in a similar effect on the surface charge as observed for the alkyne-terminated monolayers.
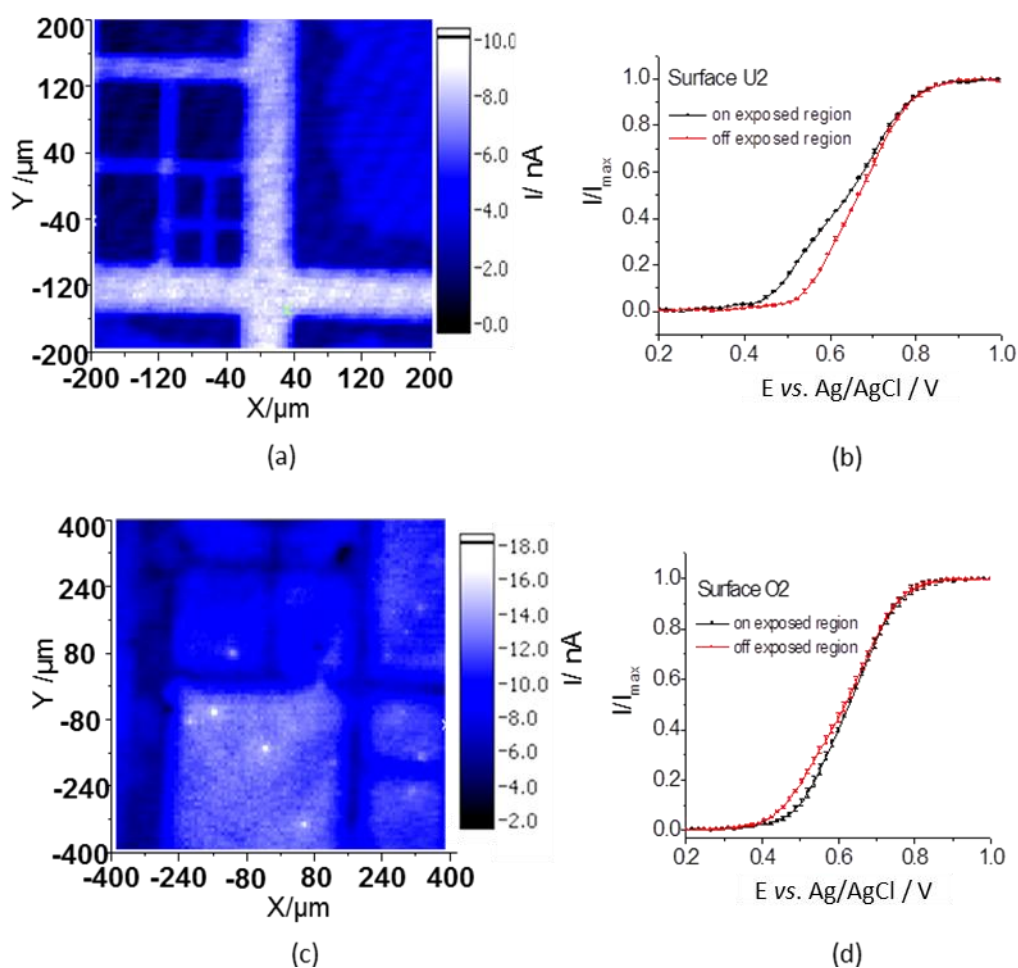
Figure 5.8 LAPS images of (a) undecylenic-modified (surface U2, bright lines: exposed to UV) and (c) 1-octadecene-modified (surface O2, dark lines: exposed to UV) SOS substrates after photolithographic treatment. Corresponding normalised I-V curves for UV-exposed and non-exposed regions on (b) undecylenic acid- and (d) 1-octadecene-modified SOS surfaces. LAPS images measured at 0.5 V (a) with a scan range: 400 μm × 400 μm, step size: 2 μm and dwell time: 30 ms; while (c) with a scan range: 800 μm × 800 μm, step size: 4 μm, dwell time: 30 ms. 10 mM phosphate buffer solution pH 7.4 containing 137 mM NaCl and 2.7 mM KCl was used.

5.3.3 "Click" chemistry on photolithographically treated 1, 8-nonadiyne-modified SOS or Si

To check the effect of the photolithographic treatment on the efficacy of CuAAC "click" modification, surface N4 was subjected to standard "click" modification with azido-OEG-NH$_2$ to generate surface N5, which was characterised. Both the water contact angle and ellipsometric thickness changed significantly, showing that "click" modification has occurred to some extent, but these differed significantly from the values seen for surface N7 (see Table 5.1). The XPS survey scan and N 1s scan also corroborated the success of the "click" surface modification (Figure 5.9 (a) and (b)). This indicates that if the terminal alkynes do indeed undergo [2+2] cycloadditions with ketene **3** during UV-exposure that a number remain viable in the CuAAC reaction. However, a lower level of nitrogen incorporation into the surface following the "click" modification of the surface when compared to surface N2, would also be expected. This would be manifested in a reduced N/C atomic ratio observed in the XPS survey scan, which is clearly seen (Figure 5.9 (d)). Furthermore, the XPS spectrum at 102-104 eV shows high levels of oxidized silicon species (Figure 5.9 (c)) and the SiO$_x$ fractional monolayer coverage was estimated to be ~0.32. This is double the level found following photolithography and indicates that chemical modification via this route results in significant perturbation of the organic monolayer and that it is no longer able to effectively protect the underlying silicon substrate from oxidation.
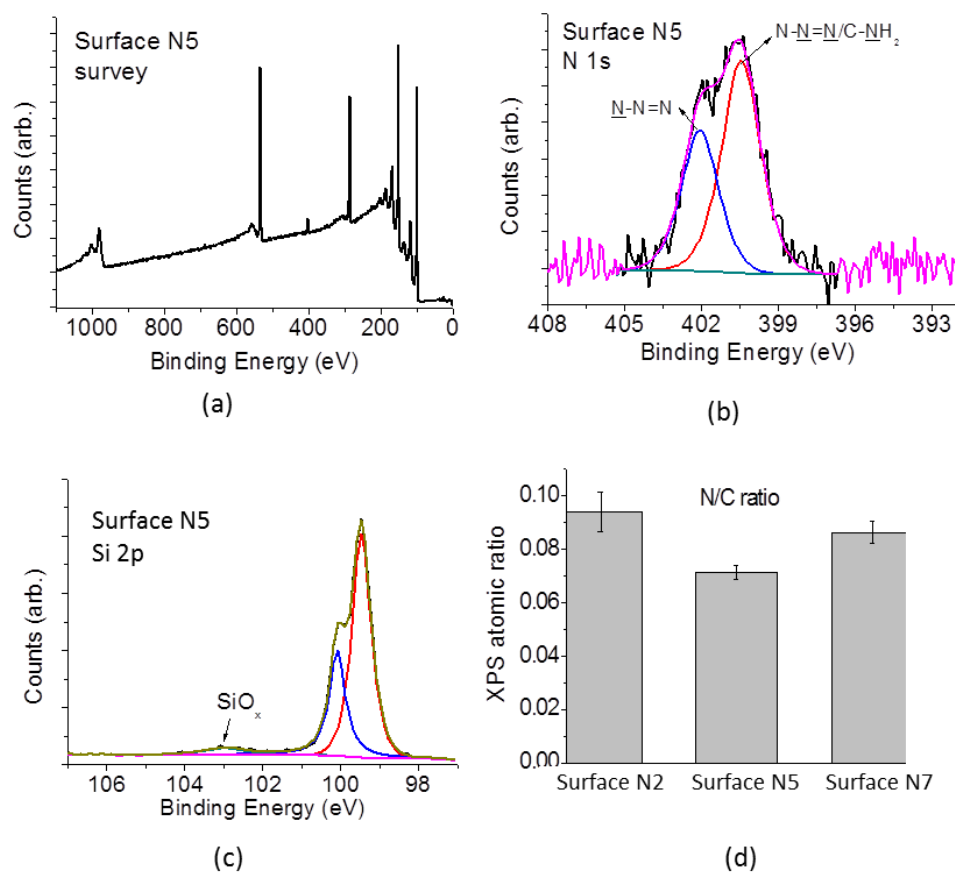
Figure 5.9 (a) XPS survey scan of photolithographically treated and then "click"-functionalised surface (surface N5) and high-resolution scans for (b) nitrogen and (c) silicon; (d) atomic ratio (N/C) of surface N2, surface N5 and surface N7 evaluated from XPS surveys scans.

5.4 Chemical patterning through the combination of μCP and "click" chemistry

Due to the surface contamination caused by photolithography, a clean and quick method -μCP- was used to chemically pattern 1, 8-nonadiyne-modified SOS or silicon substrates. As shown in Figure 5.2, the azide inks were printed onto the alkyne-terminated SAMs on SOS though "click" reactions to gain surface N6. To demonstrate that a covalent bond is formed in the nanoscale confinement, a flat featureless PDMS stamp was used to produce a homogeneously functionalised surface (surface N7). The contact angle (46 ± 2°) and monolayer thickness (15.8 Å) after the CuAAC "click" reaction via μCP are shown in Table 5.1, which are comparable to the results of surface N2. The successful coupling was further confirmed by XPS results (Figure 5.10). The N 1s peak shown in Figure 5.10 (b) can be fitted to two peaks at 400.6 eV

(C-$\underline{N}H_2$/N-$\underline{N}$=$\underline{N}$) and 402.2 eV ($\underline{N}$-N=N) [265, 280], indicative of triazole formation. The narrow scan from C 1s region was deconvoluted into three peaks assigned to Si-$\underline{C}$=C (284.2 eV), C−C (285.3 eV) and $\underline{C}$−N/−O (287.1 eV), which are similar to the results of surface N2 (see Figure 4.5). The C/N atomic ratio of surface N7 (~0.086) is close to surface N2 (~0.093), indicating a comparable level of "click" triazole incorporation on the surfaces (Figure 5.9 (d)). Importantly, the reaction time via μCP is significantly shorter than the time using the traditional "click" condition (3 h c.f. 24 h). Encouragingly, negligible amounts of silicon oxide were observed from the Si 2p narrow scan, demonstrating a non-invasive method to functionalize and pattern the oxide-free silicon surface with SAMs.
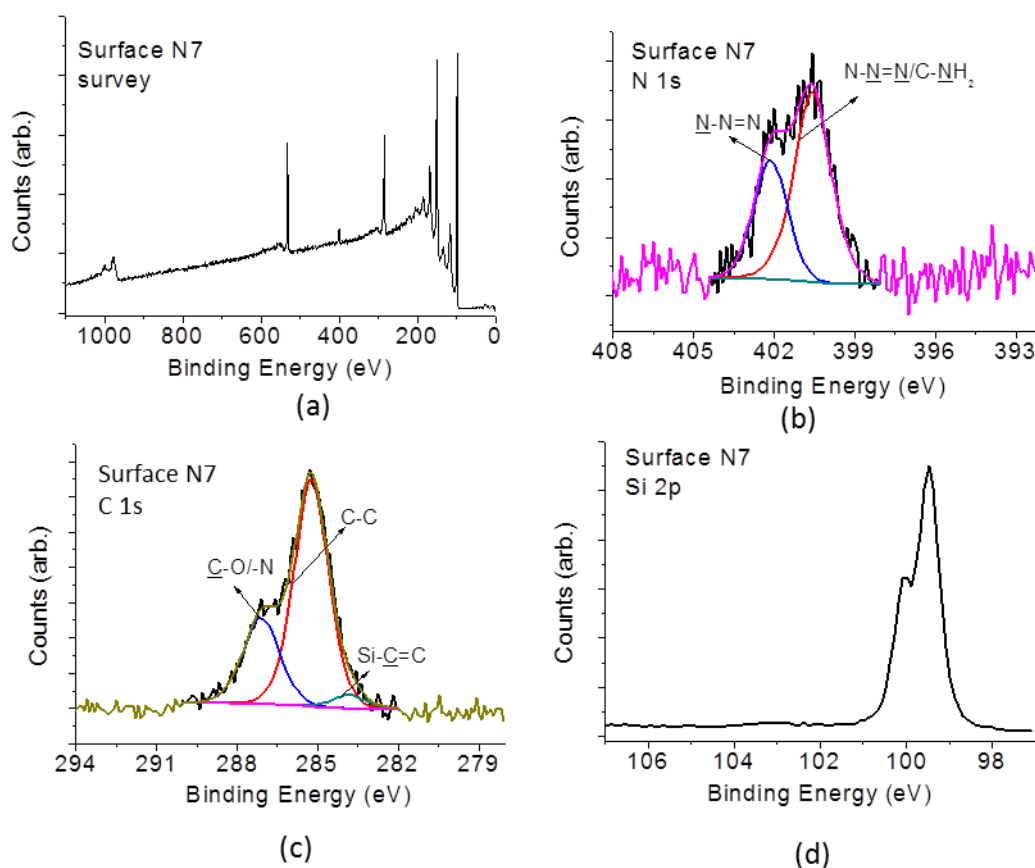
Figure 5.10 (a) XPS survey scan of the OEG-NH₂-functionalised SOS substrate via μCP (surface N7). High-resolution scans for (b) nitrogen, (c) carbon and (d) silicon.

To validate the combined patterning technique, LAPS was used to image the chemically patterned SOS substrate (surface N6). The LAPS image obtained showed very good agreement with the patterns of the PDMS stamp. At the chosen voltage (0.44 V, *vs*. Ag/AgCl), the photocurrent was greater on the "click"-functionalised

surface (bright islands shown in Figure 5.11 (a)) than on the 1, 8-nonadiyne monolayer surface, which corresponds to the positive charge introduced by NH_2-terminated monolayers. Figure 5.11 (b) shows the *I-V* curves measured on the circular feature (azido-OEG-NH_2) and the background region (1, 8-nonadiyne). The lower part of the curve on the amino-terminated region shifted by -50 mV compared to the 1, 8-nonadiyne-modified surface, which is slightly greater than the shift caused by physically absorbed PAH (-41 mV) as described in Section 4.2.1.
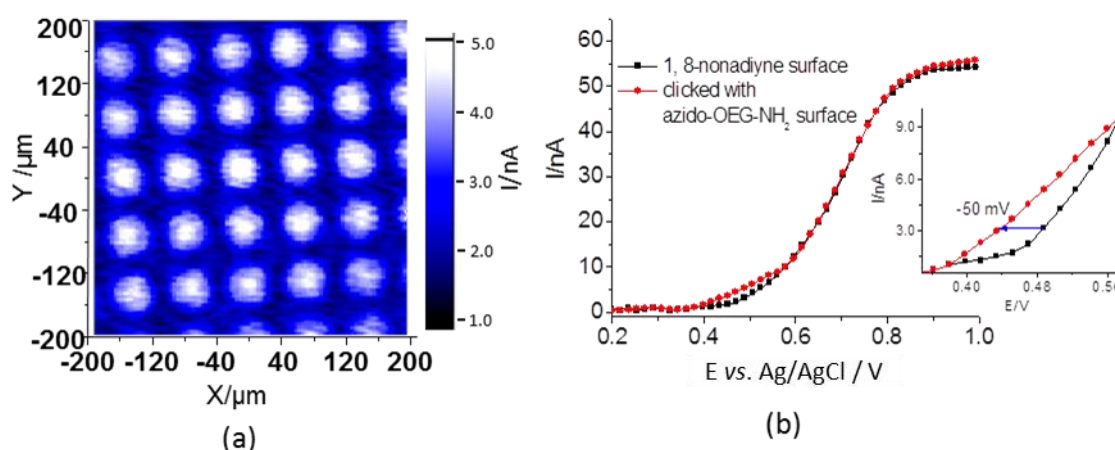
Figure 5.11 (a) LAPS image of chemically patterned non-oxide SOS substrate with azido-OEG-NH_2 on the circular regions and 1, 8-nonadiyne on the background (measured at 0.44 V, vs. Ag/AgCl, with a scan range: 400 μm × 400 μm, step size: 2 μm and dwell time: 30 ms); (b) corresponding I-V curves of the circular feature and the background region. 10 mM phosphate buffer solution pH 7.4 containing 137 mM NaCl and 2.7 mM KCl was used.

As a control, inks without azide were printed onto 1, 8-nonadiyne-modified substrates by using the procedure described in Figure 5.2. For the sample printed with a flat PDMS stamp, the contact angle showed no changes and ellipsometry showed an increase of 1 Å, which is within the error of ellipsometry. The sample contacted with a PDMS stamp structured with patterns showed no photocurrent contrast over the entire surface measured at depletion voltages.

5.5 Summary

This chapter has demonstrated that μCP followed by "click" chemistry is a mild and efficient means for chemical patterning on oxide-free silicon or SOS surfaces whereas

the combination of photolithography and "click" chemistry is not. As evidenced by XPS spectra, approximately 17% of SiO_x monolayers were formed after photoresist processing on initially oxide-free SAMs and this value was doubled after further derivatization via "click" reaction. The surface characterisation results and LAPS images demonstrated that side-reactions between the photoactive compounds in the photoresist and SAMs occurred, causing undesirable chemical contamination of the surface. However, µCP was shown to be an effective method to chemically pattern alkyne-terminated monolayers through "click" reactions. The atomic N/C ratio was comparable to that of a conventionally formed "click" monolayer, but surface modification was achieved with a much shorter reaction time. More importantly, no evidence of surface contamination with silicon oxide species was observed after µCP-induced "click" reactions. The successful chemical patterning was validated using LAPS. The voltage shift (-50 mV) in the depletion region of the photocurrent curves indicated a good sensitivity for the measurement of the surface charge effects induced by the chemically bonded NH_2-terminated molecules. Apart from being suitable for the measurement of surface charge distribution, LAPS was also shown to be extremely sensitive to surface contamination. This will broaden the application of LAPS as well as the other field-effect devices from a sensor technique to a characterisation tool for SAM-modified silicon substrates.

6. LAPS/SPIM imaging of microcapsules attached to SAM-modified SOS

6.1 Introduction

LAPS and SPIM, which are based on different bias voltages (depletion and inversion), have been developed to produce two-dimensional images of surface potential and impedance. The results presented in Chapters 4 and 5 have demonstrated the high accuracy of LAPS for surface potential measurements. However, the high performance of SPIM on local impedance has not yet been studied. Even though previous work in our laboratory has shown some impedance images of polymers such as PMMA [74], cellulose acetate [75] and photoresist [14], it is unconvincing to claim that SPIM displays high sensitivity due to the thick and highly insulating properties of these polymer films. Recently, a two-photon effect strategy has been introduced to improve the spatial resolution of LAPS/SPIM, by using a femtosecond laser with low energy photons ($E_{photon} < E_g$) rather than the traditionally used laser with high energy photons ($E_{photon} > E_g$) to generate photocurrents [14, 74]. The reason for resolution improvement has been discussed in Section 1.3.5.2. In addition, with the introduction of SAMs as the gate insulator, the sensitivity of SPIM can be significantly improved (see Chapter 3). Encouraged by all these achievements, it was therefore decided to assess the performance of the high-resolution set-up in conjunction with SAM-modified SOS substrates for SPIM imaging, and the results are presented in this chapter.

As described in Section 1.7, using a simple layer-by-layer (LBL) adsorption method, polymeric multilayer capsules (PMLCs) can be prepared with desirable size, composition, surface charge and shell thickness. Due to the series of controllable properties, PMLCs can be exploited as a model system to study cell-surface interactions. In this work, gold nanoparticle (AuNP)-modified PMLCs integrated with SAM-modified SOS substrates were used for the validation of quantitative measurement using LAPS/SPIM before progressing to cell measurements. The high resolution and high sensitivity of SPIM imaging using the 1250 nm femtosecond laser were demonstrated.

6.2 Experimental section

All the chemicals and reagents used in this chapter, unless noted otherwise, were as listed in Chapter 2. Monodisperse melamine formaldehyde (MF) microparticles (~10 μm, disperse in water) were purchased from Microparticles GmbH, Germany. A suspension of gold nanoparticles (~15 nm, disperse in water) was provided by Dr Huijuan Chen and was prepared following a procedure described elsewhere [294].

The preparation of undecylenic acid (surface U1), "click"-functionalised azido-OEG-NH_2 (surface N2) and 4-azidobenzoic acid (surface A1) monolayers on SOS or Si substrates has been described in Section 2.2.2.

6.2.1 Microcapsule preparation and characterisation

PMLCs were prepared using the layer-by-layer (LbL) technique. Positively charged MF microparticles were used as the template, and polyelectrolytes of PSS and PAH were assembled onto the templates alternatively. Figure 6.1 shows the procedure for normal PMLC preparation. Firstly, PSS (2 mg/ml in water) was deposited onto MF particles with 15 min of gentle shaking. The excess polyelectrolytes were removed by centrifugation (2000 rpm, 2 min) following by washing with pure water three times. PAH was subsequently adsorbed onto the shell of PSS from a PAH solution (2 mg/ml in water) using the same procedure. The adsorption cycle was repeated until the desired number of layers was formed. Finally, hollow capsules were obtained by dissolving MF cores in 0.1 M hydrochloric acid solution for 30 min and washing by four centrifugation circles (3500 rpm, 3 min) with pure water. Finally, hollow capsules with a shell structure of $(PSS/PAH)_4$ (C2) were prepared.
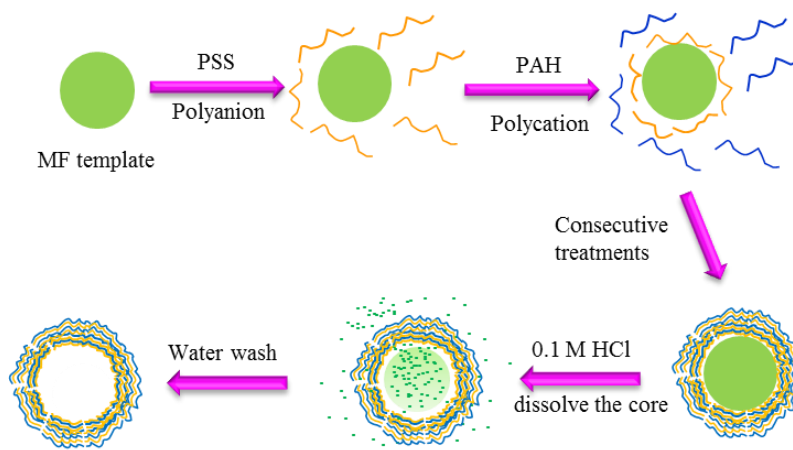
Figure 6.1 Procedure for the preparation of PMLCs.

In order to perform SPIM imaging, as well as to improve the visibility of capsules in the digital camera, an additional gold nanoparticle (AuNPs) layer was deposited on the PAH layer in a similar adsorption process. Briefly, the capsules with two bilayers of PSS/PAH were dispersed in the AuNPs suspension for 15 min. After three washing steps, the capsules were further coated with additional polyelectrolyte layers. Hollow capsules structured with $(PSS/PAH)_2$-AuNPs-PSS/PAH/PSS (C1-AuNPs) and $(PSS/PAH)_2$-AuNPs-$(PSS/PAH)_2$ (C2-AuNPs) were obtained. Table 6.1 summarises the microcapsules used in this work and their corresponding shell structures.

Table 6.1 Hollow microcapsules and the corresponding shell composition.

Microcapsules	Shell composition
C2	$(PSS/PAH)_4$
C1-AuNPs	$(PSS/PAH)_2$-AuNPs-PSS/PAH/PSS
C2-AuNPs	$(PSS/PAH)_2$-AuNPs-$(PSS/PAH)_2$

To study the effect of AuNPs on impedance using SPIM, a drop of AuNP suspension (1 μl) was directly deposited onto an amino-terminated surface (surface N2) and air-dried. The sample was then rinsed with copious amounts of water to remove the loosely absorbed AuNPs.

Apart from optical microscope and AFM, a scanning electron microscope (SEM, FEI inspect-F) was used to observe the morphology of capsules. Briefly, the diluted capsule suspension was dropped onto a SAM-modified SOS surface, air-dried, and coated with gold. SEM images were then taken with an accelerating voltage of 10 kV and a spot size of 3.5 nm at a working distance of about 10 mm. The distribution of AuNPs in the shell of microcapsules was observed by a transmission electron microscope (TEM, JEOL 2010) operated at 200 kV. The diluted capsule suspension was deposited on a carbon-coated copper grid, and air-dried for 2 h. Then, the copper grid was installed to a sample holder and placed into the vacuum chamber of the TEM for characterisation.

Zeta potentials of hollow capsules containing AuNPs were measured with a Malvern Nano ZS zetasizer (Malvern Instruments Ltd, UK). For measurements, a small volume of sample solution was transferred to a transparent cuvette, diluted with pure water and

placed in the thermostated cavity. Fifteen measurements were taken on each sample and averaged.

6.2.2 Photocurrent measurements

The experimental set-up for photocurrent measurements has been shown in Section 2.4. For measurement, capsules C1-AuNPs or a drop of AuNP suspension and C2 or C2-AuNPs were randomly absorbed through electrostatic attraction and dried on surface N2 (NH_2-terminated) and A1 (COOH-terminated), respectively. A 1250 nm femtosecond laser was used for SPIM imaging (see light profile "b" in Figure 2.6) and a digital camera was used to take *in situ* pictures (see light profile "c" in Figure 2.6).

The correlation between the photocurrent image scanned with the 1250 nm laser and the optical image recorded by camera was calibrated using an SU-8 pattern deposited on surface A1. Since the 405 nm and 1064 nm lasers will be used in the following chapter, their imaging systems were also calibrated using the same method. The preparation of SU-8 films has been described in Section 3.2. All photocurrent measurements were performed in a 10 mM PBS buffer pH 7.4 containing 137 mM NaCl and 2.7 mM KCl.

6.3 Characterisation of 4-azidobenzoic acid-functionalised SOS or Si

The successful formation of the 1, 8-nonadiyne monolayer (surface N1) and its "click" functionalisation with azido-OEG-NH_2 (surface N2) has been demonstrated in Chapters 3 and 4. Hence, this section only presents the characterisation results of the surface "click"-modified with 4-azidobenzoic acid (surface A1).

6.3.1 Contact angle measurements and ellipsometry

After the "click" reaction with 4-azidobenzoic acid, the substrate became hydrophilic with a water contact angle of ~58 ° (see Table 6.2), which is comparable with the literature result [295]. The ellipsometric thickness increased to ~18.4 Å (see Table 6.2), indicating the success of "click" modification.

Table 6.2 Advancing water contact angles and ellipsometry results for H-SOS/H-Si surfaces modified with 1, 8-nonadiyne (surface N1) and further "click"-functionalised with 4-azidobenzoic acid monolayers (surface A1). Ellipsometry fitting parameters for surface N1: MSE = 0.585; B = -0.03651 ±0.008923; C = 0.00449 ±0.001005; surface A1: MSE =3.425; B = -0.10907 ±0.028137; C = 0.01551 ±0.003213.

Surface	Water contact angle (°)	Ellipsometry thickness (Å)
N1	88 ±1	10.6 ±0.4
A1	58 ±2	18.4 ±1.5

6.3.2 XPS measurements

The XPS survey scan (Figure 6.2 (a)) showed the presence of nitrogen species at ~401 eV after "click" functionalisation. A high-resolution scan from the N 1s region (Figure 6.2 (b)) was fitted to two peaks at 400.5 eV and 402.2 eV, which are assigned to N-$\underline{N}$=$\underline{N}$ and $\underline{N}$-N=N, respectively [265, 280]. The ratio of the integrated areas (~2.2:1) is comparable to the stoichiometric ratio (2:1). The narrow scan from the C 1s region (Figure 6.2 (c)) was fitted with three peaks assigned to C−C (285.1 eV), $\underline{C}$−N/−O (286.7 eV) and $\underline{C}$=O (289.5 eV) [158, 265, 295]. The positions of the peaks are also in consistent with the results obtained from surfaces N2 (see Figure 4.5 (c)) and U1 (see Figure 3.4 (b)). Encouragingly, negligible amounts of SiO$_x$ species were observed in the Si 2p high-resolution spectrum, indicative of a high quality of the modified surface (Figure 6.2 (d)).
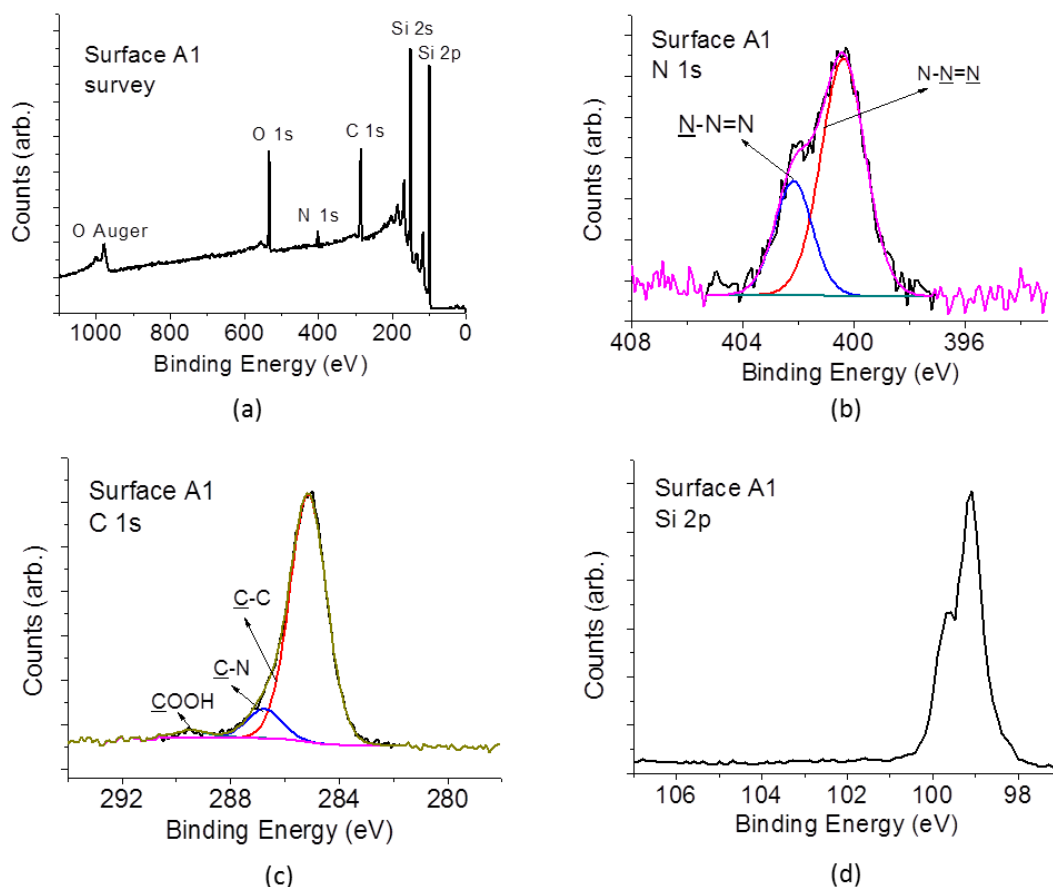
Figure 6.2 (a) XPS survey scan of 4-azidobenzoic acid-functionalised SOS surface via "click" reaction (surface A1). High-resolution scans for (b) nitrogen, (c) carbon and (d) silicon.

6.4 Two-photon effect validation and imaging system calibration

In order to confirm a two-photon effect was obtained, surface A1 was scanned with the 405 nm and 1250 nm femtosecond lasers, respectively, along the z direction (surface normal of the substrate) at 0.9 V (*vs.* Ag/AgCl). The corresponding photocurrent line scan (see Figure 6.3 (a)) using the 1250 nm laser showed a much sharper peak compared to the other one, indicating that photocurrents are only generated near the focus of the laser in silicon, thus resulting in a higher spatial resolution.

Figure 6.3 (b) further highlights the two-photon effect by comparing the double logarithmic plots of photocurrents versus laser intensities using the two lasers. In this graph, a slope close to 1 was obtained for the 405 nm laser, indicative of a linear relationship as expected for the single-photon absorption. However, when measured

with the femtosecond laser, the slope was close to 2, corresponding to a two-photon effect.
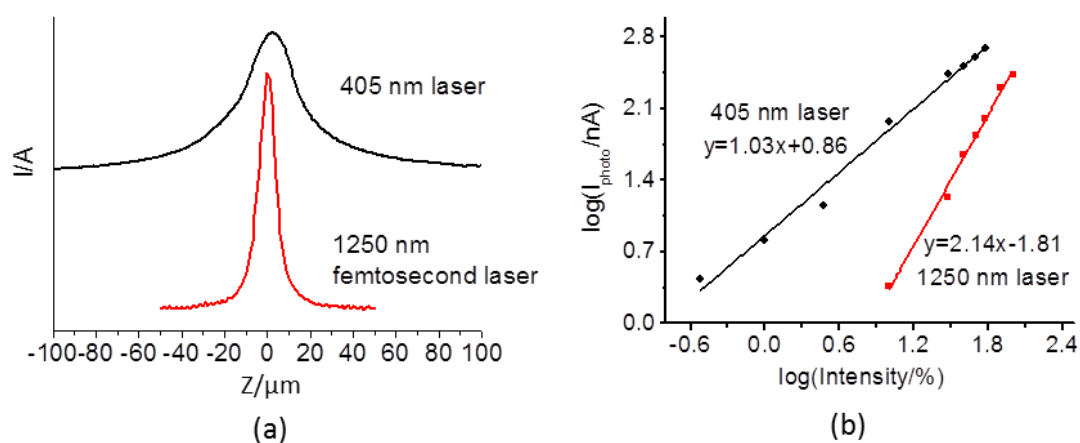
Figure 6.3 (a) Photocurrent line scans in z direction (surface normal of the substrate); (b) laser intensity dependence of the photocurrent using two different lasers. 10 mM phosphate buffer solution pH 7.4 containing 137 mM NaCl and 2.7 mM KCl was used.

Before LAPS/SPIM imaging, the true correlation between photocurrent images and the camera image was calibrated and demonstrated. Figures 6.4 (a), (b) and (c) present images measured in inversion with 405 nm, 1250 nm femtosecond and 1064 nm lasers, respectively. All three images showed nearly zero photocurrents on SU-8 (black area) and large photocurrents off SU-8 (bright area) due to the high impedance of the photoresist. Furthermore, it can be seen that the image taken with the 1250 nm laser had very sharp edges, revealing the highest spatial resolution, followed by the 405 nm and 1064 nm lasers. This is consistent with the resolution results in Section 3.5. Figure 6.4 (d) shows the optical picture recorded by camera. From the results, a good agreement of all SPIM images with the camera image was achieved.
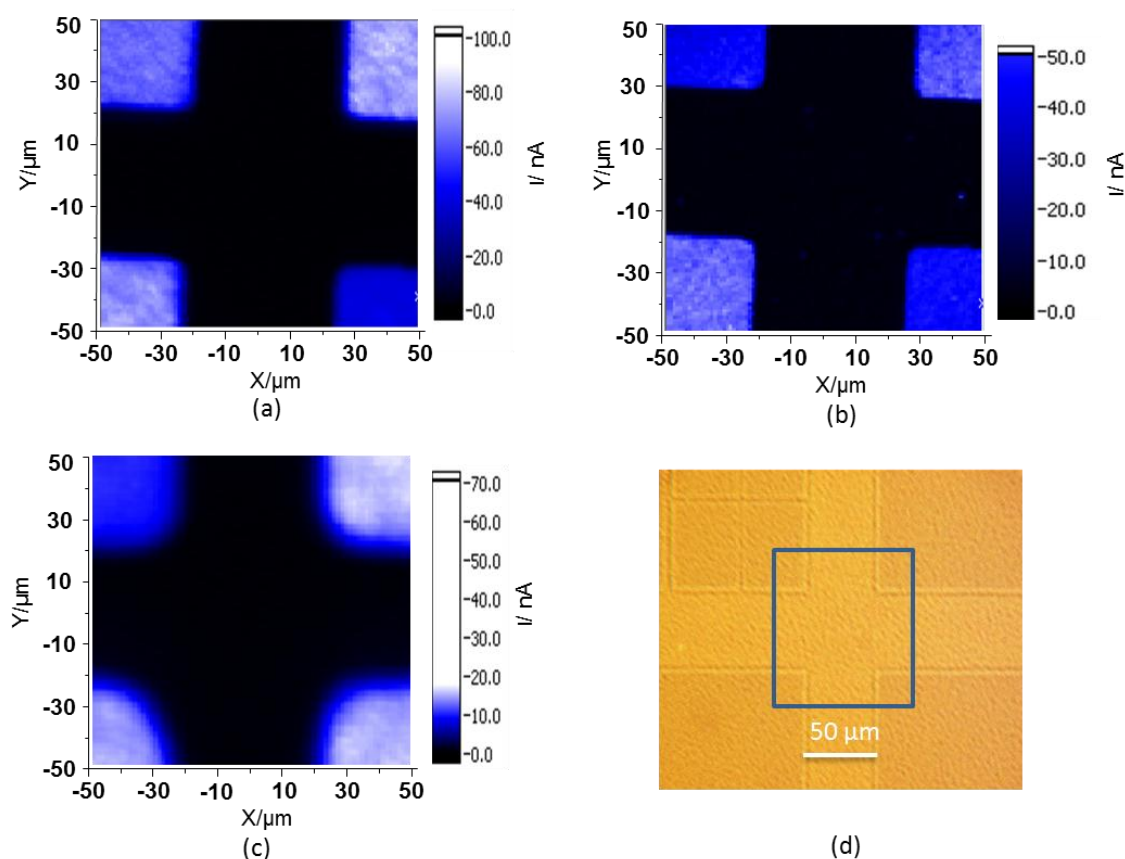
*Figure 6.4 SPIM images of an SU-8 pattern measured at 0.9 V (inversion) using (a)
405 nm laser, (b) 1250 nm femtosecond laser and (c) 1064 nm laser (dark area:
surface with SU-8 film; bright area: bare surface with monolayers); (d) corresponding
optical picture recorded by camera. 10 mM phosphate buffer solution pH 7.4
containing 137 mM NaCl and 2.7 mM KCl was used for photocurrent measurements.*

6.5 Photocurrent measurements of microcapsules attached to SAM-modified SOS

6.5.1 Characterisation of microcapsules containing gold nanoparticles (AuNPs)

Figures 6.5 (a) and (b) show the optical microscope images of microcapsules C2-AuNPs dispersed in water before and after the removal of the MF core. It can be seen that the microcapsules are evenly dispersed and their size is consistent with the MF core size (~10 μm). After drying, completely collapsed spheres were observed from the optical microscope (Figure 6.5 (c)) and SEM image (Figure 6.5 (d)), confirming the hollow nature of the microcapsules. The gold doping in the shell of microcapsules was demonstrated by TEM images (Figures 6.5 (e) and (f)). It is shown that gold nanoparticles (~15 nm) are uniformly distributed over the whole capsule surface

without aggregation. In order to enlarge the contact area between microcapsules and sensor surfaces, hollow capsules dried on SAM-modified SOS were used for all LAPS/SPIM measurements.
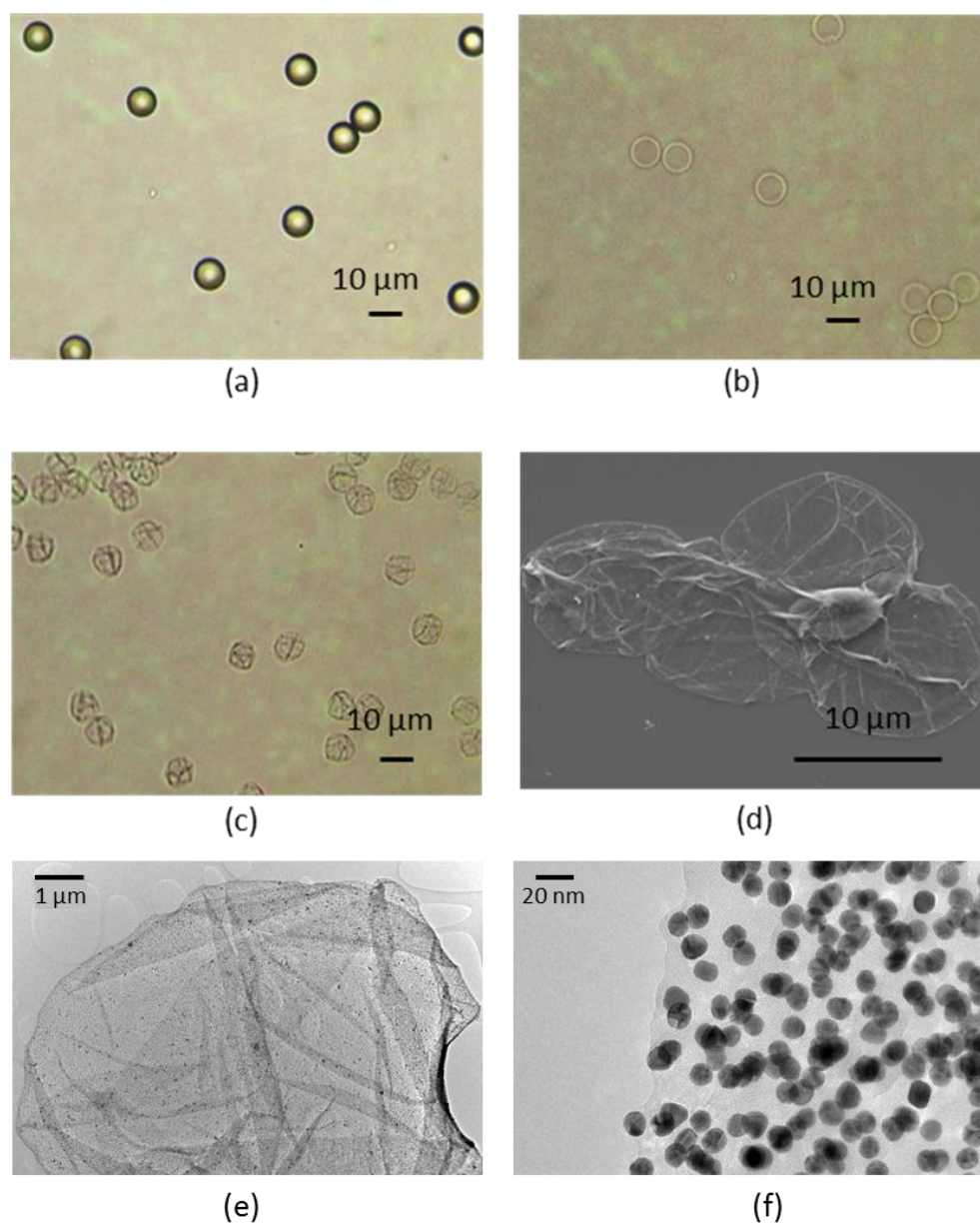
Figure 6.5 Optical microscope images of microcapsules C2-AuNPs dispersed in water (a) before and (b) after the removal of the MF core; (c) optical microscope image and (d) SEM image of C2-AuNPs dried on surface A1; TEM images of a collapsed microcapsule (C2-AuNPs) (e) overview and (f) zoomed graph showed the distribution of AuNPs in the shell of the capsule.

Figures 6.6 (a) and (b) show zeta potential distributions of hollow microcapsules C1-AuNPs and C2-AuNPs, respectively. The average zeta potentials were estimated to be

-19.1 mV for capsule C1-AuNPs due to the negatively charged PSS outer layer, and +12.1 mV for C2-AuNPs due to the PAH outer layer.
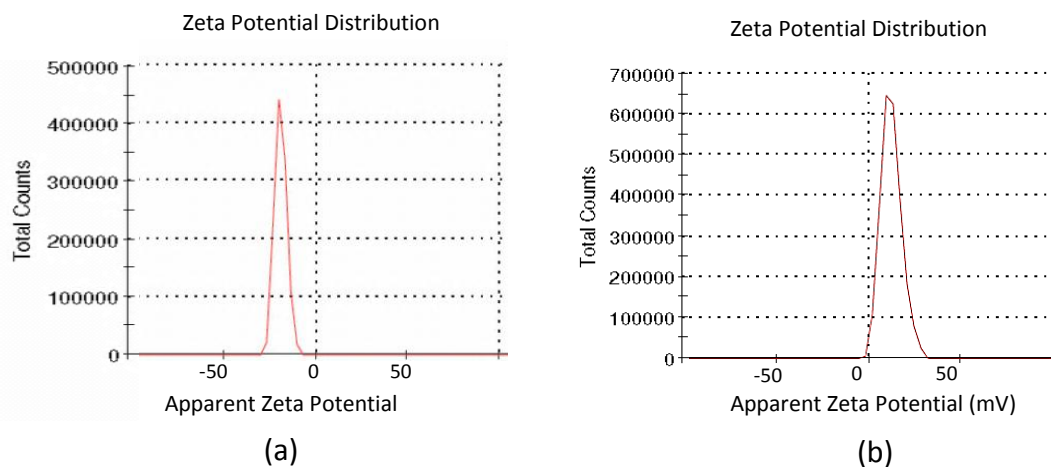
Figure 6.6 Zeta potential distributions of hollow microcapsules structured with (a) (PSS/PAH)$_2$-AuNPs-PSS/PAH/PSS (C1-AuNPs) and (b) (PSS/PAH)$_2$-AuNPs-(PSS/PAH)$_2$ (C2-AuNPs).

6.5.2 SPIM imaging of microcapsules C1-AuNPs collapsed on amino-terminated SOS

Figure 6.7 (a) shows the SPIM image of microcapsules C1-AuNPs collapsed on NH$_2$-terminated SOS (surface N2) measured at 0.9 V (*vs*. Ag/AgCl) using a 1250 nm laser, while Figure 6.7 (b) presents the corresponding optical image recorded by camera. The optical picture demonstrated a good agreement with the SPIM image of microcapsules. The photocurrents on capsule-attached areas (dark spots marked with crosses in Figure 6.7 (a)) were lower than that on background monolayer surfaces, indicating an increase of the local impedance. Remarkably, lines with relatively low photocurrents on capsules were observed from the SPIM image, which correspond to dark lines in the optical image and may be due to creases in the collapsed microcapsules.
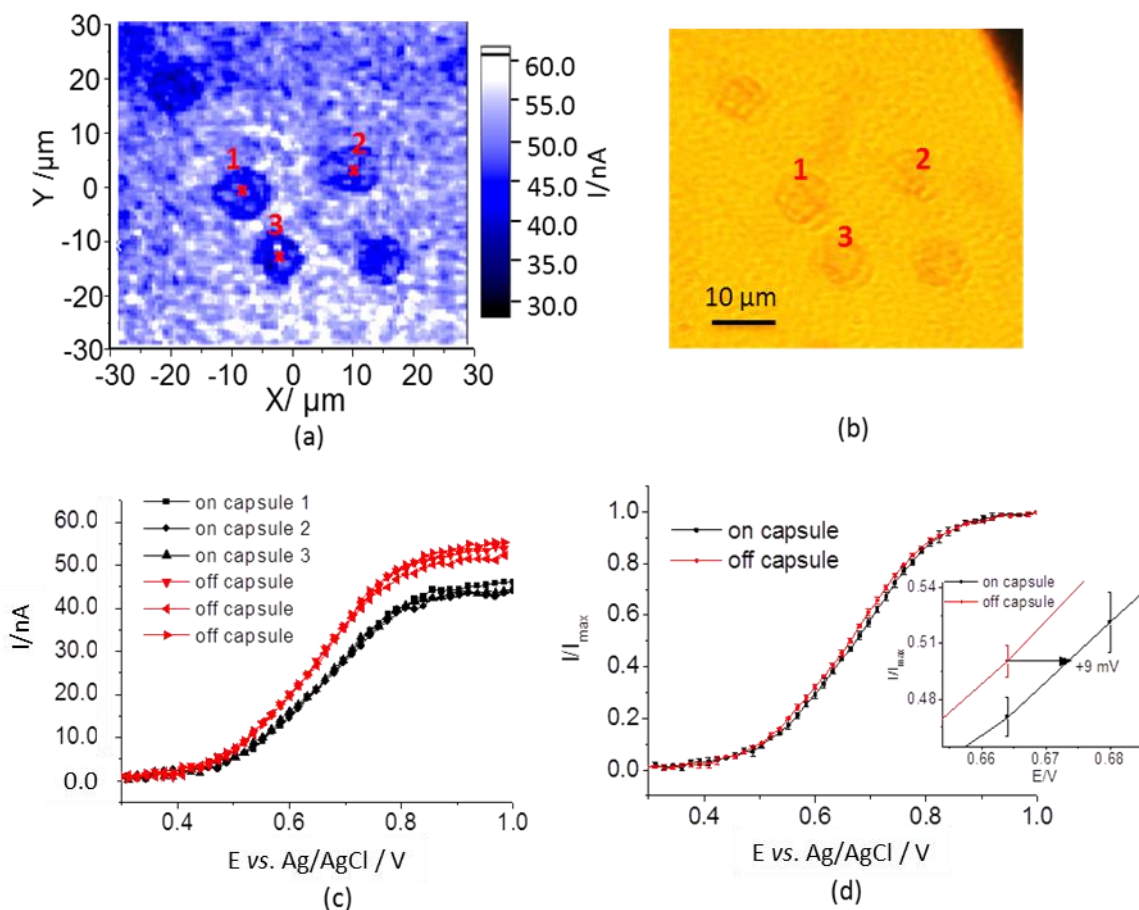
Figure 6.7 Microcapsules C1-AuNPs attached on an NH$_2$-terminated SOS substrate (surface N2); (a) SPIM image measured at 0.9 V (vs. Ag/AgCl , scan range: 60 μm $\times$ 60 μm, step size: 0.6 μm, dwell time: 30 ms); (b) corresponding optical image recorded by camera; (c) I-V curves on capsules and on the monolayer-modified surfaces; (d) normalised I-V curves and zoomed graph in the depletion region: each data point is an average of the 3 measurements (on and off capsules) and is presented as mean $\pm$SD. 10 mM phosphate buffer solution pH 7.4 containing 137 mM NaCl and 2.7 mM KCl was used.

Figure 6.7 (c) shows the photocurrent curves measured in the centre of capsules (marked with red crosses) and on monolayer surfaces. To improve the reliability of results, three different spots were measured for both on and off capsules. The normalised *I-V* curves (Figure 6.7 (d)) were then averaged by the three measurements and were presented as mean $\pm$standard derivation ($\pm$SD). Before normalisation, an average drop (~17%) of the maximum photocurrents was observed on capsule-attached areas, which resulted from the increase of local impedance. Assuming that the capsule surface within laser focus can be considered as a homogeneous dielectric with defined

thickness and dielectric constant, from Equation 1.18, the expressions for maximum photocurrents without (I_{max}) and with microcapsules ($I_{max(capsule)}$) can be simplified as below:

$$I_{max} = I_p \frac{C_m}{C_m + C_d} \text{ (Equation 6.1)}$$

$$I_{max(capsule)} = I_p \frac{C_{m-c}}{C_{m-c} + C_d} \text{ (Equation 6.2)}$$

$$C_{m-c}^{-1} = C_m^{-1} + C_c^{-1} \text{ (Equation 6.3)}$$

Where I_p is the photo-induced current; C_d, C_m, and C_c are capacitances of the depletion layer, organic monolayer and collapsed microcapsule including two overlapping layers of the shell; C_{m-c} is the total capacitance of the monolayer in series with the microcapsule.

Assuming that the photo-induced current is the same in both cases, then the equation can be written as:

$$\frac{I_{max}}{I_{max(capsule)}} = \frac{C_m}{C_m + C_d} \frac{C_{m-c} + C_d}{C_{m-c}} \text{ (Equation 6.4)}$$

From the previous *C-V* measurements (see Section 3.3.4), C_m and C_d can be approximated to be 1.7 μF cm^{-2} and 0.3 μF cm^{-2}, respectively. Thus C_c can be calculated to be ~1.2 μF cm^{-2}. When combined with the dielectric constant of PAH/PSS layer ($\varepsilon_{PAH/PSS}$ = 30) [296], the thickness of the collapsed capsule was estimated to be ~22 nm.

In parallel, the dried capsule thickness was measured by AFM. Figure 6.8 presents the AFM image of dried capsule C1-AuNPs and the height profile along the rectangle. A typical grain-like surface structure was observed in Figure 6.8 (a), which is consistent with previous studies [245]. The wall thickness of the capsule, which included two layers of the collapsed shell, was determined from the height difference between the silicon background ("i") and a fold-free region ("ii") marked in (a). From the topography (Figure 6.8 (b)), a ~19 nm thick wall was measured, which is slightly smaller than the result (~22 nm) deduced from SPIM measurements. The topography also showed that folds ("iii") are able to double the thickness. Due to the relatively poor quality of SPIM image (see Figure 6.7 (a)), *I-V* curves were measured in the centre of capsules regardless of the folded or unfolded regions. Hence, the maximum

photocurrents may have contributions from both regions, resulting in a slightly greater thickness than that measured by AFM.

(a)   (b)
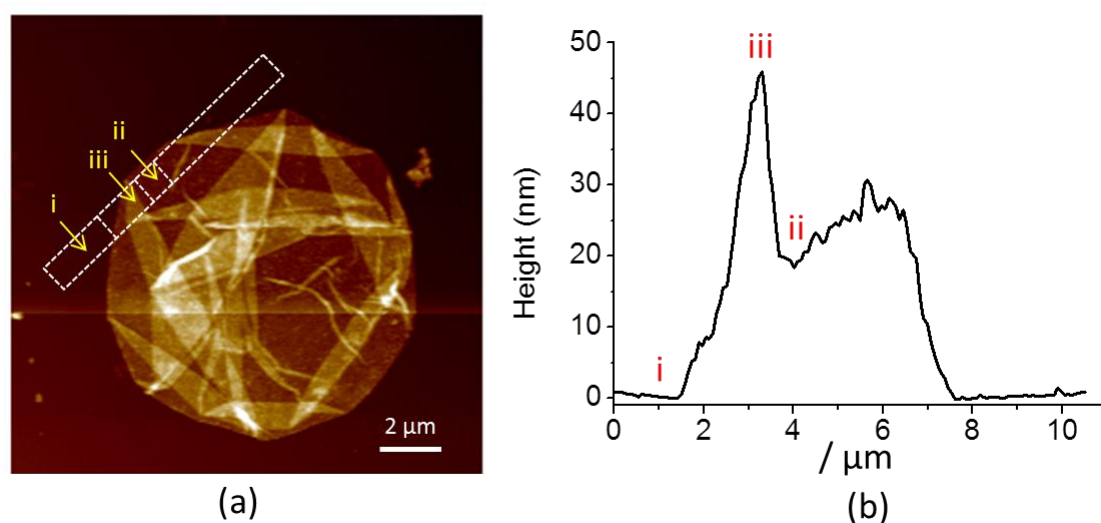
Figure 6.8 (a) AFM image of capsule C1-AuNPs dried on a silicon substrate; (b)
topography along the rectangle marked in (a). The AFM thickness of the capsule is
measured by the difference in the average heights of regions marked with "i" and "ii";
"iii" represents the height of the folded region of the capsule (PeakForce TUNA mode;
1 nN PeakForce; 1 V DC bias; 0.977 Hz scan rate; 512 × 512 pixels).

After normalising, the *I-V* curves on capsule-attached areas shifted to positive voltages by 9 mV compared to the bare amino-terminated monolayer surface (see Figure 6.7 (d)), corresponding to the negatively charged outer layer (PSS) of the capsules. Unlike the case of polyelectrolyte and molecular patterns prepared by μCP, the shift induced by microcapsule attachment occurs in the whole depletion region, which means the charge effect introduced by the presence of microcapsules is homogeneous within the laser spot. The potential shift measured by LAPS is significantly lower than the value of zeta potential (-15.8 mV) of microcapsules. This is thought to be due to the wrinkled feature of the dried capsules, which cannot guarantee a perfect contact with the sensor substrate within the laser focus area, and a gap between capsules and the substrate would cause a decay of the electric potential. Alternatively, minor oxidation may happen on the silicon surface during measurements, resulting in some negatively charged spots and thus a reduction in the potential difference between capsule attached areas and the bare insulator surface.

6.5.3 SPIM imaging of microcapsules C2-AuNPs collapsed on carboxyl-terminated SOS

In order to further confirm the origin of the SPIM images and the potential shift, microcapsules with a positively charged outer layer (C2-AuNPs) combined with a negatively charged sensor substrate (surface A1) were investigated using the same laser. Figure 6.9 (a) shows the SPIM image of a microcapsule cluster collapsed on surface A1 measured at 0.9 V (*vs*. Ag/AgCl). Similar to the result of capsule C1-AuNPs, the SPIM image of C2-AuNPs correlated closely with the optical image (see Figure 6.9 (b)), and a photocurrent drop due to the increase in local impedance was also observed. Furthermore, the lines with low photocurrents on the capsules were even more visible in this case, indicating a higher local impedance and/or a better quality of the insulator. Again, there is a good agreement between lines with low photocurrents and dark lines in the optical image probably caused by folds or overlapping capsules.

The corresponding *I-V* curves measured on capsules (points marked with "1" to "6") and off capsules are presented in Figure 6.9 (c). An average drop (~15%) of the maximum photocurrents was observed at points "1", "2" and "3". However, when measured at the dark lines, more significant drops (~31% at points "4" and "5", ~41% at point "6") of the maximum photocurrents were obtained. After normalising, the curves on capsules (averaged by the results at points "1" to "6") showed a negative shift of 15 mV (see Figure 6.9 (d)) due to the PAH outer layer of the capsules, which is consistent with the zeta potential (12.1 mV).
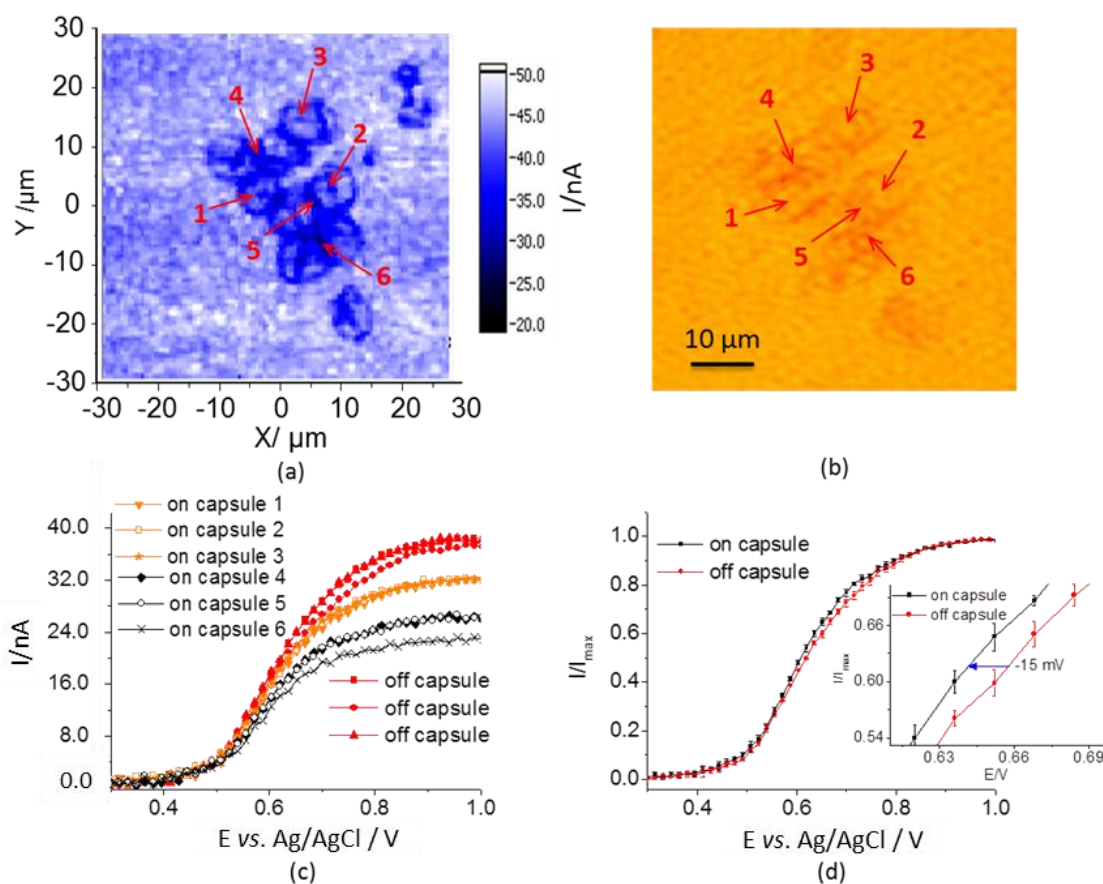
Figure 6.9 Microcapsules C2-AuNPs attached on a COOH-terminated SOS substrate (surface A1); (a) SPIM image measured at 0.9 V (vs. Ag/AgCl, scan range: 60 μm × 60 μm, step size: 0.6 μm, dwell time: 30 ms); (b) corresponding optical image recorded by camera; (c) I-V curves on capsules and on monolayer-modified surfaces; (d) normalised I-V curves: each data point on capsules is an average of the 6 measurements, while off capsules is an average of the 3 measurements. All data points are presented as mean ± SD. 10 mM phosphate buffer solution pH 7.4 containing 137 mM NaCl and 2.7 mM KCl was used.

By using the same method shown in Equation 6.4, the average thicknesses measured at the certain points of capsules were calculated to be ~19 nm (points "1", "2" and "3"), ~48 nm (points "4" and "5") and ~75 nm (point "6"), respectively. Again, AFM was performed to compare these values. The image of C2-AuNPs is shown in Figure 6.10 (a). The wall thickness evaluated from the height profile (see Figure 6.10 (b)) was ~25 nm, which is greater than the value of C1-AuNPs (~19 nm) as expected for the two additional layers of PAH. When comparing the thicknesses measured with SPIM and AFM, points "1"-"3" (~19 nm) correspond to the fold-free regions of capsules with two overlapped shells (~25 nm, "ii" shown in Figure 6.10), while points "4" and

124

"5" (~48 nm) are on the folded regions with four overlapped layers (~51 nm, "iii") and point "6" (~75 nm) is with six layers. These results demonstrated that the dark lines shown in Figure 6.9 (a) indeed corresponded to the creases in the collapsed capsules. It was also shown that a higher impedance of the analytic sample (such as folded capsules with 4 or 6 layers) resulted in a more accurate estimation of the thickness with SPIM.

(a) (b)
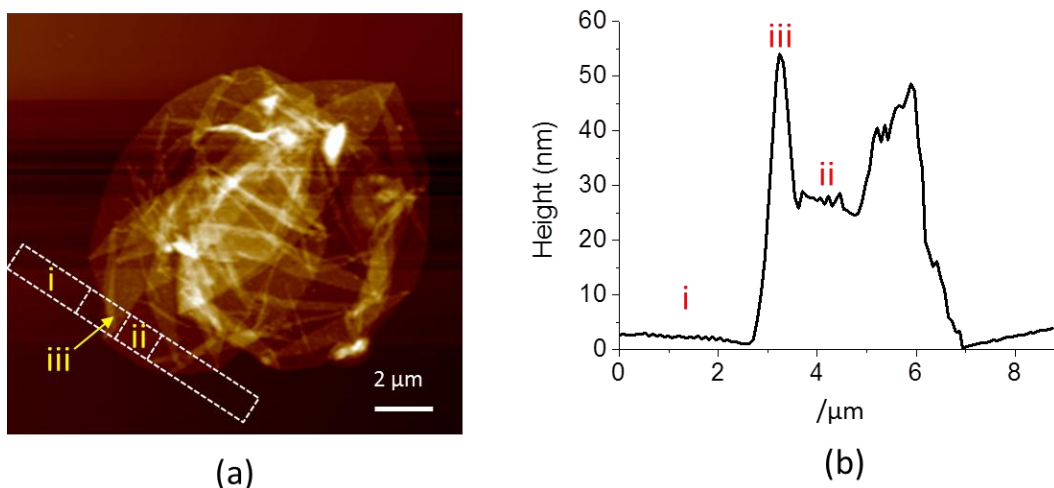
Figure 6.10 (a) AFM image of C2-AuNPs dried on a silicon substrate; (b) topography along the rectangle shown in (a). The AFM thickness of the capsule is measured by the difference in the average heights of regions marked with "i" and "ii"; "iii" represents the height of the folded region of the capsule (PeakForce TUNA mode; 1 nN PeakForce; 1 V DC bias; 0.977 Hz scan rate; 512 × 512 pixels).

6.5.4 The effect of gold nanoparticles on the impedance of microcapsules

SPIM measurements have also been performed with microcapsules C2 collapsed on surface A1 using the femtosecond laser. No impedance changes were observed with the presence of microcapsules, which is completely different from the results obtained with AuNP-modified microcapsules. A similar investigation has been carried out using an EIS sensor to measure the changes in capacitance due to the LBL adsorption of PSS and PAH onto the sensor surface [273]. It was reported that the maximum capacitance for a p-Si-SiO$_2$-Ta$_2$O$_5$ sensor after the adsorption of eight PE layers decreased by only about 0.7 nF cm^{-2} (~0.7%). Based on this result the capacitance of eight bilayers of PSS/PAH (collapsed capsule C2) can be estimated to be 7.1 μF cm^{-2} and a maximum photocurrent drop of 3.5% should be observed with SPIM from Equation 6.4. However,

because of the inhomogeneous silicon layer of the SOS substrate, the maximum photocurrents in the background area always fluctuate in a range of $\pm 5\%$ (see Figure 6.11), which exceeds the effect expected from the attachment of microcapsules. The small capacitance changes are probably due to the loose and porous structure of the polyelectrolyte multilayers [273]. However, if this is the case, a new question is raised: Why can the microcapsules containing gold nanoparticles be imaged with SPIM?
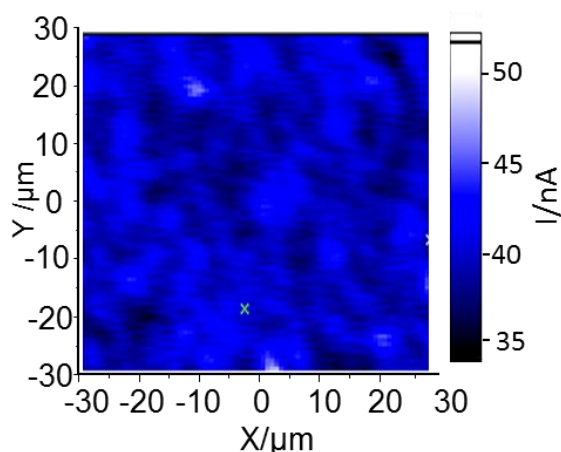
Figure 6.11 SPIM image of a blank COOH-terminated SOS substrate (surface A1) measured at 0.9 V (vs. Ag/AgCl, scan range: 60 μm × 60 μm, step size: 0.6 μm, dwell time: 30 ms). 10 mM phosphate buffer solution pH 7.4 containing 137 mM NaCl and 2.7 mM KCl was used.

To study the effect of the AuNP layer further, local electrical conduction properties of microcapsules C2 and C2-AuNPs were investigated and compared using a conductive-probe AFM. Figure 6.12 illustrates the topography images together with local current images of the two capsules on a silicon substrate. For capsule C2-AuNPs, a clear image of the local current was obtained (see Figure 6.12 (b)), which is in keeping with the morphology shown in (a). The local currents on capsule C2-AuNPs were smaller than the background, indicating a lower conductivity. Figure 6.12 (d) showed no contrast of local currents between capsule C2 and the silicon background, which reveals a higher conductivity and thus a lower impedance compared with the capsule containing gold nanoparticles. These AFM results showed a good agreement with the SPIM measurements presented above.
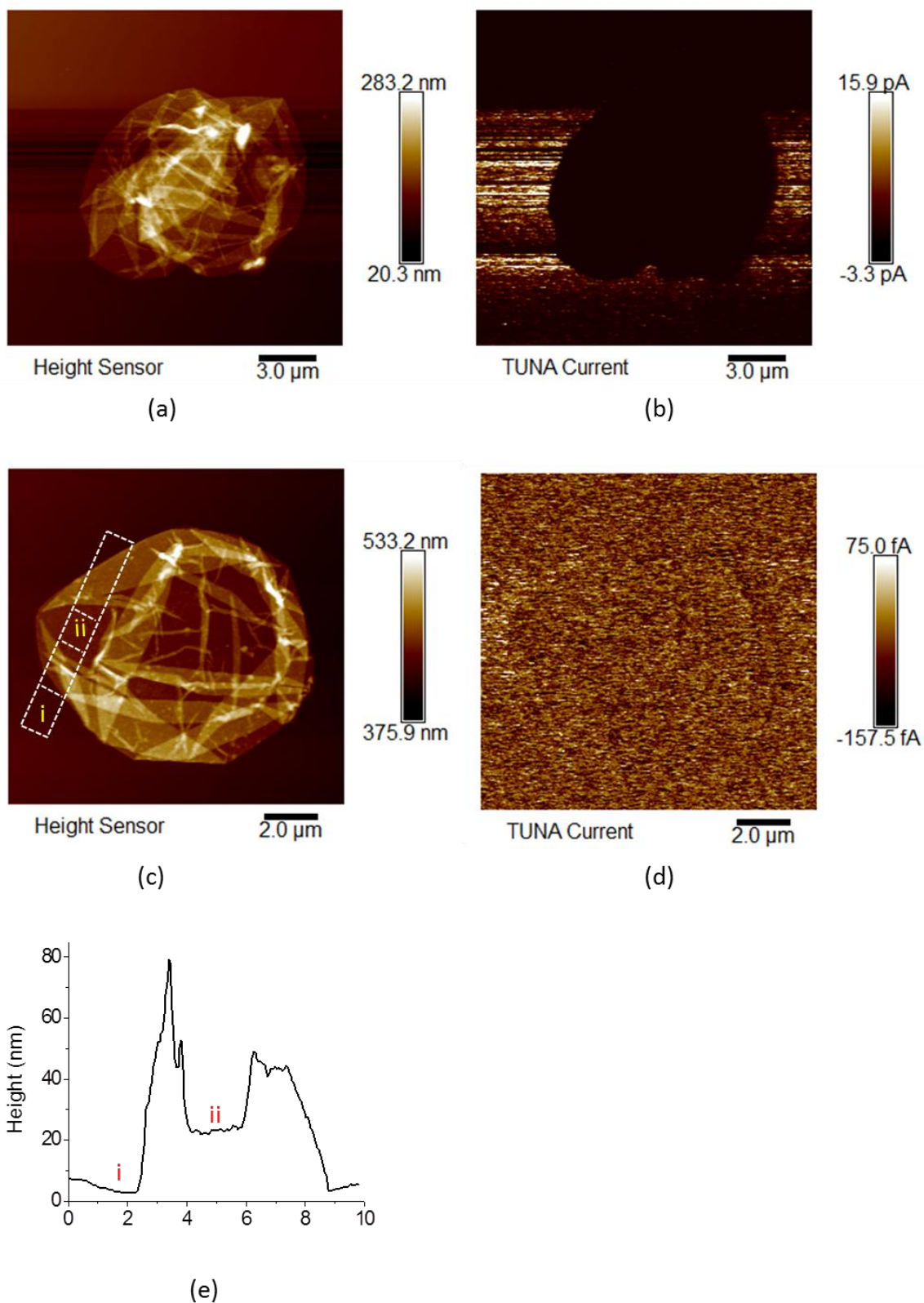
Figure 6.12 AFM images of microcapsules C2-AuNPs: (a) topography image and (b) local current image; microcapsules C2: (c) topography image, (b) local current image and (e) topography profile along the rectangle shown in (c) (PeakForce TUNA mode; 1 nN PeakForce; 1 V DC bias; 0.977 Hz scan rate; 512 × 512 pixels).

Generally, conductive gold nanoparticles on an electrode surface improve the electrochemical kinetics by providing conducting channels that facilitate electron transfer [250, 251]. This is demonstrated in Figure 6.13, which shows the SPIM image of a drop of AuNPs on surface N2 and the corresponding *I-V* curves measured at different points. As expected, the presence of AuNPs on surface N2 resulted in a reduction of local impedance and thus an increase of local maximum photocurrents (see the bright arc area in Figure 6.13 (a)), which is completely different from the results when AuNPs were integrated within polyelectrolyte multilayers.
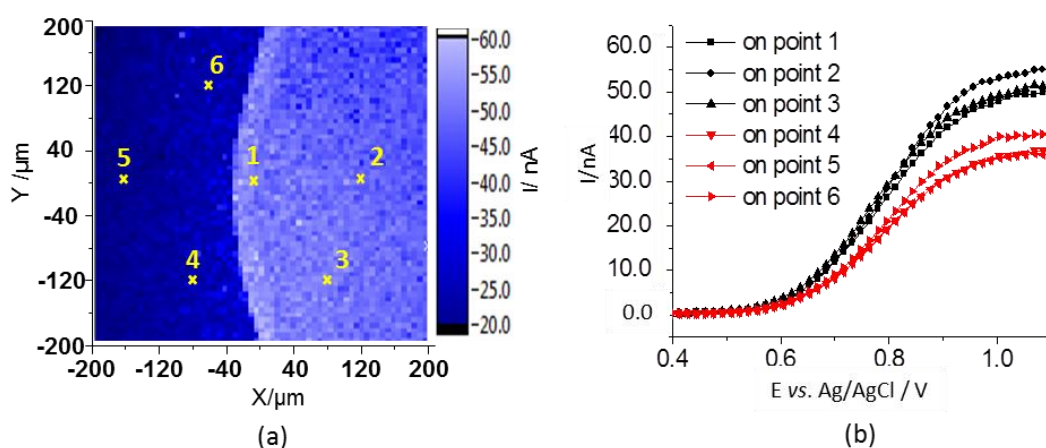
Figure 6.13 (a) SPIM image of an AuNP suspension drop dried on surface N2 and (b) corresponding I-V curves measured at different points marked in (a) ("1"-"3": on the suspension drop, "4"-"6": on the background surface). 10 mM phosphate buffer solution pH 7.4 containing 137 mM NaCl and 2.7 mM KCl was used.

In contrast, it was also reported that the absorption of gold nanoparticles on an electrode can increase the charge transfer resistance in $[Fe(CN)_6]^{-3/-4}$ solution because of the negative charge and steric hindrance of AuNPs [252]. However, in this study, since a PBS buffer without any redox couple was used, the electrostatic repulsion effect should not affect the impedance. Hence, the interactions between AuNPs and polyelectrolytes (PSS and PAH) probably cause the difference. It was reported that the assembly of AuNPs on polyelectrolyte multilayers is driven not only by electrostatic force but also ligand reactions with polyelectrolytes [255]. Hence, the incorporation of AuNPs can change the physical and chemical properties of microcapsules. For example, as shown in this work, the shell thickness of microcapsules increased from ~19 nm (C2, see Figure 6.12 (e)) to ~25 nm (C2-AuNPs, see Figure 6.10 (b)) due to

the addition of an AuNP layer. Similarly, the impedance of microcapsules could also be changed (enhanced) with the presence of AuNPs. Furthermore, since AuNPs were covered and separated by polyelectrolyte chains, these highly dispersed particles (see Figures 6.5 (e) and (f)) may block the pores that exist on the PSS/PAH shell and significantly improve the loose structure, eventually resulting in the increase of impedance of microcapsules. Further investigations are required to fully understand the effect of gold nanoparticles on LBL prepared microcapsules, which are discussed in the chapter relating to proposed future work.

6.6 Summary

It has been shown that the oxide-free Si/SOS surface can be also functionalised with carboxyl-terminated monolayers using CuAAC "click" reactions, further demonstrating a powerful and versatile protocol for silicon-based surface modifications. The success of the "click" functionalisation was demonstrated by contact angle, ellipsometry and XPS measurements.

Polymeric multilayer capsules (PMLCs) with constant size, desirable shell layers and gold nanoparticles were prepared. The hollow nature was demonstrated by optical, SEM and AFM images. The successful labelling with AuNPs was demonstrated by TEM.

Using a femtosecond 1250 nm laser with SAM-modified SOS, pure SPIM images of microcapsules containing AuNPs with high resolution and high sensitivity were obtained. The adhesion of microcapsules on sensor substrates, which was achieved by electrostatic attraction, caused a local impedance increase and thus a photocurrent decrease in inversion. Furthermore, the *I-V* curves on capsules showed voltage shifts after normalisation as the charge of the outer layer. The values of shifts are related to the zeta potentials of the capsules. Using a simple circuit model, it has been shown that the wall thickness of capsule C1-AuNPs derived from SPIM measurements (~22 nm) is comparable to the result measured from AFM (~19 nm). In the case of capsule C2-AuNPs, a higher quality SPIM image was obtained and the SPIM thicknesses measured at different parts of capsules are approximately equal to (~19 nm), double (~51 nm) and triple (~75 nm) the AFM height (~25 nm), indicating that unfolded (two overlapped layers) and folded (four or six overlapped layers) regions of capsules were

characterised, demonstrating that the dark lines with relatively low photocurrents were due to the creases in the collapsed microcapsules.

In contrast, capsules without AuNPs showed no SPIM response at all, which indicates that the impregnation with AuNPs can significantly increase the impedance of the microcapsules. Even though the effect of AuNPs has not yet been fully understood, the impedance variation of capsules with and without AuNPs deduced from SPIM was also verified by AFM conductivity measurements.

7. Imaging of rat B50 neuroblastoma cells using LAPS/SPIM

7.1 Introduction

Neuroelectronic devices are an emerging highly intelligent technology that can transfer information between the human nervous system and semiconductor-based electronics. To make this brain-like system a reality, the neuron-semiconductor interface has to be fully understood, and great progress to this end has been made over the last three decades (see Sections 1.1 and 1.4).

The main focus of this work is to study the local surface potential and impedance of single neural cells with high resolution and high sensitivity. The impedance induced by single cell adhesion can be measured using a field-effect transistor, which has been illustrated in Section 1.4.3. Due to the bilayer phospholipid structure, the surface of cell membrane generally carries net negative charges [297]. It is well known that the negative cell surface potential associates with many cellular interactions including cell adhesion [298], migration and communication [299]. It also interacts with local distributions of ions [300] or charged particles [301]. In addition, the voltage-dependent ionic channel activity is significantly affected by the surface charge density in and near these ion channels [302]. Several methods such as electrophoresis [303] and potentiometric titration [299, 303] have been developed to measure cell surface charge. However, these measurements can only apply to a cell suspension and the obtained results are often related to average properties over the entire cell membrane.

LAPS/SPIM overcomes these problems. The advantages and applications of LAPS as a cell-based biosensor have been described in Sections 1.1 and 1.3.5.4. In particular, the introduction of a new insulator - SAMs, which can modify and functionalise the silicon surface in a controllable way, makes field-effect devices even more attractive and promising cell-based biosensors. In Chapter 6, a two-photon effect strategy using a femtosecond 1250 nm laser was proposed for high resolution imaging of hollow microcapsules, with a comparable size (~10 μm) to single cells, which have been used as a surrogate to simulate cell adhesion behaviour.

In this chapter, the two-photon strategy was further advanced in photocurrent measurements. That is, to develop a combined technique that can be used to produce not only local electrochemical images but also a fluorescent image originating from the

same microenvironment. In principle, a fluorescent dye is excited by a near infrared laser, resulting in visible light due to two-photon absorption. In LAPS/SPIM, the visible light can facilitate the generation of more electron/hole pairs in the space charge layer of silicon, thus significantly enhancing the local photocurrent output. This technique is aimed to broaden the application of LAPS/SPIM in the field of single cell imaging and sensing, by relating the local distributions of extracellular potentials and cell impedance to cell morphology and cytoskeleton.

Due to long-standing practical problems with the 1250 nm femtosecond laser, a continuous wave IR laser (1064 nm) and a blue laser (405 nm) were employed for two-photon-excited fluorescence imaging and electrochemical imaging of single neuronal cells. It will be shown that this sensor system is promising for the production of two-dimensional electrochemical images of parameters such as local cell impedance under the opening or closing of ion channels, membrane-surface potential and two-photon fluorescent images of the cell-attachment area with subcellular resolution.

7.2 Experimental section

All the chemicals and reagents used in this chapter, unless noted otherwise, were as listed in Chapter 2. Rat B50 neuroblastoma cells were provided by Professor Gleb B. Sukhorukov's group and were originally purchased from Sigma. Tetraethylammonium chloride (TEA, BioUltra, $\geq$ 99%), 4-aminopyridine (4-AP, $\geq$ 99%) and reagents for cell culture including Dulbecco's Modified Eagles Media (DMEM), Fetal Bovine Serum (FBS), penicillin, L-glutamine, trypsin, Dulbecco's Phosphate Buffered Saline (DPBS) and glucose were purchased from Sigma-Aldrich. Vybrant® DiI (λ_{ex} = 549 nm, λ_{em} = 565 nm) for cell labelling was purchased from Lifetechnologies, UK. Syringe filters with 0.2 μm pore size for sterile filtration were purchased from VWR.

The method for "click" functionalisation with azido-OEG-NH$_2$ of a 1, 8-nonadiyne monolayer-modified SOS substrate (surface N2) was as described in Section 2.2.2. All solutions used for cells were prepared with sterilized ultra-pure water, and filtered with syringe filters.

7.2.1 Cell culture

Rat B50 neuroblastoma cells were cultured in 75 cm^2 flasks in a culture medium including DMEM base supplemented with 10% FBS, 1% penicillin and 0.1% L-

glutamine, in a humidified incubator containing 5% CO_2 at 37 ℃. For passaging, cells were detached from the flask by incubating with 10% trypsin in DPBS for 5 min. Prior cell seeding, the sensor substrate (surface N2) and LAPS chamber were sterilized with 70% EtOH then rinsed with sterilized pure water and blown dry. Cell suspension with culture medium was transferred to the sensor substrate at a cell density of ~10^5 m^{-2}.

7.2.2 Cell staining

Since the fluorescence excitation wavelength (λ_{ex} = 549 nm) is close to half that of the IR laser (1064 nm), Vybrant® DiI was used to stain cells for two-photon absorption. According to the manufacturer's instructions, a staining medium was prepared by adding 5 µl of the supplied dye labelling solution to 1 ml of normal culture medium. Then cells attached on the sensor substrate were incubated with the staining medium for 15 min at 37 ℃. Finally, cells were washed three times with DPBS to remove unlabelled dye.

7.2.3 Cell measurements using LAPS/SPIM

The experimental set-up for photocurrent measurements has been shown in Section 2.4. Measurements were performed about 24 h after cell seeding on the sensor substrate. The cell culture medium was substituted with a test buffer: 20 mM HEPES buffer solution pH 7.4 containing 137 mM NaCl, 2.7 mM KCl, 1 mM $MgCl_2$, 0.9 mM $CaCl_2$ and 10 mM glucose. A 405 nm laser was used for electrochemical imaging (see light profile "a" in Figure 2.6) and a 1064 nm laser was used to produce fluorescent images (see light profile "b" in Figure 2.6). Meanwhile, a digital camera was used to take *in situ* optical images (see light profile "c" in Figure 2.6).

To detect the cell response to high concentrations of calcium, 20 mM $CaCl_2$ was added to the test buffer. In another experiment, K$^+$ channel blockers (10 mM TEA and 500 µM 4-AP) were used to stimulate cells. In both cases, photocurrents on and off the cell attached regions were recorded before and after the adding the stimulus using the 405 nm laser.

7.3 Electrochemical and fluorescence imaging of B50 neuroblastoma cells

Figure 7.1 shows the optical and fluorescent images of Vybrant® DiI-labelled rat B50 cells growing on the sensor substrate (surface N2). A good adhesion of cells was

observed, indicating the suitability of the substrate for cell culture. The average size of cells is about 20-30 μm, which is much greater than the SPIM resolution (~2.2 μm), and thus making subcellular imaging possible.

(a)   (b)
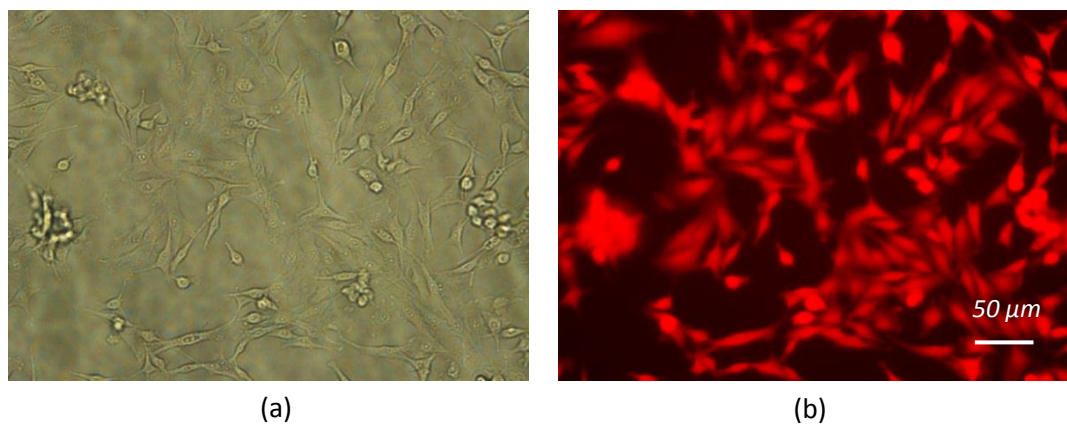
Figure 7.1 Images of rat B50 cells growing on an amino-terminated SOS substrate using (a) an optical microscope and (b) a fluorescence microscope.

The correlation between the photocurrent images measured with 405 nm and 1064 nm lasers and the optical image recorded by camera has been calibrated and demonstrated in Chapter 6 (see Figure 6.4). At 405 nm, as most of the light is absorbed by the silicon, the direct interaction between the laser and the fluorescent dye is excluded, thus resulting in a pure SPIM image of a single neural cell (see Figure 7.2 (a)). The photocurrents on the cell attachment area were lower than on the bare organic monolayer. The corresponding *I-V* curves measured at points "A" and "B" illustrated that cell adhesion led to a ~28% decrease of the maximum photocurrents (see Figure 7.2 (b)), indicating the effect of the cell-induced impedance. After normalising, the *I-V* curve measured at "B" showed a positive shift of ~90 mV(see the inset of Figure 7.2 (b)), which is due to the negative surface charge of cells [301]. The appearance of a step in the *I-V* curve in the cell attachment area resulted in uneven shifts within depletion region, which is similar to the behaviour observed with polyelectrolyte patterns. As mentioned in Section 1.4, cells attach to the extracellular matrix through the link of the transmembrane adhesion proteins and the substrate. It means that within a laser spot, some areas of the cell may be on focal attachment while some areas may be not, which can cause the uneven *I-V* shifts. In addition, the interactions between the adhesion proteins and the substrate cause a cleft between the cell and matrix. The width of the cleft may differ in different parts of a cell, which can be another reason for the step in *I-V* curves and the uneven shifts.
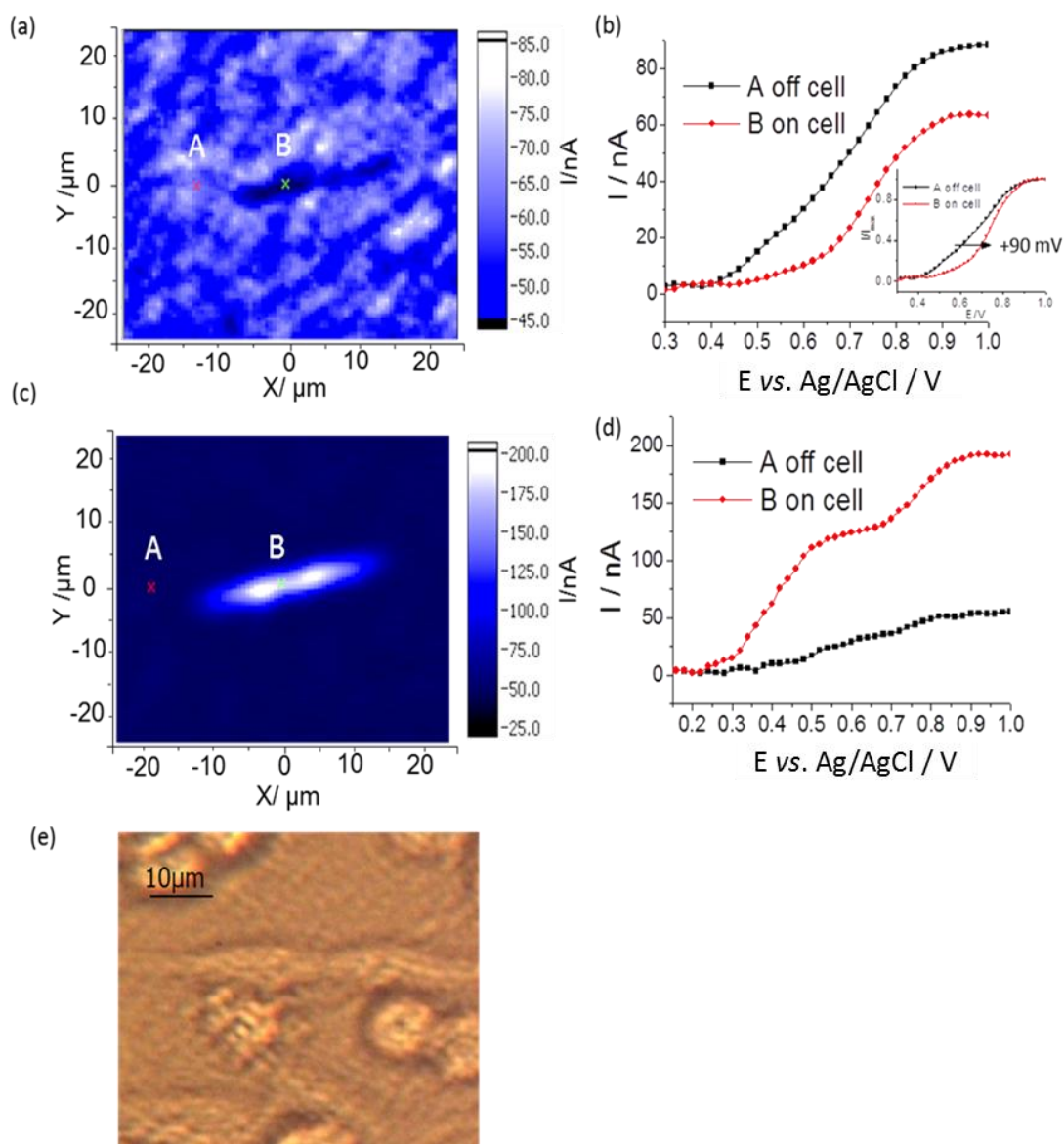
Figure 7.2 Vybrant® DiI-labelled rat B50 neural cell cultured on surface N2: (a) SPIM image and (b) corresponding I-V curves (inset: after normalised) using a 405 nm laser; (c) two-photon fluorescent image and (d) corresponding I-V curves using a 1046 nm laser; (e) real-time optical image recorded by camera. 20 mM HEPES buffer solution pH 7.4 containing 137 mM NaCl, 2.7 mM KCl, 1 mM MgCl$_2$, 0.9 mM CaCl$_2$ and 10 mM glucose was used for photocurrent measurements.

In contrast, when a 1064 nm laser was employed to address the same area of the substrate, as expected, in places where the cell was attached to the monolayer surface, the photocurrents were greatly enhanced compared to the bare monolayer surface due to the additional fluorescence signal (Figure 7.2 (c)). The fluorescent image is in good agreement with the SPIM image in terms of the size and the shape of the cell. The significant increase of local photocurrents made the cell easier to identify. Since the

1064 nm laser can penetrate the 1 μm thick silicon, it can interact with the dye within the cells. A two-photon absorption of the dye results in the local emission of visible light (~565 nm). This visible light can work as an additional light source to trigger much larger photocurrents in silicon than for those places excited by 1064 nm laser only. Hence, a pure fluorescent image of the labelled cell is produced, which means the semiconductor substrate is effectively used as a fluorescence detector in SPIM. The principle of the photocurrent enhancement effect is shown in Figure 7.3. When an IR laser illuminates a fluorescent dye-labelled cell, two photons can be absorbed simultaneously resulting in an emission of fluorescence. This fluorescence with a visible wavelength works as an additional light source from the front side of the silicon, and effectively induces the local generation of electron/hole pairs in the space charge layer of silicon. According to the principle of LAPS, the local photocurrent output can be significantly enhanced and thus a fluorescent cell image can be obtained.

The corresponding *I-V* curves are given in Figure 7.2 (d), which again showed a step in cell attachment area. In order to confirm that the two images shown in Figures 7.2 (a) and (c) were actually from a cell, an optical image (see Figure 7.2 (e)) was taken at the same position using the camera integrated into the set-up. Interestingly, unlike the case of microcapsules, the morphology of the cell observed from the camera is related but not identical to the photocurrent images. This may be due to the fact that the interaction mechanism between cell and surface is much more complicated than that between microcapsule and substrate. It indicates that our LAPS/SPIM system may be able to image the effective cell attachment sites and distinguish them from the cell optical image.
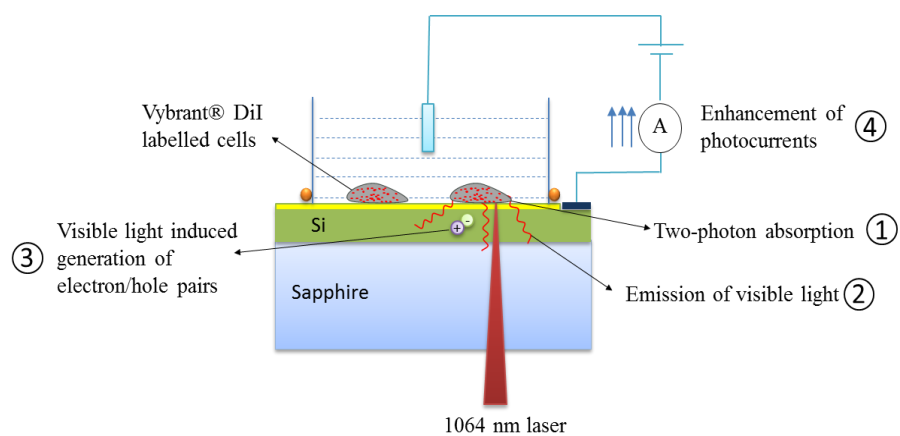
Figure 7.3 Representation of the enhancement of photocurrents due to two-photon absorption effect.

7.4 Cell responses to high Ca^{2+} and K^+ channel blockers

Cell responses to high Ca^{2+} stimulation were recorded using photocurrent measurements with the 405 nm laser. From the results shown in Figure 7.4, it can be seen that a high concentration of Ca^{2+} (20 mM) in the testing solution caused an increase in the maximum photocurrents and thus a decrease in local impedance in the cell attachment area. This may be due to either a weaker cell adhesion or a higher membrane conductance after the addition of Ca^{2+}. It is well known that a small amount of Ca^{2+} facilitates the attachment of cells to extracellular matrix by modulating the function of adhesion molecules such as integrins. Hence, 0.9 mM $CaCl_2$ was included in the test buffer solution to facilitate cell attachment. In contrast, a high concentration of Ca^{2+} (for example: 20 mM) weakens the cell adhesion to the substrate [304, 305] and this could be a reason for the increase of maximum photocurrents shown here.

Furthermore, the normalised *I-V* curve in the cell attachment area showed a negative shift of ~22 mV due to the high Ca^{2+} stimulation. This may be because the negative cell surface charge is partially neutralised by the high concentration of extracellular calcium ions. Hahin and Campbell have reported a similar result for high Ca^{2+} stimulation [302]. In their experiments, Na^+ and gating currents, which are voltage-sensitive, were recorded before and after the addition of 40 mM Ca^{2+}, and a voltage shift of around -30 mV was measured [302], which is comparable to the result obtained in this work. As a control, a place without cell attachment was also measured and only a very small shift the of *I-V* curve was observed after the addition of 20 mM Ca^{2+}. The small variation may be due to the voltage drift or inevitable error during the measurements.
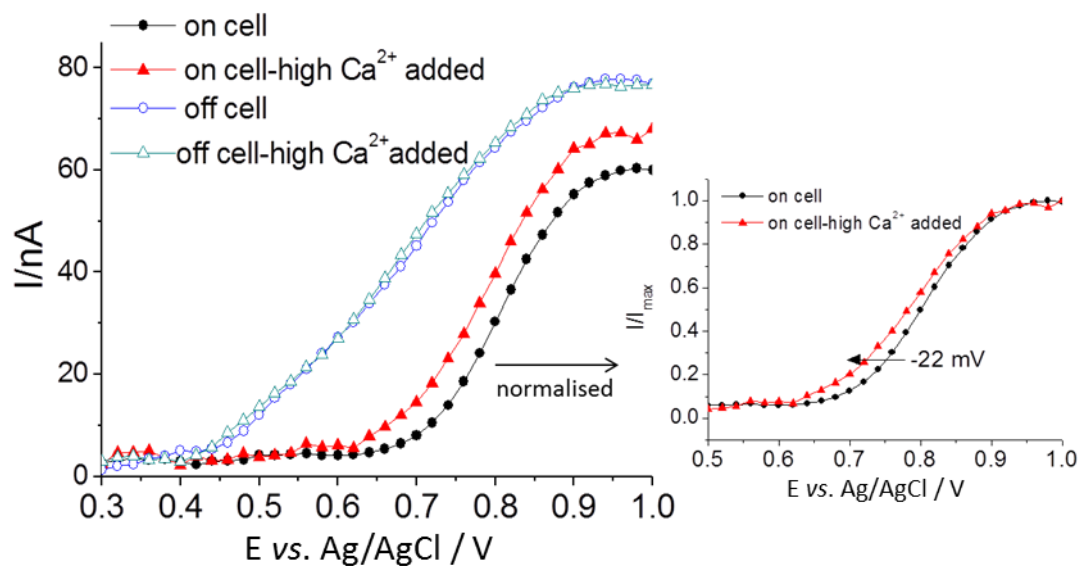
Figure 7.4 I-V curves on and off the cell attachment areas before and after the addition of 20 mM CaCl$_2$ aqueous solution to 20 mM HEPES buffer pH 7.4 containing 137 mM NaCl, 2.7 mM KCl, 1 mM MgCl$_2$, 0.9 mM CaCl$_2$ and 10 mM glucose.

In another experiment, cell responses to K$^+$ channel blockers were recorded using the same laser. To obtain more information, photocurrent-frequency (*I-f*) curves were measured in inversion (0.9 V, *vs*. Ag/AgCl). Figure 7.5 shows the *I-f* results with the addition of K$^+$ channel blockers (10 mM TEA and 500 μM 4-AP) [306]. It can be seen that the maximum photocurrents in the cell attachment area decreased within the frequency range of 1-10 kHz after the addition of the stimulus. This change in impedance is due to the fact that after the blockage of ion channels the cell membrane becomes less permeable to ions and thus less conductive [307]. However, when the light modulation frequency is very high (e.g. > 10 kHz), the effects of the drug stimulation on the spectra become less obvious. This indicates that the sensitivity of SPIM to the activity of living cells is frequency-dependent, which is analogous to the results from cell-based FETs [132]. As expected, the signals off the cell showed negligible changes in the maximum photocurrents over the whole range of frequencies.
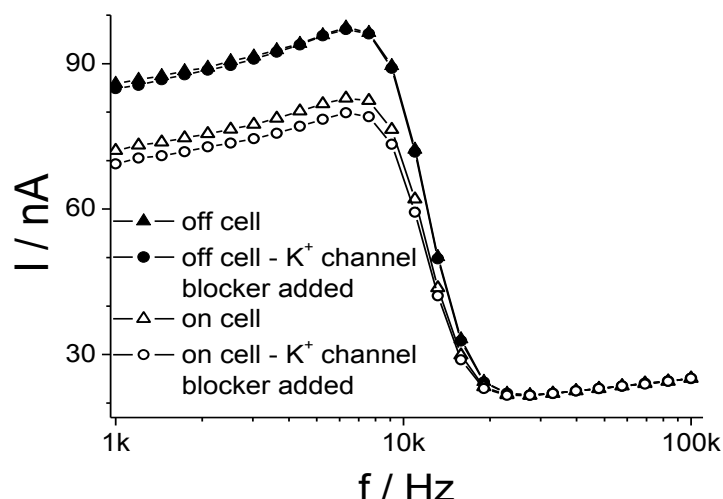
Figure 7.5 I-f spectra at 0.9 V (vs. Ag/AgCl) on the cell (solid symbols) and off the cell attachment area (open symbols) before (triangles) and after (circles) the addition of K^+ channel blocker (10 mM TEA and 500 μM 4-AP) to 20 mM HEPES buffer solution pH 7.4 containing 137 mM NaCl, 2.7 mM KCl, 1 mM $MgCl_2$, 0.9 mM $CaCl_2$ and 10 mM glucose.

7.5 Summary

Preliminary work on rat B50 neuroblastoma cell imaging and drug-induced cell responses using LAPS/SPIM has been carried out. B50 cells were successfully cultured on the amino-terminated SAM-modified SOS substrates without an additional bio-anchor. Electrochemical and fluorescent images for a single neural cell were obtained using the new combined technique with two different laser wavelengths. The corresponding *I-V* curves measured with the 405 nm laser showed a reduction of the maximum photocurrents in the cell attachment area, indicating the increase of local impedance due to cell adhesion. Meanwhile, a positive shift of the curves along voltage axis was observed, which can be explained by the effect of the negative surface charge of neurons. The fluorescent image measured with the 1064 nm laser showed much higher photocurrents in the cell attachment area due to the two-photon absorption by the dye and subsequent emission of visible light.

Furthermore, cell responses to high Ca^{2+} and K^+ channel blockers were investigated using photocurrent measurements. From *I-V* curves, a high concentration of calcium (20 mM) not only partially neutralised the negative surface charges of cells, but also weakened their adhesion to the substrate. The effect of K^+ channel blockers on *I-f*

curves indicated that SPIM may be capable of recording the activity of ion channels due to the local impedance sensitivity.

Initial results of cell imaging look promising. However, the reproducibility and sensitivity of the combined technique have to be further investigated and improved. Many factors can affect the results, such as the state of the cell, the external environment (temperature and atmosphere components), the properties of the substrate and the quality of the insulator (SAMs). In this work, all cell measurements were carried out in an open environment, which means neither temperature nor CO_2 concentration meets the optimum condition for maintenance of cell viability. In addition, since cells were cultured in a medium supplemented with 10% serum, a layer of proteins may deposit on the sensor surface and cause non-negligible effects on cell signalling and sensing. More discussions about problems and future work will be presented in more detail in the following chapter.

8. Conclusions

A new insulator - a self-assembled organic monolayer (SAM) - was introduced into the LAPS/SPIM system for the first time. The study has shown that using SAMs, which were assembled on oxide-free silicon-on-sapphire (SOS) surfaces, a comparable spatial resolution to the use of the traditional insulator (SiO_2) has been obtained. Furthermore, due to the ultrathin insulator, a high accuracy of LAPS and a high sensitivity of SPIM have also been achieved.

The work started with the modification of H-SOS or H-Si substrates with alkyl monolayers of undecylenic acid and 1-octadecene using a thermal hydrosilylation. The presence of monolayers on SOS or Si was demonstrated by water contact angle, ellipsometry and XPS measurements. Minor SiO_x emissions were observed from the XPS results. A small leakage current density (~0.7 $\mu A\ cm^{-2}$) measured in inversion and a high capacitance (~1.7 $\mu F\ cm^{-2}$) of the undecylenic acid monolayer indicated the suitability of the organic monolayers as an insulator. LAPS/SPIM measurements with a 405 nm laser using undecylenic acid-modified SOS displayed a high spatial resolution (~2.2 μm). It was clearly demonstrated that the improvement of the sensitivity of SPIM is mainly due to the employment of an organic monolayer with high capacitance as the insulator.

Based on the initial success of the alkyl monolayers, another powerful and versatile protocol involving 1, 8-nonadiyne monolayer immobilisation and its further functionalisation via the CuAAC "click" reaction was introduced. Encouragingly, no oxidation of the underlying silicon was observed from XPS measurements, indicative of a better way to achieve a high quality of organic monolayers on SOS or Si rather than the assembly of alkyl monolayers. The high performance of LAPS was validated using a PAH/PAH-DNA pattern and a PSS pattern, which were prepared on COOH-terminated and NH_2-terminated SOS, respectively, using microcontact printing (μCP). Clear LAPS images for the three patterns due to surface charge effects were obtained. The adsorption of PAH (positively charged) caused a higher photocurrent and a negative voltage shift in the lower part of *I-V* curve in depletion, compared to the bare undecylenic acid monolayer. In contrast, the presence of negatively charged DNA and PSS resulted in a lower photocurrent as well as a positive voltage shift. The partial shifts in the depletion region of the *I-V* curves resulted from the incomplete coverage with polyelectrolytes on the sensor surface, which was confirmed by AFM images.

This indicates that LAPS may be able to determine the coverage of charged polymers, DNA or other biomolecules.

During the investigation of potential strategies for chemically patterning SAMs on oxide-free SOS or Si substrates, LAPS was also found to be extremely sensitive to chemically bonded molecular patterns and surface contamination introduced by photolithography, which may broaden the application of LAPS from a sensor technique to a characterisation tool for SAM-modified silicon substrates. It was shown that μCP followed by "click" chemistry is a mild and efficient means for molecular patterning whereas the combination of photolithography and "click" chemistry is not. As evidenced by XPS spectra, the integrity of 1, 8-nonadiyne monolayer was compromised after photoresist processing. In addition, the surface characterisation results and LAPS images demonstrated that side-reactions between the photoactive compounds in the photoresist and SAMs occurred, causing undesirable chemical contamination of the surface. In contrast, μCP was shown to be an effective method to chemically pattern alkyne-terminated monolayers through "click" reactions. The "click" efficacy was comparable to that of a conventionally formed "click" monolayer, although with a much shorter reaction time (3 h c.f. 24 h). More importantly, no evidence of surface contamination with SiO_x was observed after μCP-induced "click" reactions. The successful chemical patterning was validated using LAPS, indicating the capability of LAPS for measuring surface charge effects induced by the chemically bonded NH_2-terminated molecules.

Following the demonstration of LAPS imaging, the performance of SPIM was also investigated using a femtosecond 1250 nm laser with SAM-modified SOS. Instead of regular patterns, polymeric multilayer capsules (PMLCs), which were randomly attached to SAM-modified SOS through electrostatic attraction, were used as the model system for validation. Pure SPIM images of microcapsules containing gold nanoparticles (AuNPs) with different outer layers (PSS and PAH) were obtained. It was shown that the adhesion of microcapsules caused a local impedance increase and thus a photocurrent decrease in inversion. The whole *I-V* curves on capsules showed voltage shifts after normalisation due to the charge of the outer layer and the values of the shifts were related to the zeta potentials of the capsules. Using a simple circuit model, it has been shown that the wall thicknesses of the fold-free and folded regions of capsules derived from SPIM measurements are comparable to the results measured

by AFM. Conversely, capsules without AuNPs showed no SPIM response at all, which means that the impregnation of gold nanoparticles in microcapsules significantly increased the impedance. The impedance variation of capsules was also verified by conductive AFM measurements.

Finally, a new combined technique which can provide both electrochemical and fluorescent images scanned with two different lasers has been developed. Using this technique, preliminary work on rat B50 neuroblastoma cell imaging and drug-induced cell responses has been carried out. B50 cells were successfully cultured on the amino-terminated SAM-modified SOS substrates without an additional bio-anchor. Electrochemical images due to cell adhesion were obtained using a single-photon excitation of photocurrents at 405 nm, while fluorescent images of the same cell were obtained using a 1064 nm laser. The latter showed a significant increase in the local photocurrent due to the two-photon absorption by a fluorescent dye within the cells. Furthermore, cell responses to high Ca^{2+} and K^+ channel blockers stimulations were investigated using the 405 nm laser. After the addition of 20 mM Ca^{2+}, the maximum photocurrents increased and the *I-V* curves negatively shifted along voltage axis, which means that a high concentration of Ca^{2+} weakens the cell adhesion to the substrate and partially neutralises the negative cell surface charges. The effect of K^+ channel blockers on *I-f* curves indicated that SPIM may be applicable to record the activity of ion channels due to the local impedance sensitivity.

9. Future work

To go further with this project, there still remains a lot of work to do. Regarding the insensitivity of LAPS/SPIM to microcapsules without AuNPs (see Section 6.5.4), a more homogeneous substrate such as SOI could be used instead of SOS. The effect of AuNPs on the impedance of microcapsules needs to be further studied, probably by changing the doping density, doping position within the shell, the size and the shape of the gold nanoparticles.

In terms of the new combined technique proposed in Chapter 7, further investigations are inevitably required to improve the reproducibility and controllability of the experiments. This is particularly so for the continuous wave IR laser (1064 nm) excitation, as the probability of simultaneous absorption of two photons is extremely low compared to the femtosecond laser (1250 nm). Since the technical problems with the femtosecond laser have been resolved very recently, it should be the preferred option for fluorescence imaging. Many factors can affect the success of fluorescence imaging, such as the dye concentration and distribution within cells, the contact area and distance between cells and the sensor substrate as well as the laser intensity and quality of the focus. Besides the application of providing high-resolution images of cell morphology and cytoskeleton, the two-photon effect strategy combined with LAPS/SPIM can also be used as a fluorescence detector to access the cell-matrix adhesion sites which cannot be imaged by other more traditional instruments, such as image ion channel activities, focal adhesion or extracellular potentials.

As stated above, the introduction of a 1, 8-nonadiyne monolayer on hydrogen-terminated silicon surfaces allows facile and diverse modifications of the surface using CuAAC "click" reactions. Besides the modifications with molecules terminated with amino or carboxyl functional groups that have been performed in this work, "click" reactions are also capable of directly attaching various target biomolecules (i.e. DNA, peptides and aptamers) to silicon surfaces. For example, DNA molecules can be assembled on SOS or Si substrates and subsequently, with the combination of LAPS/SPIM, a label-free and reusable DNA array to detect hybridization and dehybridization due to the charge effect could be fabricated.

Another potential application is to develop a high-sensitivity cell-based biosensor using modified substrates; examples include a LAPS substrate modified with an RGD

peptide, which is of benefit for cell adhesion, or a substrate assembled with aptamers with specificity to target integrin heterodimers to capture cells by affinity interaction between aptamers and target cells. In both cases, it is possible to bind cells to SOS substrates in the absence of proteins (serum), which will improve the communication between the cells and the sensor surface. The RGD peptide immobilisation on SOS substrates has been achieved and initial progress on cell experiments has been made within our group. The work on aptamers is currently being undertaken within our group as well.

Finally, based on the patterning strategy ("click" chemistry with µCP) that has been established in this work, several biomolecules of interest could be incorporated in a highly controlled way onto the same SOS or Si substrate. For example, with an array functionalised with different DNA sequences, a high throughput multi-spot DNA sensor could be fabricated.

10. References

[1] R. Gleixner, P. Fromherz, The extracellular electrical resistivity in cell adhesion, Biophysical Journal, 90(2006) 2600-11.

[2] D. Braun, P. Fromherz, Imaging neuronal seal resistance on silicon chip using fluorescent voltage-sensitive dye, Biophysical Journal, 87(2004) 1351-9.

[3] D. Koppenhofer, A. Susloparova, D. Docter, R.H. Stauber, S. Ingebrandt, Monitoring nanoparticle induced cell death in H441 cells using field-effect transistors, Biosensors and Bioelectronics, 40(2013) 89-95.

[4] A. Lambacher, M. Jenkner, M. Merz, B. Eversmann, R. Kaul, F. Hofmann, R. Thewes, P. Fromherz, Electrical imaging of neuronal activity by multi-transistor-array (MTA) recording at 7.8 μm resolution, Applied Physics A, 79(2004) 1607-11.

[5] B. Straub, E. Meyer, P. Fromherz, Recombinant maxi-K channels on transistor, a prototype of iono-electronic interfacing, Nature Biotechnology, 19(2001) 121-4.

[6] A. Susloparova, D. Koppenhofer, X.T. Vu, M. Weil, S. Ingebrandt, Impedance spectroscopy with field-effect transistor arrays for the analysis of anti-cancer drug action on individual cells, Biosensors and Bioelectronics, 40(2013) 50-6.

[7] R. Weis, P. Fromherz, Frequency dependent signal transfer in neuron transistors, Physical Review E, 55(1997) 877-889.

[8] P. Fromherz, S. Eick, B. Hofmann, Neuroelectronic interfacing: semiconductor chips with ion channels, nerve cells, and brain, Nanoelectronics and Information Technology: Advanced Electronic Materials and Novel Devices, Wiley-VCH2012, pp. 781-810.

[9] B. Stein, M. George, H.E. Gaub, W.J. Parak, Extracellular measurements of averaged ionic currents with the light-addressable potentiometric sensor (LAPS), Sensors and Actuators B: Chemical, 98(2004) 299-304.

[10] A. Lambacher, V. Vitzthum, R. Zeitler, M. Eickenscheidt, B. Eversmann, R. Thewes, P. Fromherz, Identifying firing mammalian neurons in networks with a high-resolution multi-transistor array (MTA), Applied Physics A, 102(2011) 1-11.

[11] P.H. Chen, X.D. Liu, B.Q. Wang, G. Cheng, P. Wang, A biomimetic taste receptor cell-based biosensor for electrophysiology recording and acidic sensation, Sensors and Actuators B: Chemical, 139(2009) 576-83.

[12] L.P. Du, C.S. Wu, H. Peng, L.H. Zhao, L.Q. Huang, P. Wang, Bioengineered olfactory sensory neuron-based biosensor for specific odorant detection, Biosensors and Bioelectronics, 40(2013) 401-6.

[13] N. Hu, C.X. Wu, D. Ha, T.X. Wang, Q.J. Liu, P. Wang, A novel microphysiometer based on high sensitivity LAPS and microfluidic system for cellular metabolism study and rapid drug screening, Biosensors and Bioelectronics, 40(2013) 167-73.

[14] L. Chen, Y. Zhou, S. Jiang, J. Kunze, P. Schmuki, S. Krause, High resolution LAPS and SPIM, Electrochemistry Communications, 12(2010) 758-60.

[15] Y. Liu, S. Yamazaki, S. Yamabe, Y. Nakato, A mild and efficient Si (111) surface modification via hydrosilylation of activated alkynes, Journal of Materials Chemistry, 15(2005) 4906-13.

[16] H. Asanuma, E.M. Bishop, H.-Z. Yu, Electrochemical impedance and solid-state electrical characterization of silicon (111) modified with ω-functionalized alkyl monolayers, Electrochimica Acta, 52(2007) 2913-9.

[17] S. Ciampi, J.B. Harper, J.J. Gooding, Wet chemical routes to the assembly of organic monolayers on silicon surfaces via the formation of Si-C bonds: surface preparation, passivation and functionalization, Chemical Society Reviews, 39(2010) 2158-83.

[18] L. Touahir, P. Allongue, D. Aureau, R. Boukherroub, J.N. Chazalviel, E. Galopin, A.C. Gouget-Laemmel, C.H. de Villeneuve, A. Moraillon, J. Niedziółka-Jönsson, F. Ozanam, J.S. Andresa, S. Sam, I. Solomon, S. Szunerits, Molecular monolayers on silicon as substrates for biosensors, Bioelectrochemistry, 80(2010) 17-25.

[19] G.-J. Zhang, M.J. Huang, J.A.J. Ang, E.T. Liu, K.V. Desai, Self-assembled monolayer-assisted silicon nanowire biosensor for detection of protein–DNA interactions in nuclear extracts from breast cancer cell, Biosensors and Bioelectronics, 26(2011) 3233-9.

[20] R. Voicu, R. Boukherroub, V. Bartzoka, T. Ward, J.T.C. Wojtyk, D.D.M. Wayner, Formation, Characterization, and chemistry of undecanoic acid-terminated silicon surfaces: patterning and immobilization of DNA, Langmuir, 20(2004) 11713-20.

[21] http://www.iue.tuwien.ac.at/phd/wittmann/node7.html.

[22] http://ecee.colorado.edu/~bart/book/book/chapter2/ch2_6.htm#fig2_6_1.

[23] http://pvcdrom.pveducation.org/SEMICON/ABSDEPTH.HTM.

[24] http://www.bog5.in.ua/lection/quantum_optics_lect/lect3_quant_eng.html.

[25] B. Sapoval, C. Hermann, Physics of Semiconductors: Springer New York; 2003.

[26] http://ecee.colorado.edu/~bart/book/book/chapter6/ch6_2.htm.

[27] S.M. Sze, K.K. Ng, Physics of semiconductor devices: John Wiley & Sons; 2006.

[28] I. Lundström, S. Shivaraman, C. Svensson, L. Lundkvist, A hydrogen– sensitive MOS field–effect transistor, Applied Physics Letters, 26(1975) 55-7.

[29] I. Lundström, M. Shivaraman, C. Svensson, A hydrogen-sensitive Pd-gate MOS transistor, Journal of Applied Physics, 46(1975) 3876-81.

[30] I. Lundström, H. Sundgren, F. Winquist, M. Eriksson, C. Krantz-Rülcker, A. Lloyd-Spetz, Twenty-five years of field effect gas sensor research in Linköping, Sensors and Actuators B: Chemical, 121(2007) 247-62.

[31] A. Spetz, U. Helmersson, F. Enquist, M. Armgarth, I. Lundström, Structure and ammonia sensitivity of thin platinum or iridium gates in metal-oxide-silicon capacitors, Thin Solid Films, 177(1989) 77-93.

[32] P. Burr, P. Jeffery, J. Benjamin, M. Uren, A gas-sensitive field effect transistor utilizing a thin film of lead phthalocyanine as the gate material, Thin Solid Films, 151(1987) L111-L113.

[33] N. Huo, S. Yang, Z. Wei, S.-S. Li, J.-B. Xia, J. Li, Photoresponsive and gas sensing field-effect transistors based on multilayer WS_2 nanoflakes, Scientific Reports, 4(2014) 1-9.

[34] H. Li, Z. Yin, Q. He, H. Li, X. Huang, G. Lu, D.W.H. Fam, A.I.Y. Tok, Q. Zhang, H. Zhang, Fabrication of single-and multilayer MoS_2 Film-based field-effect transistors for sensing NO at room temperature, Small, 8(2012) 63-67.

[35] R. Abdul Rani, O. Sidek, ISFET pH sensor characterization: towards biosensor microchip application, TENCON 2004. 2004 IEEE Region 10 Conference, 4(2004) 660-663.

[36] M.J. Schöning, "Playing around" with field-effect sensors on the basis of EIS structures, LAPS and ISFETs, Sensors, 5(2005) 126-38.

[37] M. Kleitz, J. Million-Brodaz, P. Fabry, New compounds for ISFETs, Solid State Ionics, 22(1987) 295-303.

[38] S. Jamas, S. Collins, R.L. Smith, A physical model for drift in pH ISFETs, Sensors and Actuators B: Chemical, 49(1998) 146-55.

[39] P. Bergveld, Development, operation, and application of the ion-sensitive field-effect transistor as a tool for electrophysiology, Biomedical Engineering, IEEE Transactions on, (1972) 342-51.

[40] Y.G. Vlasov, A.V. Bratov, Analytical applications of pH-ISFETs, Sensors and Actuators B: Chemical, 10(1992) 1-6.

[41] A. Bratov, N. Abramova, C. Domínguez, Investigation of chloride sensitive ISFETs with different membrane compositions suitable for medical applications, Analytica Chimica Acta, 514(2004) 99-106.

[42] Z.M. Baccar, N. Jaffrezic-Renault, C. Martelet, H. Jaffrezic, G. Marest, A. Plantier, K^+-ISFET type microsensors fabricated by ion implantation, Materials Chemistry and Physics, 48(1997) 56-9.

[43] G. Taillades, O. Valls, A. Bratov, C. Dominguez, A. Pradel, M. Ribes, ISE and ISFET microsensors based on a sensitive chalcogenide glass for copper ion detection in solution, Sensors and Actuators B: Chemical, 59(1999) 123-7.

[44] A. Bratov, N. Abramova, C. Domínguez, Lowering the detection limit of calcium selective ISFETs with polymeric membranes, Talanta, 62(2004) 91-6.

[45] A. Bratov, N. Abramova, C. Domínguez, A. Baldi, Ion-selective field effect transistor (ISFET)-based calcium ion sensor with photocured polyurethane membrane suitable for ionised calcium determination in milk, Analytica Chimica Acta, 408(2000) 57-64.

[46] W.B. Mefteh, H. Touzi, Y. Chevalier, H.B. Ouada, A. Othmane, R. Kalfat, N. Jaffrezic-Renault, Comparison of polysiloxane films substituted by undecenyl-cyclam and by naphthyl-cyclam for the design of ISFET devices sensitive to Fe^{3+} ions, Sensors and Actuators B: Chemical, 204(2014) 723-33.

[47] M.B. Ali, R. Kalfat, H. Sfihi, J.M. Chovelon, H.B. Ouada, N. Jaffrezic-Renault, Sensitive cyclodextrin–polysiloxane gel membrane on EIS structure and ISFET for heavy metal ion detection, Sensors and Actuators B: Chemical, 62(2000) 233-7.

[48] J. Shaw, Bilayer membrane for ISFETs to eliminate CO_2 mediated pH sensitivity, Sensors and Actuators B: Chemical, 15(1993) 81-5.

[49] S. Mohri, J. Shimizu, N. Goda, T. Miyasaka, A. Fujita, M. Nakamura, F. Kajiya, Measurements of CO_2, lactic acid and sodium bicarbonate secreted by cultured cells using a flow-through type pH/CO_2 sensor system based on ISFET, Sensors and Actuators B: Chemical, 115(2006) 519-25.

[50] N.F. Starodub, B.B. Dzantiev, V.M. Starodub, A.V. Zherdev, Immunosensor for the determination of the herbicide simazine based on an ion-selective field-effect transistor, Analytica Chimica Acta, 424(2000) 37-43.

[51] A.P. Soldatkin, J. Montoriol, W. Sant, C. Martelet, N. Jaffrezic-Renault, Creatinine sensitive biosensor based on ISFETs and creatinine deiminase immobilised in BSA membrane, Talanta, 58(2002) 351-7.

[52] O.A. Boubriak, A.P. Soldatkin, N.F. Starodub, A.K. Sandrovsky, A.K. El'skaya, Determination of urea in blood serum by a urease biosensor based on an ion-sensitive field-effect transistor, Sensors and Actuators B: Chemical, 27(1995) 429-31.

[53] A.P. Soldatkin, J. Montoriol, W. Sant, C. Martelet, N. Jaffrezic-Renault, A novel urea sensitive biosensor with extended dynamic range based on recombinant urease and ISFETs, Biosensors and Bioelectronics, 19(2003) 131-5.

[54] M. Kalofonou, P. Georgiou, C.-P. Ou, C. Toumazou, An ISFET based translinear sensor for DNA methylation detection, Sensors and Actuators B: Chemical, 161(2012) 156-62.

[55] D. Gonçalves, D.M.F. Prazeres, V. Chu, J.P. Conde, Detection of DNA and proteins using amorphous silicon ion-sensitive thin-film field effect transistors, Biosensors and Bioelectronics, 24(2008) 545-51.

[56] T. Sekiguchi, M. Nakamura, M. Kato, K. Nishikawa, K. Hokari, T. Sugiyama, M. Asaka, Immunological Helicobacter pylori urease analyzer based on ion-sensitive field effect transistor, Sensors and Actuators B: Chemical, 67(2000) 265-9.

[57] L. Qu, S. Xia, C. Bian, J. Sun, J. Han, A micro-potentiometric hemoglobin immunosensor based on electropolymerized polypyrrole–gold nanoparticles composite, Biosensors and Bioelectronics, 24(2009) 3419-24.

[58] M.J. Schoning, A. Poghossian, Silicon-based field-effect devices for (bio-)chemical sensing, Advanced Semiconductor Devices and Microsystems, 2008 ASDAM 2008 International Conference on2008, pp. 31-8.

[59] J.Y. Oh, H.-J. Jang, W.-J. Cho, M.S. Islam, Highly sensitive electrolyte-insulator-semiconductor pH sensors enabled by silicon nanowires with Al2O3/SiO2 sensing membrane, Sensors and Actuators B: Chemical, 171–172(2012) 238-43.

[60] A. Poghossian, T. Yoshinobu, A. Simonis, H. Ecken, H. Lüth, M.J. Schöning, Penicillin detection by means of field-effect based sensors: EnFET, capacitive EIS sensor or LAPS?, Sensors and Actuators B: Chemical, 78(2001) 237-42.

[61] O. Engström, A. Carlsson, Scanned light pulse technique for the investigation of insulator-semiconductor interfaces, Journal of Applied Physics, 54(1983) 5245-51.

[62] M. Löfdahl, I. Lundström, Monitoring of hydrogen consumption along a palladium surface by using a scanning light pulse technique, Journal of Applied Physics, 86(1999) 1106-13.

[63] H. Uchida, D. Filippini, I. Lundström, Unsupervised scanning light pulse technique for chemical sensing, Sensors and Actuators B: Chemical, 103(2004) 225-32.

[64] H. Petersson, R. Klingvall, M. Holmberg, Sensor array optimization using variable selection and a scanning light pulse technique, Sensors and Actuators B: Chemical, 142(2009) 435-45.

[65] M. Löfdahl, C. Utaiwasin, A. Carlsson, I. Lundström, M. Eriksson, Gas response dependence on gate metal morphology of field-effect devices, Sensors and Actuators B: Chemical, 80(2001) 183-92.

[66] D. Filippini, I. Lundström, Hydrogen detection on bare SiO_2 between metal gates, Journal of Applied Physics, 91(2002) 3896-903.

[67] F. Winquist, H. Sundgren, E. Hedborg, A. Spetz, I. Lundström, Visual images of gas mixtures produced with field-effect structures, Sensors and Actuators B: Chemical, 6(1992) 157-61.

[68] I. Lundstrom, R. Erlandsson, U. Frykman, E. Hedborg, A. Spetz, H. Sundgren, S. Welin, F. Winquist, Artificial 'olfactory' images from a chemical sensor using a light-pulse technique, Nature, 352(1991) 47-50.

[69] D. Filippini, I. Lundström, Chemical imaging by a computer screen aided scanning light pulse technique, Applied Physics Letters, 81(2002) 3891-3.

[70] D.G. Hafeman, J.W. Parce, H.M. McConnell, Light-addressable potentiometric sensor for biochemical systems, Science, 240(1988) 1182-5.

[71] J. Suzurikawa, M. Nakao, R. Kanzaki, H. Takahashi, Microscale pH gradient generation by electrolysis on a light-addressable planar electrode, Sensors and Actuators B: Chemical, 149(2010) 205-11.

[72] Y.G. Mourzina, Y.E. Ermolenko, T. Yoshinobu, Y. Vlasov, H. Iwasaki, M.J. Schöning, Anion-selective light-addressable potentiometric sensors (LAPS) for the determination of nitrate and sulphate ions, Sensors and Actuators B: Chemical, 91(2003) 32-8.

[73] K.-i. Miyamoto, T. Wagner, T. Yoshinobu, S.i. Kanoh, M.J. Schöning, Phase-mode LAPS and its application to chemical imaging, Sensors and Actuators B: Chemical, 154(2011) 28-32.

[74] S. Krause, W. Moritz, H. Talabani, M. Xu, A. Sabot, G. Ensell, Scanning photo-induced impedance microscopy-resolution studies and polymer characterization, Electrochimica Acta, 51(2006) 1423-30.

[75] Y. Zhou, L. Chen, S. Krause, J.-N. Chazalviel, Scanning photoinduced impedance microscopy using amorphous silicon photodiode structures, Analytical Chemistry, 79(2007) 6208-14.

[76] T. Wagner, M.J. Schöning, Chapter 5 Light-addressable potentiometric sensors (LAPS): recent trends and applications, in: S. Alegret, A. Merkoçi (Eds.), Comprehensive Analytical Chemistry, Elsevier2007, pp. 87-128.

[77] Q. Zhang, Theoretical analysis and design of submicron-LAPS, Sensors and Actuators B: Chemical, 105(2005) 304-11.

[78] M. Nakao, S. Inoue, T. Yoshinobu, H. Iwasaki, High-resolution pH imaging sensor for microscopic observation of microorganisms, Sensors and Actuators B: Chemical, 34(1996) 234-9.

[79] Y. Ito, High-spatial resolution LAPS, Sensors and Actuators B: Chemical, 52(1998) 107-11.

[80] M. Nakao, T. Yoshinobu, H. Iwasaki, Improvement of spatial resolution of a laser-scanning pH-imaging sensor, Japanese Journal of Applied Physics, 33(1994) L394-L397.

[81] W. Moritz, I. Gerhardt, D. Roden, M. Xu, S. Krause, Photocurrent measurements for laterally resolved interface characterization, Fresenius' Journal of Analytical Chemistry, 367(2000) 329-33.

[82] W. Moritz, T. Yoshinobu, F. Finger, S. Krause, M. Martin-Fernandez, M.J. Schöning, High resolution LAPS using amorphous silicon as the semiconductor material, Sensors and Actuators B: Chemical, 103(2004) 436-41.

[83] M. George, W.J. Parak, I. Gerhardt, W. Moritz, F. Kaesen, H. Geiger, I. Eisele, H.E. Gaub, Investigation of the spatial resolution of the light-addressable potentiometric sensor, Sensors and Actuators A: Physical, 86(2000) 187-96.

[84] S. Krause, H. Talabani, M. Xu, W. Moritz, J. Griffiths, Scanning photo-induced impedance microscopy-an impedance based imaging technique, Electrochimica Acta, 47(2002) 2143-8.

[85] W.J. Parak, U.G. Hofmann, H.E. Gaub, J.C. Owicki, Lateral resolution of light-addressable potentiometric sensors: an experimental and theoretical investigation, Sensors and Actuators A: Physical, 63(1997) 47-57.

[86] C. li, Investigation into the sensitivity and resolution of scanning photo-Induced impedance microscopy: Queen Mary, Univeristy of London; phD thesis, 2009.

[87] Y. Guo, K. Seki, K.-i. Miyamoto, T. Wagner, M.J. Schöning, T. Yoshinobu, Novel photoexcitation method for light-addressable potentiometric sensor with higher spatial resolution, Applied Physics Express, 7(2014) 067301.

[88] M. Nakao, S. Inoue, R. Oishi, T. Yoshinobu, H. Iwasaki, Observation of microorganism colonies using a scanning-laser-beam pH-sensing microscope, Journal of Fermentation and Bioengineering, 79(1995) 163-6.

[89] L. Chen, Y.L. Zhou, S. Krause, A.G. Munoz, J. Kunze, P. Schmuki, Repair of thin thermally grown silicon dioxide by anodic oxidation, Electrochimica Acta, 53(2008) 3395-402.

[90] S. Krause, W. Moritz, H. Talabani, M. Xu, A. Sabot, G. Ensell, Scanning photo-induced impedance microscopy-resolution studies and polymer characterization, Electrochimica Acta, 51(2006) 1423-30.

[91] S.M. Sze, Physics of Semiconductor Devices-2nd Edition, John Wiley & Son, (1981).

[92] A. Martin, P. O'Sullivan, A. Mathewson, Dielectric reliability measurement methods: a review, Microelectronics Reliability, 38(1998) 37-72.

[93] A. Seki, K. Motoya, S. Watanabe, I. Kubo, Novel sensors for potassium, calcium and magnesium ions based on a silicon transducer as a light-addressable potentiometric sensor, Analytica Chimica Acta, 382(1999) 131-6.

[94] D. Ha, N. Hu, C.X. Wu, D. Kirsanov, A. Legin, M. Khaydukova, P. Wang, Novel structured light-addressable potentiometric sensor array based on PVC membrane for determination of heavy metals, Sensors and Actuators B: Chemical, 174(2012) 59-64.

[95] A.B.M. Ismail, K. Furuichi, T. Yoshinobu, H. Iwasaki, Light-addressable potentiometric fluoride (F^-) sensor, Sensors and Actuators B: Chemical, 86(2002) 94-7.

[96] A. Seki, S.-i. Ikeda, I. Kubo, I. Karube, Biosensors based on light-addressable potentiometric sensors for urea, penicillin and glucose, Analytica Chimica Acta, 373(1998) 9-13.

[97] A. Seki, K. Kawakubo, M. Iga, S. Nomura, Microbial assay for tryptophan using silicon-based transducer, Sensors and Actuators B: Chemical, 94(2003) 253-6.

[98] T. Yoshinobu, H. Ecken, A.B. Md. Ismail, H. Iwasaki, H. Lüth, M.J. Schöning, Chemical imaging sensor and its application to biological systems, Electrochimica Acta, 47(2001) 259-63.

[99] A.G. Gehring, D.L. Patterson, S.-I. Tu, Use of a Light-Addressable Potentiometric Sensor for the detection of escherichia coli O157:H7, Analytical Biochemistry, 258(1998) 293-8.

[100] B. Stein, M. George, H.E. Gaub, J.C. Behrends, W.J. Parak, Spatially resolved monitoring of cellular metabolic activity with a semiconductor-based biosensor, Biosensors and Bioelectronics, 18(2003) 31-41.

[101] N. Hu, D. Ha, C. Wu, J. Zhou, D. Kirsanov, A. Legin, P. Wang, A LAPS array with low cross-talk for non-invasive measurement of cellular metabolism, Sensors and Actuators A: Physical, 187(2012) 50-6.

[102] N. Hu, C. Wu, D. Ha, T. Wang, Q. Liu, P. Wang, A novel microphysiometer based on high sensitivity LAPS and microfluidic system for cellular metabolism study and rapid drug screening, Biosensors and Bioelectronics, 40(2013) 167-73.

[103] Q. Liu, N. Hu, F. Zhang, H. Wang, W. Ye, P. Wang, Neurosecretory cell-based biosensor: Monitoring secretion of adrenal chromaffin cells by local extracellular acidification using light-addressable potentiometric sensor, Biosensors and Bioelectronics, 35(2012) 421-4.

[104] L. Du, L. Zou, L. Zhao, L. Huang, P. Wang, C. Wu, Label-free functional assays of chemical receptors using a bioengineered cell-based biosensor with localized extracellular acidification measurement, Biosensors and Bioelectronics, 54(2014) 623-7.

[105] C. Wu, T. Bronder, A. Poghossian, C.F. Werner, M.J. Schoning, Label-free detection of DNA using a light-addressable potentiometric sensor modified with a positively charged polyelectrolyte layer, Nanoscale, 7(2015) 6143-50.

[106] A.B.M. Ismail, T. Yoshinobu, H. Iwasaki, H. Sugihara, T. Yukimasa, I. Hirata, H. Iwata, Investigation on light-addressable potentiometric sensor as a possible cell–semiconductor hybrid, Biosensors and Bioelectronics, 18(2003) 1509-14.

[107] G. Xu, X. Ye, L. Qin, Y. Xu, Y. Li, R. Li, P. Wang, Cell-based biosensors based on light-addressable potentiometric sensors for single cell monitoring, Biosensors and Bioelectronics, 20(2005) 1757-63.

[108] Q. Liu, H. Yu, Z. Tan, H. Cai, W. Ye, M. Zhang, P. Wang, In vitro assessing the risk of drug-induced cardiotoxicity by embryonic stem cell-based biosensor, Sensors and Actuators B: Chemical, 155(2011) 214-9.

[109] L. Du, C. Wu, H. Peng, L. Zhao, L. Huang, P. Wang, Bioengineered olfactory sensory neuron-based biosensor for specific odorant detection, Biosensors and Bioelectronics, 40(2013) 401-6.

[110] K. Miyamoto, Y. Kuwabara, S.i. Kanoh, T. Yoshinobu, T. Wagner, M.J. Schöning, Chemical image scanner based on FDM-LAPS, Sensors and Actuators B: Chemical, 137(2009) 533-8.

[111] C.F. Werner, T. Wagner, K.-i. Miyamoto, T. Yoshinobu, M.J. Schöning, High speed and high resolution chemical imaging based on a new type of OLED-LAPS set-up, Sensors and Actuators B: Chemical, 175(2012) 118-22.

[112] K.-i. Miyamoto, Y. Hirayama, T. Wagner, M.J. Schöning, T. Yoshinobu, Visualization of enzymatic reaction in a microfluidic channel using chemical imaging sensor, Electrochimica Acta, 113(2013) 768-72.

[113] N. Chaffey, B. Alberts, A. Johnson, J. Lewis, M. Raff, K. Roberts and P. Walter. Molecular biology of the cell. 4th edn, Annals of Botany, 91(2003) 401.

[114] http://php.med.unsw.edu.au/cellbiology/index.php?title=Cell_Junctions.

[115] E. Sackmann, R.F. Bruinsma, Cell adhesion as wetting transition, ChemPhysChem, 3(2002) 262-9.

[116] R. Weis, P. Fromherz, Frequency dependent signal transfer in neuron transistors, Physical Review E, 55(1997) 877-89.

[117] V. Kiessling, B. Müller, P. Fromherz, Extracellular resistance in cell adhesion measured with a transistor probe, Langmuir, 16(2000) 3517-21.

[118] R. Weis, B. Müller, P. Fromherz, Neuron adhesion on a silicon chip probed by an array of field-effect transistors, Physical Review Letters, 76(1996) 327-330.

[119] A. Lambacher, P. Fromherz, Fluorescence interference-contrast microscopy on oxidized silicon using a monomolecular dye layer, Applied Physics A, 63(1996) 207-16.

[120] M. Jenkner, P. Fromherz, Bistability of membrane conductance in cell adhesion observed in a neuron transistor, Physical Review Letters, 79(1997) 4705-4708.

[121] S. Vassanelli, P. Fromherz, Transistor records of excitable neurons from rat brain, Applied Physics A: Materials Science & Processing, 66(1998) 459-63.

[122] A. Cohen, M.E. Spira, S. Yitshaik, G. Borghs, O. Shwartzglass, J. Shappir, Depletion type floating gate p-channel MOS transistor for recording action potentials generated by cultured neurons, Biosensors and Bioelectronics, 19(2004) 1703-9.

[123] B. Straub, E. Meyer, P. Fromherz, Recombinant maxi-K channels on transistor, a prototype of iono-electronic interfacing, Nature Biotechnology, 19(2001) 121-4.

[124] G. Wrobel, R. Seifert, S. Ingebrandt, J. Enderlein, H. Ecken, A. Baumann, U.B. Kaupp, A. Offenhäusser, Cell-transistor coupling: investigation of potassium currents recorded with p- and n-channel FETs, Biophysical Journal, 89(2005) 3628-38.

[125] I. Schoen, P. Fromherz, Activation of Na^+ channels in cell membrane by capacitive stimulation with silicon chip, Applied Physics Letters, 87(2005) 193901-3.

[126] M. Ulbrich, P. Fromherz, Opening of K^+ channels by capacitive stimulation from silicon chip, Applied Physics A, 81(2005) 887-91.

[127] M.A. Colicos, N.I. Syed, Neuronal networks and synaptic plasticity: understanding complex system dynamics by interfacing neurons with silicon technologies, Journal of Experimental Biology, 209(2006) 2312-9.

[128] R.A. Kaul, N.I. Syed, P. Fromherz, Neuron-semiconductor chip with chemical synapse between identified neurons, Physical Review Letters, 92(2004) 038102-3.

[129] M. Hutzler, A. Lambacher, B. Eversmann, M. Jenkner, R. Thewes, P. Fromherz, High-resolution multitransistor array recording of electrical field potentials in cultured brain slices, Journal of Neurophysiology, 96(2006) 1638-45.

[130] M. Eickenscheidt, M. Jenkner, R. Thewes, P. Fromherz, G. Zeck, Electrical stimulation of retinal neurons in epiretinal and subretinal configuration using a multicapacitor array, Journal of Neurophysiology, 107(2012) 2742-55.

[131] J. Wegener, C.R. Keese, I. Giaever, Electric cell-substrate impedance sensing (ECIS) as a noninvasive means to monitor the kinetics of cell spreading to artificial surfaces, Experimental Cell Research, 259(2000) 158-66.

[132] A. Susloparova, D. Koppenhöfer, X.T. Vu, M. Weil, S. Ingebrandt, Impedance spectroscopy with field-effect transistor arrays for the analysis of anti-cancer drug action on individual cells, Biosensors and Bioelectronics, 40(2013) 50-6.

[133] S. Schäfer, S. Eick, B. Hofmann, T. Dufaux, R. Stockmann, G. Wrobel, A. Offenhäusser, S. Ingebrandt, Time-dependent observation of individual cellular binding events to field-effect transistors, Biosensors and Bioelectronics, 24(2009) 1201-8.

[134] J.K.Y. Law, A. Susloparova, X.T. Vu, X. Zhou, F. Hempel, B. Qu, M. Hoth, S. Ingebrandt, Human T cells monitored by impedance spectrometry using field-effect transistor arrays: A novel tool for single-cell adhesion and migration studies, Biosensors and Bioelectronics, 67(2015)170-176.

[135] D. Koppenhöfer, A. Susloparova, D. Docter, R.H. Stauber, S. Ingebrandt, Monitoring nanoparticle induced cell death in H441 cells using field-effect transistors, Biosensors and Bioelectronics, 40(2013) 89-95.

[136] D.D.M. Wayner, R.A. Wolkow, Organic modification of hydrogen terminated silicon surfaces, Journal of the Chemical Society, Perkin Transactions 2, (2002) 23-34.

[137] S.P. Cummings, J. Savchenko, T. Ren, Functionalization of flat Si surfaces with inorganic compounds-towards molecular CMOS hybrid devices, Coordination Chemistry Reviews, 255(2011) 1587-602.

[138] R. Boukherroub, Chemical reactivity of hydrogen-terminated crystalline silicon surfaces, Current Opinion in Solid State and Materials Science, 9(2005) 66-72.

[139] Y. Li, C. Cai, Click chemistry-based functionalization on non-oxidized silicon substrates, Chemistry-an Asian Journal, 6(2011) 2592-605.

[140] M.R. Linford, C.E.D. Chidsey, Alkyl monolayers covalently bonded to silicon surfaces, Journal of the American Chemical Society, 115(1993) 12631-2.

[141] M.R. Linford, P. Fenter, P.M. Eisenberger, C.E.D. Chidsey, Alkyl monolayers on silicon prepared from 1-alkenes and hydrogen-terminated silicon, Journal of the American Chemical Society, 117(1995) 3145-55.

[142] R.L. Cicero, M.R. Linford, C.E.D. Chidsey, Photoreactivity of unsaturated compounds with hydrogen-terminated silicon(111), Langmuir, 16(2000) 5688-95.

[143] A. Sieval, A. Demirel, J. Nissink, M. Linford, J. Van der Maas, W. De Jeu, H. Zuilhof, E. Sudhölter, Highly stable Si-C linked functionalized monolayers on the silicon(100) surface, Langmuir, 14(1998) 1759-68.

[144] Y.J. Li, R. Tero, T. Nagasawa, T. Nagata, T. Urisu, Deposition of 10-undecenoic acid self-assembled layers on H-Si surfaces studied with AFM and FT-IR, Applied Surface Science, 238(2004) 238-41.

[145] D. Aureau, J. Rappich, A. Moraillon, P. Allongue, F. Ozanam, J.N. Chazalviel, In situ monitoring of the electronic properties and the pH stability of grafted Si(111), Journal of Electroanalytical Chemistry, 646(2010) 33-42.

[146] S. Ciampi, P.K. Eggers, G. Le Saux, M. James, J.B. Harper, J.J. Gooding, Silicon (100) electrodes resistant to oxidation in aqueous solutions: an unexpected benefit of surface acetylene moieties, Langmuir, 25(2009) 2530-9.

[147] S. Ciampi, T. Böcking, K.A. Kilian, M. James, J.B. Harper, J.J. Gooding, Functionalization of Acetylene-Terminated Monolayers on Si(100) Surfaces: a click chemistry approach, Langmuir, 23(2007) 9320-9.

[148] F. Shamsi, H. Coster, K.A. Jolliffe, Characterization of peptide immobilization on an acetylene terminated surface via click chemistry, Surface Science, 605(2011) 1763-70.

[149] R. Boukherroub, J. Wojtyk, D.D. Wayner, D.J. Lockwood, Thermal hydrosilylation of undecylenic acid with porous silicon, Journal of the Electrochemical Society, 149(2002) H59-H63.

[150] L. Scheres, M. Giesbers, H. Zuilhof, Organic monolayers onto oxide-free silicon with improved surface coverage: alkynes versus alkenes, Langmuir, 26(2010) 4790-5.

[151] A. Faucheux, A.C. Gouget-Laemmel, C. Henry de Villeneuve, R. Boukherroub, F. Ozanam, P. Allongue, J.-N. Chazalviel, Well-defined carboxyl-terminated alkyl monolayers grafted onto H-Si (111): Packing density from a combined AFM and quantitative IR study, Langmuir, 22(2006) 153-62.

[152] A. Faucheux, A. Gouget-Laemmel, P. Allongue, C. Henry de Villeneuve, F. Ozanam, J.-N. Chazalviel, Mechanisms of thermal decomposition of organic monolayers grafted on (111) silicon, Langmuir, 23(2007) 1326-32.

[153] D. Aureau, F. Ozanam, P. Allongue, J.N. Chazalviel, The titration of carboxyl-terminated monolayers revisited: in situ calibrated fourier transform infrared study of well-defined monolayers on silicon, Langmuir, 24(2008) 9440-8.

[154] Q.-Y. Sun, L.C.P.M. de Smet, B. van Lagen, M. Giesbers, P.C. Thüne, J. van Engelenburg, F.A. de Wolf, H. Zuilhof, E.J.R. Sudhölter, Covalently attached monolayers on crystalline hydrogen-terminated silicon: extremely mild attachment by visible light, Journal of the American Chemical Society, 127(2005) 2514-23.

[155] Q.-Y. Sun, L.C.P.M. de Smet, B. van Lagen, A. Wright, H. Zuilhof, E.J.R. Sudhölter, Covalently attached monolayers on hydrogen-terminated Si(100): extremely mild attachment by visible Light, Angewandte Chemie International Edition, 43(2004) 1352-5.

[156] L.C.P.M. de Smet, G.A. Stork, G.H.F. Hurenkamp, Q.-Y. Sun, H. Topal, P.J.E. Vronen, A.B. Sieval, A. Wright, G.M. Visser, H. Zuilhof, E.J.R. Sudhölter, Covalently attached saccharides on silicon surfaces, Journal of the American Chemical Society, 125(2003) 13916-7.

[157] S. Ciampi, G. Le Saux, J.B. Harper, J.J. Gooding, Optimization of click chemistry of ferrocene derivatives on acetylene-functionalized silicon(100) surfaces, Electroanalysis, 20(2008) 1513-9.

[158] S. Ciampi, J.J. Gooding, Direct electrochemistry of cytochrome c at modified Si (100) electrodes, Chemistry-A European Journal, 16(2010) 5961-8.

[159] A. Faucheux, A.C. Gouget-Laemmel, P. Allongue, C. Henry de Villeneuve, F. Ozanam, J.N. Chazalviel, Mechanisms of thermal decomposition of organic monolayers grafted on (111) silicon, Langmuir, 23(2006) 1326-32.

[160] M. Perring, S. Dutta, S. Arafat, M. Mitchell, P.J.A. Kenis, N.B. Bowden, Simple methods for the direct assembly, functionalization, and patterning of acid-terminated monolayers on si(111), Langmuir, 21(2005) 10537-44.

[161] S.N. Arafat, S. Dutta, M. Perring, M. Mitchell, P.J.A. Kenis, N.B. Bowden, Mild methods to assemble and pattern organic monolayers on hydrogen-terminated Si(111), Chemical Communications, (2005) 3198-200.

[162] A. Bansal, X. Li, I. Lauermann, N.S. Lewis, S.I. Yi, W.H. Weinberg, Alkylation of si surfaces using a two-step halogenation/Grignard route, Journal of the American Chemical Society, 118(1996) 7225-6.

[163] A. Bansal, N.S. Lewis, Electrochemical properties of (111)-oriented n-Si surfaces derivatized with covalently-attached alkyl chains, The Journal of Physical Chemistry B, 102(1998) 1067-70.

[164] T. Dubois, F. Ozanam, J. Chazalviel, Stabilization of the porous silicon surface by grafting of organic groups: direct electrochemical methylation, ECS Symp Proc, Book Ser: Electrochem Soc Ser 1997, pp. 296-310.

[165] A. Fidélis, F. Ozanam, J.N. Chazalviel, Fully methylated, atomically flat (111) silicon surface, Surface Science, 444(2000) 7-10.

[166] S. Fellah, R. Boukherroub, F. Ozanam, J.-N. Chazalviel, Hidden electrochemistry in the thermal grafting of silicon surfaces from Grignard reagents, Langmuir, 20(2004) 6359-64.

[167] S. Fellah, A. Teyssot, F. Ozanam, J.N. Chazalviel, J. Vigneron, A. Etcheberry, Kinetics of electrochemical derivatization of the silicon surface by Grignards, Langmuir, 18(2002) 5851-60.

[168] R. Boukherroub, S. Morin, F. Bensebaa, D.D.M. Wayner, New synthetic routes to alkyl monolayers on the si(111) surface, Langmuir, 15(1999) 3831-5.

[169] A.B. Sieval, R. Linke, H. Zuilhof, E.J.R. Sudhölter, High-quality alkyl monolayers on silicon surfaces, Advanced Materials, 12(2000) 1457-60.

[170] D.K. Aswal, S.P. Koiry, B. Jousselme, S.K. Gupta, S. Palacin, J.V. Yakhmi, Hybrid molecule-on-silicon nanoelectronics: Electrochemical processes for grafting and printing of monolayers, Physica E: Low-dimensional Systems and Nanostructures, 41(2009) 325-44.

[171] P. Allongue, C.H. de Villeneuve, J. Pinson, F. Ozanam, J.N. Chazalviel, X. Wallart, Organic monolayers on Si(111) by electrochemical method, Electrochimica Acta, 43(1998) 2791-8.

[172] C. Henry De Villeneuve, J. Pinson, M.C. Bernard, P. Allongue, Electrochemical formation of close-packed phenyl layers on Si(111), Journal of Physical Chemistry B, 101(1997) 2415-20.

[173] P. Allongue, C. Henry de Villeneuve, J. Pinson, Structural characterization of organic monolayers on Si<111> from capacitance measurements, Electrochimica Acta, 45(2000) 3241-8.

[174] E.G. Robins, M.P. Stewart, J.M. Buriak, Anodic and cathodic electrografting of alkynes on porous silicon, Chemical Communications, (1999) 2479-80.

[175] F. Cattaruzza, A. Cricenti, A. Flamini, M. Girasole, G. Longo, A. Mezzi, T. Prosperi, Carboxylic acid terminated monolayer formation on crystalline silicon and silicon nitride surfaces. A surface coverage determination with a fluorescent probe in solution, Journal of Materials Chemistry, 14(2004) 1461-8.

[176] F. Cattaruzza, A. Cricenti, A. Flamini, M. Girasole, G. Longo, T. Prosperi, G. Andreano, L. Cellai, E. Chirivino, Controlled loading of oligodeoxyribonucleotide monolayers onto unoxidized crystalline silicon; fluorescence-based determination of the surface coverage and of the hybridization efficiency; parallel imaging of the process by atomic force microscopy, Nucleic Acids Research, 34(2006) 32-3.

[177] T. Strother, W. Cai, X. Zhao, R.J. Hamers, L.M. Smith, Synthesis and Characterization of DNA-Modified Silicon (111) Surfaces, Journal of the American Chemical Society, 122(2000) 1205-9.

[178] T. Strother, R.J. Hamers, L.M. Smith, Covalent attachment of oligodeoxyribonucleotides to amine-modified Si (001) surfaces, Nucleic acids research, 28(2000) 3535-41.

[179] Z. Lin, T. Strother, W. Cai, X. Cao, L.M. Smith, R.J. Hamers, DNA attachment and hybridization at the silicon (100) surface, Langmuir, 18(2002) 788-96.

[180] A. Faucheux, A.C. Gouget-Laemmel, C. Henry de Villeneuve, R. Boukherroub, F. Ozanam, P. Allongue, J.-N. Chazalviel, Well-defined carboxyl-terminated alkyl monolayers grafted onto H-Si(111): packing density from a combined AFM and quantitative IR study, Langmuir, 22(2005) 153-62.

[181] S. Sam, L. Touahir, J. Salvador Andresa, P. Allongue, J.N. Chazalviel, A.C. Gouget-Laemmel, C. Henry de Villeneuve, A. Moraillon, F. Ozanam, N. Gabouze, S. Djebbar, Semiquantitative study of the EDC/NHS activation of acid terminal groups at modified porous silicon surfaces, Langmuir, 26(2009) 809-14.

[182] A. Moraillon, A.C. Gouget-Laemmel, F. Ozanam, J.N. Chazalviel, Amidation of monolayers on silicon in physiological buffers: a quantitative IR study, The Journal of Physical Chemistry C, 112(2008) 7158-67.

[183] J. Mehlich, B.J. Ravoo, Click chemistry by microcontact printing on self-assembled monolayers: A structure-reactivity study by fluorescence microscopy, Organic & Biomolecular Chemistry, 9(2011) 4108-15.

[184] N.S. Kehr, J. El-Gindi, H.-J. Galla, L. De Cola, Click chemistry on self-assembled monolayer of zeolite L crystals by microcontact printing-applications in nanobiotechnology, Microporous and Mesoporous Materials, 144(2011) 9-14.

[185] J.Y. Gerasimov, R.Y. Lai, Design and characterization of an electrochemical peptide-based sensor fabricated via "click" chemistry, Chemical Communications, 47(2011) 8688-90.

[186] V. Ganesh, V.S. Sudhir, T. Kundu, S. Chandrasekaran, 10 Years of click chemistry: synthesis and applications of ferrocene-derived triazoles, Chemistry-an Asian Journal, 6(2011) 2670-94.

[187] G. Qin, C. Santos, W. Zhang, Y. Li, A. Kumar, U.J. Erasquin, K. Liu, P. Muradov, B.W. Trautner, C. Cai, Biofunctionalization on alkylated silicon substrate surfaces via "click" chemistry, Journal of the American Chemical Society, 132(2010) 16432-41.

[188] B. Guan, S. Ciampi, G. Le Saux, K. Gaus, P.J. Reece, J.J. Gooding, Different functionalization of the internal and external surfaces in mesoporous materials for biosensing applications using "click" chemistry, Langmuir, 27(2010) 328-34.

[189] H.C. Kolb, M. Finn, K.B. Sharpless, Click chemistry: diverse chemical function from a few good reactions, Angewandte Chemie International Edition, 40(2001) 2004-21.

[190] B. Worrell, J. Malik, V. Fokin, Direct evidence of a dinuclear copper intermediate in Cu (I)-catalyzed azide-alkyne cycloadditions, Science, 340(2013) 457-60.

[191] H. Liu, F. Duclairoir, B. Fleury, L. Dubois, Y. Chenavier, J.-C. Marchon, Porphyrin anchoring on Si(100) using a [small beta]-pyrrolic position, Dalton Transactions, (2009) 3793-9.

[192] R.D. Rohde, H.D. Agnew, W.-S. Yeo, R.C. Bailey, J.R. Heath, A non-oxidative approach toward chemically and electrochemically functionalizing Si(111), Journal of the American Chemical Society, 128(2006) 9518-25.

[193] P. Michaels, M.T. Alam, S. Ciampi, W. Rouesnel, S.G. Parker, M.H. Choudhury, J.J. Gooding, A robust DNA interface on a silicon electrode, Chemical Communications, 50(2014) 7878-80.

[194] Y. Zhu, B. Gupta, B. Guan, S. Ciampi, P.J. Reece, J.J. Gooding, Photolithographic strategy for patterning preformed, chemically modified, porous silicon photonic crystal using click chemistry, ACS Applied Materials & Interfaces, 5(2013) 6514-21.

[195] Y. Zhu, A.H. Soeriyadi, S.G. Parker, P.J. Reece, J.J. Gooding, Chemical patterning on preformed porous silicon photonic crystals: towards multiplex detection of protease activity at precise positions, Journal of Materials Chemistry B, 2(2014) 3582-8.

[196] K. Itoga, J. Kobayashi, M. Yamato, A. Kikuchi, T. Okano, Maskless liquid-crystal-display projection photolithography for improved design flexibility of cellular micropatterns, Biomaterials, 27(2006) 3005-9.

[197] A.W. Flounders, D.L. Brandon, A.H. Bates, Patterning of immobilized antibody layers via photolithography and oxygen plasma exposure, Biosensors and Bioelectronics, 12(1997) 447-56.

[198] S. Marchesan, C.D. Easton, K.E. Styan, P. Leech, T.R. Gengenbach, J.S. Forsythe, P.G. Hartley, SU-8 photolithography on reactive plasma thin-films: coated microwells for peptide display, Colloids and Surfaces B: Biointerfaces, 108(2013) 313-21.

[199] M.S. Hahn, L.J. Taite, J.J. Moon, M.C. Rowland, K.A. Ruffino, J.L. West, Photolithographic patterning of polyethylene glycol hydrogels, Biomaterials, 27(2006) 2519-24.

[200] X. Chen, J. Zhang, Z. Wang, Q. Yan, Fabrication of submicron-gap electrodes by silicon volume expansion for DNA-detection, Sensors and Actuators A: Physical, 175(2012) 73-7.

[201] G.R. Prashanth, V.S. Goudar, S. Suran, A.M. Raichur, M.M. Varma, Non-covalent functionalization using lithographically patterned polyelectrolyte multilayers for high-density microarrays, Sensors and Actuators B: Chemical, 171(2012) 315-22.

[202] L. Altomare, N. Gadegaard, L. Visai, M.C. Tanzi, S. Farè, Biodegradable microgrooved polymeric surfaces obtained by photolithography for skeletal muscle cell orientation and myotube development, Acta Biomaterialia, 6(2010) 1948-57.

[203] K. Tsougeni, A. Bourkoula, P. Petrou, A. Tserepi, S. Kakabakos, E. Gogolides, Photolithography and plasma processing of polymeric lab on chip for wetting and fouling control and cell patterning, Microelectronic Engineering, 124(2014) 47-52.

[204] S. Marchesan, C.D. Easton, K.E. Styan, P. Leech, T.R. Gengenbach, J.S. Forsythe, P.G. Hartley, SU-8 photolithography on reactive plasma thin-films: coated microwells for peptide display, Colloids and Surfaces B: Biointerfaces, 108(2013) 313-21.

[205] A. Kumar, G.M. Whitesides, Features of gold having micrometer to centimeter dimensions can be formed through a combination of stamping with an elastomeric stamp and an alkanethiol ''ink''followed by chemical etching, Applied Physics Letters, 63(1993) 2002-4.

[206] M. Mrksich, G.M. Whitesides, Patterning self-assembled monolayers using microcontact printing: a new technology for biosensors, Trends in Biotechnology, 13(1995) 228-35.

[207] S. Kidambi, C. Chan, I. Lee, Selective depositions on polyelectrolyte multilayers: Self-assembled monolayers of m-dPEG acid as molecular template, Journal of the American Chemical Society, 126(2004) 4697-703.

[208] D.J. Graber, T.J. Zieziulewicz, D.A. Lawrence, W. Shain, J.N. Turner, Antigen binding specificity of antibodies patterned by microcontact printing, Langmuir, 19(2003) 5431-4.

[209] C.S. Chen, M. Mrksich, S. Huang, G.M. Whitesides, D.E. Ingber, Geometric control of cell life and death, Science, 276(1997) 1425-8.

[210] T. Cornish, D.W. Branch, B.C. Wheeler, J.T. Campanelli, Microcontact printing: a versatile technique for the study of synaptogenic molecules, Molecular and Cellular neuroscience, 20(2002) 140-53.

[211] D.I. Rozkiewicz, Y. Kraan, M.W. Werten, F.A. de Wolf, V. Subramaniam, B.J. Ravoo, D.N. Reinhoudt, Covalent microcontact printing of proteins for cell patterning, Chemistry-A European Journal, 12(2006) 6290-7.

[212] G. Csucs, R. Michel, J.W. Lussi, M. Textor, G. Danuser, Microcontact printing of novel co-polymers in combination with proteins for cell-biological applications, Biomaterials, 24(2003) 1713-20.

[213] T.P. Sullivan, M.L. van Poll, P.Y. Dankers, W.T. Huck, Forced peptide synthesis in nanoscale confinement under elastomeric stamps, Angewandte Chemie International Edition, 116(2004) 4286-9.

[214] N. Kohli, S. Vaidya, R.Y. Ofoli, R.M. Worden, I. Lee, Arrays of lipid bilayers and liposomes on patterned polyelectrolyte templates, Journal of Colloid and Interface Science, 301(2006) 461-9.

[215] D.I. Rozkiewicz, J. Gierlich, G.A. Burley, K. Gutsmiedl, T. Carell, B.J. Ravoo, D.N. Reinhoudt, Transfer printing of DNA by "click" chemistry, ChemBioChem, 8(2007) 1997-2002.

[216] Z. Wang, P. Zhang, B. Kirkland, Y. Liu, J. Guan, Microcontact printing of polyelectrolytes on PEG using an unmodified PDMS stamp for micropatterning nanoparticles, DNA, proteins and cells, Soft Matter, 8(2012) 7630-7.

[217] S.A. Lange, V. Benes, D.P. Kern, J.H. Hörber, A. Bernard, Microcontact printing of DNA molecules, Analytical Chemistry, 76(2004) 1641-7.

[218] D.I. Rozkiewicz, D. Jańczewski, W. Verboom, B.J. Ravoo, D.N. Reinhoudt, "Click" chemistry by microcontact printing, Angewandte Chemie International Edition, 45(2006) 5292-6.

[219] M.A.C. Campos, J.M.J. Paulusse, H. Zuilhof, Functional monolayers on oxide-free silicon surfaces via thiol-ene click chemistry, Chemical Communications, 46(2010) 5512-4.

[220] R.K. Smith, P.A. Lewis, P.S. Weiss, Patterning self-assembled monolayers, Progress in Surface Science, 75(2004) 1-68.

[221] R.D. Piner, J. Zhu, F. Xu, S. Hong, C.A. Mirkin, "Dip-pen" nanolithography, Science, 283(1999) 661-3.

[222] D. Nyamjav, A. Ivanisevic, Alignment of long DNA molecules on templates generated via dip-pen nanolithography, Advanced Materials, 15(2003) 1805-9.

[223] J.D. Kim, D.G. Ahn, J.W. Oh, W. Park, H. Jung, Ribosome display and dip-pen nanolithography for the fabrication of protein nanoarrays, Advanced Materials, 20(2008) 3349-53.

[224] S.W. Lee, B.K. Oh, R.G. Sanedrin, K. Salaita, T. Fujigaya, C.A. Mirkin, Biologically active protein nanoarrays generated using parallel dip-pen nanolithography, Advanced Materials, 18(2006) 1133-6.

[225] Y.H. Shin, S.H. Yun, S.H. Pyo, Y.S. Lim, H.J. Yoon, K.H. Kim, S.K. Moon, S.W. Lee, Y.G. Park, S.I. Chang, Polymer-coated tips for patterning of viruses by dip-pen nanolithography, Angewandte Chemie International Edition, 49(2010) 9689-92.

[226] S.W. Lee, R.G. Sanedrin, B.K. Oh, C.A. Mirkin, Nanostructured polyelectrolyte multilayer organic thin films generated via parallel dip-pen nanolithography, Advanced Materials, 17(2005) 2749-53.

[227] D.A. Long, K. Unal, R.C. Pratt, M. Malkoch, J. Frommer, Localized "click" chemistry through dip-pen nanolithography, Advanced Materials, 19(2007) 4471-3.

[228] F.K. Perkins, E.A. Dobisz, S.L. Brandow, J.M. Calvert, J.E. Kosakowski, C.R.K. Marrian, Fabrication of 15 nm wide trenches in Si by vacuum scanning tunneling microscope lithography of an organosilane self-assembled film and reactive ion etching, Applied Physics Letters, 68(1996) 550-2.

[229] M. Lercel, G. Redinbo, F. Pardo, M. Rooks, R. Tiberio, P. Simpson, H. Craighead, C. Sheen, A. Parikh, D. Allara, Electron beam lithography with monolayers of alkylthiols and alkylsiloxanes, Journal of Vacuum Science & Technology B, 12(1994) 3663-7.

[230] G. Yang, J. Garno, G. Liu, Scanning probe-based lithography for production of biological and organic nanostructures on surfaces, Comprehensive Nanoscience and Technology, 6(2010) 335-8.

[231] G. Decher, Fuzzy nanoassemblies: toward layered polymeric multicomposites, Science, 277(1997) 1232-7.

[232] E. Donath, G.B. Sukhorukov, F. Caruso, S.A. Davis, H. Möhwald, Novel hollow polymer shells by colloid-templated assembly of polyelectrolytes, Angewandte Chemie International Edition, 37(1998) 2201-5.

[233] G. Gao, S. Moya, H. Lichtenfeld, A. Casoli, H. Fiedler, E. Donath, H. Mohwald, The decomposition process of melamine formaldehyde cores: the key step in the fabrication of ultrathin polyelectrolyte multilayer capsules, Macromolecular Materials and Engineering, 286(2001) 355-61.

[234] M.-K. Park, C. Xia, R.C. Advincula, P. Schütz, F. Caruso, Cross-linked, luminescent spherical colloidal and hollow-shell particles, Langmuir, 17(2001) 7670-4.

[235] X.-F. Guo, Y.-S. Kim, G.-J. Kim, Fabrication of SiO_2, Al_2O_3, and TiO_2 microcapsules with hollow core and mesoporous shell structure, The Journal of Physical Chemistry C, 113(2009) 8313-9.

[236] D.V. Volodkin, N.I. Larionova, G.B. Sukhorukov, Protein encapsulation via porous $CaCO_3$ microparticles templating, Biomacromolecules, 5(2004) 1962-72.

[237] D.V. Volodkin, A.I. Petrov, M. Prevot, G.B. Sukhorukov, Matrix polyelectrolyte microcapsules: new system for macromolecule encapsulation, Langmuir, 20(2004) 3398-406.

[238] C. Déjugnat, G.B. Sukhorukov, pH-responsive properties of hollow polyelectrolyte microcapsules templated on various cores, Langmuir, 20(2004) 7265-9.

[239] O. Shchepelina, M.O. Lisunova, I. Drachuk, V.V. Tsukruk, Morphology and properties of microcapsules with different core releases, Chemistry of Materials, 24(2012) 1245-54.

[240] Y. Zhang, Y. Guan, S. Yang, J. Xu, C.C. Han, Fabrication of hollow capsules based on hydrogen bonding, Advanced Materials, 15(2003) 832-5.

[241] S. Moya, R. Georgieva, H. Bäumler, W. Richter, E. Donath, Composite lipid polyelectrolyte capsules templated on red blood cells: fabrication and structural characterisation, Medical and Biological Engineering and Computing, 41(2003) 504-8.

[242] M.V. Lomova, G.B. Sukhorukov, M.N. Antipina, Antioxidant coating of micronsize droplets for prevention of lipid peroxidation in oil-in-water emulsion, ACS Applied Materials & Interfaces, 2(2010) 3669-76.

[243] S. Leporatti, C. Gao, A. Voigt, E. Donath, H. Möhwald, Shrinking of ultrathin polyelectrolyte multilayer capsules upon annealing: a confocal laser scanning microscopy and scanning force microscopy study, The European Physical Journal E, 5(2001) 13-20.

[244] V.V. Lulevich, S. Nordschild, O.I. Vinogradova, Investigation of molecular weight and aging effects on the stiffness of polyelectrolyte multilayer microcapsules, Macromolecules, 37(2004) 7736-41.

[245] R. Georgieva, R. Dimova, G. Sukhorukov, G. Ibarz, H. Möhwald, Influence of different salts on micro-sized polyelectrolyte hollow capsules, Journal of Materials Chemistry, 15(2005) 4301-10.

[246] K. Köhler, H. Möhwald, G.B. Sukhorukov, Thermal behavior of polyelectrolyte multilayer microcapsules: 2. Insight into molecular mechanisms for the PDADMAC/PSS system, The Journal of Physical Chemistry B, 110(2006) 24002-10.

[247] S.-F. Chong, A. Sexton, R. De Rose, S.J. Kent, A.N. Zelikin, F. Caruso, A paradigm for peptide vaccine delivery using viral epitopes encapsulated in degradable polymer hydrogel capsules, Biomaterials, 30(2009) 5178-86.

[248] N.G. Balabushevich, E.P. Zimina, N.I. Larionova, Encapsulation of catalase in polyelectrolyte microspheres composed of melamine formaldehyde, Dextran Sulfate, and Protamine, Biochemistry (Moscow), 69(2004) 763-9.

[249] N.G. Balabushevich, N.I. Larionova, Fabrication and characterization of polyelectrolyte microparticles with protein, Biochemistry (Moscow), 69(2004) 757-62.

[250] G. Liu, S.G. Iyengar, J.J. Gooding, An electrochemical impedance immunosensor based on gold nanoparticle-modified electrodes for the detection of HbA1c in human blood, Electroanalysis, 24(2012) 1509-16.

[251] F.M. El-Cheick, F.A. Rashwan, H.A. Mahmoud, M. El-Rouby, Gold nanoparticle-modified glassy carbon electrode for electrochemical investigation of aliphatic di-carboxylic acids in aqueous media, J Solid State Electrochem, 14(2010) 1425-43.

[252] A. Bonanni, M. Pumera, Y. Miyahara, Influence of gold nanoparticle size (2–50 nm) upon its electrochemical behavior: an electrochemical impedance spectroscopic and voltammetric study, Physical Chemistry Chemical Physics, 13(2011) 4980-6.

[253] Y.C. Cao, R. Jin, C.A. Mirkin, Nanoparticles with Raman spectroscopic fingerprints for DNA and RNA detection, Science, 297(2002) 1536-40.

[254] P. Ghosh, G. Han, M. De, C.K. Kim, V.M. Rotello, Gold nanoparticles in delivery applications, Advanced Drug Delivery Reviews, 60(2008) 1307-15.

[255] W.-F. Dong, G.B. Sukhorukov, H. Möhwald, Enhanced Raman imaging and optical spectra of gold nanoparticle doped microcapsules, Physical Chemistry Chemical Physics, 5(2003) 3003-12.

[256] M.F. Bédard, D. Braun, G.B. Sukhorukov, A.G. Skirtach, Toward self-assembly of nanoparticles on polymeric microshells: near-IR release and permeability, ACS Nano, 2(2008) 1807-16.

[257] M.F. Bédard, B.G. De Geest, A.G. Skirtach, H. Möhwald, G.B. Sukhorukov, Polymeric microcapsules with light responsive properties for encapsulation and release, Advances in Colloid and Interface Science, 158(2010) 2-14.

[258] T. Hoare, J. Santamaria, G.F. Goya, S. Irusta, D. Lin, S. Lau, R. Padera, R. Langer, D.S. Kohane, A magnetically triggered composite membrane for on-demand drug delivery, Nano Letters, 9(2009) 3651-7.

[259] T.A. Kolesnikova, D.A. Gorin, P. Fernandes, S. Kessel, G.B. Khomutov, A. Fery, D.G. Shchukin, H. Möhwald, Nanocomposite microcontainers with high ultrasound sensitivity, Advanced Functional Materials, 20(2010) 1189-95.

[260] T.Y. Liu, K.H. Liu, D.M. Liu, S.Y. Chen, I.W. Chen, Temperature-sensitive nanocapsules for controlled drug release caused by magnetically triggered structural disruption, Advanced Functional Materials, 19(2009) 616-23.

[261] T. Mauser, C. Déjugnat, G.B. Sukhorukov, Reversible pH-dependent properties of multilayer microcapsules made of weak polyelectrolytes, Macromolecular Rapid Communications, 25(2004) 1781-5.

[262] A. Fery, B. Schöler, T. Cassagneau, F. Caruso, Nanoporous thin films formed by salt-induced structural changes in multilayers of poly (acrylic acid) and poly (allylamine), Langmuir, 17(2001) 3779-83.

[263] A.D. Price, A.N. Zelikin, Y. Wang, F. Caruso, Triggered enzymatic degradation of DNA within selectively permeable polymer capsule microreactors, Angewandte Chemie International Edition, 48(2009) 329-32.

[264] A. Faucheux, A.C. Gouget-Laemmel, C.H. de Villeneuve, R. Boukherroub, F. Ozanam, P. Allongue, J.N. Chazalviel, Well-defined carboxyl-terminated alkyl monolayers grafted onto H-Si(111): Packing density from a combined AFM and quantitative IR study, Langmuir, 22(2006) 153-62.

[265] M. James, S. Ciampi, T.A. Darwish, T.L. Hanley, S.O. Sylvester, J.J. Gooding, Nanoscale water condensation on click-functionalized self-assembled monolayers, Langmuir, 27(2011) 10753-62.

[266]http://www2.warwick.ac.uk/fac/sci/physics/current/postgraduate/regs/mpags/ex5/techniques/optical/ellipsometry/.

[267] K.R. Spring, M.W. Davidson, Introduction to fluorescence microscopy, Nikon Microscopy microscopyu com/articles/fluorescence/fluorescenceintro html.

[268] L.E. Averett, M.H. Schoenfisch, Atomic force microscope studies of fibrinogen adsorption, Analyst, 135(2010) 1201-9.

[269] A.B. Sieval, A.L. Demirel, J.W.M. Nissink, M.R. Linford, J.H. van der Maas, W.H. de Jeu, H. Zuilhof, E.J.R. Sudhölter, Highly stable Si–C linked functionalized monolayers on the silicon (100) surface, Langmuir, 14(1998) 1759-68.

[270] J. Wang, Y. Zhou, M. Watkinson, J. Gautrot, S. Krause, High-sensitivity light-addressable potentiometric sensors using silicon on sapphire functionalized with self-assembled organic monolayers, Sensors and Actuators B: Chemical, 209(2015) 230-6.

[271] O. Koster, W. Schuhmann, H. Vogt, W. Mokwa, Quality control of ultra-microelectrode arrays using cyclic voltammetry, electrochemical impedance spectroscopy and scanning electrochemical microscopy, Sensors and Actuators B: Chemical, 76(2001) 573-81.

[272] V. Molinero, E.J Calvo, Eletrostatic interactions at self-assembled molecular films of charged thiols on gold, Journal of Electroanalytical Chemistry, 445(1998) 17-25.

[273] A. Poghossian, M.H. Abouzar, M. Sakkari, T. Kassab, Y. Han, S. Ingebrandt, A. Offenhäusser, M.J. Schöning, Field-effect sensors for monitoring the layer-by-layer adsorption of charged macromolecules, Sensors and Actuators B: Chemical, 118(2006) 163-70.

[274] J. Wang, L.M. Frostman, M.D. Ward, Self-assembled thiol monolayers with carboxylic acid functionality: measuring pH-dependent phase transitions with the quartz crystal microbalance, J. Phys. Chem, 96(1992) 5224-5228.

[275] J.E. Gautrot, B. Trappmann, F. Oceguera-Yanez, J. Connelly, X. He, F.M. Watt, W.T. Huck, Exploiting the superior protein resistance of polymer brushes to control single cell adhesion and polarisation at the micron scale, Biomaterials, 31(2010) 5030-41.

[276] Y. Qiangying, UV-triggered Encapsulation and Release by Multilayer Microcapsules: Queen Mary University of London; PhD thesis, 2013.

[277] A. Ng, S. Ciampi, M. James, J.B. Harper, J.J. Gooding, Comparing the reactivity of alkynes and alkenes on silicon (100) surfaces, Langmuir, 25(2009) 13934-41.

[278] C.C.A. Ng, S. Ciampi, J.B. Harper, J.J. Gooding, Antifouling behaviour of silicon surfaces modified with self-assembled monolayers containing both ethylene glycol and charged moieties, Surface Science, 604(2010) 1388-94.

[279] S. Ciampi, M. James, P. Michaels, J.J. Gooding, Tandem "click" reactions at acetylene-terminated Si (100) monolayers, Langmuir, 27(2011) 6940-9.

[280] T. Palacin, H.L. Khanh, B. Jousselme, P. Jegou, A. Filoramo, C. Ehli, D.M. Guldi, S. Campidelli, Efficient functionalization of carbon nanotubes with porphyrin dendrons via click chemistry, Journal of the American Chemical Society, 131(2009) 15394-402.

[281] A. Poghossian, S. Ingebrandt, M. Abouzar, M. Schöning, Label-free detection of charged macromolecules by using a field-effect-based sensor platform: Experiments and possible mechanisms of signal generation, Applied Physics A, 87(2007) 517-24.

[282] J. Szeponik, W. Moritz, A new structure for chemical senspr devices, Sensors and Actuators B: Chemical, 2(1990) 243-6.

[283] C.-S. Lee, S.-H. Lee, S.-S. Park, Y.-K. Kim, B.-G. Kim, Protein patterning on silicon-based surface using background hydrophobic thin film, Biosensors and Bioelectronics, 18(2003) 437-44.

[284] S. Lenci, L. Tedeschi, F. Pieri, C. Domenici, UV lithography-based protein patterning on silicon: Towards the integration of bioactive surfaces and CMOS electronics, Applied Surface Science, 257(2011) 8413-9.

[285] H. Sorribas, C. Padeste, L. Tiefenauer, Photolithographic generation of protein micropatterns for neuron culture applications, Biomaterials, 23(2002) 893-900.

[286] E. Balaur, T. Djenizian, R. Boukherroub, J. Chazalviel, F. Ozanam, P. Schmuki, Electron beam-induced modification of organic monolayers on Si (111) surfaces used for selective electrodeposition, Electrochemistry Communications, 6(2004) 153-7.

[287] N. Saito, S. Youda, K. Hayashi, H. Sugimura, O. Takai, Chemical resistivity of self-assembled monolayer covalently attached to silicon substrate to hydrofluoric acid and ammonium fluoride, Surface Science, 532(2003) 970-5.

[288] G. Saini, R. Gates, M.C. Asplund, S. Blair, S. Attavar, M.R. Linford, Directing polyallylamine adsorption on microlens array patterned silicon for microarray fabrication, Lab on a Chip, 9(2009) 1789-96.

[289] A.R. Pike, S.N. Patole, N.C. Murray, T. Ilyas, B.A. Connolly, B.R. Horrocks, A. Houlton, Covalent and non-covalent attachment and patterning of polypyrrole at silicon surfaces, Advanced Materials, 15(2003) 254-7.

[290] J.A. Haber, N.S. Lewis, Infrared and X-ray photoelectron spectroscopic studies of the reactions of hydrogen-terminated crystalline Si (111) and Si (100) surfaces with Br_2, I_2, and ferrocenium in alcohol solvents, The Journal of Physical Chemistry B, 106(2002) 3639-56.

[291] H.G. Monbouquette, M. Garcia-Garibay, Surface nanopatterning, Google Patents 2004.

[292] Y. Xia, X.-M. Zhao, G.M. Whitesides, Pattern transfer: Self-assembled monolayers as ultrathin resists, Microelectronic Engineering, 32(1996) 255-68.

[293] M.B. Smith, in: M.B. Smith (Ed.) Organic Synthesis (Third Edition), Academic Press, Oxford, 2010.

[294] H.-J. Chen, D. Wen, Ultrasonic-aided fabrication of gold nanofluids, Nanoscale Research Letters, 6(2011) 1-8.

[295] C.C.A. Ng, S. Ciampi, J.B. Harper, J.J. Gooding, Antifouling behaviour of silicon surfaces modified with self-assembled monolayers containing both ethylene glycol and charged moieties, Surface Science, 604(2010) 1388-94.

[296] M. Schönhoff, V. Ball, A.R. Bausch, C. Dejugnat, N. Delorme, K. Glinel, R.v. Klitzing, R. Steitz, Hydration and internal properties of polyelectrolyte multilayers, Colloids and Surfaces A: Physicochemical and Engineering Aspects, 303(2007) 14-29.

[297] M. Pekker, M. Schneider, The surface charge of a cell lipid membrane, arXiv preprint arXiv:14014707, (2014).

[298] S. Marcelja, Electrostatics of membrane adhesion, Biophysical Journal, 61(1992) 1117-1121.

[299] K. Thethi, P. Jurasz, A. MacDonald, A. Befus, S. Man, M. Duszyk, Determination of cell surface charge by photometric titration, Journal of Biochemical and Biophysical Methods, 34(1997) 137-45.

[300] S. McLaughlin, G. Szabo, G. Eisenman, Divalent ions and the surface potential of charged phospholipid membranes, The Journal of General Physiology, 58(1971) 667-87.

[301] L. Weiss, R. Zeigel, Cell surface negativity and the binding of positively charged particles, Journal of cellular physiology, 77(1971) 179-85.

[302] R. Hahin, D.T. Campbell, Simple shifts in the voltage dependence of sodium channel gating caused by divalent cations, The Journal of General Physiology, 82(1983) 785-805.

[303] E. Dziubakiewicz, K. Hrynkiewicz, M. Walczyk, B. Buszewski, Study of charge distribution on the surface of biocolloids, Colloids and Surfaces B: Biointerfaces, 104(2013) 122-7.

[304] Z.A. Lu, V. Ramanujamand, M. Luo, D. Herndon, K. Kita, The effect of extracellular calcium on cellular adhesion of mesenchymal stem cells to substrates, The FASEB Journal, 25(2011) 678-7.

[305] M. Takeichi, T.S. Okada, Roles of magnesium and calcium ions in cell-to-substrate adhesion, Experimental Cell Research, 74(1972) 51-60.

[306] J. Devaux, M. Gola, G. Jacquet, M. Crest, Effects of K^+ channel blockers on developing rat myelinated CNS axons: identification of four types of K^+ channels, Journal of Neurophysiology, 87(2002) 1376-85.

[307] A. Han, A.B. Frazier, Ion channel characterization using single cell impedance spectroscopy, Lab on a Chip, 6(2006) 1412-4.